

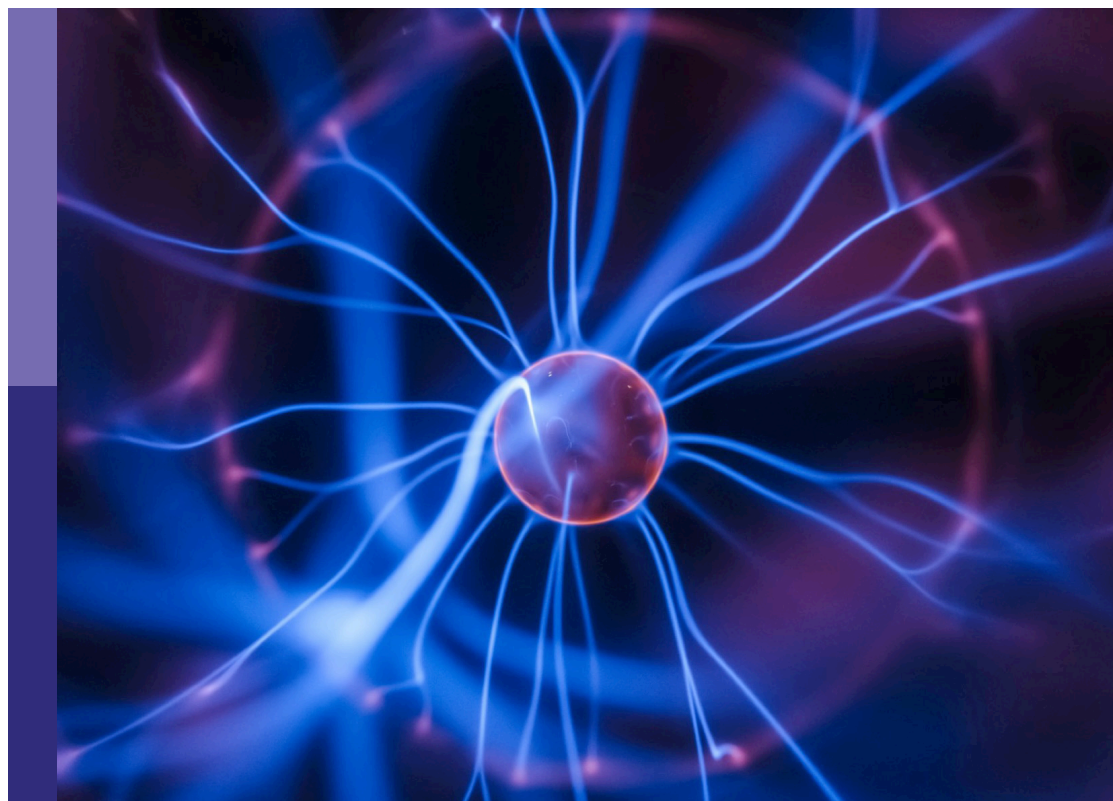
Application of spectroscopy in agricultural environment and livestock breeding

Edited by

Jinchang Ren, Leizi Jiao
and Kun Wang

Published in

Frontiers in Physics
Frontiers in Plant Science
Frontiers in Nutrition



FRONTIERS EBOOK COPYRIGHT STATEMENT

The copyright in the text of individual articles in this ebook is the property of their respective authors or their respective institutions or funders. The copyright in graphics and images within each article may be subject to copyright of other parties. In both cases this is subject to a license granted to Frontiers.

The compilation of articles constituting this ebook is the property of Frontiers.

Each article within this ebook, and the ebook itself, are published under the most recent version of the Creative Commons CC-BY licence. The version current at the date of publication of this ebook is CC-BY 4.0. If the CC-BY licence is updated, the licence granted by Frontiers is automatically updated to the new version.

When exercising any right under the CC-BY licence, Frontiers must be attributed as the original publisher of the article or ebook, as applicable.

Authors have the responsibility of ensuring that any graphics or other materials which are the property of others may be included in the CC-BY licence, but this should be checked before relying on the CC-BY licence to reproduce those materials. Any copyright notices relating to those materials must be complied with.

Copyright and source acknowledgement notices may not be removed and must be displayed in any copy, derivative work or partial copy which includes the elements in question.

All copyright, and all rights therein, are protected by national and international copyright laws. The above represents a summary only. For further information please read Frontiers' Conditions for Website Use and Copyright Statement, and the applicable CC-BY licence.

ISSN 1664-8714
ISBN 978-2-8325-3257-7
DOI 10.3389/978-2-8325-3257-7

About Frontiers

Frontiers is more than just an open access publisher of scholarly articles: it is a pioneering approach to the world of academia, radically improving the way scholarly research is managed. The grand vision of Frontiers is a world where all people have an equal opportunity to seek, share and generate knowledge. Frontiers provides immediate and permanent online open access to all its publications, but this alone is not enough to realize our grand goals.

Frontiers journal series

The Frontiers journal series is a multi-tier and interdisciplinary set of open-access, online journals, promising a paradigm shift from the current review, selection and dissemination processes in academic publishing. All Frontiers journals are driven by researchers for researchers; therefore, they constitute a service to the scholarly community. At the same time, the *Frontiers journal series* operates on a revolutionary invention, the tiered publishing system, initially addressing specific communities of scholars, and gradually climbing up to broader public understanding, thus serving the interests of the lay society, too.

Dedication to quality

Each Frontiers article is a landmark of the highest quality, thanks to genuinely collaborative interactions between authors and review editors, who include some of the world's best academicians. Research must be certified by peers before entering a stream of knowledge that may eventually reach the public - and shape society; therefore, Frontiers only applies the most rigorous and unbiased reviews. Frontiers revolutionizes research publishing by freely delivering the most outstanding research, evaluated with no bias from both the academic and social point of view. By applying the most advanced information technologies, Frontiers is catapulting scholarly publishing into a new generation.

What are Frontiers Research Topics?

Frontiers Research Topics are very popular trademarks of the *Frontiers journals series*: they are collections of at least ten articles, all centered on a particular subject. With their unique mix of varied contributions from Original Research to Review Articles, Frontiers Research Topics unify the most influential researchers, the latest key findings and historical advances in a hot research area.

Find out more on how to host your own Frontiers Research Topic or contribute to one as an author by contacting the Frontiers editorial office: frontiersin.org/about/contact

Application of spectroscopy in agricultural environment and livestock breeding

Topic editors

Jinchang Ren — Robert Gordon University, United Kingdom

Leizi Jiao — National Research Center of Intelligent Equipment for Agriculture, Beijing Academy of Agriculture and Forestry Sciences, China

Kun Wang — Aerospace Information Research Institute, Chinese Academy of Sciences (CAS), China

Citation

Ren, J., Jiao, L., Wang, K., eds. (2023). *Application of spectroscopy in agricultural environment and livestock breeding*. Lausanne: Frontiers Media SA.
doi: 10.3389/978-2-8325-3257-7

Table of contents

- 05 **Automatic detection of sow posture and estrus based on convolutional neural network**
Hongxiang Xue, Jinxin Chen, Qi'an Ding, Yuwen Sun, Mingxia Shen, Longshen Liu, Xudong Chen and Junyi Zhou
- 18 **Hyperspectral estimation of the soluble solid content of intact netted melons decomposed by continuous wavelet transform**
Chao Zhang, Yue Shi, Zhonghui Wei, Ruiqi Wang, Ting Li, Yubin Wang, Xiaoyan Zhao and Xiaohe Gu
- 25 **Detection of NH_3 in poultry housing based on tunable diode laser absorption spectroscopy combined with a micro circular absorption cell**
Ke Wang, Rui Guo, Yunhai Zhou, Leizi Jiao and Daming Dong
- 33 **High-pressure treatment enhanced aromatic compound concentrations of melon juice and its mechanism**
Xiao Liu, Ruiqi Wang, He Liu, Yubin Wang, Yue Shi and Chao Zhang
- 46 **The estimation of broiler respiration rate based on the semantic segmentation and video amplification**
Jintao Wang, Longshen Liu, Mingzhou Lu, Cedric Okinda, Daniela Lovarelli, Marcella Guarino and Mingxia Shen
- 59 **Visualizing changes of metabolites during iron deficiency chlorosis in field-grown pear leaves using micro-Raman spectral imaging**
Zhen Gao, Chunjiang Zhao, Daming Dong, Songzhong Liu, Xuelin Wen, Yifan Gu and Leizi Jiao
- 68 **Extraction of 3D distribution of potato plant CWSI based on thermal infrared image and binocular stereovision system**
Liuyang Wang, Yanlong Miao, Yuxiao Han, Han Li, Man Zhang and Cheng Peng
- 88 **Application of deep learning methods in behavior recognition of laying hens**
Fujie Wang, Jiquan Cui, Yingying Xiong and Huishan Lu
- 98 **Non-destructive prediction and visualization of anthocyanin content in mulberry fruits using hyperspectral imaging**
Xunlan Li, Zhaoxin Wei, Fangfang Peng, Jianfei Liu and Guohui Han
- 110 **Oil content analysis of corn seeds using a hand-held Raman spectrometer and spectral peak decomposition algorithm**
Yuan Jin, Hongwu Tian, Zhen Gao, Guiyan Yang and Daming Dong

- 118 **Novel candidate genes for lignin structure identified through genome-wide association study of naturally varying *Populus trichocarpa***
Nathan Bryant, Jin Zhang, Kai Feng, Mengjun Shu, Raphael Ployet, Jin-Gui Chen, Wellington Muchero, Chang Geun Yoo, Timothy J. Tschaplinski, Yunqiao Pu and Arthur J. Ragauskas
- 128 **Rapid automatic detection of water Ca, Mg elements using laser-induced breakdown spectroscopy**
Yijun Zhu, Shixiang Ma, Guiyan Yang, Hongwu Tian and Daming Dong



OPEN ACCESS

EDITED BY

Leizi Jiao,
Beijing Academy of Agriculture and
Forestry Sciences, China

REVIEWED BY

Huaibo Song,
Northwest A&F University, China
Guofeng Han,
Jiangsu Academy of Agricultural
Sciences (JAAS), China

*CORRESPONDENCE

Mingxia Shen,
mingxia@njau.edu.cn

SPECIALTY SECTION

This article was submitted to Optics and
Photonics,
a section of the journal
Frontiers in Physics

RECEIVED 05 September 2022

ACCEPTED 26 September 2022

PUBLISHED 11 October 2022

CITATION

Xue H, Chen J, Ding Q, Sun Y, Shen M,
Liu L, Chen X and Zhou J (2022),
Automatic detection of sow posture and
estrus based on convolutional
neural network.
Front. Phys. 10:1037129.
doi: 10.3389/fphy.2022.1037129

COPYRIGHT

© 2022 Xue, Chen, Ding, Sun, Shen, Liu,
Chen and Zhou. This is an open-access
article distributed under the terms of the
[Creative Commons Attribution License](https://creativecommons.org/licenses/by/4.0/)
(CC BY). The use, distribution or
reproduction in other forums is
permitted, provided the original
author(s) and the copyright owner(s) are
credited and that the original
publication in this journal is cited, in
accordance with accepted academic
practice. No use, distribution or
reproduction is permitted which does
not comply with these terms.

Automatic detection of sow posture and estrus based on convolutional neural network

Hongxiang Xue^{1,2}, Jinxin Chen^{1,2}, Qi'an Ding^{1,2}, Yuwen Sun^{1,2},
Mingxia Shen^{2,3*}, Longshen Liu^{2,3}, Xudong Chen⁴ and
Junyi Zhou⁴

¹School of Engineering, Nanjing Agricultural University, Nanjing, China, ²Key Laboratory of Breeding Equipment, Ministry of Agriculture and Rural Affairs, Nanjing, China, ³School of Artificial Intelligence, Nanjing Agricultural University, Nanjing, China, ⁴Sheyang County Bureau of Agriculture and Rural Affairs, Yancheng, China

Estrus detection is an essential operation in the breeding of sows, and accurate estrus detection is immensely important to maintain the productivity and reproductive performance of sow. However, traditional sow estrus detection relies on the manually back-pressure test, which is time-consuming and labor-intensive. This study aimed to develop an automatic method to detect estrus. In this study, a model based on the optimized yolov5s algorithm was constructed to detect the four sow postures of standing, sitting, sternum, lateral, and calculated the frequency of posture change in sows. Based on this, we studied the behavior of sows before and after estrus. The method embedded a [convolutional block attention module](#) into the backbone network to improve the feature extraction capability of the model. In addition, the object box judgment module was used to avoid interference from other sows in the detection region. Accelerate the optimized model on the TensorRT platform, ensuring that the embedded graphics card can run the model with lower latency. The result shows that the precision of estrus detection is 97.1%, and the accuracy of estrus detection is 94.1%. The processing time of a single image on the embedded graphics card is 74.4 ms, and this method could better meet the estrus detection demand in sow production.

KEYWORDS

sow, posture, estrus, machine vision, YOLOv5

1 Introduction

Estrus detection is an important link in reproductive management of sows, and the accuracy and timeliness of estrus detection directly affect the judgments of swine farm workers on ovulation time in post-weaning sows [1]. Behavioral expression of sow is a reflection of dynamic changes of hormone levels [2]. In estrus, sow rest time decreased, frequency and duration of activity, and standing time increased. Real-time detection of the sow posture helps to automatically monitor their estrus status and health status [3].

Some scholars have done some studies about sow's visits to boars or bionic boars. Houwers 1988) [4] used a 'ticket-window' to monitor the frequency of boar visits, and the results showed that when sows were estrus, the frequency of sow visits gradually increased significantly. However, when multiple sows were present in the detection area, the system could not detect the estrus status of the sows. In order to solve the above problems, Bressers et al 1995) improved the 'ticket-window' and divided the data into subsets according to time, the accuracy rate of the proposed method was over 90%, and the false negative rate was less than 5% [5]. On this basis, Korthals 1999) comprehensively considered the sow's behavior of visiting boars and the activity of individual sows. The sensitivity and accuracy of the model were further improved, but the response time of the system was slow [6]. To reduce response time and the number of false alarms, Ostensen et al (2010) modeled separately the duration and frequency of sow visits, and then fused the two models. The results showed that the model was more specific than this previous study [7]. The above studies are all based on the 'ticket window' of boars, but few studies have been reported based on the 'contact window' of bionic boars. Lei et al (2021) used bionic boar and image acquisition device to detect estrus in sows. The results showed that the interaction frequencies during the estrus period was significantly higher than that of sows during the non-estrus period [8]. In summary, the use of boars or bionic boars to detect estrus is an effective method. However, in recent years, with the outbreak of African swine fever, large-scale pig farms have begun to reduce the use of boars.

In order to solve the problem mentioned above, many scholars began to try to find some reliable alternative methods. Bressers 1993) used an accelerometer and set activity thresholds to detect estrus in sows. Findings showed that the acceleration change range of sows during the estrus period was significantly higher than that of sows during the non-estrus period [9]. However, due to some factors such as service life, wearable sensors cannot be popularized and applied in large-scale pig farms. Freson et al 1998) used infrared sensor to continuously monitor the body activity of the sows. According to the results, when using the daily body activity of sows as the model parameters, the accuracy rate of the estrus of sows was 86% [10]. This study is the first published literature on estrus detection in individually housed sows. Jeong et al (2013) used the wireless sensor network to measure the activity in real time, and found that sows in estrus increase in activity [11]. Wang et al (2020) put posture sensors on the neck of the sows to collect the posture data, the results showed that when the recognition time of estrus behavior was 30 min, the recognition error rate was 13.43%, the recall rate was 90.63%, and the specificity was 81.63% [12]. However, the device used in this study needs to be worn on the neck of the sow and cannot work for long periods of time. According to the above, it is feasible to predict the estrus time of a sow through detecting the frequency of posture change in sows.

With the development of the deep learning theories and edge-computing device, the convolutional neural network

(CNN) has been widely applied in image classification, image segmentation, object detection [13]. However, most traditional CNN is limited by hardware resource, and made it difficult to be deployed in the edge device or mobile terminal. Lightweight design is the major Frontier to improve the detection speed and minimize expenditures [14, 15]. At present, lightweight CNN has been gradually applied in space target detection, unmanned aerial systems (UAS) and so on [16].

In modern sow production, estrus detection in sows still rely largely on workers' experience. After stimulation of the ribs, abdomen and vulva, the estrus state is determined according to the back-pressure test. However, this method is often time-consuming and laborious and mainly depend on the experience of the breeders, which is difficult to meet the needs of real-time detection of sows in modern large-scale sow production.

In response to the above problems, this paper proposes an automatic estrus detection method based on lightweight CNN, and deploy it on a low-cost embedded GPU. This research approach is highly automated, contactless. The main contributions of this paper are presented as follows.

- 1) The YOLOv5s model was used as the base models, and added a convolutional block attention module (CBAM) for feature fusion.
- 2) The estrus status of sows was analyzed according to the frequency of posture change in sows.
- 3) The posture change characteristics of different types of abnormal estrus sows was further explored.

2 Materials and methods

All experimental design and procedures of this study were approved by the Animal Care and Use Committee of Nanjing Agricultural University, in compliance with the Regulations for the Administration of Affairs Concerning Experimental Animals of China (Certification No. SYXK [Su]2011-0036).

2.1 Animals, housing, data acquisition

The data were collected at the Shangbao pig farm, Yancheng City, Jiangsu Province, from 15 September 2021 to 12 January 2022. 72 sows (Yorkshire × Landrace). We used 72 empty sows (Yorkshire × Landrace) that were second or third parity sows. They were transferred to gestation crates (2.2 m × 0.8 m × 0.7 m) after lactation. House temperature was maintained at 24–27 °C, and the relative humidity was 66–82%.

The video acquisition system was mainly composed of three parts: the camera, the wireless, the embedded graphics card (GPU). The system designed for this study is shown in

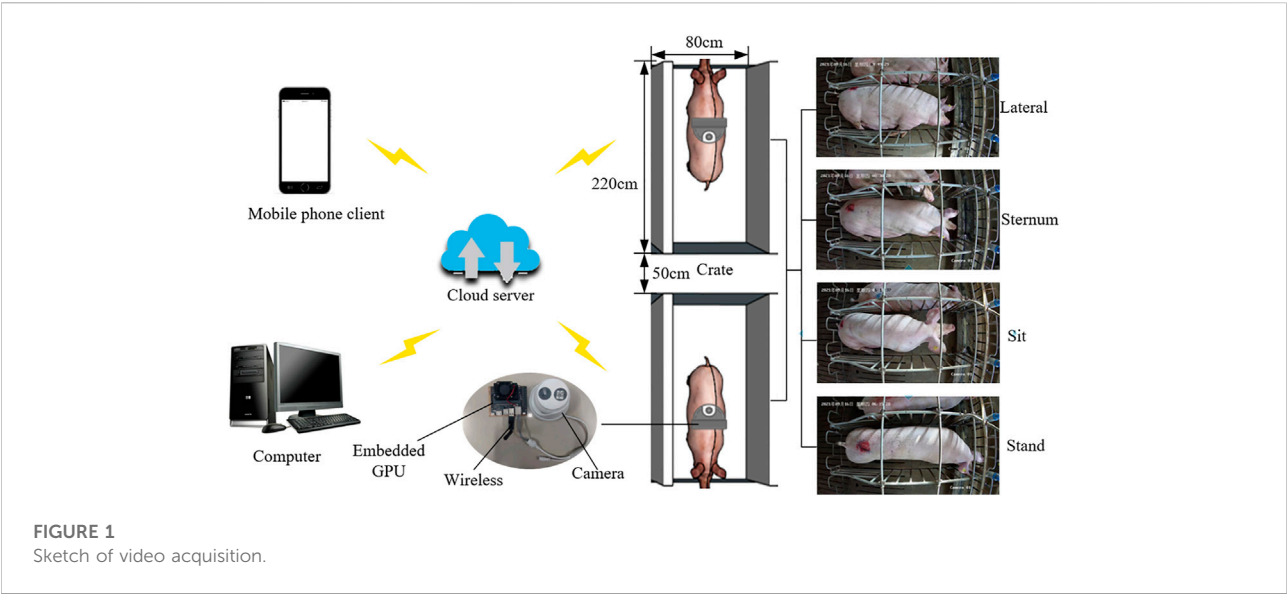
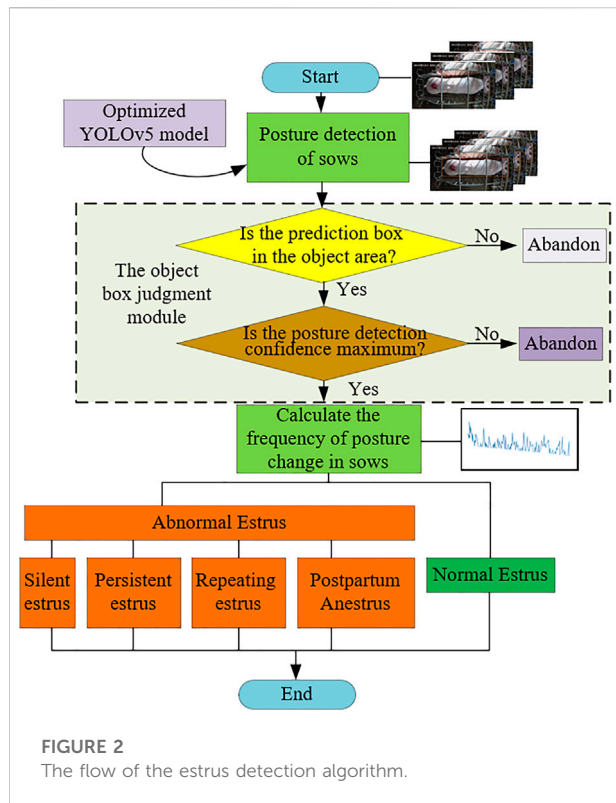


TABLE 1 Definition of different sow postures.

Posture	Definition	Sample
Lateral	The limbs are fully extended and the breast region is clearly visible	
Sternum	The limbs are hidden under the body, and the breast area is not visible	
Sit	The head region is significantly higher than the tail region	
Stand	There is no contact between the abdomen and the ground, and there is no extrusion deformation of the body	

Figure 1. The RGB camera (DS-2CD3346WD-I, HIKVISION, Hangzhou, China) was installed 2.3 m above the gestation crate. Each camera was connected to an embedded GPU (Jetson Nano 4 GB Developer Kit, Nvidia, America) *via* an ethernet cable. For the image acquisition device, the acquisition frequency was set to 1,500 fps, and the resolution was 2,560 (horizontal resolution) ×1,440 (Vertical resolution). The wireless is used for data transmission, and the embedded GPU is used for data processing. During the experiment, the estrus of sows was detected by artificial estrus check and hormone determination.



The estrus frequency was checked twice a day, at 9:00 a.m. and 3:00 p.m.

2.2 Data set realization

Compared with the sows in non-estrus, most sows in estrus are more active. In order to compare the activity of sows in estrus and non-estrus, the postures were divided into four categories, including lateral, sternum, sit, stand. The definition of each posture is shown in Table 1.

In order to improve the generalization ability of the model and ensure that the dataset could cover different times, 6,000 pictures were selected as data samples. Furthermore, the images with high similarity were removed, and a total of 5,863 pictures were saved. In these pictures, sows in four different postures (stand, sit, sternum, lateral) were annotated using Labellmg software. The dataset is randomly partitioned into three subsets: 80% of them as the training set, 10% as the validation set, and the remaining 10% as the testing set.

2.3 Model building

This study developed a new method for estrus detection in sows. The flow of the estrus detection algorithm is presented in

Figure 2. First, the images of the sows were captured regularly using an embedded GPU. Second, use the optimized yolov5 algorithm to detect the posture of the sow. Third, the object box judgment module determines the coordinates of the sow to be tested and outputs the posture with the highest confidence. Fourth, according to the results of sow posture detection, the frequency of posture transition before and after the sow estrus and the activity characteristics of abnormal estrus sows were analyzed. There are four types of abnormal estrus sows studied in this paper, namely silent estrus, persistent estrus, repeating estrus and postpartum anestrus. The silent estrus sows are reduced feed intake and restlessness, but no significant changes in vulva color and shape. The persistent estrus sows remain depressed or excited, and their estrus go exceeded the normal period, even for more than 10 days. The estrus duration of repeating estrus sows is short, and it heat up again a few days later. The postpartum anestrus sows have no change in feed intake, no estrus symptoms, and no estrus within 10 days after weaning.

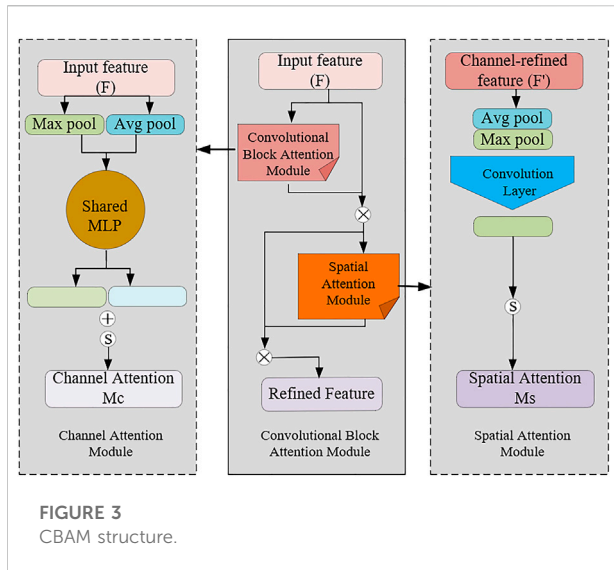
2.3.1 Program environment and training parameter

The model of this paper relies on the Pytorch1.6 deep learning framework. The processor model of the test platform is Intel® Core™ i7 - 11700 k, the graphics card model is NVIDIA GTX3090, and the graphics card memory is 24G. The deep learning environments such as Python3.8, CUDA11.4, and Opencv4.5.1 are configured on the Ubuntu18.04. Optimized model applied to embedded GPU. The number of epochs was set to 300 to allow adequate time for model convergence.

2.3.2 Basic model

YOLOv5 was selected to work as the base model in this study. According to different network depth and width, YOLOv5 can be divided into four basic network structures: YOLOv5s, YOLOv5m, YOLOv5l and YOLOv5x [17]. The model is mainly composed of four modules: the input module, the backbone module, the neck module, the prediction module. The input module is used to input the image of sow posture, the backbone module for sow posture image feature extraction, the neck module for sow posture image feature fusion, and the prediction module for sow position prediction [18].

In input module, to improve generalization of the model, image mosaic is used to enhance the datasets [19]. In backbone module, it mainly includes the focus structure and the cross stage partial Network (CSPNet). Among them, the focus structure is mainly used to complete the slice operation, to extract the posture features more fully, and effectively to reduce the loss of data in the down-sampling process. The CSPNet is mainly used to reduce the computational bottleneck and memory overhead. Optimizing the core network with CSPNet can improve the model detection performance, enhance the



learning ability of CNN, and fully reduce the computation and inference time. In neck module, it mainly includes the feature pyramid network (FPN) and the path augmentation network (PAN). Among them, FPN uses a top-down architecture to fuse the feature of high-level layers. Conversely, PAN uses a down-top architecture to transfer strong location features. In prediction module, to improve location precision and recognition accuracy, we used the generalized intersection over union (GIoU_loss) as the loss foundation [20].

The performance evaluation indicators of the sow posture classification model mainly include model size, precision, recall, f1score, detection speed, parameters. The calculation method of precision is shown in Eq. 1, the calculation method of recall is shown in Eq. 2, and the calculation method of f1 score is shown in Eq. 3.

$$\text{Precision} = \frac{TP}{TP + FP} \quad (1)$$

$$\text{Recall} = \frac{TP}{TP + FN} \quad (2)$$

$$\text{F1score} = 2 \times \frac{\text{Precision} \times \text{Recall}}{\text{Precision} + \text{Recall}} \quad (3)$$

2.3.3 The object box judgment module

The accurate detection of sow posture to be tested is the basis of analyzing sow estrus status. Since multiple sows appear in the region to be tested, we set a rectangular bounding box surrounded by four pixels [150,350], [2,380,350] [150,1,020], and [2380,1020]. Furthermore, due to the existence of transition posture, a single sow has multiple output results. To solve this issue, a judgment module was added after the prediction module, and this ensured that the output is the highest degree of confidence score.

2.3.4 CBAM module

Due to the influence of sow body pollution and poor light conditions, it is difficult to extract the characteristics of limbs, breast region and abdominal areas. Using the attention mechanism can suppress the redundant background information, enhance the feature representation of the sow limb parts in the image, and improve the recognition performance of the posture detection model. The channel attention and spatial attention are combined in the reverse residual block to highlight the target features in the feature graph generated by the deep convolution and improve the recognition performance of the model [21, 22]. The output feature map of the CBAM module acting on the deep convolution. CBAM is a simple and efficient attention module for feed-forward CNN, which takes a given feature map in turn along the channel attention module (CAM) and the spatial attention module (SAM). CBAM can assist the sow posture detection model to locate the region of interest and suppress useless information. The overall flow of the CBAM module is shown in Figure 3.

In Figure 3, M_C represents channel attention in the Convolutional Block Attention Model, and M_S represents spatial attention model. The M_C calculation formula is shown as in Eq. 4, The M_S calculation formula is shown as in Eq. 5.

$$M_C(F) = \sigma(\text{MLP}(\text{AvgPool}(F)) + \text{MLP}(\text{MaxPool}(F))), \quad (4)$$

$$= \sigma(W_1(W_0(F_{\text{avg}}^c)) + W_1(W_0(F_{\text{max}}^c))),$$

$$M_S(F) = \sigma(f^{7 \times 7}([\text{AvgPool}(F); \text{MaxPool}(F)])), \quad (5)$$

$$= \sigma(f^{7 \times 7}([F_{\text{avg}}^s; F_{\text{max}}^s])).$$

In Eq. 4, MLP is a Multi-Layer Perceptron Neural network [23], Avg pool () represents the module averaging pooling of the feature graph, Max pool () means the module maximizing pooling of the feature graph, and $F_{\text{avg}}^c, F_{\text{max}}^c$ represent the global average pooling and the maximum average pooling of the channel attention mechanism [24], respectively.

$$F_S = \sigma(\text{Conv}(\text{Cat}(F_{\text{avg}}^s, F_{\text{max}}^s))) \otimes F_X, \quad (6)$$

$$= \sigma(f^{7 \times 7}([F_{\text{avg}}^s; F_{\text{max}}^s])).$$

In Eq. 6: Cat represents the connection operation, $f^{7 \times 7}$ is a convolution of 7×7 , and $F_{\text{avg}}^s, F_{\text{max}}^s$ represent the global average pooling and the maximum average pooling operations of the spatial attention mechanism, respectively. YOLOv5s has no attention preference during feature extraction, and uses the same weighting method for features of different degrees of importance. In this study, we solve the problem of no attention preference in the original network by introducing CBAM modules respectively after three CSP modules, enabling the network to pay more attention to the target of interest during the detection process.

2.3.5 Model lightweight

To achieve rapid inference of the posture classification model, the CNN model was optimized. First, to ensure that the embedding can run this model with higher throughput and

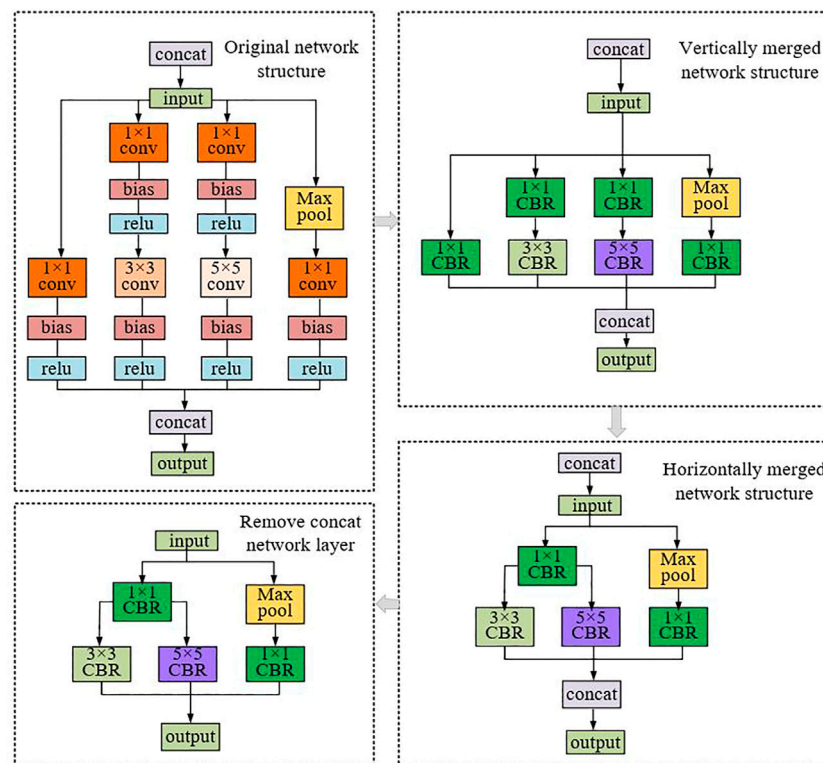


FIGURE 4
The lightweight process of the model.

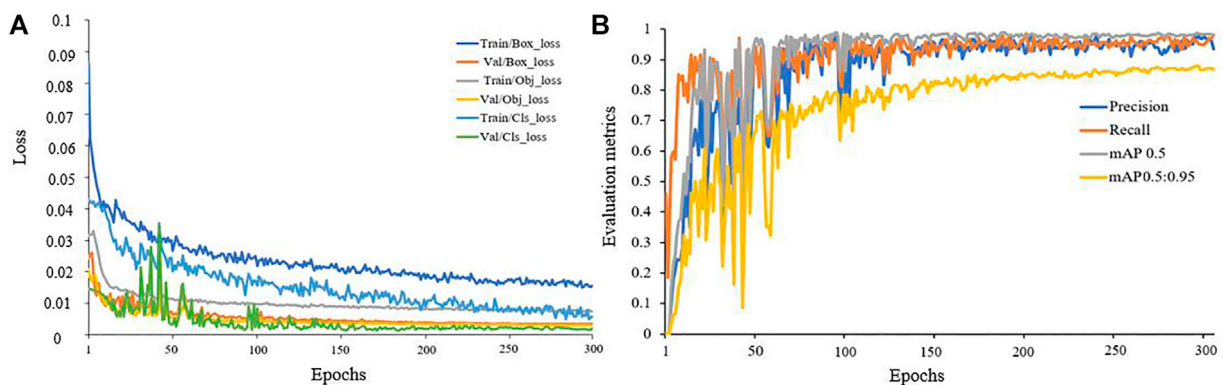


FIGURE 5
Training and test results for the sow posture detection model. (A) Loss curve (B) Evaluate metrics curve.

lower latency, we remove the useless output layer in the model. Second, to achieve the vertical integration of the network structure, the three layers of CONV, BN, and Leaky Relu were integrated into one CBL layer. Third, to achieve a horizontal combination of the network structures, the three 1×1 CBL layers

were fused into one 1×1 CBL layer. Fourth, to reduce the transmission throughput, the contact layers in the network structure were removed. After completing the above steps, the model was deployed to the embedded GPU. The model lightweight procedure is shown in Figure 4.

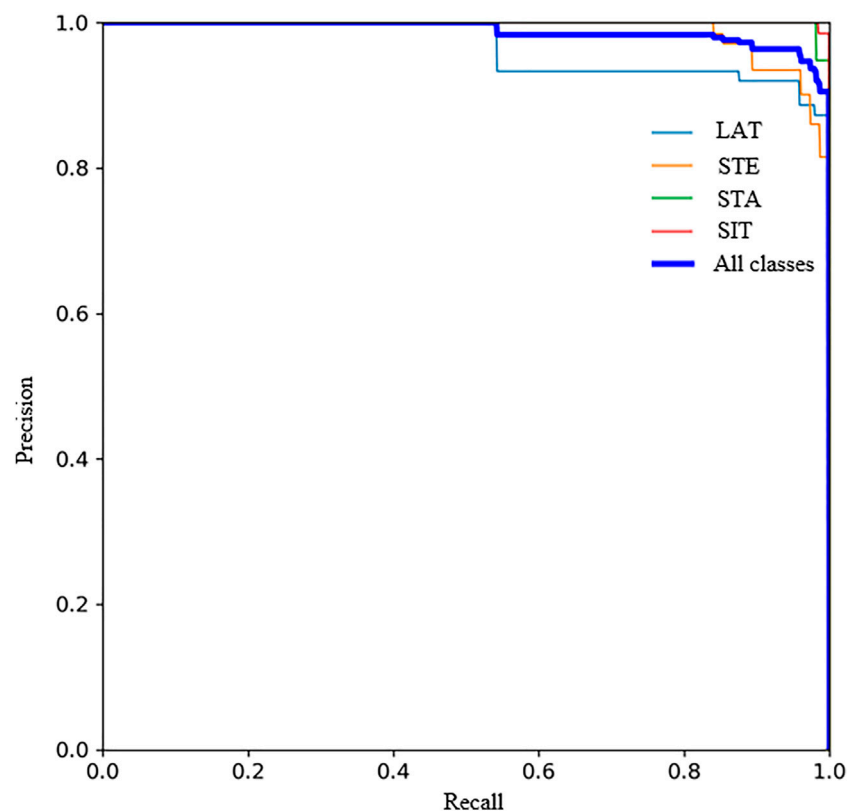


FIGURE 6
P-R curve.

2.3.6 Contrast models

In order to select the optimal model, this study compared the detection performance of different size YOLOv5 models (YOLOv5x, YOLOv5l, YOLOv5m, YOLOv5s), multiple attention mechanisms, including CAM, efficient channel attention module (ECA), and squeeze and excitation module (SE) [25, 26]. In addition, this study compared the optimization effect of the bidirectional feature pyramid network and the attention mechanism. Furthermore, we compared the proposed model with some representative lightweight object detection models, including MobileDets, NanoDet. MobileDets is a model based on the extended search space series, which can achieve a better balance between delay and accuracy on mobile devices [27]. NanoDet is an ultra-fast and lightweight mobile Anchor-free object detection model, and it is also convenient for training and transplantation [28, 29].

3 Results and Discussion

In Section 3.1, this study analyzes the training and testing results of the model. In Section 3.2, Section 3.3 and Section 3.4,

the sow posture detection performance of different models is compared. In Section 3.5, the detection performance of the model on night and daytime data is tested. In Section 3.6, the characteristics of the frequency of posture change in empty sows before and after estrus are analyzed and tested. In Section 3.7, the characteristics of the frequency of posture change in abnormal estrus sows were explored. In Section 3.8, The shortcomings of the study are analyzed.

3.1 Training and testing results

The loss curve for posture detection model is shown in Figure 5A. Train/Box_loss, Train/Obj_loss, Train/Cls_loss represent the position coordinate prediction loss, confidence prediction loss, and category prediction loss of the training dataset, respectively. Val/Box_loss, Val/Obj_loss, Train/Cls_loss represent the position coordinate prediction loss, confidence prediction loss, and category prediction loss of the validation dataset set, respectively. In the initial stage, the loss value decreases rapidly, and then gradually stabilizes, which means that the model gradually converges.

TABLE 2 Experimental results of YOLOv5 with different sizes.

Model	Size (MB)	Precision (%)	Recall (%)	F1score (%)	Speed (ms)	Parameters
YOLOv5s	14.4	96.8	94.9	95.8	7.6	7.03×10^6
YOLOv5m	42.2	96.1	95.7	95.9	8.8	2.09×10^7
YOLOv5l	92.8	98.4	93.9	96.1	10.3	4.61×10^7
YOLOv5x	173.1	96.3	94.7	95.5	12.8	8.62×10^7

TABLE 3 Experimental results of different optimization methods.

Model	Size (MB)	Precision (%)	Recall (%)	F1score (%)	Parameters
YOLOv5s	14.4	96.8	94.9	95.8	7.03×10^6
YOLOv5s + Bi-FPN	15.5	97.3	93.1	95.2	7.09×10^6
YOLOv5s + CA	14.8	95.1	96.1	95.6	7.22×10^6
YOLOv5s + ECA	14.7	97.2	95.2	96.2	7.20×10^6
YOLOv5s + SE	14.8	94.9	97.6	96.2	7.23×10^6
YOLOv5s + CBAM	14.8	97.1	96.1	96.6	7.23×10^6

TABLE 4 Experimental results of different lightweight models.

Model	Size (MB)	Precision (%)	Recall (%)	F1 score (%)	Speed (ms)
YOLOv5s + CBAM	14.8	97.1	96.1	96.6	10.4
MobileDets	16.0	95.3	89.9	92.5	8.2
Nanodet	17.1	97.5	91.4	94.3	10.0

Figure 5B shows the test results of the sow posture detection model. Where mAP 0.5 is the mean average precision (mAP) of IoU (Intersection over Union) at 0.5, mAP 0.5:0.95 is the average of IoU in the threshold range [0.5,0.95] (the average precision is calculated every 0.05). As can be seen from the four curves, the model can converge quickly and has high detection performance.

To evaluate the detection performance of the model, we plotted and analyzed the PR curve. The PR curve is formed by the precision and recall rate of the model. Among them, the recall (R) is the *x*-axis, and the precision (P) is the *y*-axis. It can be seen from Figure 6 that as the recall continues to increase, precision gradually decreases, and gradually reaches a balance point. At this time, recall and precision are both above 95%, which shows that the model has better performance for sow posture detection.

3.2 Results of YOLOv5

Test results for different sizes of YOLOv5 are shown in Table 2. YOLOv5s is the network with the smallest depth and the smallest width of the feature map in the YOLOv5 series.

Although the detection accuracy is slightly lower than YOLOv5l, and the recall rate is slightly lower than that of YOLOv5m, it still can maintain a high F1score, and the number of parameters and the detection times are greatly reduced. The model size is only 14.4 MB, which can meet the deployment and use of embedded GPU. Therefore, YOLOv5s is selected for further optimization in this paper.

3.3 Results of optimization methods

The test results of different optimization methods are shown in Table 3. The Bi-FPN network has the best effect on improving the precision of model detection, but with slightly lower recall. Among the optimization methods based on attention mechanism, ECA module has the best effect on improving the precision of the model, and SE module has the best effect on improving the precision of the model. Based on different evaluation indexes, CBAM module has the best comprehensive improvement effect on sow posture detection.

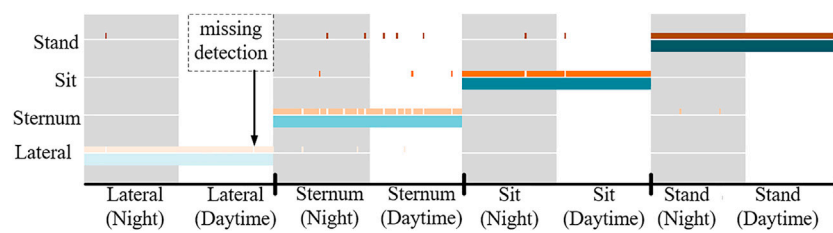


FIGURE 7

Different sow posture detection results.

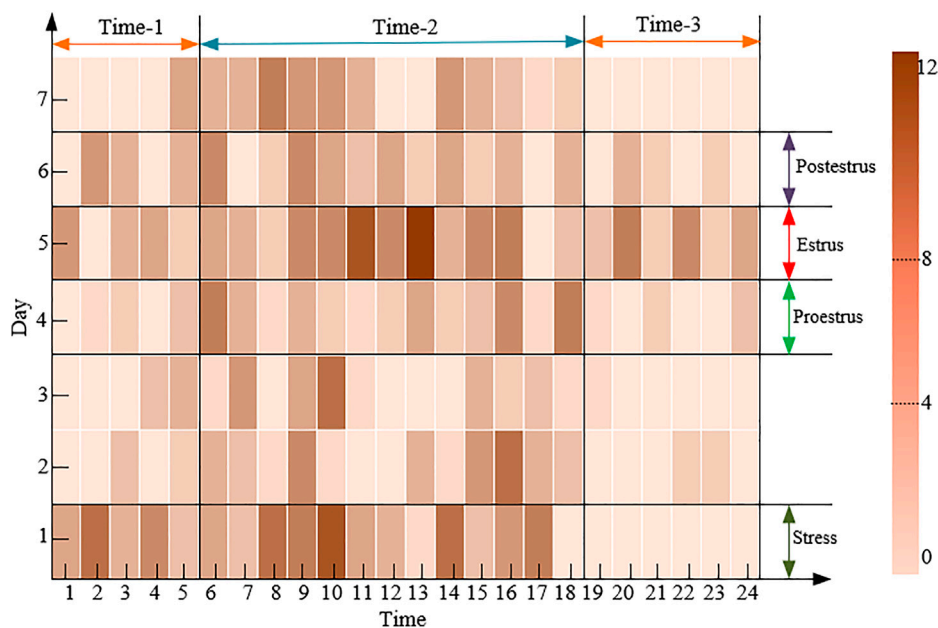


FIGURE 8

The frequency of posture change in sow (sow-2) within 7 days after lactation.

3.4 Contrast model

The test results of different lightweight models are shown in Table 4. Compared with the optimized model, MobileDets can achieve faster detection of sow posture, but precision and recall are lower than the optimized model. The precision and detection speed of Nanodet model are slightly faster than that of the optimized model, but the recall is far lower than that of the optimized model. Combining precision, recall, f1score and detection speed, the optimized model has the best detection performance. The test results show that the processing time of a single picture on the embedded GPU is 74.4 ms, which can meet the needs of real-time detection.

3.5 Model testing

To further test the performance of the model for sow posture detection, 100 images of each of the four postures were selected and tested. Among them, there are 50 images collected at night and 50 during the day, for a total of 400 images. The detection results of different sow posture are shown in Figure 7. Below the white segmentation line is the manually marked sow posture (blue line), and above the white segmentation line is the model automatic detection result (orange line), the night image annotation and identification results are gray background area, and the daytime image annotation and identification results are white background area. According to Figure 7, The model classified stand, sit and lateral postures more well, but a

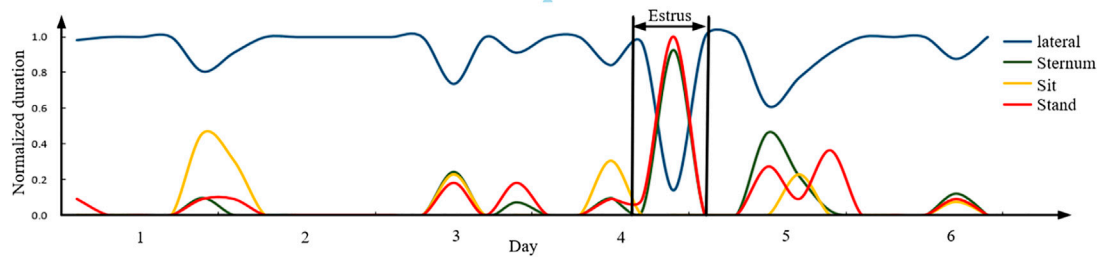


FIGURE 9

The time of each posture at 1–6 days after the end of the stress phase.

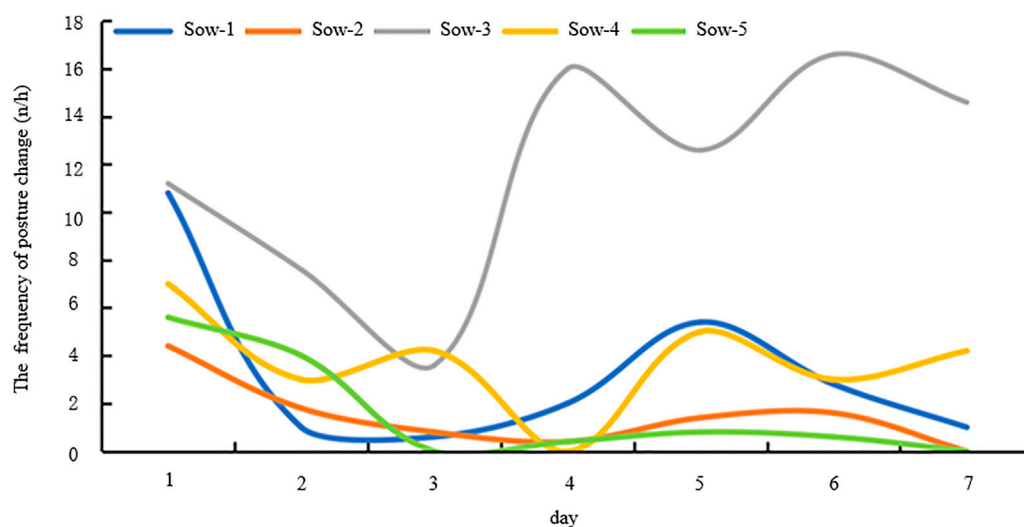


FIGURE 10

The frequency of posture change in different types of sows.

little inferior for sternum, that is because the inter class gap between sternum and the others is smaller than that between stand, lateral, and sit. Furthermore, there are a few missed detections, which is caused by changes in light. Overall, the model is able to accurately detect daytime and nighttime sow posture.

3.6 Estrus analysis

To explore the daily patterns of empty sow behavior, this study analyzed the frequency of posture change in 52 empty sows within 7 days after lactation. The study selected the remaining 20 sows as test samples. For a fifth day estrus sow (sow-2), the statistical results are shown in Figure 8. The study divides a day into three time periods: Time-1, Time-2, and

Time-3. Time-1 is 0–5 am, Time-1 is 6 am–6 pm, and Time-3 is the remaining time.

The frequency of posture change in sow-2 on the first day remained high after lactation, which is caused by the stress of transfer group. At time-1, the average frequency of posture change in sow was up to 6.98 times per hour. When sows changed from stress to proestrus, the frequency of posture change was significantly reduced, with the average frequency of posture change in the sow decreased to 1.43 times per hour. When the sow was in estrus, its frequency of posture change in the sow increased significantly. With the average frequency of posture change in sows up to 6.14 times per hour, which generally increased 3–4 times compared with proestrus. When the sow ends in the estrus period, its average PTF will gradually increase, with the average frequency of posture change in sows decreasing to 5.69 times per hour, generally down by

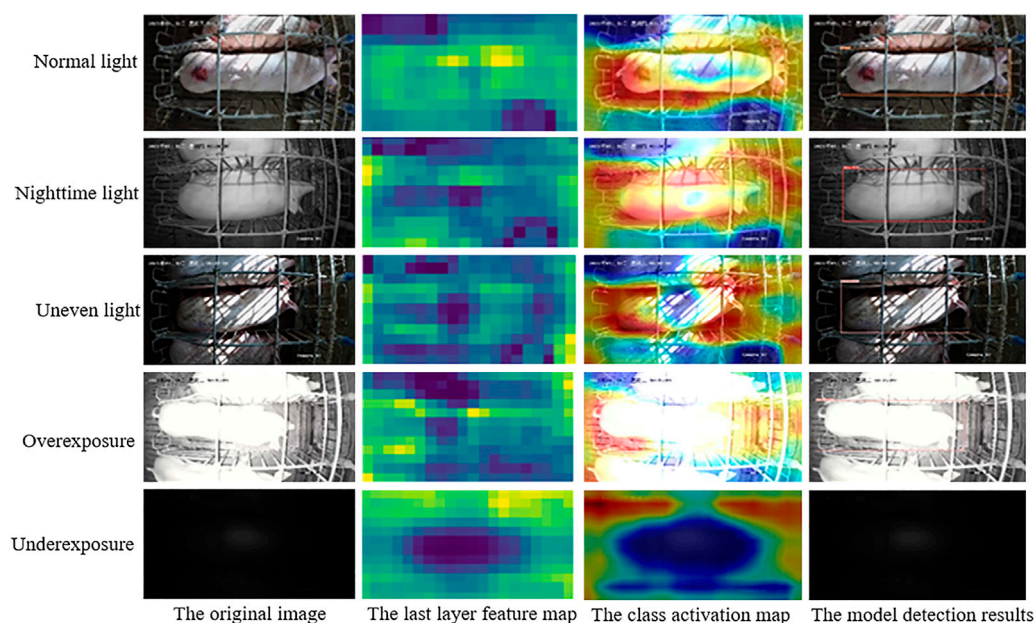


FIGURE 11
Detection results in different light.

0.2–0.3 from the estrus period. However, this trend is not statistically significant for time-2 or time-3. The study further analyzed the time of each posture after stress, and the results are shown in Figure 9. It can be seen that when an empty sow is estrus, the stand and sternum time increases and the lateral time decreases. This is consistent with the conclusion of Lee et al [30].

Based on the above conclusions, the remaining 20 sows were selected for testing in this study. Among the 20 sows, including 3 with abnormal estrus sows and 17 with normal estrus sows. The test results showed that among the remaining 17 sows, only one with estrus was wrongly detected, and 94.1% of estrus sows could be accurately detected.

3.7 Abnormal estrus analysis

Due to nutrition, disease, sow house environment and other factors, some sows are unable to estrus and ovulate normally after weaning [31]. Abnormal estrus sows were placed into five main categories: silent estrus, persistent estrus, repeating estrus and postpartum anestrus, accounting for 12.5% of the experimental sows. The frequency of posture change of different types of empty sows is shown in Figure 10. Sow-1 is normal estrus sow, sow-2 is silent estrus sow, sow-3 is persistent estrus sows, sow-4 is repeating estrus sow, and sow-5 is postpartum anestrus sow. For silent estrus (sow-2) or postpartum anestrus sow (sow-5), the frequency of posture change remained relatively low. In the

Time-1, the average frequency of posture change of two kinds of sows is less than 1.63 times per hour. For persistent estrus sows (sow-3), the frequency of posture change is at high levels. In the time-1, the average frequency of posture change of this kind of sows is higher than 11.74 times per hour, significantly lower than those in normal estrus. However, for postpartum anestrus sows, the average frequency of posture change of this kind of sows fluctuates up and down irregularly, which is usually caused by sow malnutrition or ovarian dysfunction.

3.8 Current deficiencies and subsequent studies

For this study, although the preliminary method for detection of estrus had been achieved, there are still shortcomings in this study. It was found that the light condition had some influence on the sow posture detection. The feature map of the five light conditions, including normal light, nighttime light, uneven light, overexposure, underexposure, were visualized, and class activation maps (CAM) were generated, as shown in Figure 11. In normal light, nighttime, overexposure, the model can accurately identify the sow object and classify its postures. However, in uneven light, the model can accurately predict sow position, but there is some false detection of posture. Through testing, it was found that due to the dim light in the breast area of some sow

images, the model could not accurately distinguish between the lateral and sternum. In uneven light, the model had difficulty in identifying sows. In the next phase of the study, we will synthesize the dynamic detection results of the video data to further improve the posture detection precision of the model.

4 Conclusion

In this past study, we proposed an algorithm for sow posture detection based on optimized YOLOv5s and used it for activity analysis of sows in estrus. It could be concluded from the testing results and discussions that:

- 1) Combining a CBAM module with the YOLOv5 model helped in the detection of sow postures. This method could be used to continuously and automatically monitor sow behavior.
- 2) The study found that when empty sows reached in estrus, the frequency of posture change in most sows increased. The standing and sternum time of sows increased, and the lateral time decreased compared with the non-estrus period.
- 3) This study compared the frequency of posture change in abnormal estrus abnormal estrus sows. In the follow-up study, the testing range of abnormal estrus sows will be further expanded

Data availability statement

The raw data supporting the conclusion of this article will be made available by the authors, without undue reservation.

Ethics statement

The animal study was reviewed and approved by The Committee of Animal Research Institute.

References

1. McGlone JJ, Garcia A, Rakhshandeh A. Multi-Farm analyses indicate a novel boar pheromone improves sow reproductive performance. *Animals* (2019) 9(2):37. doi:10.3390/ani9020037
2. Liang G, Yan J, Guo J, Tang Z. Identification of ovarian circular RNAs and differential expression analysis between MeiShan and large white pigs. *Animals* (2020) 10(7):1114. doi:10.3390/ani10071114
3. Zhang Y, Cai J, Xiao D, Li Z, Xiong B. Real-time sow behavior detection based on deep learning. *Comput Electron Agr* (2019) 163. 104884 doi:10.1016/j.compag.2019.104884
4. Houwers H. "Locality registration as a way of oestrus detection in an integrated group-housing for sows," in: Unshellj, Van PuttenG, ZeebK, EkesboI, editors *Proceedings of the international congress on applied ethology in farm animals*. (Skara, Sweden) (1988). p. 44–55.
5. Bressers H, Te Brake J, Noordhuizen J. Automated oestrus detection in group-housed sows by recording visits to the boar. *Livestock Prod Sci* (1995) 41(2):183–91. doi:10.1016/0301-6226(94)00053-A
6. Korthals RL. The effectiveness of using electronic identification for the identification of estrus in swine. *ASAE CSAE SCGR Annu Int Meet* (1999) 18(21):10.
7. Ostensen T, Cornou C, Kristensen AR. Detecting oestrus by monitoring sows' visits to a boar. *Comput Electron Agr* (2010) 74(1):51–8. doi:10.1016/j.compag.2010.06.003
8. Lei K, Zong C, Du X, Teng G, Feng F. Oestrus analysis of sows based on bionic boars and machine vision technology. *Animals* (2021) 11(6):1485. doi:10.3390/ani110618510.3390/ani11061485
9. Bressers HPM. *Monitoring individual sows in group-housing: Possibilities for automation*. Wageningen, Netherlands: Wageningen University and Research (1993). 139–48.
10. Freson L, Godrie S, Bos N, Jourquin J, Geers R. Validation of an infra-red sensor for oestrus detection of individually housed sows. *Comput Electron Agr* (1998) 20(1):21–9. doi:10.1016/S0168-1699(98)00005-2

Author contributions

HX completed data collection, model construction, and paper writing. JC and QD completed the labeling of the data. YS participated in the feasibility analysis, and MS directed the data collation and writing. LL directed the paper revision. XU and JZ helped validate the model.

Funding

This research was funded by the National Key Research and Development Program of China (Grant No. 2021YFD2000800) and the Jiangsu Provincial Key Research and Development Program (Grant No: BE2021363).

Acknowledgments

Thanks to Ruqian Zhao and Professor Wen Yao for their guidance on the experiment.

Conflict of interest

The authors declare that the research was conducted in the absence of any commercial or financial relationships that could be construed as a potential conflict of interest.

Publisher's note

All claims expressed in this article are solely those of the authors and do not necessarily represent those of their affiliated organizations, or those of the publisher, the editors and the reviewers. Any product that may be evaluated in this article, or claim that may be made by its manufacturer, is not guaranteed or endorsed by the publisher.

11. Jeong H, Yoe H (2013). "A study on the estrus detection system of the sow using the wireless sensor network," in *Proceedings of the international conference on wireless networks* (Suncheon, South Korea: Department of Information and Communication Engineering, Suncheon National University), 101–8.
12. Wang K, Liu C, Duan Q. Identification of sow estrus behavior based on MFO-LSTM. *Trans CSAE* (2020) 36(14):211–9. doi:10.11975/j.issn.1002-6819.2020.14.026
13. Li X, Luo M, Ji S, Zhang L, Lu M. Evaluating generative adversarial networks based image-level domain transfer for multi-source remote sensing image segmentation and object detection. *Int J Remote Sensing* (2020) 41(19):7343–67. doi:10.1080/01431161.2020.175778210
14. Moini S, Alizadeh B, Emad M, Ebrahimpour R. A Resource-Limited hardware accelerator for convolutional neural networks in embedded vision applications. *IEEE Trans Circuits Syst Express Briefs* (2017) 64:1217–21. doi:10.1109/TCSIL.2017.2690919
15. Ghimire D, Kil D, Kim SH. A survey on efficient convolutional neural networks and hardware acceleration. *Electronics* (2022) 11(6):945. doi:10.3390/electronics11060945
16. Nousi P, Mademlis I, Karakostas I, Tefas A, Pitas I (2019). "Embedded UAV Real-Time visual object detection and tracking," in *Proceedings of the IEEE international conference on real-time computing and robotics*, Irkutsk, Russia, 04–09 August 2019 (IEEE), 708–13. doi:10.1109/RCAR47638.2019.9043931
17. Zhou F, Zhao H, Nie Z (2021). "Safety helmet detection based on YOLOv5," in *Proceedings of the IEEE international conference on power electronics. Computer Applications*, Shenyang, China, 22–24 January 2021 (IEEE), 6–11. doi:10.1109/ICPECA51329.2021.9362711
18. Zhao Z, Yang X, Zhou Y, Sun Q, Ge Z, Liu D. Real-time detection of particleboard surface defects based on improved YOLOV5 target detection. *Sci Rep* (2021) 11(1):1–15. doi:10.1038/s41598-021-01084-x
19. Niu J, Chen Y, Yu X, Li Z, Gao H (2020). "Data augmentation on defect detection of sanitary ceramics," in *Proceedings of the 2021 IEEE international conference on power electronics, Computer Applications*, Singapore, 18–21 October 2020 (IEEE), 5317–22. doi:10.1109/IECON43393.2020.9254518
20. Rezatofighi H, Tsoi N, Gwak J, Sadeghian A, Reid I, Savarese S (2019). "Generalized intersection over union: A metric and a loss for bounding box regression," in *Proceedings of the IEEE/CVF conference on computer vision and pattern recognition*, Long Beach, CA, USA, 15–20 June 2019 (IEEE), 658–66. doi:10.1109/CVPR.2019.00075
21. Jiang M, Song L, Wang Y, Li Z, Song H. Fusion of the YOLOv4 network model and visual attention mechanism to detect low-quality young apples in a complex environment. *Precision Agric* (2022) 23(2):559–77. doi:10.1007/s11119-021-09849-0
22. Zhu L, Geng X, Li Z, Liu C. Improving YOLOv5 with attention mechanism for detecting boulders from planetary images. *Remote Sensing* (2021) 13(18):3776. doi:10.3390/rs1318377610.3390/rs13183776
23. Desai M, Shah M. An anatomization on breast cancer detection and diagnosis employing multi-layer perceptron neural network (MLP) and Convolutional neural network (CNN). *Clin Ehealth* (2021) 4:1–11. doi:10.1016/j.ceh.2020.11.002
24. Lakshmi B, S.Parthasarathy S. Human action recognition using median attention-based and max pool convolution with nearest neighbor. *Int J Ambient Comput Intelligence (Ijaci)* (2019) 10(2):34–47. doi:10.4018/IJACI.2019040103
25. Gao R, Wang R, Feng L, Li Q, Wu H. Dual-branch, efficient, channel attention-based crop disease identification. *Comput Electron Agr* (2021) 190:10641. doi:10.1016/j.compag.2021.106410
26. Zakir Ullah M, Zheng Y, Song J, Aslam S, Xu C, Kiazolu GD, et al. An Attention-Based convolutional neural network for acute lymphoblastic leukemia classification. *Appl Sci* (2021) 11(22):10662. doi:10.3390/app112210662
27. Xiong Y, Liu H, Gupta S, Akin B, Bender G, Wang YZ, et al. (2021). "MobileDets: Searching for object detection architectures for mobile accelerators," in *Proceedings of the IEEE/CVF conference on computer vision and pattern recognition*, Nashville, TN, USA, June 20 2021 to June 25 2021 (IEEE), 3824–33. doi:10.1109/CVPR46437.2021.00382
28. Zhou Z, Hu Y, Deng X, Huang D, Lin Y (2021). "Fault detection of Train height valve based on nanodet-resnet101," in *Proceedings of the 2021 36th youth academic annual conference of Chinese association of automation. YAC*, Nanchang, China, 28–30 May 2021 (IEEE), 709–14. doi:10.1109/YAC53711.2021.9486540
29. Sim I, Lim JH, Jang YW, You JH, Oh ST, Kim YK, et al. Developing a compressed object detection model based on YOLOv4 for deployment on embedded GPU platform of autonomous system. *arXiv* (2021). doi:10.48550/arXiv.2108.00392
30. Lee JH, Lee DH, Yun W, Oh HJ, An JS, Kim YG, et al. Quantifiable and feasible estrus detection using the ultrasonic sensor array and digital infrared thermography. *J Anim Sci Technol* (2019) 61(3):163–9. doi:10.5187/jast.2019.61.3.163
31. Kraeling R, Webel S. Current strategies for reproductive management of gilts and sows in North America. *J Anim Sci Biotechnol* (2015) 6(1):1–14. doi:10.1186/2049-1891-6-3



OPEN ACCESS

EDITED BY
Kun Wang,
Aerospace Information Research
Institute (CAS), China

REVIEWED BY
Ye Liu,
Beijing Technology and Business
University, China
Chifang Peng,
Jiangnan University, China

*CORRESPONDENCE
Xiaohe Gu,
guxh@nercita.org.cn

SPECIALTY SECTION
This article was submitted to Optics and
Photonics,
a section of the journal
Frontiers in Physics

RECEIVED 02 September 2022
ACCEPTED 29 September 2022
PUBLISHED 14 October 2022

CITATION
Zhang C, Shi Y, Wei Z, Wang R, Li T,
Wang Y, Zhao X and Gu X (2022),
Hyperspectral estimation of the soluble
solid content of intact netted melons
decomposed by continuous
wavelet transform.
Front. Phys. 10:1034982.
doi: 10.3389/fphy.2022.1034982

COPYRIGHT
© 2022 Zhang, Shi, Wei, Wang, Li, Wang,
Zhao and Gu. This is an open-access
article distributed under the terms of the
[Creative Commons Attribution License](https://creativecommons.org/licenses/by/4.0/)
(CC BY). The use, distribution or
reproduction in other forums is
permitted, provided the original
author(s) and the copyright owner(s) are
credited and that the original
publication in this journal is cited, in
accordance with accepted academic
practice. No use, distribution or
reproduction is permitted which does
not comply with these terms.

Hyperspectral estimation of the soluble solid content of intact netted melons decomposed by continuous wavelet transform

Chao Zhang^{1,2}, Yue Shi^{1,2}, Zhonghui Wei³, Ruiqi Wang^{1,2},
Ting Li⁴, Yubin Wang^{1,5}, Xiaoyan Zhao^{1,5} and Xiaohe Gu^{3*}

¹Institute of Agri-Food Processing and Nutrition, Beijing Academy of Agriculture and Forestry Sciences, Beijing, China, ²Beijing Agricultural Technology Extension Station, Beijing, China, ³Beijing Key Laboratory of Fruit and Vegetable Storage and Processing, Beijing, China, ⁴Research Center of Information Technology, Beijing Academy of Agriculture and Forestry Sciences, Beijing, China, ⁵Key Laboratory of Vegetable Postharvest Processing of Ministry of Agriculture and Rural Affairs, Beijing, China

Netted melons are welcomed for their soft and sweet pulp and strong aroma during the best-tasting period. The best-tasting period was highly correlated with its soluble solid content (SSC). However, the SSC of the intact melon was difficult to determine due to the low relationship between the hardness, color, or appearance of fruit peel and its SSC. Consequently, a rapid, accurate, and non-destructive method to determine the SSC of netted melons was the key to determining the best-tasting period. A hyperspectral model was constructed to estimate the SSC of intact netted melons. The combination of continuous wavelet transform and partial least squares or random forest algorithm was employed to improve the estimation accuracy of the hyperspectral model. Specifically, the hyperspectra of the diffuse reflection and SSC of 261 fruit samples were collected. The sensitivity band was screened based on the correlation analysis and continuous wavelet transform decomposition. The correlation coefficient and RMSE of the random forest regression model decomposed by the continuous wavelet transform were 0.72 and 0.98%, respectively. The decomposition of the continuous wavelet transform improved the correlation coefficient by 5 and 1.178 times at 754 and 880 nm, respectively. The random forest regression model enhanced the determination coefficient by at least 56.5% than the partial least squares regression model, and the continuous wavelet transform decomposition further enhanced the determination coefficient of the random forest regression model by 4.34%. Meanwhile, the RMSE of the random forest regression model was reduced. Therefore, the decomposition of the continuous wavelet transform improved the stability and prediction ability of the random forest regression model.

KEYWORDS

netted melon, soluble solid content, hyperspectra, continuous wavelet transform, random forest

1 Introduction

Netted melon (*Cucumis melo* L. var. *reticulatus* Naud.) is a member of the genus *Cucumis*, subtribe Cucumerinae. Netted melon shows soft and sweet pulp and strong aroma for only 3–5 days which is known as the best-tasting period [1, 2]. The best-tasting period of netted melons is highly correlated with their soluble solid content (SSC). Specifically, the SSC increased slowly when the pulp of fruit was hard with low sweetness and weak aroma in the expansion stage of the fruit. The SSC reached a certain threshold which remained for about 3–5 days when the fruit showed a soft and sweet pulp and strong aroma. After the best-tasting period, the SSC increased quickly with the obvious drip loss and fibrosis of the pulp. Consequently, the SSC showed a plateau for about 3–5 days during the whole growth period [3]. However, the plateau of the SSC was not related to the hardness, color, or appearance of the fruit peel [1]. Therefore, the SSC was the key to determining the best-tasting period of netted melons.

Hyperspectra was a non-destructive method for the internal quality of intact fruit, which had determined the SSC of apple, pear, pineapple, and jujube successfully based on the spectral responses of the reflectance, transmission, or diffuse reflection of fruit [4–10]. The peel of the netted melon was about 1.0 cm which was thicker than that of apple, pear, pineapple, and jujube, which was an obstacle to the acquisition of the transmission of spectral [11]. Moreover, the chemical ingredient of the peel was not related to the variation of the SSC. Consequently, the reflectance of the peel would not reflect the variation of the SSC. The diffuse reflection came from the multi-reflection in the peel and edge pulp of the fruit. Therefore, the spectra of the diffuse reflection showed the potential to include the SSC information of fruit. However, the diffuse reflection had not been used to construct the estimation model of intact netted melons.

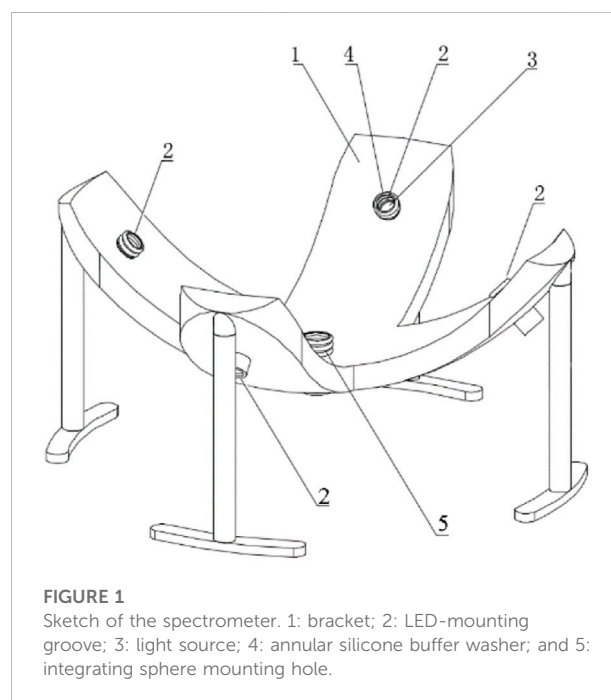
The diffuse reflection collected information on each ingredient of the fruit, including the moisture, SSC, pectin, cellulose, and even pollutants on the surface of the peel [12]. The SSC was relatively low which led to a relatively weak spectral response [5]. Therefore, an effective decomposition of the spectrum could improve the estimation accuracy of the SSC. Spectral analysis techniques such as mathematical transformation, principal component analysis, and spectral absorption characteristic analysis had been used to decompose the spectra to explore the SSC of fruit and enhance its spectral sensitivity. Moreover, partial least squares (PLS), neural networks, random forest (RF), and deep learning methods have been used to acquire higher precision regression models of the SSC [8–10, 13, 14]. However, recent studies focused on the enhancement of the sensitivity of spectral information of the SSC, rather than finding the directions of different spectral information in depth. Exploring an efficient spectrum transformation to decompose the weak sensitive information would improve the estimation accuracy of the SSC of the intact netted melon.

A hyperspectral regression model was constructed to estimate the SSC of intact netted melons in the current study. The combination of continuous wavelet transform (CWT) and PLS or RF was used to extract weak useful information and improve the estimation accuracy of the SSC of intact netted melon. Specifically, the spectra of the diffuse reflection and SSC of 261 fruit samples were collected. The diffuse reflection was collected based on the optimization of the incidence angle and intensity of the light source, and acquisition times of the spectrometer. The CWT algorithm was used to extract high- and low-frequency detailed information at multiple decomposition scales. Sensitive wavelet coefficients with the SSC of the fruit were selected. Finally, an estimation model was constructed to predict the SSC of the intact netted melon by the PLS or RF.

2 Materials and methods

2.1 Sample preparation

A total of 261 netted melons (*Cucumis melo* L. var. *reticulatus* Naud.) were harvested in June and July 2021 in Beijing Tongzhou District International Seed Industry Science and Technology Park (Tongzhou District, Beijing). During the best-tasting period, the fruit was nearly round and light green with a light yellow net. The fruit was around 1.50 kg per fruit with an SSC of 6%–11%. Specifically, the melon was colonized on 5 February 2021 and pollinated on 2 April 2021. The random fruit was harvested on June 2, June 12, June 22, and 2 July 2021,



respectively. The harvested fruit was transported to the laboratory immediately. The SSC and hyperspectra of the diffuse reflection of the fruit were recorded.

2.2 Measurement of the hyperspectra of the diffuse reflection

The hyperspectra of the diffuse reflection of fruit samples were collected by a self-made spectrometer whose sketch was shown in Figure 1. The sketch was 3D printed by the Acrylonitrile Butadiene Styrene resin. The LED lights and integrating spheres were mounted in a hemispherical frame. A total of four LED lights with a color temperature of 6,500 K, light flux of 210 Lux, and power of 3 W were mounted in the frame as the light source (Guanghong HG-SG1XHH-F-3W, Guangzhou Hengguang Light Co. Ltd., Guangzhou, China). The integrating sphere was mounted on the bottom of the hemispherical frame and connected to a spectral sensor. The spectral sensor collected the spectrum ranging from 650 to 950 nm with a resolution of 2.5 nm based on the previous studies [7, 11]. The annular silicone buffer washer was mounted on the grooves of the LED lights and integrating sphere, which ensured the well fit of the fruit and hemispherical frame. Specifically, the netted melon was placed on the frame and ensured the well contact between the fruit surface and the buffer washers. The LED light sent the light signal when the spectral sensor collected the spectrum of the diffuse reflection of fruit for 60 ms. A total of 30 hyperspectral were collected and averaged as the sample spectrum. The surface of the fruit contacted with the buffer washer on the integrating sphere was marked for the SSC analysis.

2.3 Measurement of the soluble solid content

After the measurement of the hyperspectra, a circle with a radius of 1.0 cm was drawn with a marked point as the center on the fruit surface. The cylinder of the fruit was cut. The edge pulp with 1.0–2.0 cm from the exocarp of the cylinder was used for the measurement of the SSC. The SSC of samples was measured by a digital refractometer (PAL- α , ATAGO Company Ltd., Japan) at room temperature with water as blank.

2.4 Screening of the sensitivity band

The sensitivity band was screened based on the correlation analysis and CWT decomposition. The CWT is a signal processing technology derived from the Fourier transform. It analyzes in the field of time and frequency at the same time, which is helpful to extract the effective information in the signal [15]. Specifically, the spectrum of the fruit was processed based

on the mexh wavelet base written in MATLAB language. The original spectrum was decomposed by 10 layers of wavelet to generate a series of wavelet coefficients (Eq. 1 and Eq. 2).

$$\Psi_{a,b} = \frac{1}{\sqrt{a}} \Psi\left(\frac{\lambda - b}{a}\right), \quad (1)$$

where a is the expansion factor, b is the translation factor and λ is the number of bands of spectral data.

$$W_f(a, b) = \left(f, \Psi_{a,b}\right) = \int_{-\infty}^{+\infty} f(\lambda) \Psi_{a,b}(\lambda) d\lambda, \quad (2)$$

where $f(\lambda)$ is the spectral reflectance, and the wavelet coefficients include two dimensions, including wavelength (650–950 nm) and decomposition scale (1, 2, 3, ..., and 10). The wavelet coefficient is the number of scales, and the list is the matrix of the number of wavelengths.

2.5 Establishment and validation of the regression model

The spectral estimation models were prepared by the PLS and RF, respectively. Specifically, the sensitivity bands based on the correlation analysis and CWT were used as the independent variables with the SSC as the dependent variables.

A training set and testing set were prepared with a sample number of 3:1. In order to ensure the uniform distribution of each set, all samples were sorted from large to small according to the SSC of the fruit. The samples with the number of multiples of four were nominated as the testing set (66 samples), and the others were nominated as the training set (195 samples). The testing set of 66 samples was used to validate the determination coefficient (R^2) (Eq. 3) and root mean squared error (RMSE) (Eq. 4), and Line $y = x$ of the prediction spectral model, respectively.

$$R^2 = \frac{\sum_{i=1}^N \left(\text{PSSC}_i - \overline{\text{ASSC}} \right)^2}{\sum_{i=1}^N \left(\text{ASSC}_i - \overline{\text{ASSC}} \right)^2}, \quad (3)$$

$$\text{RMSE} = \sqrt{\frac{\sum_{i=1}^N (\text{ASSC}_i - \text{PSSC}_i)^2}{N}}, \quad (4)$$

where ASSC_i and PSSC_i represent the actual and predicted SSC of fruit i , respectively; N represents the number of validation samples; and $\overline{\text{ASSC}}$ represents the average measured value of SSC.

Specifically, R^2 is used to characterize the stability of the model. The closer it is to 1, the more stable and better fitting the model is. RMSE is used to detect the prediction ability of the model. The smaller the RMSE is, the better the prediction ability of the model is. Line $y = x$ represents the deviation of the point composed of the measured value and the predicted value from in the Line $y = x$.

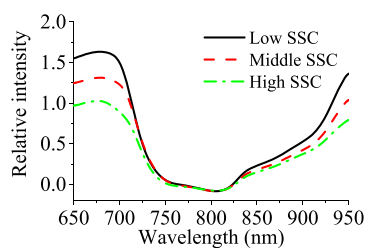


FIGURE 2
Spectral profiles of netted melons.

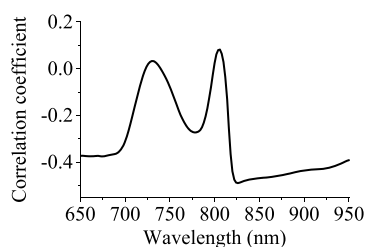


FIGURE 3
Correlation coefficient between the SSC and relative intensity of the hyperspectra of netted melons.

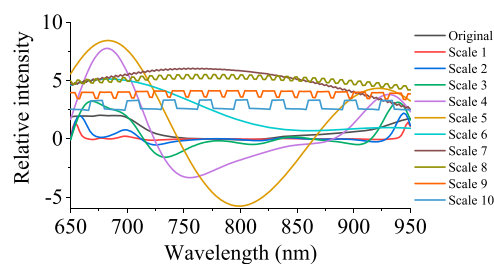


FIGURE 4
Decomposed spectra of netted melons by CWT.

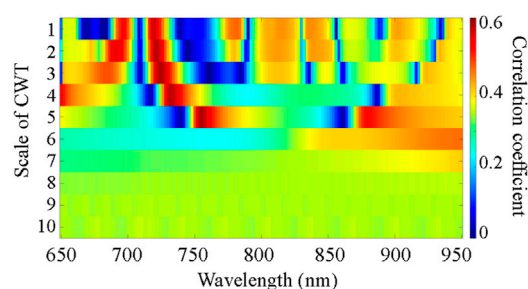


FIGURE 5
Correlation coefficient matrix between the relative intensity of CWT decomposed spectra and SSC of netted melons.

3 Results and discussion

3.1 Hyperspectra and SSC of netted melons

The hyperspectra and SSC of 261 fruit were collected. The SSC covered a relatively wide range from 3.8% to 9.6% with the average value and standard deviation of 6.93% and 1.60%, respectively. The samples were divided into high-SSC, middle-SSC, and low-SSC groups based on the SSC. Specifically, the SSC of the high-SSC, middle-SSC, and low-SSC groups was 6.9%–9.6%, 5.8%–6.9%, and 3.8%–5.8%, respectively. The hyperspectra of the three groups were averaged and shown in Figure 2. The relative intensity of the hyperspectra decreased sharply at 690–750 nm, remained relatively constant at 770–830 nm, and increased at 850–950 nm. The relative intensity of the hyperspectra was negatively related to the SSC. The fruit of the high SSC group showed the weakest relative intensity, while that of the low SSC group showed the strongest relative intensity. Being different from our results, the spectra with the wavelength of 750–950 nm were used to estimate the SSC of melon [11]. The narrow range of the spectra possibly missed the sensitivity band of the SSC information.

3.2 Screening the sensitivity band of the hyperspectra

The sensitivity band was screened based on the correlation analysis and CWT decomposition, respectively. The profile of the correlation coefficient between the SSC and relative intensity of the hyperspectra of netted melons is shown in Figure 3, which is based on 301 points due to the resolution of 2.5 nm of the spectrometer. A positive correlation was shown in 724–739 nm and 800–810 nm, while a negative correlation was shown in the other bands. The correlation coefficient ranged from -0.49 to 0.08. The absolute value of the correlation coefficient reached the highest at 826 nm with a correlation coefficient of -0.49. Therefore, the band of 826 nm was the sensitivity band based on the correlation analysis.

CWT served as a time-frequency window with shorter time-window width for higher frequencies and wider time-window width for lower frequencies. Consequently, CWT possibly raised the spectral response of useful information and removed the noise of the spectra [15, 16]. Figure 4 showed the spectra decomposed by the CWT on a 10 scale. The decomposed spectra of Scale 1–6 showed a large variety smoothly, while

those of Scale 7–10 were relatively flat but jagged. The CWT decomposition amplified and highlighted the features of the original spectra. Consequently, the spectra decomposed by CWT provided more efficient information on the feature band.

The correlation coefficient between the relative intensity of CWT decomposed spectra and SSC of netted melons was shown in Figure 5. The red represented the high correlation band, while the blue represented the low correlation band. The spectral effective information is mainly presented in the 700–800 nm of the scale 1–6, while no spectral effective information is presented in the scale 7–10. The correlation coefficient reached the highest at 754 nm of scale 5 with a correlation coefficient of 0.60.

The red light band (670–760 nm) and near-infrared band (761–950 nm) represent the sample feathers in a different dimension [17]. Consequently, the sensitivity band was selected in the red light band and near-infrared band based on the correlation coefficient respectively. The correlation coefficient matrix reached the highest in the 754 nm of scale 5 with the correlation coefficient of 0.60 in the red light band, while that in the 880 nm of the scale 5 with the correlation coefficient of -0.53 in the near-infrared band. Therefore, the bands of 754 and 880 nm were the sensitivity bands based on the CWT decomposition.

The absolute value of the correlation coefficient of 754 and 880 nm in the CWT decomposition was 5 and 1.178 times that without CWT decomposition. The CWT decomposition improved the correlation coefficient of the selected sensitivity bands. Therefore, the bands of 754 and 880 nm were selected as the sensitivity bands for the estimation model. Similar to our results, the CWT decomposition significantly improved the estimation accuracy of chicory leaf Cu content when the best decomposition scales were Scale 3, 4, and 5 [18].

3.3 Modeling and validation of the regression models

PLS and RF were employed to construct the estimation model of the SSC of intact netted melons. The PLS regression model has related the independent variables (e.g., spectra) to an integer that designates the class of the sample [19], while RF is integrated several classifiers to achieve better performance than a single classifier and is especially good for resolving two-class problems based on a bootstrap aggregating algorithm [14]. PLS has been used to construct the estimation model of the SSC successfully [6, 12, 20, 21]. Specifically, the relative intensities of sensitivity bands (754 and 880 nm) with or without CWT decomposition were employed to construct the estimation model by the PLS and RF regression respectively. The R^2 and RMSE of the models were measured respectively (Table 1). The R^2 of the training set of the RF regression model was raised by 64.3% without CWT decomposition and 56.5% with CWT

TABLE 1 Determination coefficient and root mean squared error of the estimation models.

Model	R^2 of the training set	R^2 of the testing set	RMSE/%
RF	0.69	0.39	1.04
RF/CWT	0.72	0.47	0.98
PLS	0.42	0.41	0.74
PLS/CWT	0.46	0.43	0.73

decomposition than that of the PLS regression model, respectively. The R^2 of the testing set of the RF regression model was raised by -4.87% without CWT decomposition and 9.30% with the CWT decomposition than that of the PLS regression model, respectively. The R^2 of the training set of the RF regression model was 50% higher than that of the PLS regression model. Being different from our results, the PLS and lambda-lambda r^2 regression models were used to analyze the relationships between leaf Cu content and the hyperspectral reflectance. They demonstrated the better feasibility of the CWT and PLS algorithms for estimating the Cu status of chicory [18]. This phenomenon resulted from the different hyperspectral reflectance data and different estimating objects. Moreover, the RF constructed many classification and regression trees, which integrated several classifiers to achieve better performance than a single classifier. The hyperspectra provided more classifiers rather than a single one [14]. Therefore, the RF regression model showed higher stability than the PLS regression model.

The R^2 of the training set and testing set of the RF regression model were raised by 4.34% and 20.5% by the CWT decomposition. The RMSE of the RF regression model decreased by 6.12% based on the CWT decomposition. Moreover, the R^2 of the training set and testing set of the PLS model was raised by 9.52% and 4.88% based on the CWT decomposition. The RMSE of the RF regression model decreased by 1.37% based on the CWT decomposition. Consequently, the CWT decomposition raised R^2 and decreased the RMSE of both models. Therefore, the CWT decomposition improved the stability and estimation ability of the model. Being consistent with our result, the spectral model denoised by the CWT decomposition was better to predict the Vc content of navel orange than that by 11 different decomposition approaches [22]. The improvement of the predicting capacity was a possible result of the noise removal ability of CWT decomposition on the spectra [16]. Remarkably, the R^2 and RMSE of the competitive adaptive reweighted sampling-PLS model for the SSC of melon were 0.83 and 0.73, respectively [11]. This difference resulted from the different algorithms and number of the samples.

Figure 6 compared the estimation profile of the regression models with Line $y = x$. The Line $y = x$ reflected the deviation of

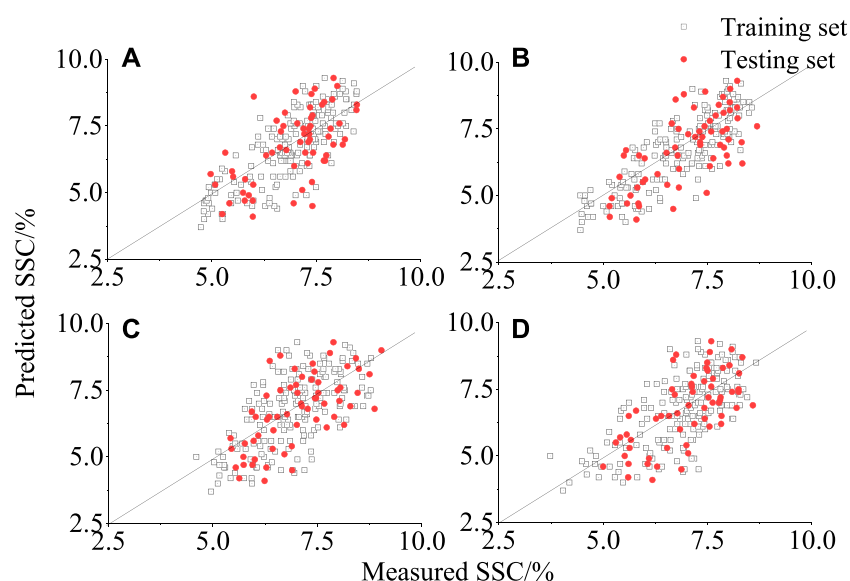


FIGURE 6
Estimation profiles of the RF (A), RF/CWT (B), PLS (C), and PLS/CWT (D) models.

the point composed of the measured value and the predicted value. The points of each model are distributed along the Line $y = x$. Remarkably, the points of the training set of the RF/CWT and PLS models are evenly distributed around the Line $y = x$, while that of the RF and PLS/CWT is biased toward the high-value session of the Line $y = x$. The points of the testing set of the RF, RF/CWT, and PLS are evenly distributed around the Line $y = x$, while that of the PLS/CWT is biased towards the high-value session of the Line $y = x$. These phenomena possibly resulted from the overestimate of the RF and PLS/CWT models.

The RF regression model enhanced the R^2 by at least 56.5% more than the PLS model, and the CWT decomposition further enhanced the R^2 of the RF regression model by 4.34%. Meanwhile, the RMSE of the RF/CWT model was reduced. Consequently, the stability and estimation ability of the RF/CWT model was significantly improved.

4 Conclusion

The combination of CWT and PLS or RF algorithm was employed to improve the estimation accuracy of the hyperspectral model. Specifically, the SSC and hyperspectra of the diffuse reflection of 261 fruit samples were collected to construct the hyperspectral estimation model. The SSC covered a relatively wide range from 3.8% to 9.6% with the average value and standard deviation of 6.93% and 1.60%, respectively. The relative intensity of the spectra was negatively related to the SSC. The sensitivity band was screened based on the correlation analysis and CWT decomposition. The correlation coefficient reached the

highest in the 754 nm of the scale 5, being 0.60 by the CWT decomposition, while that was -0.53 in the 880 nm of the scale 5. The absolute value of the correlation coefficient of 754 and 880 nm with the CWT decomposition was 5 and 1.178 times of those without CWT decomposition. The PLS and RF algorithm were employed to construct the estimation model of the SSC of intact netted melons. The RF regression model enhanced the R^2 by at least 56.5% than the PLS model, and the CWT decomposition further enhanced the R^2 by 4.34%. Meanwhile, the RMSE of the RF/CWT model was reduced. The points of the testing set of the RF, RF/CWT, and PLS are evenly distributed around the line $y = x$, while that of the PLS/CWT is biased towards the high-value session of the line $y = x$. Consequently, the stability and estimation ability of the RF/CWT regression model were improved significantly. The RF/CWT regression model had the potential to estimate the SSC of the intact netted melons in the industry.

Data availability statement

The raw data supporting the conclusions of this article will be made available by the authors, without undue reservation.

Author contributions

All authors agreed to be accountable for the content of the work. CZ: investigation, formal analysis, and prepare draft; YS: investigation; ZW: investigation; RW: validation and methodology; TL: conceptualization, methodology, and

funding acquisition; YW: investigation and methodology; XZ: funding acquisition; and XG: writing, review and editing, project administration, and funding acquisition.

Funding

The authors are grateful for the financial support of the National Natural Science Foundation of China (32172237), Beijing Academy of Agricultural and Forestry Sciences (KJCX20211004), China Agricultural Research System (CARS-25), Collaborative Innovation Center of the Beijing Academy of Agricultural and Forestry Sciences (KJCX201915), and Beijing Innovation Consortium of Agriculture Research System (BAIC4-2022).

References

1. Saltveit ME. 2 - melon (*Cucumis melo* L.). In: EM Yahia, editor. *Postharvest biology and technology of tropical and subtropical fruits*. Sawston, United Kingdom: Woodhead Publishing (2011). p. 31–45e.
2. Schaffer AA, Paris HS. *Melons, squashes, and gourds. Reference module in food science*. Amsterdam, Netherlands: Elsevier (2016).
3. Kesh H, Kaushik P. Advances in melon (*Cucumis melo* L.) breeding: An update. *Scientia Horticulturae* (2021) 282:110045. doi:10.1016/j.scienta.2021.110045
4. Zeb A, Qureshi WS, Ghafoor A, Malik A, Imran M, Iqbal J, et al. Is this melon sweet? A quantitative classification for near-infrared spectroscopy. *Infrared Phys Tech* (2021) 114:103645. doi:10.1016/j.infrared.2021.103645
5. Sun M, Zhang D, Liu L, Wang Z. How to predict the sugariness and hardness of melons: A near-infrared hyperspectral imaging method. *Food Chem* (2017) 218: 413–21. doi:10.1016/j.foodchem.2016.09.023
6. Wang F, Zhao C, Yang H, Jiang H, Li L, Yang G. Non-destructive and in-situ estimation of apple quality and maturity by hyperspectral imaging. *Comput Electron Agric* (2022) 195:106843. doi:10.1016/j.compag.2022.106843
7. Manthou E, Lago S-L, Dagres E, Lianou A, Tsakanikas P, Panagou EZ, et al. Application of spectroscopic and multispectral imaging technologies on the assessment of ready-to-eat pineapple quality: A performance evaluation study of machine learning models generated from two commercial data analytics tools. *Comput Electron Agric* (2020) 175:105529. doi:10.1016/j.compag.2020.105529
8. Li Y, Ma B, Li C, Yu G. Accurate prediction of soluble solid content in dried Hami jujube using SWIR hyperspectral imaging with comparative analysis of models. *Comput Electron Agric* (2022) 193:106655. doi:10.1016/j.compag.2021.106655
9. Tian X, Li J, Wang Q, Fan S, Huang W. A bi-layer model for nondestructive prediction of soluble solids content in apple based on reflectance spectra and peel pigments. *Food Chem* (2018) 239:1055–63. doi:10.1016/j.foodchem.2017.07.045
10. Kusumiyati HY, Putri IE, Munawar AA. Multi-product calibration model for soluble solids and water content quantification in Cucurbitaceae family, using visible/near-infrared spectroscopy. *Heliyon* (2021) 7(8):e07677. doi:10.1016/j.heliyon.2021.e07677
11. Li M, Han D, Liu W. Non-destructive measurement of soluble solids content of three melon cultivars using portable visible/near infrared spectroscopy. *Biosyst Eng* (2019) 188:31–9. doi:10.1016/j.biosystemseng.2019.10.003
12. Xia Y, Huang W, Fan S, Li J, Chen L. Effect of spectral measurement orientation on online prediction of soluble solids content of apple using Vis/NIR diffuse reflectance. *Infrared Phys Tech* (2019) 97:467–77. doi:10.1016/j.infrared.2019.01.012
13. Vasques GM, Grunwald S, Sickman JO. Comparison of multivariate methods for inferential modeling of soil carbon using visible/near-infrared spectra. *Geoderma* (2008) 146(1–2):14–25. doi:10.1016/j.geoderma.2008.04.007
14. Hou L, Liu Y, Wei A. Geographical variations in the fatty acids of zanthoxylum seed oils: A chemometric classification based on the random forest algorithm. *Ind Crops Prod* (2019) 134:146–53. doi:10.1016/j.indcrop.2019.03.070
15. Huang S-Y, Wavelets BZ. Advanced. In: RA Meyers, editor. *Encyclopedia of physical science and technology*. 3rd ed. New York: Academic Press (2003). p. 753–71.
16. Abasi S, Minaei S, Jamshidi B, Fathi D, Khoshtaghaza MH. Rapid measurement of apple quality parameters using wavelet de-noising transform with Vis/NIR analysis. *Scientia Horticulturae* (2019) 252:7–13. doi:10.1016/j.scienta.2019.02.085
17. Pan S, Zhang X, Xu W, Yin J, Gu H, Yu X. Rapid On-site identification of geographical origin and storage age of tangerine peel by Near-infrared spectroscopy. *Spectrochimica Acta A: Mol Biomol Spectrosc* (2022) 271:120936. doi:10.1016/j.saa.2022.120936
18. Lin D, Li G, Zhu Y, Liu H, Li L, Fahad S, et al. Predicting copper content in chicory leaves using hyperspectral data with continuous wavelet transforms and partial least squares. *Comput Electron Agric* (2021) 187:106293. doi:10.1016/j.compag.2021.106293
19. Luna AS, de Gois JS. Chapter seven - application of chemometric methods coupled with vibrational spectroscopy for the discrimination of plant cultivars and to predict physicochemical properties using R. In: J Lopes C Sousa, editors. *Comprehensive analytical chemistry*, 80. Amsterdam, Netherlands: Elsevier (2018). p. 165–94.
20. Li H, Zhu J, Jiao T, Wang B, Wei W, Ali S, et al. Development of a novel wavelength selection method VCPA-PLS for robust quantification of soluble solids in tomato by on-line diffuse reflectance NIR. *Spectrochimica Acta Part A: Mol Biomol Spectrosc* (2020) 243:118765. doi:10.1016/j.saa.2020.118765
21. Fan S, Wang Q, Tian X, Yang G, Xia Y, Li J, et al. Non-destructive evaluation of soluble solids content of apples using a developed portable Vis/NIR device. *Biosyst Eng* (2020) 193:138–48. doi:10.1016/j.biosystemseng.2020.02.017
22. Xia J-F, Li X-Y, Li P-W, Ma Q, Ding X-X. Application of wavelet transform in the prediction of navel orange vitamin C content by near-infrared spectroscopy. *Agric Sci China* (2007) 6(9):1067–73. doi:10.1016/S1671-2927(07)60148-5

Conflict of interest

The authors declare that the research was conducted in the absence of any commercial or financial relationships that could be construed as a potential conflict of interest.

Publisher's note

All claims expressed in this article are solely those of the authors and do not necessarily represent those of their affiliated organizations, or those of the publisher, the editors, and the reviewers. Any product that may be evaluated in this article, or claim that may be made by its manufacturer, is not guaranteed or endorsed by the publisher.



OPEN ACCESS

EDITED BY

Rui Min,
Beijing Normal University, China

REVIEWED BY

Diming Zhang,
Zhejiang Lab, China
Zhuo Wang,
Beijing Normal University, China
Hongyi Bai,
Heilongjiang University, China

*CORRESPONDENCE

Leizi Jiao,
jiaoleizi@126.com

SPECIALTY SECTION

This article was submitted to Optics and Photonics,
a section of the journal
Frontiers in Physics

RECEIVED 23 September 2022

ACCEPTED 19 October 2022

PUBLISHED 02 November 2022

CITATION

Wang K, Guo R, Zhou Y, Jiao L and Dong D (2022), Detection of NH_3 in poultry housing based on tunable diode laser absorption spectroscopy combined with a micro circular absorption cell.
Front. Phys. 10:1051719.
doi: 10.3389/fphy.2022.1051719

COPYRIGHT

© 2022 Wang, Guo, Zhou, Jiao and Dong. This is an open-access article distributed under the terms of the [Creative Commons Attribution License \(CC BY\)](https://creativecommons.org/licenses/by/4.0/). The use, distribution or reproduction in other forums is permitted, provided the original author(s) and the copyright owner(s) are credited and that the original publication in this journal is cited, in accordance with accepted academic practice. No use, distribution or reproduction is permitted which does not comply with these terms.

Detection of NH_3 in poultry housing based on tunable diode laser absorption spectroscopy combined with a micro circular absorption cell

Ke Wang^{1,2}, Rui Guo², Yunhai Zhou², Leizi Jiao^{2*} and Daming Dong^{1,2}

¹School of Electronic Engineering and Automation, China Guangxi Key Laboratory of Optoelectronic Information Processing, Guilin University of Electronic Technology, Guilin, China, ²National Research Center of Intelligent Equipment for Agriculture, Beijing Academy of Agriculture and Forestry Sciences, Beijing, China

Accurate monitoring of ammonia has decisive significance for the environmental control of poultry housing. Existing sensors based on semiconductor or electrochemistry have the defects of short life, severe baseline drift and delayed response when facing the harsh environment of poultry housing. In this work, we developed a portable sensor based on tunable diode laser absorption spectroscopy with a micro circular absorption cell for sensitive detection of ammonia in poultry housing. The micro circular absorption cell has a volume of only 25 ml, but the effective absorption path is up to 5 m, which allows the sensor to achieve the ability of less than 15 s response time and 0.2 ppm measurement accuracy. The results of continuous monitoring for 6 days showed that the ammonia concentration in the range of 0–6 ppm was accurately detected in a poultry house with 36 roosters. Through analyzing dynamic changes in ammonia concentration, we successfully identified some abnormal activity caused by humans or weather. Therefore, our sensor has performances of accurate, stable, real-time measurement of ammonia and can provide strong technical support for environmental control of poultry housing.

KEYWORDS

tunable diode laser absorption spectroscopy, circular absorption cell, ammonia, environment, poultry housing

Introduction

With the development of the economy, the poultry breeding mode has changed from free-ranging to intensive farming mode. However, in intensive farming, fecal decomposition, animal respiration and padding decay produce large quantities of harmful gases such as ammonia [1–3]. Especially during the winter, farmers often close their poultry housing to ensure the proper temperature for the growth of poultry. Ammonia (NH_3) concentration in the housing remains high due to the lack

of air circulation, and poultry exposed to such high ammonia levels for a long time can become ill or die [4–6]. Livestock farming is the primary source of ammonia emissions. Ammonia diffused from the livestock to the atmosphere will harm the health of breeders and surrounding residents, and induce various respiratory diseases [7–9]. Therefore, quick and accurate detection of ammonia concentration in poultry housing to timely guide ventilation and deodorization is not only the health needs of poultry and people but also the urgent needs of environmental protection and food safety.

Detection methods of ammonia in poultry housing are divided into laboratory methods and sensor methods [10]. The laboratory methods usually use Fourier transform infrared spectrometer, photoacoustic spectrometer and mass spectrometry to detect harmful gas concentration in livestock with a sub-ppm accuracy [11–14]. These instruments have the advantages of qualitative and quantitative accuracy, high sensitivity and multi-component measurement simultaneously, they are generally large, costly and complex in operation, making them difficult to use in the field for long-term monitoring. The sensor methods often integrated semiconductor or electrochemical gas sensors to detect ammonia in poultry housing. Compared with laboratory methods, these sensors have advantages of small size, low cost and easy operation [15–19]. However, these sensors have poor sensitivity, severe baseline drift, cross interference and short lifetime when used in poor poultry housing environments. This is why these sensors are not widely used for long-term monitoring of ammonia in poultry houses.

Tunable diode laser absorption spectroscopy (TDLAS) uses a tunable distributed feedback (DFB) laser which has a narrow band wavelength corresponding to the gas absorption line to detect gas concentration specifically and sensitively. In recent years, TDLAS has been widely used to monitor harmful gases in industry [20–22]. However, existing commercial TDLAS sensors used for industrial gas monitoring usually have a high detection limit and large size with a heavy frontal absorption cell, which makes them unsuitable for high-precision, on-site measurement of trace ammonia in poultry houses. In this paper, we aimed to develop a portable TDLAS sensor for monitoring trace ammonia in poultry houses. For this, a unique and micro circular absorption cell was designed. In addition, the sensor also integrated temperature, humidity, total volatile organic compounds (TVOC), dust and carbon dioxide (CO₂) sensors to obtain parameters related to air quality in poultry houses.

Structure of the sensor and circular absorption cell

Measurement principle

TDLAS mainly uses the property of tunable semiconductor lasers that the narrowband wavelength of the laser change with

the injection current and temperature to achieve a high-resolution quantitative analysis of gas concentration. After passing through the gas to be measured, the laser intensity has a specific attenuation. However, direct analysis of the change of laser intensity is easy to be affected by various noises in the environment and equipment, and the measurement accuracy cannot meet the actual needs. Therefore, wavelength modulation spectroscopy (WMS) improves the sensor's measurement accuracy.

The principle of WMS is summarized as follows: Based on the Lamber-Beer law, when the laser passes through the measured gas, the relationship between the transmitted and incident light intensities at a specific wavenumber is:

$$I_{(t)} = I_0 \exp [-\alpha(v)], \quad (1)$$

Where $I_{(t)}$ is the transmitted light intensity and I_0 is the incident light intensity, $\alpha(v)$ is the spectral absorption coefficient, $\alpha(v) = PLXS(T)\varphi$, where P is pressure, L is the optical path, X is the concentration of the measured gas, $S(T)$ and φ are the transition line strength and line shape function. The selected peak of detect gas is in the near infrared band, and the spectral absorption coefficient is small. Therefore, the formula can be expressed as:

$$I_{(t)} = I_0 [1 - PLXS(T)\varphi], \quad (2)$$

WMS is to transfer the detection object of the absorption spectrum from the low-frequency signal to the relatively high-frequency signal. The reason is that the noise in the system, such as 1/f noise or mechanical noise, has a greater impact on the low-frequency signal, while the high-frequency signal is not easily affected. By modulating the injection current of the tunable semiconductor laser, the wavelength and intensity of the output laser can be modulated at high frequency. When the high-frequency sine wave modulates the laser frequency, the instantaneous frequency and intensity of the incident laser can be expressed as:

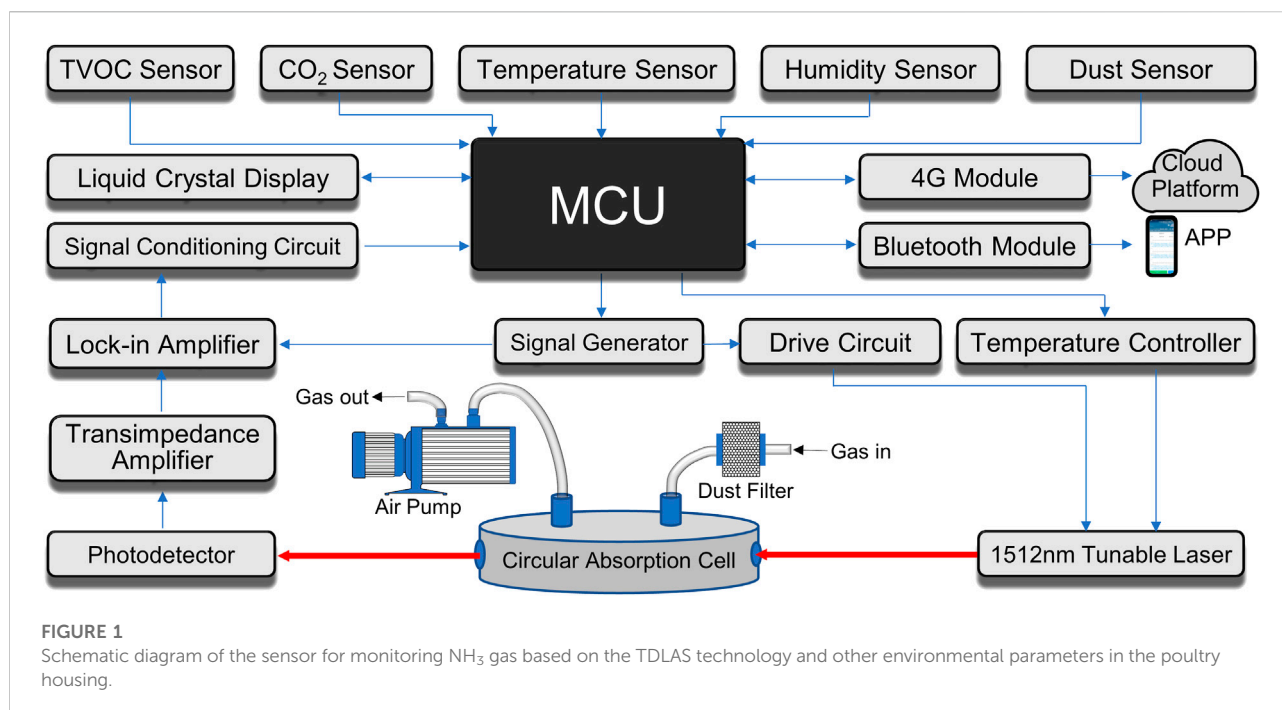
$$v_{(t)} = v_0 + a \cos(\omega t), \quad (3)$$

$$I_{(t)} = I_0 [1 + i_1 \cos(\omega t + \psi_1) + i_2 \cos(\omega t + \psi_2)], \quad (4)$$

Where a is the modulation depth, i_1 and i_2 are the intensity modulation coefficient, ψ_1 and ψ_2 are the intensity modulation phase shift. Expand the spectral absorption coefficient $\alpha(v)$ at central frequency v_0 in Fourier cosine series, the Fourier coefficients H_k can be shown as follows:

$$H_k(v_0, a) = \frac{PLX}{2\pi} 2\pi \int_{-\pi}^{\pi} S(T)\varphi[v_0 + a \cos(\omega t)] \cos(k\omega t) d\omega t, \quad (5)$$

The amplitude of second harmonic signal extracted by lock-in amplifier can be expressed as:



$$X_{2f} = \frac{GI_0}{2} \left[H_2 + \frac{i_1}{2} (H_1 + H_3) \cos \psi_1 + i_2 \left(H_0 + \frac{H_4}{2} \right) \cos \psi_2 \right], \quad (6)$$

Where G is the optical-electrical gain of the detection system. At the condition of low absorption and constant parameters such as optical path, pressure and temperature in the measurement environment, the concentration of the measured gas is proportional to the amplitude of second harmonic signal. The harmonic signal is proportional to the measured gas concentration using the lock-in amplifier to demodulate the high-frequency signal. WMS can detect trace gas by extracting weak signals and has a strong anti-interference ability.

Structure of the sensor

According to the HITRAN database [23] and commercially available lasers, we selected a tunable laser with the spectral line of 1,512 nm from Wuhan 69 Sensor Technology Co. LTD for specific and sensitive detection of NH₃ gas. The structure of the sensor is shown in Figure 1. The 1,512 nm tunable laser works at a constant temperature by a temperature controller. The working temperature is 25°C, and the current scan range is 55–65 mA. Its spectral line will be scanned by a drive circuit combined a high-frequency and small amplitude sine wave superimposed on a low-frequency and large amplitude sawtooth wave. The frequency of the sawtooth wave is 5 Hz, and the sine wave is 5 kHz. This scanning method is usually called wavelength

modulation spectroscopy which can extract weak absorption signals from the strong background noise. When the NH₃ gas was pumped into the circular absorption cell, the laser beam was absorbed and detected by the photodetector. The type of photodetector is g10899-01k from Hamamatsu Photonics (China) Co. LTD. Then the second harmonic signal for concentration inversion was demodulated by the lock-in amplifier and collected by the microcontroller (MCU). The type of MCU is STM32F103. According to Beer-Lambert law [24], the gas concentration is proportional to the second harmonic amplitude, absorption line strength, optical path and pressure. At normal temperature and pressure, the absorption line strength, optical path and pressure are known and constant. Therefore, the ammonia concentration has a positive proportional relationship with the second harmonic amplitude.

In addition, TVOC, CO₂, temperature, humidity and dust sensors are also integrated into our sensor system to obtain parameters related to air quality in poultry houses. Various sensor modules integrated into the system have their measurement accuracy, and the system adopted the all-in-one sensor module PTQS1005A from Beijing Planttower Co. LTD. Among them, the temperature range is between −10–55°C, the resolution is 0.1°C; The humidity measurement range is 0–99%, the resolution is 0.1%; The TVOC range is 0–10 ppm, the resolution is 0.01 ppm; The minimum detection limit of dust sensor is 1ppb; The range of CO₂ sensor is 400–3000 ppm. The data transmitted through the communication module is the value of the gas content in the environment obtained at the

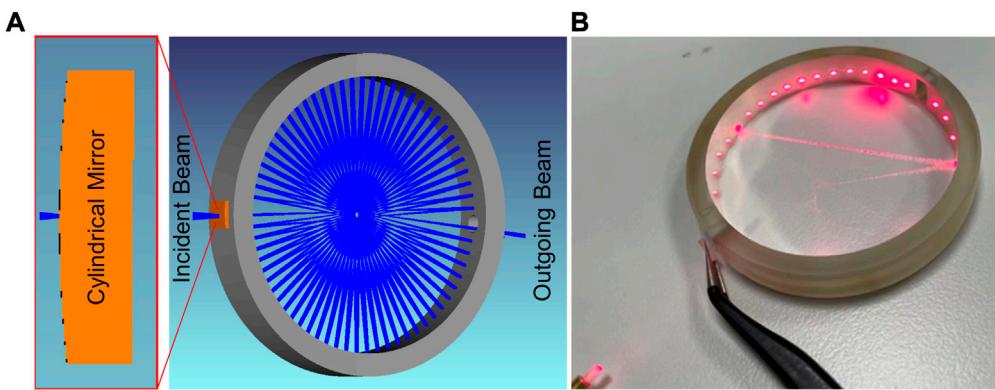


FIGURE 2
The micro circular absorption cell: (A) Optical path structure diagram; (B) Photograph.

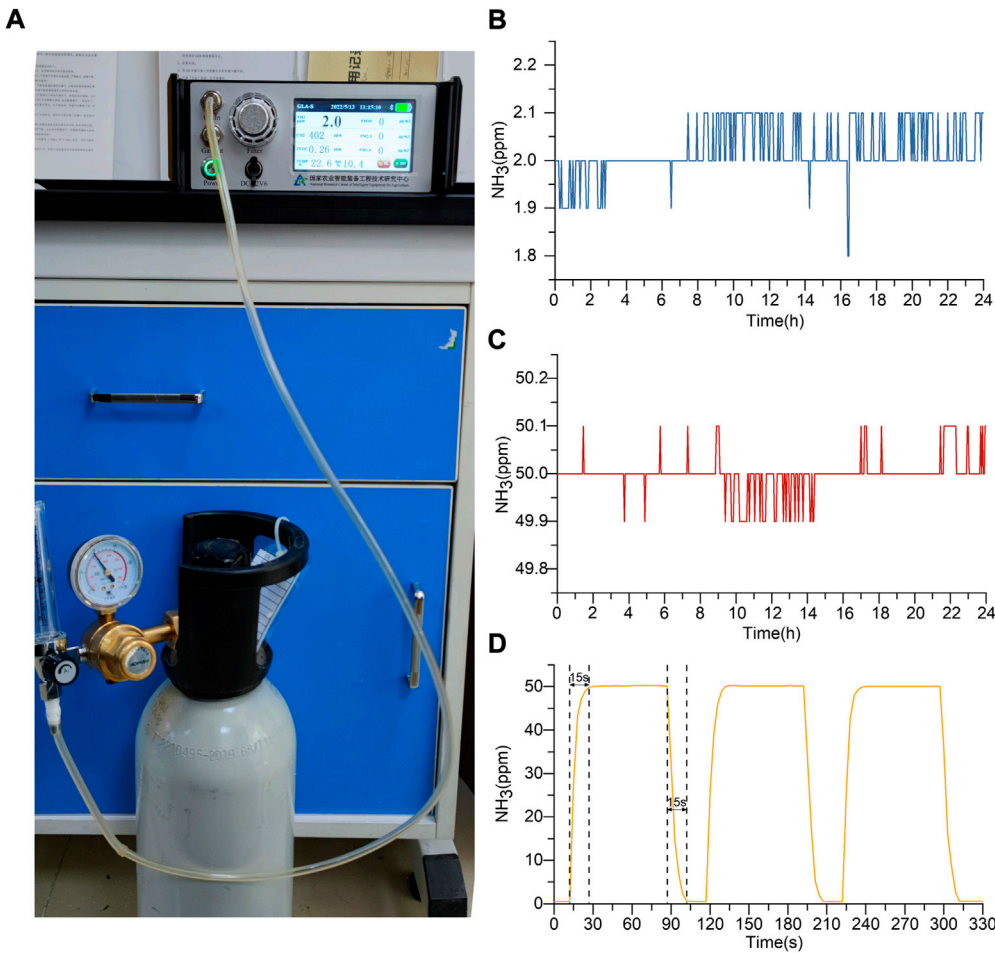


FIGURE 3
(A) Photograph of measuring standard ammonia; (B) Monitoring data for 2 ppm ammonia within 24 h; (C) Monitoring data for 50 ppm ammonia within 24 h; (D) Repeat measurement of 50 ppm ammonia.

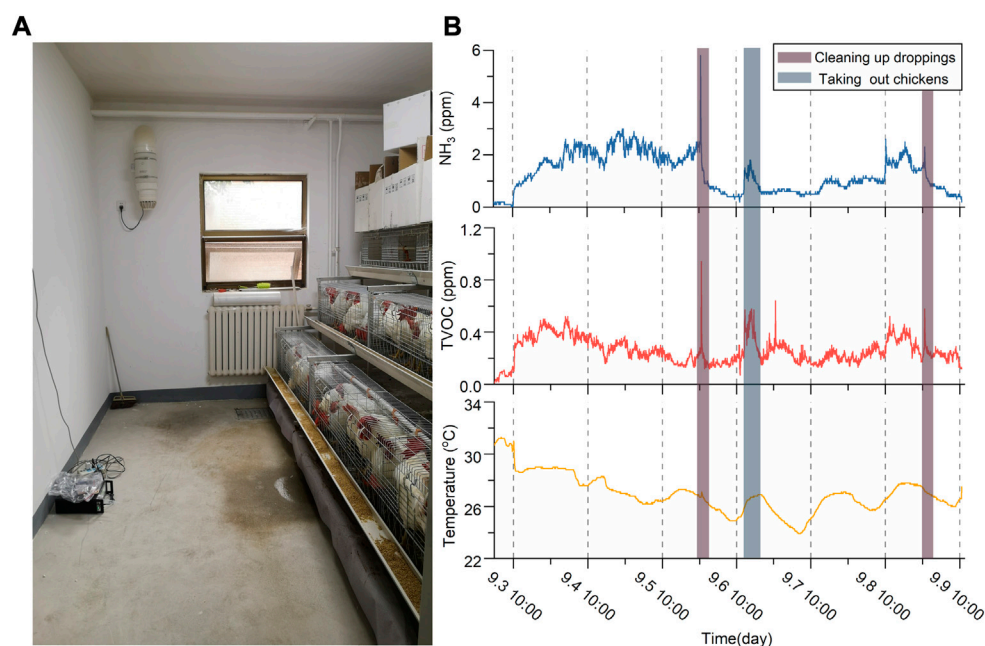


FIGURE 4

(A) Photograph from field measurement at the broiler house; (B) NH_3 , TVOC and temperature monitoring data in 6 days.

corresponding time, which will be transmitted to the mobile app in real time and automatically saved in the Excel table for the measurement personnel to view and analyze.

Design of the circular absorption cell

The measurement principle of TDLAS is based on Beer-Lambert law [24]. The detection sensitivity is often improved by increasing the effective absorption path at the same absorption line. However, the volume of the absorption cell with a long optical path is usually large. This results in a long response time and inapplicability to develop compact and portable TDLAS sensors [25]. With the trend of miniaturization of TDLAS sensors, more and more attention has been paid to the micro absorption cell with a long optical path [26]. Absorption cells based on several structures have developed to satisfy different application situations [27]. In this paper, by borrowing from published technologies [28–30], we designed a micro circular absorption cell for ammonia detection in poultry housing, just as shown in Figure 2. Compared to the circular absorption cell made up of many small reflectors in the Ref. [31], our cell used an integral ring reflector with the diameter of 60 mm and height of 10 mm to make it easy to install and has a better stability. The ring reflector was coated with an enhanced silver metal film with a reflectivity of more than 99% within the spectral region of 800–2000 nm. Using a cylindrical mirror, the incident beam with a diameter of 1.5 mm was shined on the ring reflector and

reflected about 70 times. Therefore, the cell could reach up to a 5 m optical path only within a volume of 30 ml, which ensures high sensitivity and fast response time for NH_3 detection.

Sensor performance and application in poultry housing

Sensor performance

Ammonia concentration in poultry housing is regulated to protect worker health and animal productivity in countries and regions worldwide. The European Union limits ammonia in poultry to 20 ppm, America allows a weighted average exposure limit of 50 ppm for humans for 8 h, and The United Egg Producers state indicates that ammonia levels in chicken houses should ideally be less than 10 ppm and not more than 25 ppm [32–34]. We fit the second harmonic peak obtained by measuring standard ammonia according to the variation range of ammonia concentration in poultry housing. The harmonic peak has an excellent linear relationship with the low ammonia concentration in poultry housing.

As shown in Figure 3A, we continuously measured the standard gas to verify the sensor performance and conducted it under laboratory conditions to ensure accuracy. As shown in Figure 3B,C, the standard gas concentration of 2 ppm and 50 ppm were continuously measured at 24 h with intervals of 3 min. The data fluctuated by 0.2 ppm during measured

TABLE 1 Comparison of different ammonia sensors.

Volume	Sensor	Response object	Time	LoD	References
On-chip	Semiconductors Sensor	Non-specificity	7 s	1ppm	[37]
On-chip	Electrochemical Sensor	Non-specificity	18 min	2ppm	[38]
/	TDLAS-based Sensor	NH ₃	778.4 s	0.5ppm	[39]
31.4 × 13 × 13.5 cm ³	TDLAS-based Sensor	NH ₃	38 s	3.95ppb	[40]
43 × 18 × 16 cm ³	TDLAS-based Sensor	NH ₃	184 s	0.16ppm	[25]
15 × 8 × 6 cm ³	TDLAS-based Sensor	NH ₃	15 s	0.2ppm	This work

ammonia concentration of 2 ppm and fluctuated by 0.1 ppm when measured ammonia concentration of 50 ppm. The time-corresponding concentration data in Figures 3B–D is obtained by using Origin to draw the data from the mobile app. Prolonged monitoring observed that the signal baseline had no drift, and the measurement of low concentration ammonia also had excellent precision and stability. The response time and recovery time are also essential performance metrics. To demonstrate the reversibility of the sensor, we measured the standard gas several times. Figure 3D shows the signal response when switching from air to 50 ppm ammonia three times. As a result, the sensor response time and recovery time remain within 15 s, and measurements can be quickly restored to air levels, meaning the sensor has excellent reversibility. The data indicated that the sensor could be used to monitor the dynamic changes at low concentrations of ammonia to meet the need for ammonia monitoring in poultry housing.

Application in poultry housing

We used the sensor to monitor the broiler chicken house environment on the farm for 6 days. There are 36 mature roosters in the monitoring field, staff regularly clean up and sanitize, and fewer external factors influence the data. As shown in Figure 4A, the sensor was placed in the broiler house on September 3 at 10:00 a.m., measurements were taken at intervals of 5 min, and normal production activities continued in the house.

Figure 4B shows that ammonia concentration in the broiler house varied over time. In 6 days, the staff grabbed 16 chickens from the house (grey shadow) and cleaned up manure twice (brown shadow). As the manure accumulated, ammonia concentration continued to rise in the house and cleaning the manure caused a precipitous drop in ammonia concentration. The data confirmed that manure is the main source of ammonia in poultry housing [35]. Ammonia evaporated rapidly while cleaning manure, which caused the ammonia concentration to fluctuate significantly in a short period [36]. The concentration curve in Figure 4B is obtained using Origin to draw the data from the mobile app.

Similarly, measurements changed when some chickens were grabbed because of fluctuation in ammonia concentration by shaking the coop. The rapid rise and fall of ammonia caused by human activities demonstrated the rapid response of the sensor to monitor ammonia change in poultry housing. According to the Environmental Quality Standard For The Livestock And Poultry Farm of the People's Republic of China, the concentration of ammonia in adult poultry housing is less than 15 ppm, and the measurement results meet the standards.

The environmental requirements of modern poultry housing are not limited to harmful gas concentration but also include temperature and humidity, dust and CO₂ concentration. Abnormal temperature, humidity and other environmental factors affect the development of animals. The TVOC concentration and temperature in Figure 4B reflect the broiler house environment from the side. TVOC levels suddenly increased when cleaning the house and grabbing chickens, similar to the change in ammonia concentration. The temperature changed with the day and night rule and never exceeded 30°C. Upon completion of the measurement, the device was re-measured for standard ammonia and found to be unchanged, indicating that the measured concentration in the broiler house was accurate.

Conclusion

The experimental data shows a good ability to monitor the ammonia of the sensor in poultry housing. The performance of this sensor and some previous sensors is shown in Table 1. The volume of this sensor in Table 1 only includes the part of measure ammonia, excluding other integrated sensor modules. The sensor designed in this paper can quickly measure ammonia. As the volume is reduced, the accuracy remains at an excellent level.

Based on the TDLAS and circular absorption cell, the portable sensor of low monitor concentration of ammonia was studied. WMS reduces environmental noise interference and detects fainter signals. The sensor has an incredible increase in performance using the circular absorption cell. The small size of the absorption cell makes the chamber highly efficient for gas exchange at a fixed velocity. The low exposure

area reduces ammonia memory effects on the inner surface. Experimental data shows that the sensor has the advantages of high sensitivity, high stability and fast response time in long-term monitoring. The system realized the multiple component measurement in a complex environment using integrated sensor modules. As an effective low concentration ammonia monitoring system, the sensor has considerable application potential in poultry housing.

Data availability statement

The original contributions presented in the study are included in the article/supplementary material, further inquiries can be directed to the corresponding author.

Author contributions

KW, RG, YZ, LJ, and DD contributed to the conception and design of the study. RG and LJ performed the simulation analysis and performed the experimental verification. KW and YZ wrote the first draft of the manuscript. LJ and DD presented the revision of the manuscript. All authors have read and agreed to the published version of the manuscript vision.

References

- Webb J, Menzi H, Pain BF, Misselbrook TH, Dammgen U, Hendriks H, et al. Managing ammonia emissions from livestock production in Europe. *Environ Pollut* (2005) 135(3):399–406. doi:10.1016/j.envpol.2004.11.013
- Meda B, Hassouna M, Aubert C, Robin P, Dourmad JY. Influence of rearing conditions and manure management practices on ammonia and greenhouse gas emissions from poultry houses. *World's Poult Sci J* (2011) 67(3):441–56. doi:10.1017/s0043933911000493
- Kupper T, Bonjour C, Menzi H. Evolution of farm and manure management and their influence on ammonia emissions from agriculture in Switzerland between 1990 and 2010. *Atmos Environ* (2015) 103:215–21. doi:10.1016/j.atmosenv.2014.12.024
- Shah SWA, Chen D, Zhang J, Liu Y, Ishfaq M, Tang Y, et al. The effect of ammonia exposure on energy metabolism and mitochondrial dynamic proteins in chicken thymus: Through oxidative stress, apoptosis, and autophagy. *Ecotoxicol Environ Saf* (2020) 206:111413. doi:10.1016/j.ecoenv.2020.111413
- Wei FX, Hu XF, Xu B, Zhang MH, Li SY, Sun QY, et al. Ammonia concentration and relative humidity in poultry houses affect the immune response of broilers. *Genet Mol Res* (2015) 14(2):3160–9. doi:10.4238/2015.April.10.27
- Kocaman B, Esenbuga N, Yildiz A, Lacin E, Macit M. Effect of environmental conditions in poultry houses on the performance of laying hens. *Int J Poult Sci* (2005) 5(1):26–30. doi:10.3923/ijps.2006.26.30
- Kilic I, Yaslioglu E. Ammonia and carbon dioxide concentrations in a layer house. *Asian-australas J Anim Sci* (2014) 27(8):1211–8. doi:10.5713/ajas.2014.14099
- Naseem S, King AJ. Ammonia production in poultry houses can affect health of humans, birds, and the environment-techniques for its reduction during poultry production. *Environ Sci Pollut Res* (2018) 25(16):15269–93. doi:10.1007/s11356-018-2018-y
- Green AR, Wesley I, Trampel DW, Xin H. Air quality and bird health status in three types of commercial Egg layer houses. *J Appl Poult Res* (2009) 18(3):605–21. doi:10.3382/japr.2007-00086
- Kwak D, Lei Y, Maric R. Ammonia gas sensors: A comprehensive review. *Talanta* (2019) 204:713–30. doi:10.1016/j.talanta.2019.06.034
- Mohan T, Sheik Farid K. V. S., Sustainable biological system for the removal of high strength ammoniacal nitrogen and organic pollutants in poultry waste processing industrial effluent. *J Air Waste Manag Assoc* (2020) 70(12):1236–43. doi:10.1080/10962247.2020.1731013
- Van Huffel K, Heynderickx PM, Dewulf J, Van Langenhove HJCE. Measurement of odorants in livestock buildings: Sift-ms and td-gc-ms. *Chemical Engineering* (2012) 30. 978–88. doi:10.3303/CTE1230012
- Ngwabie NM, Jeppsson KH, Gustafsson G, Nimmermark S. Effects of animal activity and air temperature on methane and ammonia emissions from a naturally ventilated building for dairy cows. *Atmos Environ* (2011) 45(37):6760–8. doi:10.1016/j.atmosenv.2011.08.027
- Li H, Zhang C, Xin H. Performance of an infrared photoacoustic single gas analyzer in measuring ammonia from poultry houses. *Appl Eng Agric* (2015) 31(3):471–7. doi:10.13031/aea.31.10826
- Lin T, Shah SB, Wang-Li L, Oviedo-Rondón EO, Post J. Development of mos sensor-based NH₃ monitor for use in poultry houses. *Comput Elect Agric* (2016) 127:708–15. doi:10.1016/j.compag.2016.07.033
- Gates RS, Xin H, Casey KD, Liang Y, Wheeler EF. Method for measuring ammonia emissions from poultry houses. *J Appl Poult Res* (2005) 14(3):622–34. doi:10.1093/japr/14.3.622
- Wheeler E. F., Casey K. D., Zajacz kowski J., Topper P. A., Ammonia emissions from U.S. Poultry houses: Part Iii – broiler houses. Third International Conference on Air Pollution from Agricultural Operations, Research Triangle Park, NC, USA, (October, 2003) (2003).
- Aunsa-Ard W, Pobkrut T, Kerdcharoen T, Prombaingoen N, Kijpreedaborisuthi O. Electronic nose for monitoring of livestock farm odors (poultry farms). 2021 13th international Conference on Knowledge and smart technology. KST. (January, 2021). Bangsaen, Chonburi, Thailand. Thailand: IEEE (2021). 176–80.

Funding

This research was funded by the Science and Technology Innovation 2030- Key Project of China (2021ZD0113801), National Natural Science Foundation of China (32101609), Innovation Capacity Building Project of Beijing Academy of Agriculture and Forestry Sciences (KJCX20200417), Beijing Innovation Consortium of Agriculture Research System (BAIC08-2022), and National and Local Joint Engineering Laboratory For Agricultural Internet of Things (PT2022-23).

Conflict of interest

The authors declare that the research was conducted in the absence of any commercial or financial relationships that could be construed as a potential conflict of interest.

Publisher's note

All claims expressed in this article are solely those of the authors and do not necessarily represent those of their affiliated organizations, or those of the publisher, the editors and the reviewers. Any product that may be evaluated in this article, or claim that may be made by its manufacturer, is not guaranteed or endorsed by the publisher.

19. Lahav O, Mor T, Heber AJ, Molchanov S, Ramirez JC, Li C, et al. A new approach for minimizing ammonia emissions from poultry houses. *Water Air Soil Pollut* (2008) 191(1-4):183–97. doi:10.1007/s11270-008-9616-0
20. Li G, Dong E, Ji W. H. A near-infrared trace Co₂ detection system based on an 1,580 Nm tunable diode laser using a cascaded integrator comb (cic) filter-assisted wavelength modulation technique and a digital lock-in amplifier. *Front Phys* (2019) 7: 9. doi:10.3389/fphy.2019.00199
21. Guo Y, Qiu X, Li N, Feng S, Cheng T, Liu Q, et al. A portable laser-based sensor for detecting H₂s in domestic natural gas. *Infrared Phys Tech* (2020) 105: 103153. doi:10.1016/j.infrared.2019.103153
22. Li G, Jiang Q, Hua C, Ma K, Jiao Y, Ji W. Temperature and pressure insensitive spectroscopic method for measuring 13ch₄ during oil and natural gas drilling operations. *Front Phys* (2021) 9:9. doi:10.3389/fphy.2021.633012
23. Rothman LS, Gordon IE, Babikov Y, Barbe A, Chris Benner D, Bernath PF, et al. The Hitran2012 molecular spectroscopic database. *J Quantitative Spectrosc Radiative Transfer* (2013) 130:4–50. doi:10.1016/j.jqsrt.2013.07.002
24. Lin S, Chang J, Sun J, Xu P. Improvement of the detection sensitivity for tunable diode laser absorption spectroscopy: A review. *Front Phys* (2022) 10:10. doi:10.3389/fphy.2022.853966
25. Guo X, Zheng F, Li C, Yang X, Li N, Liu S, et al. A portable sensor for *in-situ* measurement of ammonia based on near-infrared laser absorption spectroscopy. *Opt Lasers Eng* (2019) 115:243–8. doi:10.1016/j.optlaseng.2018.12.005
26. Liu K, Wang L, Tan T, Wang G, Zhang W, Chen W, et al. Highly sensitive detection of methane by near-infrared laser absorption spectroscopy using a compact dense-pattern multipass cell. *Sensors Actuators B: Chem* (2015) 220: 1000–5. doi:10.1016/j.snb.2015.05.136
27. Kong R, Sun T, Liu P, Zhou X. Optical design and analysis of a two-spherical-mirror-based multipass cell. *Appl Opt* (2020) 59(6):1545–52. doi:10.1364/AO.381632
28. Chang H, Feng S, Qiu X, Meng H, Guo G, He X, et al. Implementation of the toroidal absorption cell with multi-layer patterns by a single ring surface. *Opt Lett* (2020) 45(21):5897–900. doi:10.1364/OL.404198
29. Rothbart N, Schmalz K, Hubers H-W. A compact circular multipass cell for millimeter-wave/terahertz gas spectroscopy. *IEEE Trans Terahertz Sci Technol* (2020) 10(1):9–14. doi:10.1109/tthz.2019.2950123
30. Mangold M., Tuzson B., Hundt M., Jagerska J., Looser H., Emmenegger L. Circular paraboloid reflection cell for laser spectroscopic trace gas analysis. *J Opt Soc Am A* (2016) 33(5):913–9. doi:10.1364/JOSAA.33.000913
31. Graf M., Emmenegger L., Tuzson B. Compact, circular, and optically stable multipass cell for mobile laser absorption spectroscopy. *Opt Lett* (2018) 43(11): 2434–7. doi:10.1364/OL.43.002434
32. Santonja G. G., Georgitzakis K., Scalet B. M., Montobbio P., Roudier S., Sancho L. D. J. E. E. Best available techniques (bat) reference document for the intensive rearing of poultry or pigs. *European IPPC Bureau*, (2017) 11:898.
33. Producers U. E. *United Egg Producers animal husbandry guidelines for us Egg laying flocks* (2006) Alpharetta, Georgia: United Egg Producers.
34. Safety O, Gov H. A. J. O. (2007). Occupational Safety and Health Administration *Ammonia in workplace atmospheres—solid sorbent* United States: OSHA.
35. Ti C., Xia L., Chang S. X., Yan X. Potential for mitigating global agricultural ammonia emission: A meta-analysis. *Environ Pollut* (2019) 245:141–8. doi:10.1016/j.envpol.2018.10.124
36. Zhang X., Li J., Shao L., Huan H., Qin F., Zhai P., et al. Effects of manure removal frequencies and deodorants on ammonia and ghg concentrations in livestock house. *Atmosphere* (2022) 13(7):1033. doi:10.3390/atmos13071033
37. Qi Q., Wang P.-P., Zhao J., Feng L.-L., Zhou L.-J., Xuan R.-F., et al. SnO₂ nanoparticle-coated In₂O₃ nanofibers with improved NH₃ sensing properties. *Sensors Actuators B: Chem* (2014) 194:440–6. doi:10.1016/j.snb.2013.12.115
38. Liu W., Liu Y.-Y., Do J.-S., Li J. Highly sensitive room temperature ammonia gas sensor based on Ir-doped Pt porous ceramic electrodes. *Appl Surf Sci* (2016) 390: 929–35. doi:10.1016/j.apsusc.2016.08.121
39. Lu H., Zheng C., Zhang L., Liu Z., Song F., Li X., et al. A remote sensor system based on tdas technique for ammonia leakage monitoring. *Sensors (Basel)* (2021) 21(7):2448. doi:10.3390/s21072448
40. Li G., Zhang X., Zhang Z., Wu Y., Ma K., Jiao Y., et al. Performance enhancement of a near-infrared NH₃ sensor based on pso-lssvm for denitrification industrial process. *Infrared Phys Tech* (2022) 125:104226. doi:10.1016/j.infrared.2022.104226



OPEN ACCESS

EDITED BY

Leizi Jiao,
Beijing Academy of Agriculture and
Forestry Sciences, China

REVIEWED BY

Shouliang Yi,
National Energy Technology
Laboratory (DOE), United States
Ye Liu,
Beijing Technology and Business
University, China
Zhangying Zhang,
Queensland University of
Technology, Australia

*CORRESPONDENCE

Chao Zhang
zhangchao_3@163.com

SPECIALTY SECTION

This article was submitted to
Food Chemistry,
a section of the journal
Frontiers in Nutrition

RECEIVED 13 October 2022

ACCEPTED 10 November 2022

PUBLISHED 01 December 2022

CITATION

Liu X, Wang R, Liu H, Wang Y, Shi Y and
Zhang C (2022) High-pressure
treatment enhanced aromatic
compound concentrations of melon
juice and its mechanism.
Front. Nutr. 9:1052820.
doi: 10.3389/fnut.2022.1052820

COPYRIGHT

© 2022 Liu, Wang, Liu, Wang, Shi and
Zhang. This is an open-access article
distributed under the terms of the
[Creative Commons Attribution License](#)
(CC BY). The use, distribution or
reproduction in other forums is
permitted, provided the original
author(s) and the copyright owner(s)
are credited and that the original
publication in this journal is cited, in
accordance with accepted academic
practice. No use, distribution or
reproduction is permitted which does
not comply with these terms.

High-pressure treatment enhanced aromatic compound concentrations of melon juice and its mechanism

Xiao Liu^{1,2}, Ruiqi Wang¹, He Liu², Yubin Wang¹, Yue Shi¹ and Chao Zhang^{1*}

¹Institute of Agri-Food Processing and Nutrition, Beijing Academy of Agriculture and Forestry Sciences, Beijing Key Laboratory of Agricultural Products of Fruits and Vegetables Preservation and Processing, Key Laboratory of Vegetable Postharvest Processing, Ministry of Agriculture and Rural Affairs, Beijing, China, ²College of Food Science and Technology, Bohai University, Jinzhou, China

Introduction: The flavor deterioration blocks the development of melon juice.

Methods: The effects of ultra-high temperature (UHT) and high pressure (HP) treatments on the aromatic compound concentrations of melon juice and their mechanisms were explored with fresh juice as the control.

Results: A total of 57 volatile compounds were identified by gas chromatography-tandem mass spectrometry analysis. β -ionone was shown to be the major aromatic component of melon juice for the first time. The HP at 200 MPa for 20 min increased the total volatile concentration of melon juice by 1.54 and 3.77 times the control and UHT, respectively. Moreover, the sum concentration of a major aromatic component in the HP treatment was 1.49 and 5.94 times higher than that of the control and UHT, respectively.

Discussion: The HP treatment raised the concentration of volatile and aromatic components of melon juice by reducing their surface tension.

KEYWORDS

melon juice, high pressure treatment, GC-MS analysis, β -ionone, surface tension, weight loss rate

Introduction

Melons (*Cucumis melo* L.) are favored by people worldwide for their distinctive aroma and sweetness. However, commercialized production of melon juice is hard to realize due to the unsolved obstacle of flavor deterioration (1). Ultra-high temperature (UHT) is the most widely used juice sterilization technology. However, the UHT also leads to serious flavor deterioration. The UHT treatment of sea buckthorn juice resulted in a decrease of 3.48 and 14.60% in total volatiles and esters at 140°C for 2 s and a sharp decrease of 6.90% at 140°C in alcohol contents (2).

Moreover, the UHT also caused an unacceptable cooked off-flavor odor similar to mature pumpkin in melon juice. Dimethyl sulfide, methional, methanethiol, dimethyl trisulfide, dimethyl disulfide, and acetaldehyde have been identified as the off-flavors (3). The formation of volatile sulfur compounds has been inhibited by reducing the pH of melon juice to 2.0 or adding epicatechin (4). However, this method was difficult to use in commercialized production.

High-pressure (HP) technology is a non-thermal process that applies high hydrostatic pressure to the food matrix through a specific liquid transfer medium (5). Compared with the thermal treatment, the HP had a lower impact on the nutrition and flavor of foods due to its better control of the temperature during processing (6, 7). For foods with high moisture content, the temperature increased to $\sim 3^{\circ}\text{C}$ per 100 MPa. Therefore, HP processing led to better flavor retention for fruit juice. Recent studies showed that the HP treatment (500 MPa for 10 min) of kiwifruit juice maintained the retention rate of characteristic aromas from esters and alcohols (8). Similar results were also demonstrated in the pineapple juice (9). Despite most studies focusing on flavor retention, the effects of HP processing on the concentrations of melon juice flavor and their mechanism were ignored.

This study explored the effect of the UHT and HP treatments on the aromatic compounds of melon juice and their potential mechanism. Specifically, the concentration of volatile components of the UHT and HP treatments was measured by the GC-MS analysis with the fresh juice as the control. The major aromatic compounds were compared to determine the optimal HP parameters. The physical properties of the optimal HP and UHT treatments were compared to discover the potential mechanism.

Materials and methods

Experiment design

The UHT and HP treatments were compared with the fresh melon juice as the control. Melon was purchased from Guoxiangsiyi Fruit Supermarket in June 2021 in Haidian District, Beijing. The melon (*C. melo* L. var. Xizhoumi No. 25) was oval and light gray with a shallow net and weighed about 1.2–2.5 kg per fruit. The flesh of the fruits was light orange and crispy, with a soluble solid concentration of 9.5%–13%.

Control

The surface of the fruits was washed in an icy sodium hypochlorite solution (100 mg/L) and flushed two times with icy water. The peel and seeds were removed in a sanitary processing workshop. The flesh was cut into cubes and smashed in a Philips juicer for 5 min (HR1861, Philips Ltd., Beijing, China). After quickly removing the top foam, the mixture was sealed in an aluminum foil bag of 200 mL and stored in a refrigerator at -4°C for subsequent sample determination.

UHT

The fresh melon juice was sterilized in the ultra-high temperature unit (FT74X-40-44-A, Armfield Ltd.) at room temperature. Then, 1.5 L of juice were poured into the UHT

equipment's feeder and heated at 135°C for 15 s. For the subsequent analysis, the sterilized sample was quickly sealed and cooled in an icy bath in a 200-ml aluminum foil bag.

HP

The fresh melon juice was processed in the ultra-high pressure unit (BDS200-FL, Stansted Fluid Power Ltd., England) at room temperature. The melon juice sealed in the 200-mL aluminum foil bag was subjected to six kinds of treatments: (1) 200 MPa for 10 min; (2) 200 MPa for 20 min; (3) 400 MPa for 10 min; (4) 400 MPa for 20 min; (5) 600 MPa for 10 min; and (6) 600 MPa for 20 min. They were nominated as HP2-1, HP2-2, HP4-1, HP4-2, HP6-1, and HP6-2, respectively. The holding time did not include the time to increase and release the pressure. After reaching the pressure holding time, the system automatically released the pressure within 10–20 s. The pressured sample was cooled in an icy bath quickly for subsequent analysis.

Analysis of volatile compounds

The volatile compounds were detected by using a headspace solid-phase microextraction tandem gas chromatography-mass spectrometer (GC-MS) method, as described by Luo et al. (10), with a few modifications. The sample (6.0 g) was transferred into 20-ml headspace glass vials containing 2.0 g of sodium chloride and 10 μL of octanol (30 $\mu\text{g}/\text{mL}$) as an inner standard. The sample was stirred at 100 rpm, and its volatile compounds in the headspace were extracted and absorbed by an SPME fiber (57329-U PDMS/DVB/CAR, Sigma-Aldrich Company, USA) at 50°C for 30 min. After being absorbed, the absorbed compounds were thermally desorbed at 250°C for 3 min in a splitless mode by a GC-MS system (6890N/5977B, Agilent Technologies Company, USA). Volatile compounds were separated on a DB-5MS elastic capillary column (30 m \times 0.25 mm \times 0.25 μm ; Agilent Technologies, USA). Helium was used as a carrier gas with a constant flow rate of 1.0 mL/min. The initial temperature in the oven was set at 35°C for 5 min and increased at a rate of $4^{\circ}\text{C}/\text{min}$ to 150°C , held for 3 min, and increased at a rate of $8^{\circ}\text{C}/\text{min}$ to 190°C , again held for 1 min, and ramped to 250°C at $30^{\circ}\text{C}/\text{min}$, and held at 250°C for an additional 5 min. The full scan mode was adopted to collect signals at a scan speed of 1,562 u/s. The mass detector was operated in electron impact mode (70 eV). The ion source temperature was 230°C , the transmission line temperature was 250°C , and the quadrupole temperature was 150°C . The detected volatile compounds were identified by comparing the mass spectra with those in mass spectral libraries (NIST17). An MS match index of $\geq 80\%$ was listed and verified manually, point by point. The concentration of each aromatic compound was calculated based on the peak areas of 1-octanol, an internal standard with a

known concentration (Equation 1):

$$m_x = \frac{C_i \times V_i \times A_x}{m_s \times A_i} \times 1,000 \quad (1)$$

where C_i refers to the mass concentration of the standard internal compound and the unit was $\mu\text{g/ml}$; V_i refers to the additional amount of the internal standard in the sample, 10 μl ; m_s refers to the sample mass of 6 g; A_x and A_i refer to the peak areas of the target compound and the standard internal compound, respectively. m_x refers to the concentration of the target compound, expressed in $\mu\text{g/kg}$ fresh weight (FW).

Calculation of odor activity values

The odor activity values (OAV) were the ratio of the concentration to their corresponding odor threshold in water (11) and were calculated according to Equation (2). Normally, compounds with OAVs of no <1.0 were potential flavoring agents:

$$OAV_i = \frac{C_i}{O_i} \quad (2)$$

where C_i is the concentration of the compound, and O_i is the odor threshold of the compound.

Surface tension analysis

The juice sample of 50 ml was put into the glass container of the surface tension tester (K100C-MK2, KRUS, Germany). The surface tension was tested with the platinum tablet plate at 25°C . The instrument was calibrated with water. The testing parameters were set as follows: the measurement speed was 10 mm/min, the immersion depth was 2.00 mm, the maximum measurement time was 60 s, and the deviation value was 0.1 mN/m. The result was the average of five measured values with a stable measurement of less than the deviation value. The platinum tablet plate was thoroughly cleaned and flame-dried before each measurement.

Thermogravimetric analysis

The thermogravimetric differential thermal synchronous analyzer (TGA/DSC 1, Mettler Toledo, Switzerland) was preheated for half an hour. The crucibles were heated at 500°C before the test. The heating chamber was preheated to 60°C in advance. The 25- μL sample was then loaded into the crucibles and placed isothermally in the chamber at 60°C for 20 min, with distilled water serving as the control. The weight loss rate was the mass loss caused by sample evaporation, which was determined in an area with constant temperature and varied linearly with

time (12). The curve of the weight loss rate in Figure 6A was calculated after the original quality data was normalized. The curve in Figure 6B is named Y' , which indicates the normalized data of melon juice samples minus the water sample.

Statistical analysis

All the measurements were repeated three times. A one-way analysis of variance was conducted on different groups using SPSS Statistics 26.0. The results were shown as mean \pm standard deviation at a significance level of a P -value of < 0.05 . The graphs were all plotted using Origin 2021. The profile of the mechanism was prepared with PowerPoint.

Results and discussion

Identification of volatile compounds in melon juice

A total of 57 volatile components were detected in control, UHT treatment, and HP treatment, including 20 esters, 15 alcohols, 14 aldehydes, and eight ketones (Table 1). The volatile component number of the control, UHT, HP2-1, HP2-2, HP4-1, HP4-2, HP6-1, and HP6-2, was 16, 37, 19, 20, 25, 29, 25, and 26, respectively. The UHT included more volatile components than the other treatments. The composition of volatile compounds in the control and HP groups was similar, such as ethyl acetate and nonanal. There were clear differences between the control and UHT treatment. In addition, with the increase of HP parameters between HP groups, the same components as those in the UHT group appear in the HP4-1, HP4-2, HP6-1, and HP6-2 groups, such as (Z)-3-hexenyl acetate and decyl aldehyde. These volatile components were combined to form the final flavor of melon juice.

The total volatile concentration of melon juice was highest (532.27 $\mu\text{g/kg}$) in the HP2-2 group, which was 1.54 and 3.77 times that of the control and UHT, respectively. The HP2-2 increased the concentration of total volatile components in melon juice, while the UHT treatment significantly reduced it.

β -Ionone was detected in each melon juice for the first time. β -Ionone was produced by the cleavage at the C9 and C10 keys from the β -Carotene metabolic pathways (13), which was a common aromatic volatile compound that existed in a variety of fruits, including raspberry juice (14) and apple juice (15), but had not been reported in melons before. The concentration of β -ionone was highest (4.12 $\mu\text{g/kg}$) in the HP2-2, which was 1.66 and 1.45 times that of the control and the UHT treatment, respectively.

TABLE 1 Identification and concentrations of volatile components of melon juice.

ID	Volatile components ¹	CAS	Molecular formula	Control (μg/kg) ²	UHT (μg/kg) ²	HP2-1 (μg/kg) ²	HP2-2 (μg/kg) ²	HP4-1 (μg/kg) ²	HP4-2 (μg/kg) ²	HP6-1 (μg/kg) ²	HP6-2 (μg/kg) ²
Ester											
1	Diisobutyl phthalate	84-69-5	C ₁₆ H ₂₂ O ₄	–	–	–	–	–	0.42 ± 0.02	–	–
2	Butyl-octyl phthalate	84-78-6	C ₂₀ H ₃₀ O ₄	8.50 ± 2.12	0.43 ± 0.01	–	–	–	–	–	–
3	2-Methyl-1-butyl acetate	624-41-9	C ₇ H ₁₄ O ₂	–	0.84 ± 0.02	8.19 ± 0.12	9.76 ± 0.50	9.22 ± 0.32	7.08 ± 1.20	3.45 ± 0.24	3.11 ± 0.32
4	Isoamyl acetate	123-92-2	C ₇ H ₁₄ O ₂	–	–	–	–	–	0.73 ± 0.11	–	–
5	2,2,4-Trimethyl-1,3-pentanediol diisobutyrate	6846-50-0	C ₁₆ H ₃₀ O ₄	–	0.95 ± 0.23	–	–	–	–	–	–
6	2,4-Pentanediol,2,4-diacetate	7371-86-0	C ₉ H ₁₆ O ₄	–	0.62 ± 0.12	–	–	0.75 ± 0.04	–	–	–
4	1-(Benzoyloxy)-2,5-pyrrolidinedione	23405-15-4	C ₁₁ H ₉ NO ₄	–	0.61 ± 0.11	–	2.31 ± 0.02	1.44 ± 0.11	–	–	–
8	2-Methylacetic acid-2-alkenyl ester	33425-30-8	C ₅ H ₁₀ O·C ₂ H ₄ O ₂	–	–	–	–	0.52 ± 0.01	0.40 ± 0.03	–	–
9	(Z)-3-Hexenyl acetate	3681-71-8	C ₈ H ₁₄ O ₂	–	1.97 ± 0.22	–	–	–	–	0.95 ± 0.01	0.88 ± 0.02
10	2-Ethylhexyl acetate	103-09-3	C ₁₀ H ₂₀ O ₂	–	–	–	–	–	–	–	0.66 ± 0.05
11	Phenethyl acetate	103-45-7	C ₁₀ H ₁₂ O ₂	–	1.13 ± 0.01	–	–	–	–	–	–
12	Butyl acetate	123-86-4	C ₆ H ₁₂ O ₂	1.44 ± 0.25	0.29 ± 0.06	1.75 ± 0.25	2.40 ± 0.26	2.45 ± 0.18	2.47 ± 0.15	1.32 ± 0.13	1.25 ± 0.01
13	(Z)-non-3-enyl ester acetic acid	13049-88-2	C ₁₁ H ₂₀ O ₂	–	0.32 ± 0.03	–	–	–	–	–	–
14	Benzyl acetate	140-11-4	C ₉ H ₁₀ O ₂	–	31.09 ± 2.23	–	–	4.55 ± 0.54	3.71 ± 0.25	0.86 ± 0.11	1.08 ± 0.32
15	2,4-Dimethylbenzoate	55000-43-6	C ₁₈ H ₂₀ O ₂	–	1.82 ± 0.02	–	–	–	–	–	–
16	Ethyl acetate	141-78-6	C ₄ H ₈ O ₂	21.06 ± 2.24	2.38 ± 0.21	18.68 ± 2.12	21.59 ± 2.42	22.98 ± 2.54	16.59 ± 2.01	10.59 ± 1.58	5.54 ± 1.01
17	Isobutyl acetate	110-19-0	C ₆ H ₁₂ O ₂	8.14 ± 1.52	1.39 ± 0.23	9.17 ± 1.15	12.25 ± 1.65	10.90 ± 1.12	9.91 ± 1.14	5.33 ± 1.25	4.74 ± 0.52
18	Isopulegol acetate	57576-09-7	C ₁₂ H ₂₀ O ₂	–	–	–	–	–	0.44 ± 0.02	–	–
19	n-Propyl acetate	109-60-4	C ₅ H ₁₀ O ₂	–	–	–	–	–	–	–	0.54 ± 0.12
20	Propanoic acid, 2-methyl-, 3-hydroxy-2,2,4-trimethylpentyl ester	77-68-9	C ₁₂ H ₂₄ O ₃	–	0.37 ± 0.03	–	–	–	–	–	–
Alcohol											
1	(Z)-6-nonen-1-ol	35854-86-5	C ₉ H ₁₈ O	–	3.05 ± 0.52	–	–	–	–	0.91 ± 0.23	–
2	1-Hexanol	111-27-3	C ₆ H ₁₄ O	–	–	–	–	–	–	0.36 ± 0.15	–

(Continued)

TABLE 1 (Continued)

ID	Volatile components ¹	CAS	Molecular formula	Control (μg/kg) ²	UHT (μg/kg) ²	HP2-1 (μg/kg) ²	HP2-2 (μg/kg) ²	HP4-1 (μg/kg) ²	HP4-2 (μg/kg) ²	HP6-1 (μg/kg) ²	HP6-2 (μg/kg) ²
3	2-Ethylhexanol	104-76-7	C ₈ H ₁₈ O	8.71 ± 2.23	2.61 ± 0.56	9.12 ± 2.52	13.55 ± 2.65	7.92 ± 1.25	8.30 ± 1.34	4.38 ± 0.98	4.36 ± 1.25
4	1-Nonanol	143-08-8	C ₉ H ₂₀ O	24.49 ± 3.65	9.67 ± 2.54	23.88 ± 5.65	25.14 ± 4.25	1.68 ± 0.35	1.73 ± 0.52	4.17 ± 0.87	
5	1-Octen-3-ol	3391-86-4	C ₈ H ₁₆ O	–	–	–	–	0.41 ± 0.02	0.56 ± 0.08	0.25 ± 0.03	0.30 ± 0.01
6	2,2,4-Trimethyl-1,3-pentanediol diisobutyrate	6846-50-0	C ₁₆ H ₃₀ O ₄	–	0.95 ± 0.05	–	–	–	–	–	–
7	2-Ethylhex-2-enol	50639-00-4	C ₈ H ₁₆ O	–	–	–	–	–	0.45 ± 0.02	–	–
8	2-Nonen-1-ol	22104-79-6	C ₉ H ₁₈ O	2.31 ± 0.25	–	1.81 ± 0.12	2.52 ± 0.23	–	–	–	–
9	(E,Z)-3,6-Nonadien-1-ol	56805-23-3	C ₉ H ₁₆ O	32.84 ± 5.65	13.54 ± 2.56	32.60 ± 4.25	51.68 ± 5.89	16.26 ± 2.25	15.82 ± 1.12	7.22 ± 2.23	5.80 ± 1.13
10	(E)-3-Hepten-1-ol	2108-05-06	C ₇ H ₁₄ O	–	–	–	1.24 ± 0.23	–	–	–	–
11	(Z)-3-Nonen-1-ol	10340-23-5	C ₉ H ₁₈ O	127.55 ± 12.25	33.26 ± 8.23	120.96 ± 12.25	183.21 ± 16.25	46.21 ± 4.32	40.75 ± 6.25	15.02 ± 3.25	12.96 ± 3.52
12	1-Methyl-4-(1-methylethenyl)-Cyclohexanol	138-87-4	C ₁₀ H ₁₈ O	–	–	–	–	0.43 ± 0.03	–	–	–
13	3,5-Dimethylcyclohexanol	5441-52-1	C ₈ H ₁₆ O	–	–	–	–	–	0.37 ± 0.05	–	–
14	1,8-Oxido-p-menthane(Cineole)	470-82-6	C ₁₀ H ₁₈ O	–	0.42 ± 0.04	–	–	–	–	–	–
15	2-Phenylethanol	60-12-8	C ₈ H ₁₀ O	–	1.01 ± 0.12	–	–	–	–	–	–
Aldehyde											
1	2,6,6-Trimethyl-1-Cyclohexene-1-acetaldehyde	472-66-2	C ₁₁ H ₁₈ O	–	1.27 ± 0.23	1.67 ± 0.21	2.55 ± 0.25	2.74 ± 0.35	2.98 ± 0.36	1.46 ± 0.15	1.62 ± 0.14
2	2,6,6-Trimethyl-1-cyclohexene-1-carboxaldehyde (β-Cyclocitral)	432-25-7	C ₁₀ H ₁₆ O	–	2.54 ± 0.53	–	–	–	–	–	–
3	2,4-Decadienal	25152-84-5	C ₁₀ H ₁₆ O	–	0.39 ± 0.12	–	–	0.45 ± 0.08	–	0.25 ± 0.04	0.29 ± 0.02
4	(E)-2-Heptenal	18829-55-5	C ₇ H ₁₂ O	–	–	10.36 ± 3.59	18.69 ± 2.85	–	–	–	–
5	(E)-2-Nonenal	18829-56-6	C ₉ H ₁₆ O	–	–	–	–	–	13.01 ± 1.25	2.26 ± 0.25	1.64 ± 0.52
6	(E)-6-Nonenal	2277-20-5	C ₉ H ₁₆ O	11.70 ± 1.23	–	–	–	–	–	–	–
7	(Z)-7-Tetradecenal	65128-96-3	C ₁₄ H ₂₆ O	–	3.97 ± 0.23	–	–	–	–	–	–
8	Phenylacetaldehyde	122-78-1	C ₈ H ₈ O	–	2.76 ± 0.27	1.62 ± 0.12	–	–	1.00 ± 0.26	–	0.69 ± 0.02
9	Decyl aldehyde	112-31-2	C ₁₀ H ₂₀ O	–	0.52 ± 0.15	–	–	–	0.80 ± 0.02	–	1.05 ± 0.01

(Continued)

TABLE 1 (Continued)

ID	Volatile components ¹	CAS	Molecular formula	Control (μg/kg) ²	UHT (μg/kg) ²	HP2-1 (μg/kg) ²	HP2-2 (μg/kg) ²	HP4-1 (μg/kg) ²	HP4-2 (μg/kg) ²	HP6-1 (μg/kg) ²	HP6-2 (μg/kg) ²
10	Heptaldehyde	111-71-7	C ₇ H ₁₄ O	–	–	–	–	1.43 ± 0.55	2.12 ± 0.25	1.12 ± 0.23	2.81 ± 0.01
11	Hexanal	66-25-1	C ₆ H ₁₂ O	0.94 ± 0.23	–	–	–	–	–	–	–
12	Nonanal	124-19-6	C ₉ H ₁₈ O	20.95 ± 2.56	4.26 ± 0.87	27.10 ± 2.25	42.18 ± 5.58	8.52 ± 1.23	7.21 ± 2.21	1.79 ± 0.05	2.19 ± 0.04
13	Octanal	124-13-0	C ₈ H ₁₆ O	60.85 ± 9.58	–	68.69 ± 14.22	96.87 ± 13.13	76.81 ± 11.02	71.80 ± 5.89	0.79 ± 0.01	0.65 ± 0.01
14	Acetal	105-57-7	C ₆ H ₁₄ O ₂	7.50 ± 2.13	2.76 ± 0.12	8.30 ± 1.23	10.59 ± 2.45	8.81 ± 1.23	9.76 ± 2.96	4.24 ± 0.12	3.33 ± 0.02
Ketone											
1	2,6-Bis(1,1-dimethylethyl)-4-hydroxy-4-methyl-2,5-Cyclohexadien-1-one	10396-80-2	C ₁₅ H ₂₄ O ₂	6.65 ± 1.12	–	–	15.12 ± 2.23	12.53 ± 4.02	12.39 ± 1.23	5.44 ± 1.01	4.08 ± 0.25
2	Octahydro-1,1,8a-trimethyl-(E)-2,6-Naphthalenedione	57289-17-5	–	–	1.30 ± 0.05	0.76 ± 0.05	1.08 ± 0.54	–	–	–	–
3	4-(2,2,6-trimethyl-7-oxabicyclo[4.1.0]hept-1-yl)-3-Buten-2-one	23267-57-4	C ₁₃ H ₂₀ O ₂	–	–	–	–	0.43 ± 0.25	0.60 ± 0.02	0.29 ± 0.01	0.33 ± 0.02
4	4-Hydroxy-3-methylacetophenone	876-02-8	C ₉ H ₁₀ O ₂	–	0.32 ± 0.02	–	–	–	–	–	–
5	6,10-Dimethylundeca-5,9-dien-2-one	3796-70-1	C ₁₃ H ₂₂ O	–	8.74 ± 1.12	6.48 ± 1.12	15.45 ± 2.89	45.62 ± 4.25	50.84 ± 2.02	25.81 ± 0.03	29.04 ± 1.25
6	6-Methyl-5-hepten-2-one	110-93-0	C ₈ H ₁₄ O	–	0.75 ± 0.23	–	–	2.20 ± 0.01	2.68 ± 0.02	1.36 ± 0.24	1.54 ± 0.54
7	1,1,3-Trimethyl-3-cyclohexene-5-one	78-59-1	C ₉ H ₁₄ O	–	–	0.63 ± 0.04	–	–	–	–	–
8	(E)-4-(2,6,6-Trimethyl-1-cyclohexen-1-yl)-3-buten-2-one (β-Ionone)	79-77-6	C ₁₃ H ₂₀ O	2.48 ± 1.02	2.83 ± 0.25	3.27 ± 0.42	4.12 ± 1.54	4.44 ± 1.12	3.71 ± 0.25	1.82 ± 0.56	2.08 ± 0.01
	All ester			39.14 ± 6.13	44.20 ± 3.53	37.79 ± 3.64	48.31 ± 4.85	52.81 ± 4.84	41.74 ± 4.91	22.51 ± 2.32	17.78 ± 2.37
	All alcohol			195.89 ± 30.01	64.51 ± 14.62	188.36 ± 24.79	277.34 ± 36.63	72.89 ± 8.22	67.98 ± 9.38	32.31 ± 7.74	23.42 ± 5.91
	All aldehyde			101.94 ± 13.73	18.45 ± 2.52	117.72 ± 21.62	170.87 ± 24.26	98.76 ± 14.46	108.66 ± 13.30	11.90 ± 0.85	14.25 ± 0.79
	All ketone			9.13 ± 2.14	13.95 ± 1.67	11.14 ± 1.63	35.76 ± 7.20	64.21 ± 9.65	70.22 ± 2.54	34.72 ± 1.85	37.07 ± 2.07
	Total			346.09 ± 52.01	141.11 ± 22.34	355.01 ± 51.68	532.27 ± 72.94	288.67 ± 37.17	288.59 ± 30.13	101.44 ± 12.76	92.51 ± 11.14

¹ Volatile components detected by the GC-MS compared with the standard mass spectrum in the NIST 17 library.² Each value is the mean of triplicate biological samples.

“–” is not detected.

TABLE 2 Threshold and odor activity values of aromatic compounds of melon juice.

ID	Aromatic compounds	Threshold (μg/kg)	OAV ¹							
			Control	UHT	HP2-1	HP2-2	HP4-1	HP4-2	HP6-1	HP6-2
1	2-Methyl-1-butyl acetate	8	1.06	0.48	1.02	1.22	1.15	0.89	0.43	0.39
2	Ethyl acetate	5	4.21	0.48	3.74	4.32	4.60	3.32	2.12	1.11
3	(E,Z)-3,6-Nonadien-1-ol	3	10.95	4.51	10.87	17.23	5.42	5.27	2.41	1.93
4	(Z)-3-Nonen-1-ol	1	127.55	33.26	120.96	183.21	46.21	40.75	15.02	12.96
5	Acetal	4.9	1.53	–	1.69	2.16	1.80	1.99	0.87	0.68
6	Nonanal	1.1	19.04	3.87	13.26	38.34	7.74	6.56	1.63	1.99
7	Octanal	0.587	103.66	–	117.01	165.02	130.85	122.31	1.34	1.10
8	β-Ionone	0.007	353.98	404.70	467.51	587.87	491.79	530.64	259.38	296.50
Total			621.99	447.30	736.06	999.37	689.55	711.72	283.20	316.66

^aEach value is the mean of triplicate biological samples.
¹“–”is not detected.

Screen of major aromatic components and flavor difference analysis

The odor activity values (OAV) reasonably assess aroma effectiveness based on the balance between food substrate and air (16). The OAV was the ratio of aromatic component concentration to the aroma threshold value. When the OAV was >1.0, the aromatic component contributed to its aroma. The greater the OAV, the greater the aromatic component's contribution to the overall aroma. A total of eight major aromatic components were screened from 57 volatile components based on the OAV calculation (Table 2). The major aromatic components included 2-methyl-1-butyl acetate and ethyl acetate, (E, Z)-3,6-nonadien-1-ol, (Z)-3-nonen-1-ol, acetal, nonanal, octanal, and β-ionone.

Ester was a key component in the flavor of melon juice (17). 2-Methyl-1-butyl acetate was a branched chain ester showing apple aroma and fragrance (18). Ethyl acetate was not only the major aromatic component of melon but also the origin of most fruit aromas (13, 19). (E, Z)-3,6-nonadien-1-ol showed a strong aroma of cucumber (20). (Z)-3-nonen-1-ol was the major aromatic component of melon, showing a grassy aroma (21). The C6–C9 aldehydes were the key component providing the main flavor for melon juice (22). Acetal and nonanal showed an orange aroma and grassy aroma (14). Octanal had an immature orange aroma (19, 23).

The total OAV of the HP2-2 was 1.61 and 2.23 times that of the control and UHT, respectively (Table 2). The HP2-2 significantly enhanced the flavor of the aromatic components of the melon juice. Moreover, the effect of treatments on the OAV value of aromatic components is shown in Figure 1. Y value represents the times of the OAV value of aromatic components to that of the control. The positive value meant an increase in the components, while the negative value meant a decrease in them. The Y values of the major aromatic components of

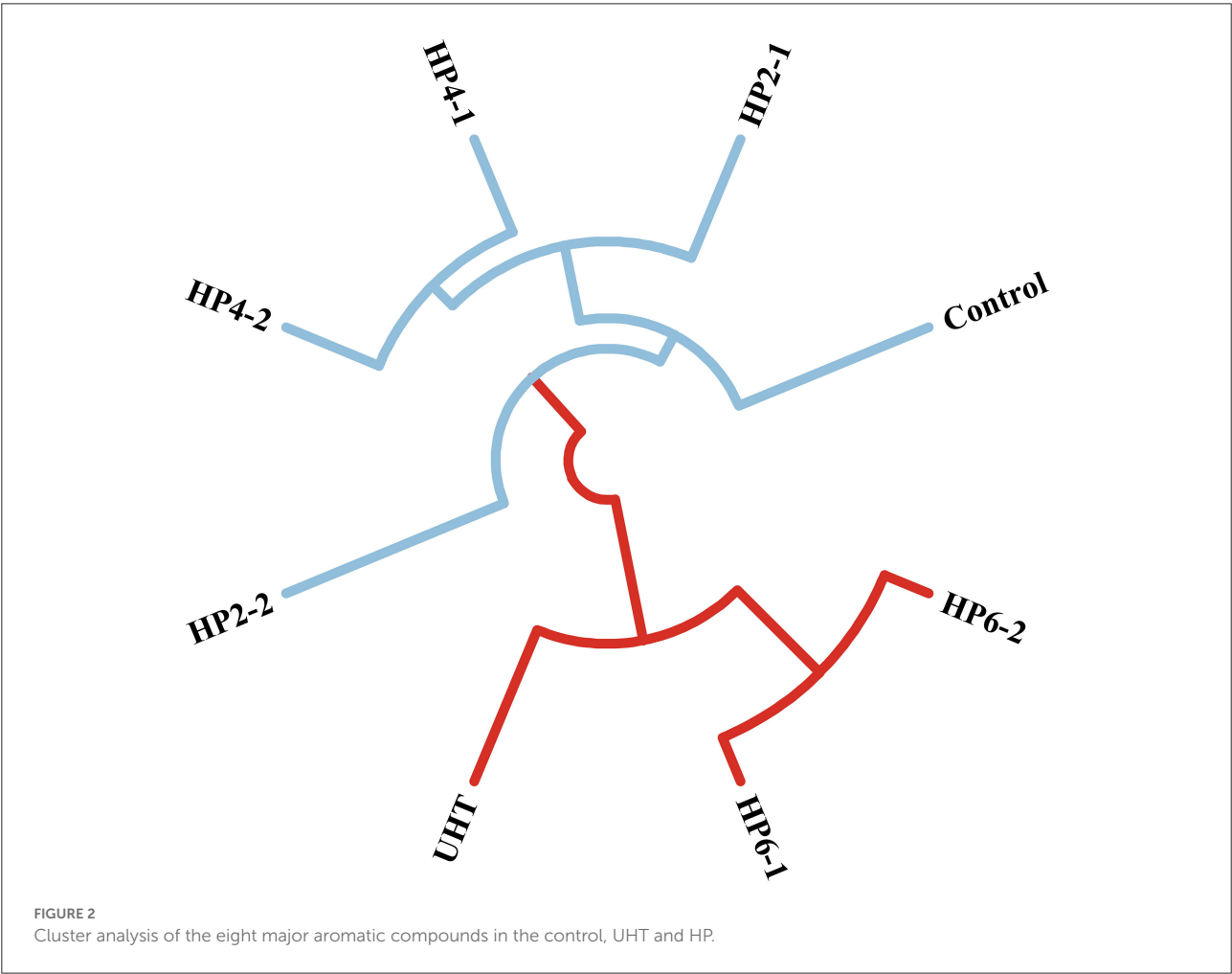
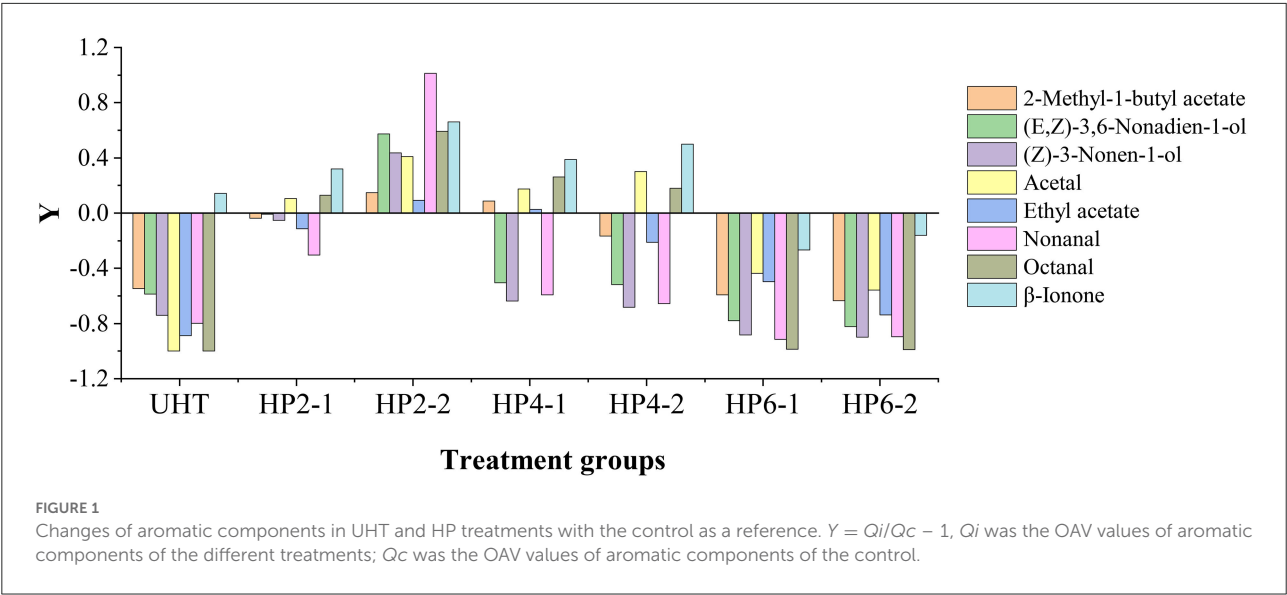
all treatments were negative, except for that of the HP2-2. The UHT, HP6-1, and HP6-2 reduced the Y value significantly. The Y value of all aromatic components in the HP2-2 was positive. Therefore, the HP2-2 significantly enhanced the content of the major aromatic components of the melon juice. However, the Y values of the HP6-1 and HP6-2 were similar to that of the UHT. This phenomenon indicated that the excess pressure of the HP treatment led to the deterioration of the aroma. Similar results were reported in the mango juice (24). Therefore, the optimum parameters of the HP processing were 200 MPa for 20 min for the melon juice.

The cluster analysis was used to find the flavor difference between treatments (Figure 2). The composition of aromatic components from the HP2-1, HP2-2, HP4-1, and HP4-2 was similar to those of the control, with that of the HP2-2 being the most similar. This phenomenon was consistent with the result of the OAV evaluation. Similar results were also reported in cloudy pomegranate juice (25), strawberry juice (26), and mulberry juice (27). The UHT was similar to the HP6-1 and HP6-2. The reason for this was the significant change in the flavor of melon juice due to the temperature change caused by the excessive pressure.

Therefore, the HP2-2 enhanced the aromatic components of melon juice.

Effects of treatments on the concentration of major aromatic components of melon juice

Figure 3 shows the effect of treatments on the concentration of major aromatic components of melon juice. The UHT significantly reduced the concentration of eight aromatic components in all treatments. The total concentration of eight aromatic components in the HP2-2 group was highest,



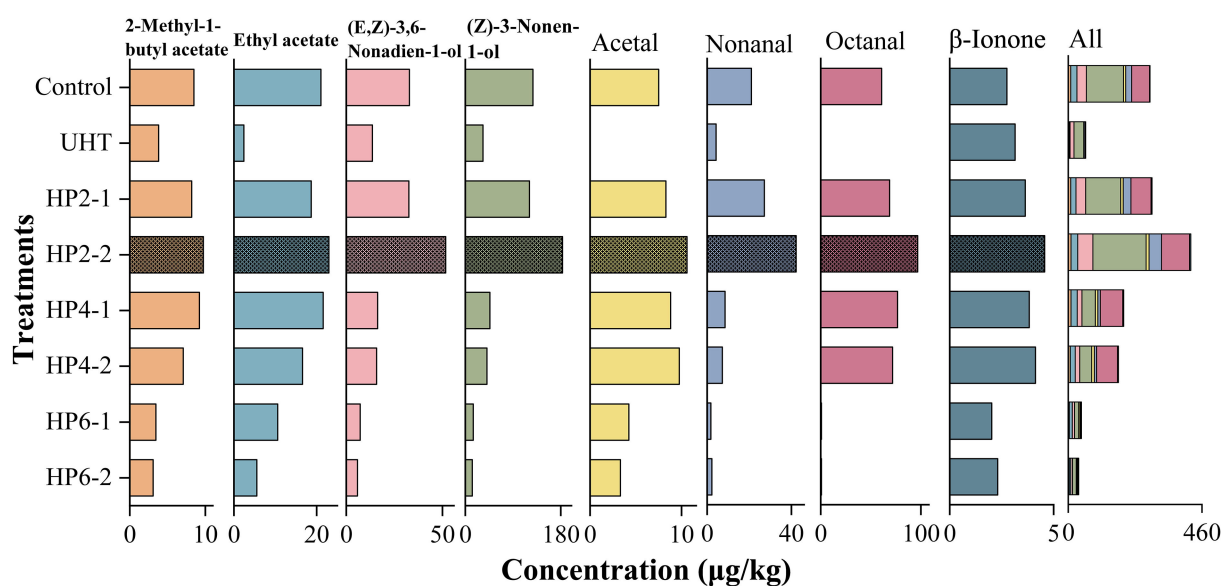


FIGURE 3
The concentration of eight major aromatic compounds of melon juice. Each value is the mean of triplicate biological samples.

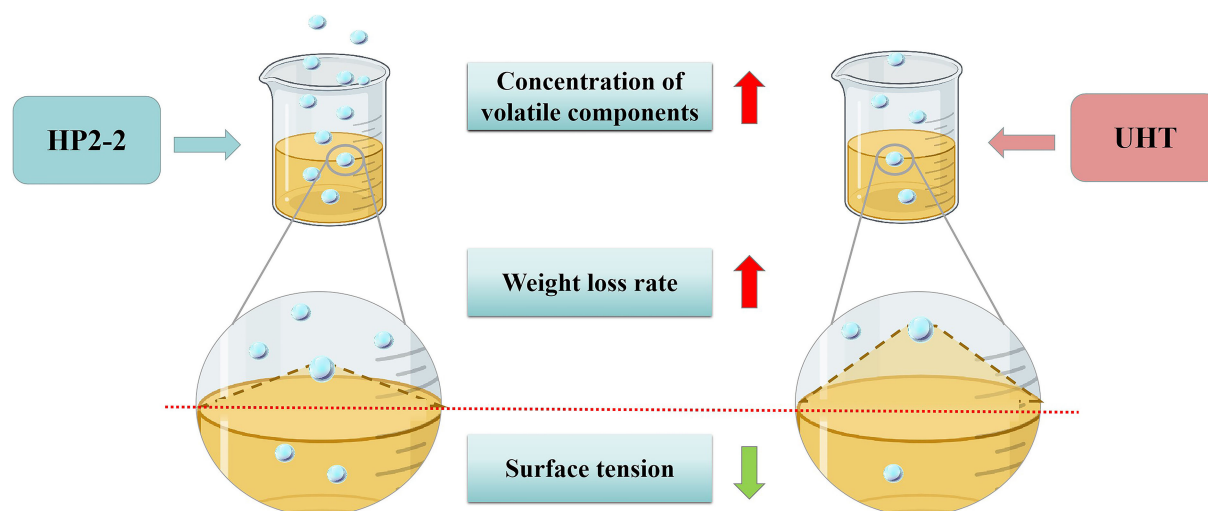


FIGURE 4
The mechanism profile of the UHT and HP2-2 on aromatic components of melon juice. The blue ball refers to the aromatic components in melon juice.

which was 1.49 and 6.99 times that of the control and UHT, respectively.

The concentrations of 2-methyl-1-butyl acetate and ethyl acetate were significantly decreased by the UHT. This phenomenon was probably because the thermal treatment of the UHT was more intensive than the non-thermal treatment of the HP (28).

The HP2-2 increased the concentration of (E, Z)-3,6-nonadien-1-ol and (Z)-3-nonen-1-ol in each treatment. This

phenomenon was possible because the proper pressure activated the activity of certain glycosidases and released glycoside-bound alcohols in fruit juices (8).

The UHT reduced acetal, nonanal, and octanal concentrations to a very low level. The high temperature had the greatest effect on aldehydes. Consistent with our results, the aldehydes showed the highest thermal sensitivity and the lowest thermal stability in melon juice, so the high temperature significantly reduced the odor intensity (19).

β -Ionone was the only flavor compound whose concentration was increased by the UHT. The first-order kinetics of β -carotene degradation products can only be produced after long-term exposure to high temperatures, which also promotes the formation of β -ionone (29). The HP2-2 increased the concentration of β -ionone to the maximum, 1.66 and 1.45 times the control and UHT, respectively.

Interestingly, the HP6-1 and HP6-2 reduced the concentrations of major aromatic components, and some of them were reduced to an undetectable level, which resulted from the fact that the excessive pressure destroyed the structure

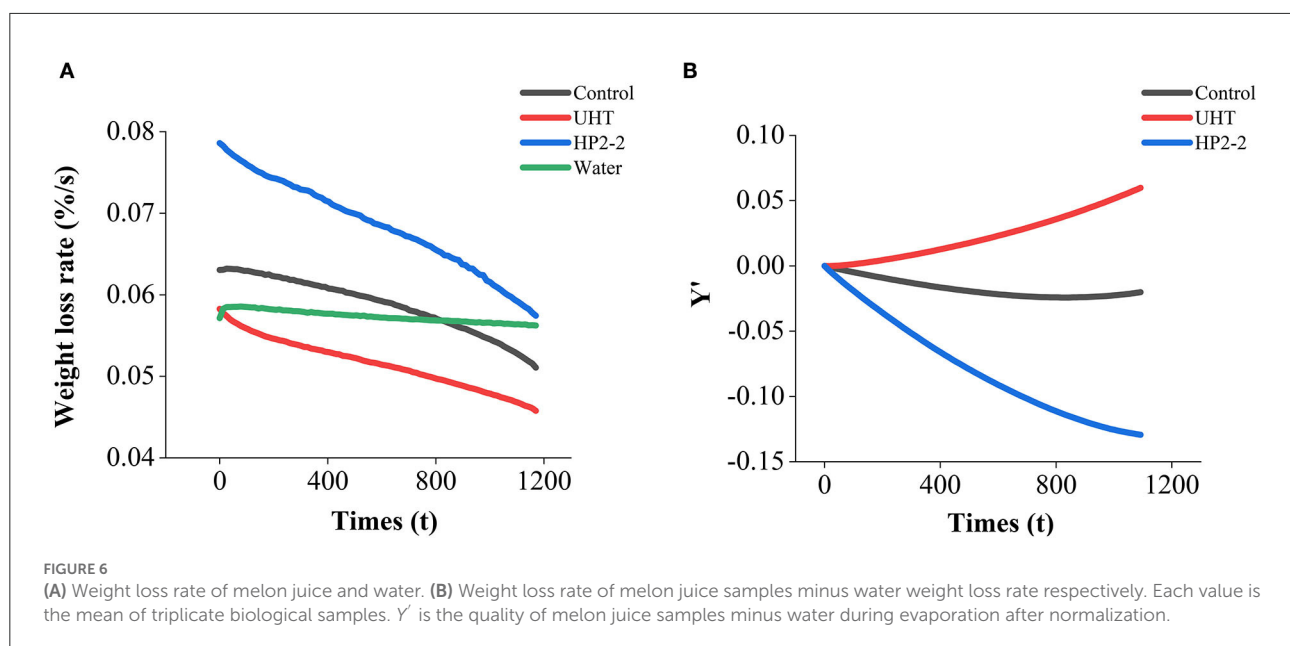
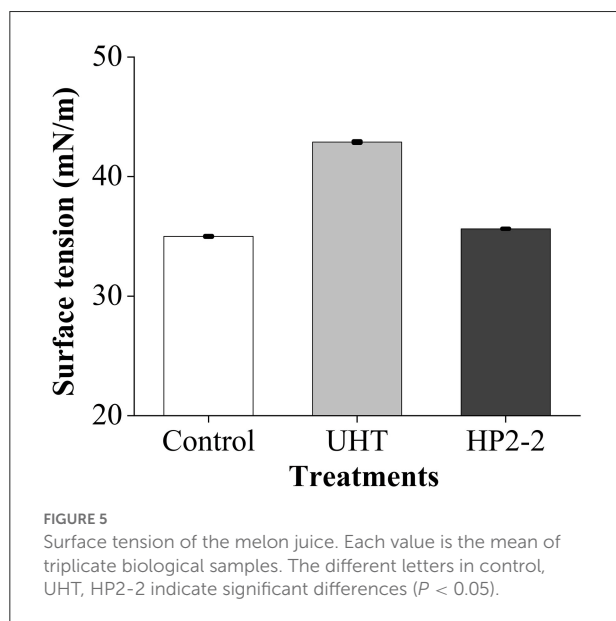
of aromatic compounds. A similar phenomenon was also reported: the HP treatment of 200–400 MPa maintained the volatile components of pumpkin, while the excessive pressure reduced them (30).

Possible mechanisms of the HP treatment

The aromatic components of melon juice were mostly C6 and C9 aldehydes and their corresponding alcohols, which were mainly products of the fatty acid metabolism catalyzed by the related enzymes (22). Remarkably, the HP treatment would inactivate the enzymes and terminate the synthesis of aromatic components (31–33). However, the concentration of aromatic components in the HP2-2 was significantly higher than that of the control, as indicated by the GC-MS results in our study. These phenomena proved that the enhancement of the aromatic components of the HP2-2 did not result from the catalysis of the related enzymes in the fatty acid metabolism. Research showed that the HP treatment enhanced van der Waals interaction by reducing the C–C bond lengths, which led to molecular aggregation (34, 35). The molecular aggregation reduced the surface tension of the liquid (36, 37), thus enhancing the volatilization (38, 39).

Consequently, the surface tension was an important factor affecting the aromatic components of the melon juice. The surface tension reduction would raise the liquid volatilization of the juice. The liquid volatilization could be expressed through weight loss. Hence, the surface tension and weight loss of melon juice were evaluated (Figure 4).

The surface tension of the UHT treatment was the highest, which was 1.23 times and 1.20 times that of the control and



HP2-2, respectively (Figure 5). The surface tension of the HP2-2 was similar to that of the control. Research showed that the reduced surface tension would promote evaporation and recoiling properties (40). The reduction of surface tension will make the aromatic components more volatile. The HP2-2 reduced the surface tension between aromatic components and the water matrix, thereby enhancing the volatilization of aromatic components. Similar results also proved that a pressure higher than 150 MPa would reduce the molecular force between aromatic components and the water matrix (41).

In Figure 6A, the weight loss rate of the melon juice decreased, while that of the water was held constant. The decrease resulted from the evaporation of moisture in the juice and the increase in melon juice concentration. On the one hand, the energy required to evaporate the same amount of water per unit of time was increased (42). Since the temperature of the TGA/DSC analysis was isothermal at 60°C and the energy provided was constant, the evaporation flux was reduced, and the weight loss rate was also reduced accordingly.

Meanwhile, the increase in melon juice concentration led to an increase in viscosity, which reduced the transfer coefficient in the liquid phase (43). Increasing the solution's viscosity improved the resistance to mass transfer in the liquid phase (44). Consequently, the melon juice showed a polarization effect and induced a lower driving force. The cross point met by the weight loss rate profiles of the control sample, and the water suggested the moment when the evaporation flux of the two samples was the same (Figure 6A). The concentration of melon juice corresponding to this point was 49.66%. Similar to our results, the energy efficiency, specific water removal rate, and exergy efficiency reached maximum values at about 30% total soluble solid content during the concentration of pomegranate juice. Those decreased in the further concentration process (42).

The weight loss rate between the treatments was different after deducting the effect of water evaporation (Figure 6B). The weight loss rate of the HP2-2 treatment was the highest, while that of the UHT treatment was the lowest. The HP reduced the surface tension between the aromatic components and the water matrix in the HP2-2, thus enhancing the volatilization of the aromatic components. The results further confirmed the results of the surface tension analysis.

The results of the surface tension and weight loss rate of the melon juice confirmed our prediction. Therefore, reducing the surface tension might be one of the reasons that the HP treatment enhanced the concentration of the total volatile components of melon juice.

Conclusions

A total of 57 volatile compounds were identified from melon juice by GC-MS analysis. Among them, eight major

aromatic components were identified: 2-methyl-1-butyl acetate, ethyl acetate, (E, Z)-3,6-nonadien-1-ol, (Z)-3-nonen-1-ol, acetal, nonanal, octanal, and β -ionone. β -Ionone was detected as the major aromatic component in melon juice for the first time. Its OAV value was as high as 587.87 in the HP2-2. The total volatile concentration of melon juice was highest (532.27 $\mu\text{g/kg}$) in the HP2-2 group, which was 1.54 and 3.77 times that of the control and the UHT treatment, respectively. Meanwhile, the total concentration of 8 aromatic components in the HP2-2 group was highest, which was 1.49 and 6.99 times that of the control and UHT, respectively. Hence, the HP2-2 was considered the optimal parameter of the HP treatment.

The potential mechanism of the HP treatment was explored by measuring the surface tension and the weight loss rate. The HP2-2 reduced the surface tension between aromatic components and the water matrix and enhanced the weight loss rate of the melon juice, thereby enhancing the volatilization of aromatic components. This result provided more explicit evidence for the HP flavor retention technology.

Data availability statement

The raw data supporting the conclusions of this article will be made available by the authors, without undue reservation.

Author contributions

CZ, XL, and YW contributed to conception and design of the study. XL, YS, and RW organized the database. XL and RW performed the statistical analysis. XL wrote the manuscript. CZ and XL reviewed the manuscript. CZ and HL supervised this study. All authors contributed to manuscript revision, and approved the submitted version.

Funding

This research was funded by National Natural Science Foundation of China (32172237 and 82074276), China Agricultural Research System (CARS-25), and Collaborative Innovation Center of the Beijing Academy of Agricultural and Forestry Sciences (KJCX201915).

Acknowledgments

We express our thanks to the National Natural Science Foundation of China, the Beijing Academy of Agricultural and

Forestry Sciences and the Ministry of Agriculture and Rural Affairs for the financial support.

Conflict of interest

The authors declare that the research was conducted in the absence of any commercial or financial relationships that could be construed as a potential conflict of interest.

References

- Chen G, Chen J, Feng Z, Mao X, Guo D. Physiological responses and quality attributes of Jiashi muskmelon (*Cucurbitaceae. Cucumis melo* L.) following postharvest hydrogen peroxide treatment during storage. *Eur J Horticult Sci.* (2015) 80:288–95. doi: 10.17660/eJHS.2015/80.6.4
- Ao X, Mu YH, Xie S, Meng DH, Zheng YQ, Meng XS, et al. Impact of UHT processing on volatile components and chemical composition of sea buckthorn (*Hippophae rhamnoides*) pulp: a prediction of the biochemical pathway underlying aroma compound formation. *Food Chem.* (2022) 390:133142. doi: 10.1016/j.foodchem.2022.133142
- Pang XL, Zhang YZ, Qiu J, Cao JM, Sun YQ, Li HH, et al. Coupled multidimensional GC and odor activity value calculation to identify off-odors in thermally processed muskmelon juice. *Food Chem.* (2019) 301:125307. doi: 10.1016/j.foodchem.2019.125307
- Pan X, Zhang WT, Lao F, Mi RF, Liao XJ, Luo DS, et al. Isolation and identification of putative precursors of the volatile sulfur compounds and their inhibition methods in heat-sterilized melon juices. *Food Chem.* (2021) 343:128459. doi: 10.1016/j.foodchem.2021.128459
- Wibowo S, Essel EA, De Man S, Bernaert N, Van Droogenbroeck B, Grauwet T, et al. Comparing the impact of high pressure, pulsed electric field and thermal pasteurization on quality attributes of cloudy apple juice using targeted and untargeted analyses. *Innov Food Sci Emerg Technol.* (2019) 54:64–77. doi: 10.1016/j.ifset.2019.03.004
- Liu FX, Zhang XX, Zhao L, Wang YT, Liao XJ. Potential of high-pressure processing and high-temperature/short-time thermal processing on microbial, physicochemical and sensory assurance of clear cucumber juice. *Innov Food Sci Emerg Technol.* (2016) 34:51–8. doi: 10.1016/j.ifset.2015.12.030
- Balasubramaniam V, Martinez-Monteaugudo SI, Gupta R. Principles and application of high pressure-based technologies in the food industry. *Annu Rev Food Sci Technol.* (2015) 6:435–62. doi: 10.1146/annurev-food-022814-015539
- Zhao Y, Wang P, Zhan P, Tian HL, Lu C, Tian P, et al. Aroma characteristics of cloudy kiwifruit juices treated with high hydrostatic pressure and representative thermal processes. *Food Res Int.* (2021) 139:109841. doi: 10.1016/j.foodres.2020.109841
- Wu WL, Xiao GS, Yu YS, Xu YJ, Wu JJ, Peng J, et al. Effects of high pressure and thermal processing on quality properties and volatile compounds of pineapple fruit juice. *Food Control.* (2021) 130:108293. doi: 10.1016/j.foodcont.2021.108293
- Luo DS, Pan X, Zhang WT, Bi S, Wu JH. Effect of glucose oxidase treatment on the aroma qualities and release of cooked off-odor components from heat-treated Hami melon juice. *Food Chem.* (2022) 371:131166. doi: 10.1016/j.foodchem.2021.131166
- Guo J, Yue TL, Yuan YH, Sun N, Liu P. Characterization of volatile and sensory profiles of apple juices to trace fruit origins and investigation of the relationship between the aroma properties and volatile constituents. *LWT.* (2020) 124:109203. doi: 10.1016/j.lwt.2020.109203
- Moyo DS, Mapossa AB, Rademeyer M, Merwe EM, Focke WW. TGA investigation of the volatilisation of fipronil at elevated temperatures. *Thermochim Acta.* (2022) 179379. doi: 10.1016/j.tca.2022.179379
- Paparella A, Shaltiel-Harpaza L, Ibdah M. β -Ionone: its occurrence and biological function and metabolic engineering. *Plants.* (2021) 10:754–65. doi: 10.3390/plants10040754
- Zhang WT, Lao F, Bi S, Pan X, Pang XL, Hu XS, et al. Insights into the major aroma-active compounds in clear red raspberry juice (*Rubus idaeus* L. cv Heritage) by molecular sensory science approaches. *Food Chem.* (2021) 336:127721. doi: 10.1016/j.foodchem.2020.127721
- Yan D, Shi JR, Ren XL, Tao YS, Ma FW, Li R, et al. Insights into the aroma profiles and characteristic aroma of 'Honeycrisp' apple (*Malus domestica*). *Food Chem.* (2020) 327:127074. doi: 10.1016/j.foodchem.2020.127074
- Yu W, Zhang Y, Lin Y, Pang X, Zhao L, Wu J, et al. Differential sensitivity to thermal processing of two muskmelon cultivars with contrasting differences in aroma profile. *LWT.* (2021) 138:110769. doi: 10.1016/j.lwt.2020.110769
- Farcuh M, Copes B, Le-Navenec G, Marroquin J, Cantu D, Bradford KJ, et al. Sensory, physicochemical and volatile compound analysis of short and long shelf-life melon (*Cucumis melo* L.) genotypes at harvest and after postharvest storage. *Food Chem X.* (2020) 8:100107. doi: 10.1016/j.fochx.2020.100107
- Shi JD, Wu HB, Xiong M, Chen YJ, Chen JH, Zhou B, et al. Comparative analysis of volatile compounds in thirty nine melon cultivars by headspace solid-phase microextraction and gas chromatography-mass spectrometry. *Food Chem.* (2020) 316:126342. doi: 10.1016/j.foodchem.2020.126342
- Yang F, Liu Y, Wang B, Song H, Zou T. Screening of the volatile compounds in fresh and thermally treated watermelon juice via headspace-gas chromatography-ion mobility spectrometry and comprehensive two-dimensional gas chromatography-olfactory-mass spectrometry analysis. *LWT.* (2020) 137:110478. doi: 10.1016/j.lwt.2020.110478
- Yi JJ, Kebede BT, Dang DNH, Buvé C, Grauwet T, Van Loey A, et al. Quality change during high pressure processing and thermal processing of cloudy apple juice. *LWT.* (2017) 75:85–92. doi: 10.1016/j.lwt.2016.08.041
- Nagashima Y, He K, Singh J, Metrani R, Crosby KM, Jifon J, et al. Transition of aromatic volatile and transcriptome profiles during melon fruit ripening. *Plant Sci.* (2021) 304:110809. doi: 10.1016/j.plantsci.2020.110809
- Rattanathanalerk M, Chiewchan N, Srichumpoung W. Effect of thermal processing on the quality loss of pineapple juice. *J Food Eng.* (2005) 66:259–65. doi: 10.1016/j.jfoodeng.2004.03.016
- Goff SA, Klee HJ. Plant volatile compounds: sensory cues for health and nutritional value? *Science.* (2006) 311:815–9. doi: 10.1126/science.1112614
- Zhang WT, Dong P, Lao F, Liu JY, Liao XJ, Wu JH, et al. Characterization of the major aroma-active compounds in Keitt mango juice: comparison among fresh, pasteurization and high hydrostatic pressure processing juices. *Food Chem.* (2019) 289:215–22. doi: 10.1016/j.foodchem.2019.03.064
- Chen D, Xi HP, Guo XF, Qin ZH, Pang XL, Hu XS, et al. Comparative study of quality of cloudy pomegranate juice treated by high hydrostatic pressure and high temperature short time. *Innov Food Sci Emerg Technol.* (2013) 19:85–94. doi: 10.1016/j.ifset.2013.03.003
- Cao XM, Bi XF, Huang WS, Wu JH, Hu XS, Liao XJ, et al. Changes of quality of high hydrostatic pressure processed cloudy and clear strawberry juices during storage. *Innov Food Sci Emerg Technol.* (2012) 16:181–90. doi: 10.1016/j.ifset.2012.05.008
- Zou H, Lin TT, Bi XF, Zhao L, Wang YT, Liao XJ, et al. Comparison of high hydrostatic pressure, high-pressure carbon dioxide and high-temperature short-time processing on quality of mulberry juice. *Food Bioprocess Technol.* (2016) 9:217–31. doi: 10.1007/s11947-015-1606-9
- Bi S, Sun SC, Lao F, Liao XJ, Wu JH. Gas chromatography-mass spectrometry combined with multivariate data analysis as a tool for differentiating between processed orange juice samples on the basis of their volatile markers. *Food Chem.* (2020) 311:125913. doi: 10.1016/j.foodchem.2019.125913
- Vásquez-Cañedo AL, Schilling S, Carle R, Neidhart S. Effects of thermal processing and fruit matrix on β -carotene stability and enzyme inactivation during transformation of mangoes into purée and nectar. *Food Chem.* (2007) 102:1172–86. doi: 10.1016/j.foodchem.2006.07.005

Publisher's note

All claims expressed in this article are solely those of the authors and do not necessarily represent those of their affiliated organizations, or those of the publisher, the editors and the reviewers. Any product that may be evaluated in this article, or claim that may be made by its manufacturer, is not guaranteed or endorsed by the publisher.

30. Dhenge R, Rinaldi M, Ganino T, Santi S, Ferrarese I, Dall'Acqua S. Variations of polyphenols, sugars, carotenoids, and volatile constituents in pumpkin (*Cucurbita moschata*) during high pressure processing: a kinetic study *Innov Food Sci Emerg Technol.* (2022) 78:103005. doi: 10.1016/j.ifset.2022.103005
31. Murtaza A, Iqbal A, Linhu Z, Liu Y, Xu X, Pan S, et al. Effect of high-pressure carbon dioxide on the aggregation and conformational changes of polyphenol oxidase from apple (*Malus domestica*) juice. *Innov Food Sci Emerg Technol.* (2019) 54:43–50. doi: 10.1016/j.ifset.2019.03.001
32. Bayindirli A, Alpas H, Bozoglu F, Hizal M. Efficiency of high pressure treatment on inactivation of pathogenic microorganisms and enzymes in apple, orange, apricot and sour cherry juices. *Food Control.* (2006) 17:52–8. doi: 10.1016/j.foodcont.2004.09.002
33. Andreou V, Dimopoulos G, Katsaros G, Taoukis P. Comparison of the application of high pressure and pulsed electric fields technologies on the selective inactivation of endogenous enzymes in tomato products. *Innov Food Sci Emerg Technol.* (2016) 38:349–55. doi: 10.1016/j.ifset.2016.07.026
34. Takizawa K, Wakita J, Azami S, Ando S. Relationship between molecular aggregation structures and optical properties of polyimide films analyzed by synchrotron wide-angle X-ray diffraction, infrared absorption, and UV/visible absorption spectroscopy at very high pressure. *Macromolecules.* (2011) 44:349–59. doi: 10.1021/ma101765k
35. Takizawa K, Wakita J, Sekiguchi K, Ando S. Variations in aggregation structures and fluorescence properties of a semialiphatic fluorinated polyimide induced by very high pressure. *Macromolecules.* (2012) 45:4764–71. doi: 10.1021/ma300497a
36. Yu Z, Li J, Zhang X. A new hypothesis for cavitation nucleation in gas saturated solutions: clustering of gas molecules lowers significantly the surface tension. *Chin J Chem Eng.* (2022). doi: 10.1016/j.cjche.2022.06.009
37. Sastry NV, Vaghela NM, Macwan PM, Soni SS, Aswal VK, Gibaud A, et al. Aggregation behavior of pyridinium based ionic liquids in water – surface tension, ¹H NMR chemical shifts, SANS and SAXS measurements. *J Colloid Interface Sci.* (2012) 371:52–61. doi: 10.1016/j.jcis.2011.12.077
38. Chibowski E, Szcześ A, Holysz L. Influence of magnetic field on evaporation rate and surface tension of water. *Colloids Interfaces.* (2018) 2:68. doi: 10.3390/colloids2040068
39. Amor H, Elaoud A, Ben Salah N, El Moueddeb K. Effect of magnetic treatment on surface tension and water evaporation. *Int J Adv Indus Eng.* (2017) 5:119–24. doi: 10.14741/Ijiae/5.3.4
40. Mohapatra SS, Pradhan S, Pati AR, Barik K. Theoretical and experimental investigation of the role of viscosity and surface tension in dropwise evaporation at very high substrate temperature. *Thermal Sci Eng Prog.* (2019) 9:200–14. doi: 10.1016/j.tsep.2018.11.007
41. Leng X, Zhang L, Huang M, Xu X, Zhou G. Mass transfer dynamics during high pressure brining of chicken breast. *J Food Eng.* (2013) 118:296–301. doi: 10.1016/j.jfoodeng.2013.04.022
42. Cokgezme OF, Sabanci S, Cevik M, Yildiz H, Icier F. Performance analyses for evaporation of pomegranate juice in ohmic heating assisted vacuum system. *J Food Eng.* (2017) 207:1–9. doi: 10.1016/j.jfoodeng.2017.03.015
43. Hongvaleerat C, Cabral LMC, Dornier M, Reynes M, Ningsanond S. Concentration of pineapple juice by osmotic evaporation. *J Food Eng.* (2008) 88:548–52. doi: 10.1016/j.jfoodeng.2008.03.017
44. Ciss017, Vaillant F, Bouquet S, Pallet D, Lutin F, Reynes M, et al. Athermal concentration by osmotic evaporation of roselle extract, apple and grape juices and impact on quality. *Innov Food Sci Emerg Technol.* (2011) 12:352od Sci Emerg doi: 10.16/j.ifset.2011.02.009



OPEN ACCESS

EDITED BY

Leizi Jiao,
Beijing Academy of Agriculture and
Forestry Sciences, China

REVIEWED BY

Shen Weizheng,
Northeast Agricultural University, China
Deqin Xiao,
South China Agricultural University,
China

*CORRESPONDENCE

Mingxia Shen,
mingxia@njau.edu.cn

SPECIALTY SECTION

This article was submitted to Optics and
Photonics,
a section of the journal
Frontiers in Physics

RECEIVED 17 September 2022

ACCEPTED 11 November 2022

PUBLISHED 21 December 2022

CITATION

Wang J, Liu L, Lu M, Okinda C,
Lovarelli D, Guarino M and Shen M
(2022), The estimation of broiler
respiration rate based on the semantic
segmentation and video amplification.
Front. Phys. 10:1047077.
doi: 10.3389/fphy.2022.1047077

COPYRIGHT

© 2022 Wang, Liu, Lu, Okinda, Lovarelli,
Guarino and Shen. This is an open-
access article distributed under the
terms of the [Creative Commons
Attribution License \(CC BY\)](#). The use,
distribution or reproduction in other
forums is permitted, provided the
original author(s) and the copyright
owner(s) are credited and that the
original publication in this journal is
cited, in accordance with accepted
academic practice. No use, distribution
or reproduction is permitted which does
not comply with these terms.

The estimation of broiler respiration rate based on the semantic segmentation and video amplification

Jintao Wang^{1,2}, Longshen Liu², Mingzhou Lu², Cedric Okinda^{2,3},
Daniela Lovarelli⁴, Marcella Guarino⁴ and Mingxia Shen^{2*}

¹School of Mechanical and Power Engineering, Henan Polytechnic University, Jiaozuo, Henan, China,

²Laboratory of Modern Facility Agriculture Technology and Equipment Engineering of Jiangsu Province, College of Engineering, Nanjing Agricultural University, Nanjing, Jiangsu, China,

³Department of Electrical and Communications Engineering, School of Engineering and Built Environment, Masinde Muliro University of Science and Technology, Kakamega, Kenya, ⁴Department of Science and Environmental Policy, University of Milan, Milan, Italy

Respiratory rate is an indicator of a broilers' stress and health status, thus, it is essential to detect respiratory rate contactless and stress-freely. This study proposed an estimation method of broiler respiratory rate by deep learning and machine vision. Experiments were performed at New Hope (Shandong Province, P. R. China) and Wen's group (Guangdong Province, P. R. China), and a total of 300 min of video data were collected. By separating video frames, a data set of 3,000 images was made, and two semantic segmentation models were trained. The single-channel Euler video magnification algorithm was used to amplify the belly fluctuation of the broiler, which saved 55% operation time compared with the traditional Eulerian video magnification algorithm. The contour features significantly related to respiration were used to obtain the signals that could estimate broilers' respiratory rate. Detrending and band-pass filtering eliminated the influence of broiler posture conversion and motion on the signal. The mean absolute error, root mean square error, average accuracy of the proposed respiratory rate estimation technique for broilers were 3.72%, 16.92%, and 92.19%, respectively.

KEYWORDS

broiler, respiration rate, computer vision, semantic segmentation, Euler video magnification

1 Introduction

According to the United Nations (UN) prediction, the global population will exceed nine billion by 2050, thus, food security has become a challenging factor [1,2]. Alexandratos and Bruinsma [3] estimated that the demand for animal-derived food could increase by 70% between 2005 and 2050 and that poultry meat production is crucial. Additionally, meat consumption is notably dominant, especially in countries with significant Gross Domestic Product (GDP) growth. Broilers are an essential source of

protein, and according to the prediction, the demand for broilers will further increase in the next decade [4].

Regarding animal welfare and productivity (economics) in broilers production systems, some aspects still need attention. In particular, broilers' respiratory rate (RR) is related to health and feeding environment [5]. The RR of broilers provides farmers with the basis for diagnosing respiratory-related diseases and stress [6]. In the current commercial broiler husbandry, farmers judge the disease and stress of broilers by manually observing the RR and listening to their abnormal respiratory sounds. However, this is laborious, objective, and has low accuracy. Therefore, an effective accurate and automatic estimation of broiler RR is of significant importance in reducing diseases and improving animal welfare.

Several studies have reported on the detection of RR in animals. Xie et al. [7] developed a method by computer vision to detect the RR of pigs. This method extracted the maximum curvature radius of the pig's back contour in each frame and constructed the respiratory waveform according to the extracted curvature radius. The average relative error between the method and manual count results was 2.28%. Stewart et al. [8] reported on detecting cows RR by infrared thermal imaging technology. A thermal infrared camera was used to monitor the air temperature near the nostrils of cattle and detect breathing. Zhao et al. [9] applied the Horn-Schunck optical flow method to calculate the periodic change of optical flow direction of abdominal fluctuation of dairy cows, which obtained their RR at a detection accuracy of 95.68%. Song et al. [10] proposed a Lucas Kanade sparse optical flow algorithm to calculate the optical flow of cow plaque boundary. According to the change law of average optical flow of plaque boundary in video sequence frame, the detection of cow respiratory behavior was obtained, and the average accuracy was 98.58%. Presently, RR monitoring in animals focuses on those of larger size, such as pigs and dairy cows. Due to poultry, such as broilers, being smaller, contactless estimation of RR in poultry has not been studied.

Due to a large number of broilers in the broiler house, it is unfeasible to detect broiler RR using the equipment mentioned before, including radar and depth camera, for their high cost. In contrast, computer vision technology is contactless and stress-free for broilers. It is an ideal means to realize non-contact detection of broiler RR. At present, some scholars use machine vision and artificial intelligence to realize chicken disease early warning and recognition. Okinda et al. [11] used the feature variables which were extracted based on 2D posture shape descriptors (circle variance, elongation, convexity, complexity, and eccentricity) and mobility feature (walk speed) achieved the early diagnosis of Newcastle disease virus infection in broiler chickens. Wang et al. [12] realized the recognition and classification of abnormal feces by using deep learning and machine vision, so as to achieve the purpose of monitoring digestive diseases of broilers. However, presently, no research

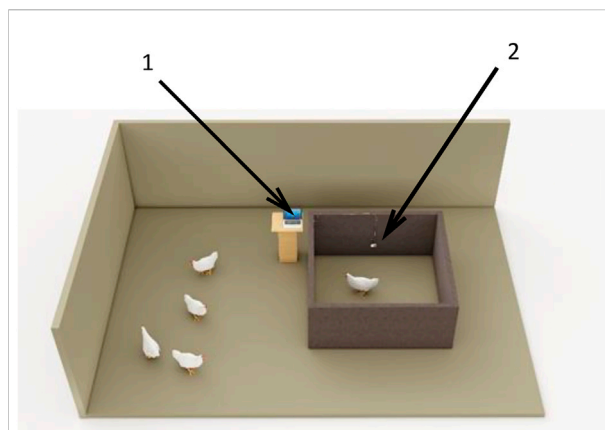


FIGURE 1
Experimental arrangement schematic (1. Computer. 2. Camera).

has reported on the use of computer vision technology to detect the RR of broilers.

In this context, this paper presents a novel approach to broiler RR estimation based on semantic segmentation, contour feature, and video magnification. The main objective of this study is to estimate the RR of broilers without contact and stress, and achieve the estimation with movement and multiple postures of broilers in actual farm environment. This introduced technique will significantly improve automation and could be considered a new tool in the field of precision livestock farming to improve animal welfare and production efficiency.

2 Materials and methods

2.1 Experiment design and data collection

Two experiments were conducted in this study. At New Hope broiler farm, Weifang, Shandong Province, P. R. China, in October 2019, and at Wen's research farm, Yunfu, Guangdong Province, P. R. China in September 2021. A total of 30 15 to 35-day-old Arbor Acres broilers were used in the experiment. The farmer randomly selected the birds with average body shape and good health. The temperature, humidity, and light setting were kept up with the broiler production during the experiment. With the increase of broiler age, the internal temperature decreased from 28°C to 22°C, and the humidity decreased between 80% and 50%, gradually. The floor was litter (50% sphagnum and 50% wood shavings). The illumination was DC adjustable light in the breeding house, and the light intensity varied between 30 and 50lx.

An experimental broiler pen of 1 m (length) by 1 m (width) by 0.5 m (height) was built with a carton board (the color was close to the fence in the broiler house), and the pen hosted one

broiler at a time. The pens were set up in the broiler house (in the aisles of the broiler house) and in this way the experimental conditions were kept consistent with the production. Before the broilers were brought into the pen, a camera (SARGO A8, $1,920 \times 1,080$) was pre-installed in the front and center of the pen 0.2 m away from the ground shown in Figure 1. The camera was connected to an Intel Core i5-4,500 u CPU, 4 GHz, 16 GB physical memory Microsoft Windows 10 PC via USB port and the SARGO software. The data was stored to a 500 GB drive (SSD) installed in the PC for subsequent analysis.

The experimental broilers were placed in the chamber, one at a time. When the birds were quiet (no stress), the computer-controlled camera began to record the video for 10 min for every broiler. In total, 200 min of videos were captured in New Hope farm and 100 min in Wen's research farm.

The proposed methods mainly include image segmentation, feature extraction, posture conversion and motion influence elimination, and RR estimation. To improve the algorithm's accuracy, a method of video motion amplification before feature extraction was proposed.

2.2 Data labeling

An expert visual manual count was used as a gold standard for RR measurement. An experienced veterinarian manually labelled the captured videos and the broiler was considered breathed once as the belly fluctuated once. The respiratory times were recorded every 10 s, then multiplied by 6, the RR of broilers (times/minute). Each 1-min video had six values (RR).

2.3 Image preprocessing and semantic segmentation

The conditions during the data acquisition environment were consistent with the actual farm environment. However, the video background was complex and could not be processed directly. Therefore, it was necessary to preprocess the image to remove the background.

2.4 Image preprocessing

To obtain the image object, a variety of traditional image processing methods were tested, including the OTSU [13] algorithm, watershed algorithm [14], and edge detection algorithm [15]. However, they were not satisfactory enough to remove the background. Moreover, these methods had poor performance on the images due to the interferences such as light, broiler feathers, and dust in the broiler house, leading to wrong or missing segmentation.

2.5 Semantic segmentation

In this study, two semantic segmentation algorithms based on deep learning were used to locate and segment broiler individuals, i.e., the Mask R-CNN [16] and YOLACT [17].

2.5.1 Mask R-CNN

Mask R-CNN follows the framework of Fast R-CNN and adds a fully connected segmentation subnet after the primary feature network to realize the new function of segmentation in addition to classification and regression. It is a two-stage framework [16]. In the first stage, the suggestion box is scanned and generated, and in the second stage, the suggestion box is classified, and the boundary box and mask are formed [16]. Figure 2A shows the frame diagram of Mask R-CNN. The convolution layer down sampling is realized through the cross-layer connection of the residual network (RESNET) [16]. Combined with the feature pyramid network (FPN), the feature maps obtained from different sampling layers are fused and transmitted to the next operation [16].

The regional recommendation network (RPN) obtains several anchor boxes and adjusts them to fit the target better. If multiple anchor boxes overlap, the optimal anchor box is selected for transmission according to the score for the prospect, and the ROI alignment improved by ROI pooling is given for pooling [16]. Finally, boundary box and mask prediction are realized through the fully connected network [16].

2.5.2 YOLACT

YOACT is a one-stage instance segmentation method that adds mask branches to the target detection network. However, unlike the standard serial way, this method abandons the step of feature location. It divides the instance segmentation task into two parallel subtasks to improve efficiency: prototype mask and target detection. The former uses the network results of the complete convolutional network (FCN) to generate a series of prototype masks that can cover the whole image [17], while the latter predicts the masking coefficient based on the detection branch to obtain the coordinate position of the instance in the image and non-maximum suppression (NMS) screening [17]. The final prediction results are obtained by the linear combination of the two branches.

Figure 2B shows the frame diagram of YOACT. Similar to other networks, this method also performs feature extraction through the backbone network and FPN. One part of the multi-layer FPN is used to generate the prototype mask in the prototype mask branch, and the other part is used to calculate the information such as detection and positioning and mask coefficient through the prediction head network, and then screened through NMS [17]. The processing result is combined with the generated prototype mask, and the final result is obtained.

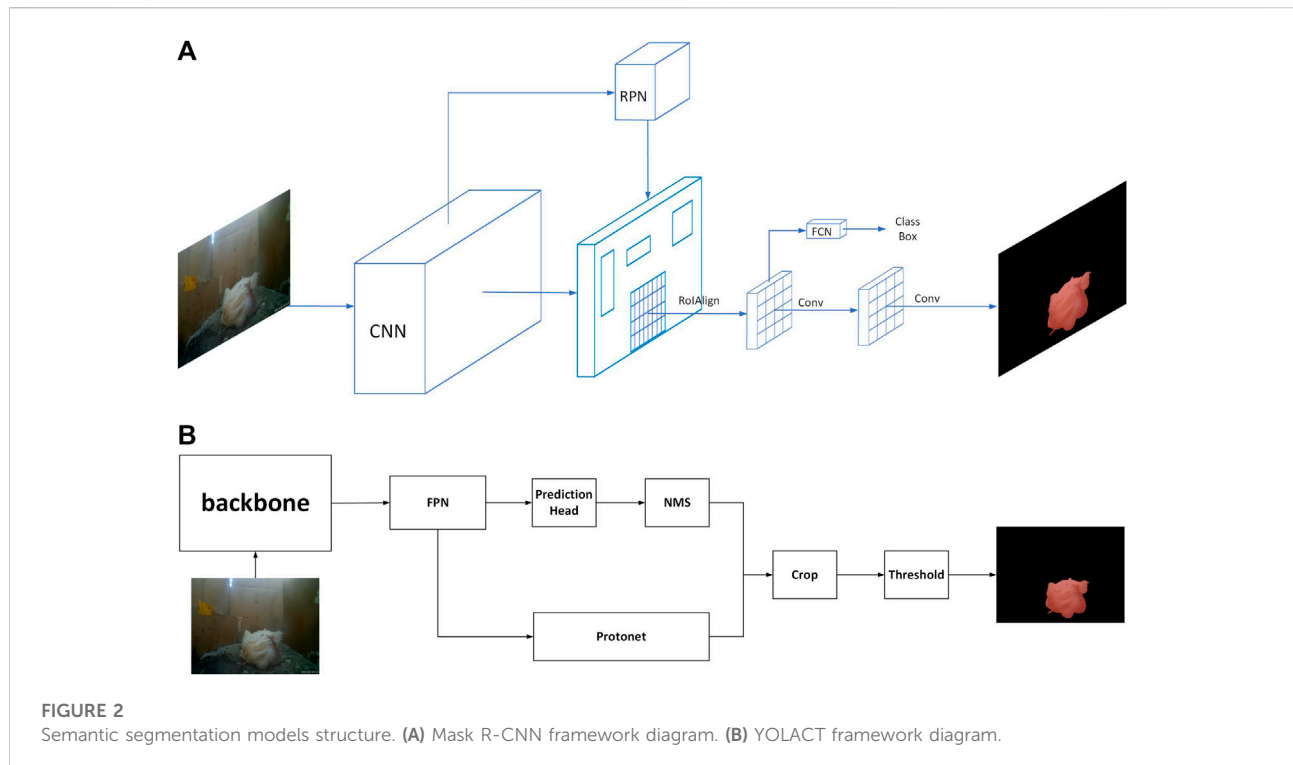


FIGURE 2
Semantic segmentation models structure. **(A)** Mask R-CNN framework diagram. **(B)** YOLACT framework diagram.

2.5.3 Semantic segmentation model development

The images were labeled by the open-source image annotation software Labelme. A data set containing 3,000 groups of data was obtained, in which the labeled data were randomly divided into the training set, verification set, and test set, according to 8:1:1.

In this study, Mask R-CNN used a resnet101 network structure. The learning rate of the first 20 epochs was 0.001, and that of the last 40 epochs was 0.0001. There were 1,000 iterations per epoch, 60,000 iterations in total.

YOACT used resnet50 network structure, trained 60,000 iterations, and the initial learning rate was 0.001. It was attenuated in the 20,000 and 40,000 iterations, respectively, and the attenuation was 10% of the current learning rate.

2.6 Video magnification algorithm

Because broilers are small, their belly fluctuates slightly during breathing. To improve the detection accuracy of broilers' RR, a video magnification algorithm was used to amplify the micromotion of broilers. The Euler video magnification (EVM) algorithm was proposed by Wu et al. [18]. The EVM method mainly includes color space conversion, spatial decomposition, time-domain filtering,

linear amplification, and video reconstruction. Spatial decomposition is a multi-spatial resolution image that decomposes the video sequence through the image pyramid. Time-domain filtering filters the images of different scales obtained by spatial decomposition in the frequency domain to obtain the frequency band of interest. Linear amplification linearly amplifies the bandpass filtered signal and adds it to the original signal. Video reconstruction is used to pyramid reconstruct the processed multi-scale image to obtain the enlarged image and then rebuild the video. For example, if a one-dimensional (1D) signal is in the following form [19] as in Eq. 1.

$$I(x, t) = f(x + \delta(t)) \quad (1)$$

Where $I(x, t)$ is the value of position x in the signal at time t and $\delta(t)$ is the displacement function.

If the first-order Taylor series expansion can express the signal, it can be approximately described as by Eq. 2.

$$I(x, t) \approx f(s) + \delta(t) \frac{\partial f(x)}{\partial x} \quad (2)$$

When bandpass filtering is performed on all positions x in signal $I(x, t)$, and $B(x, t)$ represents the filtered signal, assuming that the translation movement $\delta(t)$ is in the band of the bandpass filter, then the filtered signal can be determined by Eq. 3.

$$B(x, t) = \delta(t) \frac{\partial f(x)}{\partial x} \quad (3)$$

Then the signal is amplified by α and added back to $I(x, t)$ (Eq. 4):

$$\tilde{I}(x, t) = I(x, t) + \alpha B(x, t) \quad (4)$$

Adding Eqs 1–3 gives Eq. 5.

$$\tilde{I}(x, t) \approx f(x) + (1 + \alpha)\delta(t) \frac{\partial f(x)}{\partial x} \quad (5)$$

Assuming that the amplified motion $(1 + \alpha)\delta(t)$ also satisfies the first-order Taylor series, the band-pass filter in the time domain can be connected with motion amplification. The processed output can be obtained by Eq. 6.

$$\tilde{I}(x, t) \approx f(x + (1 + \alpha)\delta(t)) \quad (6)$$

Thus, the band of interest is extracted by a bandpass filter, multiplied by a specific magnification factor, and added back to the original signal to achieve motion amplification. The magnification factor α had a limiting condition (Eq. 7).

$$(1 + \alpha)\delta(t) < \frac{\lambda}{8} \quad (7)$$

Where λ was the spatial wavelength of the signal.

The EVM algorithm is based on the YIQ color space of the image. Before processing, the video image should be converted from RGB space to YIQ space and then back to RGB space. In the process of magnification, however, the information of three-color channels is processed simultaneously, which is time-consuming.

It was found that the abdominal fluctuation of broilers in the video is mainly the change of pixel brightness value. Therefore, the RR estimate did not demand the image's color information to improve the processing speed, so the image was transferred from RGB to grayscale. The conversion speed was considerably enhanced since the gray image was a single-channel image.

2.7 Contours feature extraction

To associate the changes of broiler image with broiler respiration, it is necessary to extract the correlated features. Two 1-min videos were randomly selected, which the broiler images were extracted by the semantic segmentation algorithm. At the same time, we had manually checked the video frame by frame according to the time axis and judged that the frame was in the broiler inspiratory or expiratory state according to the fluctuation state of the broiler belly. By recording these states as the parameter “Breath,” the inspiratory process was set as “1” and the expiratory as “0.” A total of 3,000 frames were obtained, so the parameter “Breath” obtains a total of 3,000 data. Some image contour features were extracted for the segmented broiler images, shown in Table 1.

Using the software SPSS, the Pearson correlation analysis was carried out between each feature and “Breath.”

TABLE 1 The extracted feature variables.

Extracted features	Defining equations
Centroid X	$X = \frac{\sum P_i x_i}{\sum P_i}$ (Eq. 8)
Centroid Y	$Y = \frac{\sum P_i y_i}{\sum P_i}$ (Eq. 9)
Area	$S = \sum_x \sum_y v(x, y)$ (Eq. 10)
Aspect Ratio	$AR = \frac{W}{H}$ (Eq. 11)
Extent	$EX = \frac{S_c}{S_b}$ (Eq. 12)
Solidity	$SO = \frac{S_c}{S_{H_1}}$ (Eq. 13)

Where, x_i and y_i are the pixel coordinates, and P_i is the pixel's value. $v(x, y)$ is the gray value of the point (x, y) . W and H are the width and height of the contour. S_c and S_b are the contour area and bounding rectangle area. S_c and S_H are the contours and convex hull areas.

2.8 Estimation of respiratory rate based on signal power spectral density

The feature which significantly correlated with “Breath” was regard as a time-dependent signal. Then, the signal was transformed into a frequency domain by fast Fourier transform (FFT) [20], and its power spectral density (PSD) [21] was analyzed. After PSD analysis, the frequency with the maximum power density results being the RR estimated by the feature signal.

2.9 Evaluation methods

When evaluating the performance of the semantic segmentation algorithm, the accuracy P and intersection over union (IoU) were used (Eq. 14 and Eq. 15).

$$P = \frac{T_p}{T_p + F_p} \times 100\% \quad (14)$$

$$IoU = \frac{T_p}{T_p + F_p + F_N} \times 100\% \quad (15)$$

Where T_p is the total number of correctly segmented pixels, the total number of incorrectly segmented pixels, and the total number of missed pixels.

We used three indicators, mean absolute error (RR_{me}), root mean squared error (RMSE), average accuracy (RR_{acc}), to evaluate the effects of the broiler RR estimation models (Eqs 16–18).




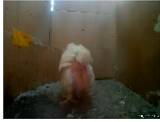








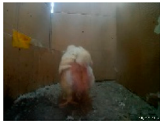



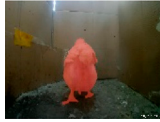

$$RR_{me} = \frac{1}{N} \sum_{i=1}^N |RR_D(i) - RR_m(i)| \quad (16)$$

$$RMSE = \sqrt{\frac{1}{N} \sum_{i=1}^N [RR_D - RR_m(i)]^2} \quad (17)$$

$$RR_{acc} = (1 - \frac{1}{N} \sum_{i=1}^N \frac{|RR_D(i) - RR_m(i)|}{RR_m(i)}) \times 100\% \quad (18)$$

Where RR_D is the RR detected by RR-D and RR-D-EVM, RR_m is the RR observed manually. N is the number of tested videos.

TABLE 2 The semantic segmentation algorithm output.

Model	Image ID	Input	Output	Mask
Mask R-CNN	58			
	173			
	255			
YOACT	58			
	173			
	255			

3 Results and discussions

3.1 Semantic segmentation algorithm

The two semantic segmentation models have been evaluated with the test dataset. Table 2 shows the segmentation results of Mask R-CNN and YOACT models in this study. The average accuracy of the YOACT results is 95%, and the average IoU is 94%; the average accuracy of Mask R-CNN is 95%, and the average IoU is 90%.

3.2 Feature acquisition

The results of Pearson correlation analysis between contours features and “Breath” are shown in Table 3. It can be found that the feature “Centroid Y” is significantly correlated with “Breath” ($p > 0.4$), while “Centroid X” is weakly correlated ($0.1 < |P| < 0.2$)

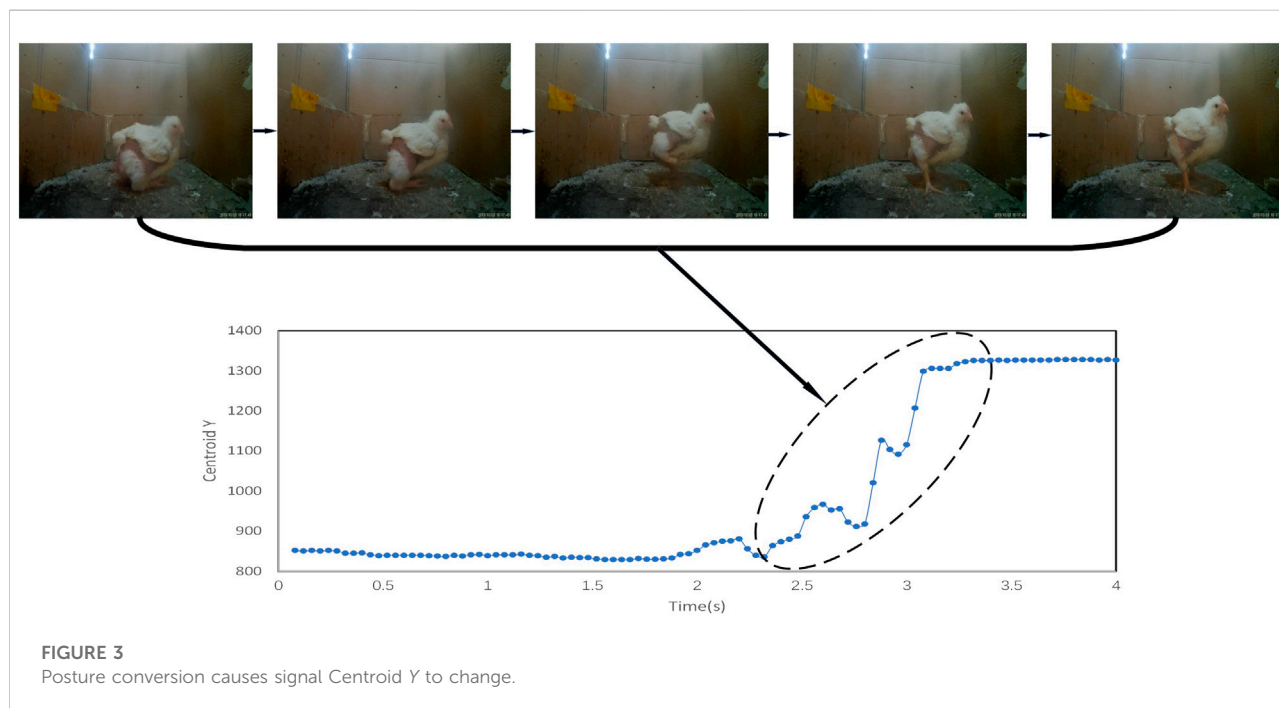
and the feature “Area,” “Aspect Ratio,” “Extent,” “Solidity” is not significantly correlated ($|P| < 0.1$). Therefore, this study applied “Centroid Y” as the feature for RR estimation.

According to Eq. 9, the “Centroid Y” is affected by the height of the broiler contour in the image and the different postures influenced the height of the broiler contour, thus, it is necessary to eliminate the impact of these different poses. Based on manual observation and ethograms by [22,23], the broiler postures were divided as standing, lying, and hanging their heads.

During the posture transformation of broilers, the “Centroid Y” changes considerably. As shown in Figure 3, “Centroid Y” suddenly increases due to the changes of broilers from lying to standing posture. Considering that this study regarded the “Centroid Y” as a time-dependent signal, then the broilers’ posture changes will influence the signal trend. Because the signal is assumed to be stable in power spectral density (PSD), hence, it is necessary to eliminate the signal trend caused by posture changes.

TABLE 3 Correlation analysis between the extracted features and breath.

		Centroid X	Centroid Y	Area	Aspect ration	Extent	Solidity
Breath	Pearson Correlation(P)	0.166	0.417	-0.048	0.024	0.026	0.048
	Sig. (2-tailed)	0.001	0.011	0.062	0.364	0.325	0.065



The smoot priors approach (SPA) by Tarvainen et al. [24] is an effective nonlinear signal detrending method and is often used to process human ECG signals. The SPA algorithm was used to detrend the “Centroid Y” signal. Figure 4 shows the “Centroid Y” signal obtained from a 10-s video. Due to the changes in broiler posture from standing to lying, the “Centroid Y” signal has an apparent trend change. After the processing with the detrend algorithm, the signal trend caused by posture change was eliminated, as shown in Figure 4.

It was also observed that the broilers frequently movements, i.e., flipping of wings and walking. These movements lead to the change in the “Centroid Y,” as shown in Figure 5, where the broiler flipping of wings caused the signal to change.

A band-pass filter was used to filter the noise caused by the movement of broilers. As shown in Figure 6, the signal fluctuated due to the wing shaking of the broiler. After band-pass filtering, the processed signal filter the noise and eliminate the influence of wing shaking.

3.3 Respiratory rate estimation

According to “Broiler production,” the RR of broilers are different at different ages [25]. The RR of young broilers is higher, reaching up to 65 times per minute on average. After 21 days of age, the RR of broilers decreases to about 45 times per minute. Besides, stress influences the RR significantly. RR reaches 130 times per minute or even more when the broiler suffers from thermal stress. Therefore, considering the influence of age and stress on RR, the range of broiler RR was set as 25–150.

In this study, two RR estimation techniques were explored, i.e., without video magnification algorithm (RR-D), and with video magnification algorithm (RR-D-EVMGS). Fifty 10-s videos were randomly selected from the dataset to test the two methods’ performance. The test result is shown in Figure 7.

The evaluation results of the two models are shown in Table 4.

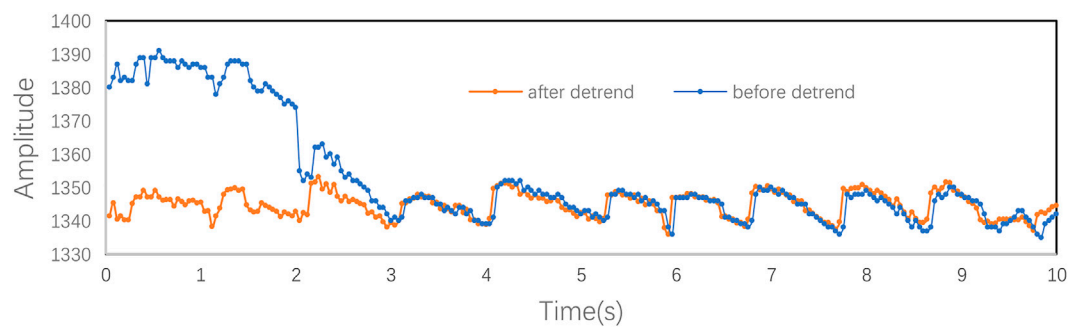


FIGURE 4
Comparison between before and after signal detrend.

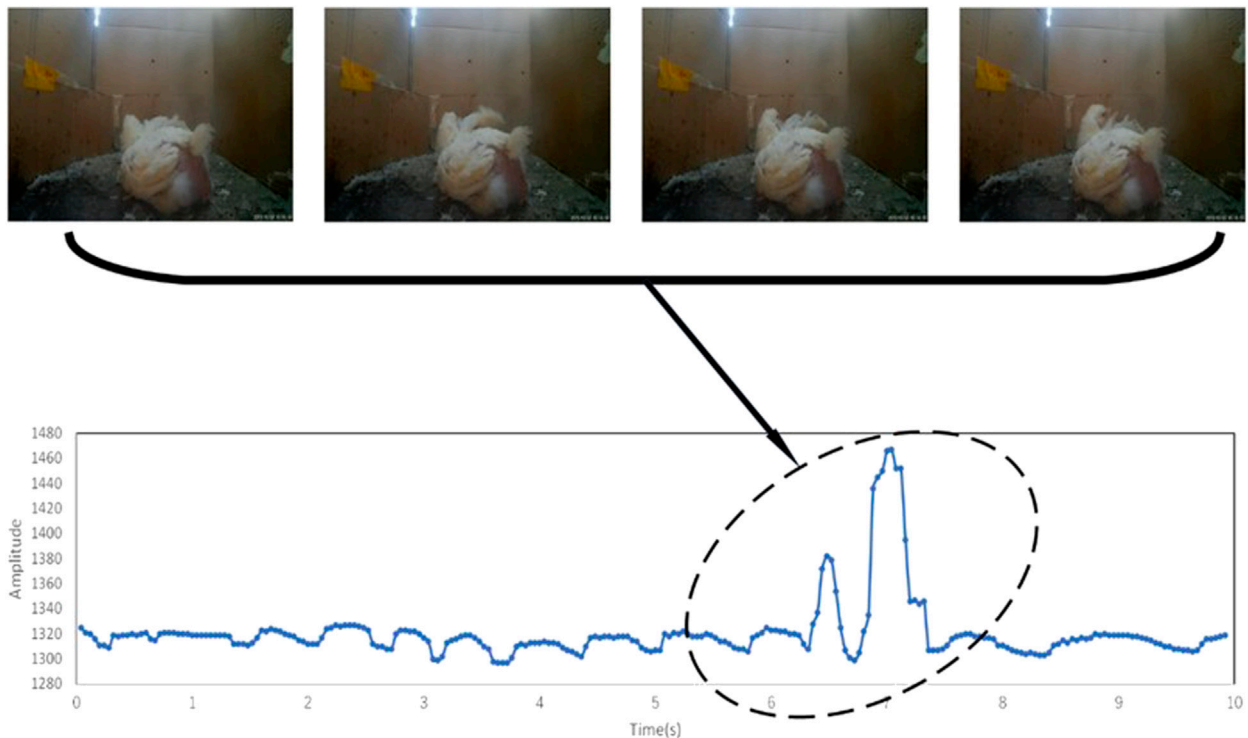


FIGURE 5
Centroid Y signal changes due to broiler movements.

3.4 Euler video magnification based on grayscale

The speed of the EVM algorithm based on grayscale had been improved. Table 5 shows the time consumed by two algorithms for processing the same five videos on the same computer (CPU 4500 u, 4 GHZ). In this study, the speed of EVM based on grayscale was improved by more than 55% compared with EVM.

3.5 Performance evaluation

To test the non-contact broiler RR estimation method proposed in this paper, it is necessary to compare the results obtained by this method and the reference standard (expert visual manual count). To keep the consistency between the proposed method and the reference standard, the Bland-Altman way [26] was used to evaluate the consistency

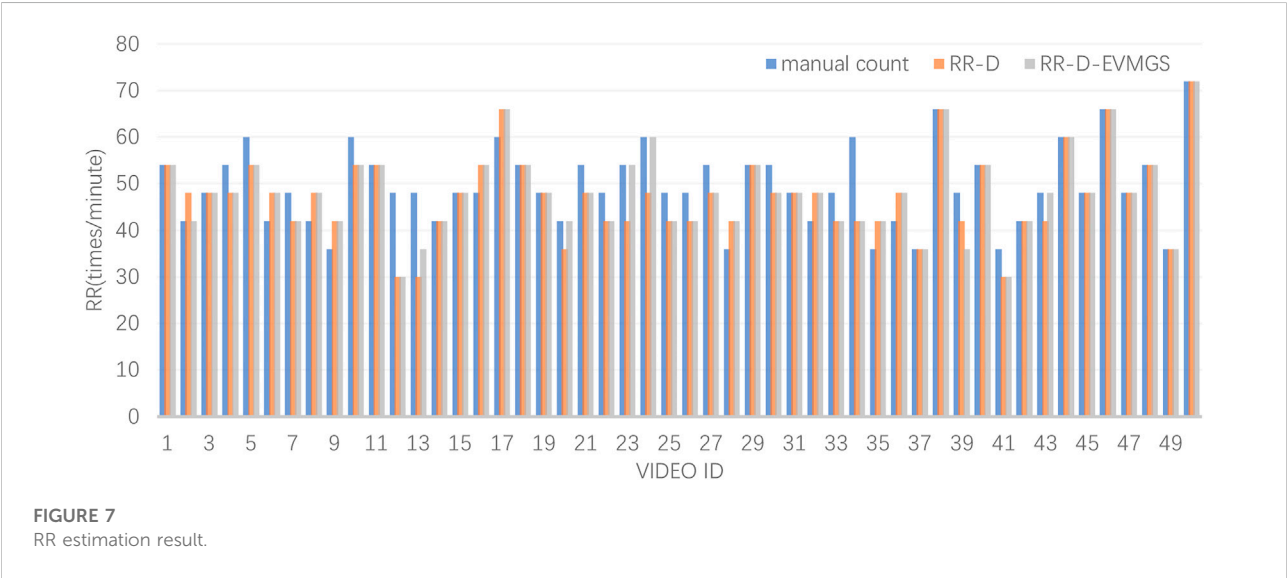
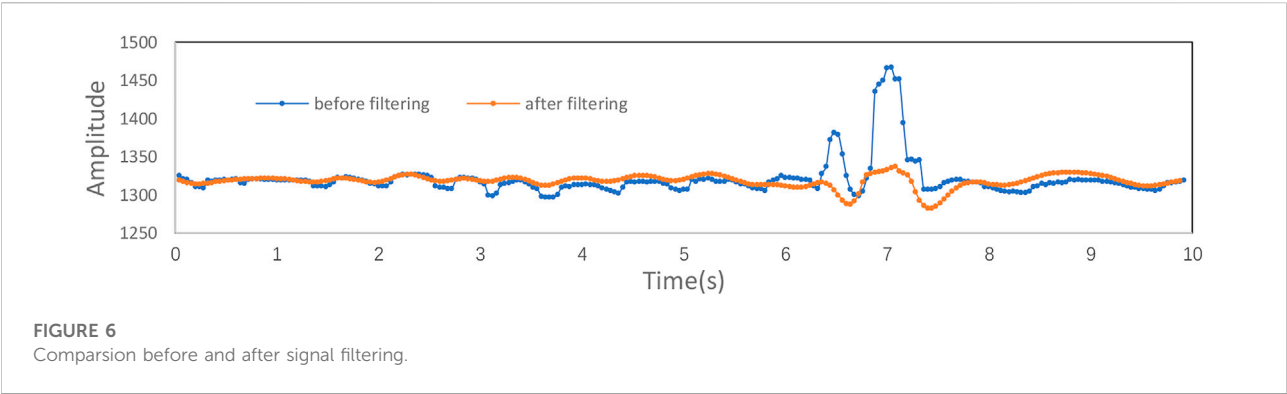


TABLE 4 Test results of RR-D and RR-D-EVMGS.

	RR _{me} (times/minute)	RMSE (times/minute)	RR _{acc} (%)
RR-D	4.56	21.26	90.52
RR-D-EVMGS	3.72	16.92	92.19

between the results of RR-D, RR-D-EVMGS, and expert visual manual count.

As shown in Figure 8, the *x*-axis is the mean of the RR estimated by RR-D, RR-D-EVMGS, and expert visual manual count, and the *y*-axis is the difference between them. The 95% consistency interval for RR-D and RR-D-EVMGS between expert visual manual count is (−10.57, 13.45) and (−9.27, 11.48), respectively. It can be observed that most of the RR data measured by the two methods are

TABLE 5 EVM and EVM based grayscale processing time.

Video ID	EVM(s)	EVM based on grayscale(s)
1	70.22	30.18
2	93.41	37.23
3	95.67	38.10
4	102.84	41.71
5	107.29	43.11

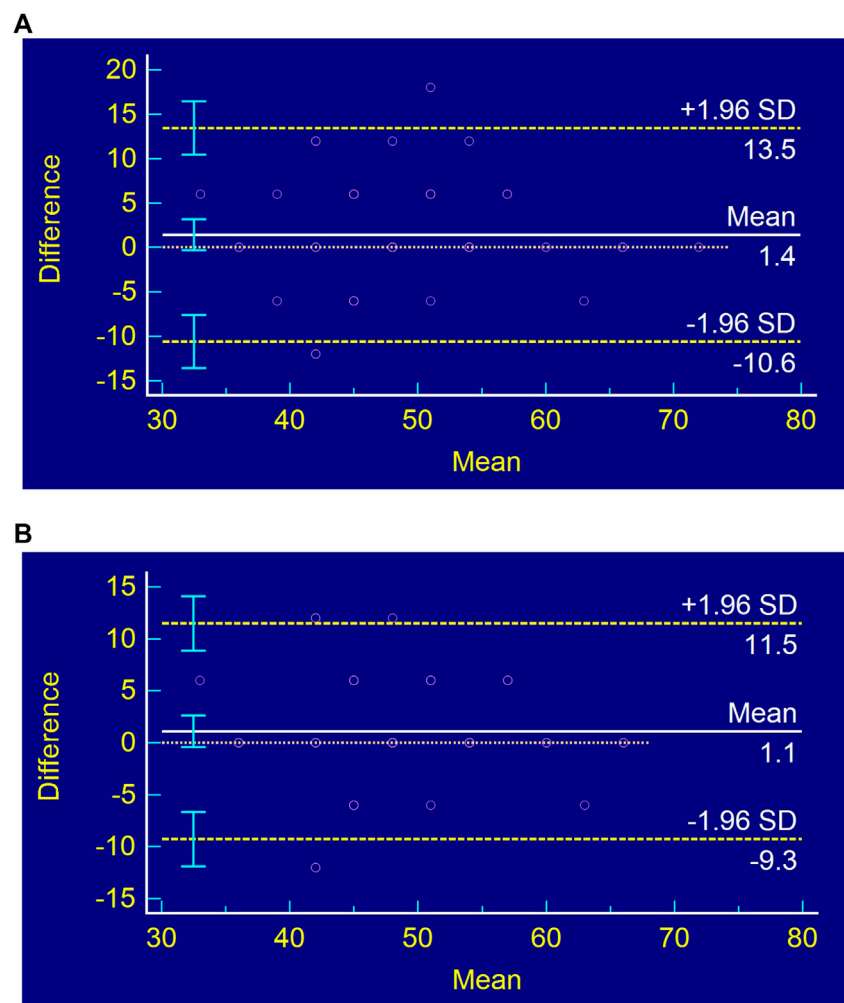


FIGURE 8
Bland-Altman plot. (A) Bland-Altman plot of RR-D. (B) Bland-Altman plot of RR-D-EVMGS.

within the confidence interval, indicating that the consistency between RR-D, RR-D-EVMGS, and the expert visual manual count is good.

3.6 Influence of factors that affects the estimation of respiratory rate

Due to the broiler farming environment being complex and dynamic, in addition to the broiler moving frequently, there is numerous interferences affecting the performance of the broiler RR estimation. Therefore, these interference factors were analyzed to verify the effectiveness of the proposed method.

3.6.1 Effects of the angles between broiler and camera on the estimation of respiratory rate

Because the camera was fixed and the broiler would move freely, there were different angles between the broiler and the camera. According to the angle of Broiler in the video, we divided the data into three kinds: frontal, lateral, and back. Five 1-min videos were selected from each of the three kinds and tested with RR-D-EVMGS. The results are shown in Table 6. It can be seen that the estimation of frontal performance is worst. We suspect that this is because the broiler's head is stable, so when the front of the broiler faces the camera, the respiratory body movement is less evident than that of the back and lateral.

TABLE 6 The test result of different angles between broiler and camera.

	RR _{me} (times/minute)	RMSE (times/minute)	RR _{acc} (%)
Frontal	6.6	24.5	88.16
Back	4	13.6	93.67
Lateral	3.6	8.2	93.35

TABLE 7 The test result of the accelerated and original video.

	RR _{me} (times/minute)	RMSE (times/minute)	RR _{acc} (%)
Original video test result	3.4	6.3	94.35
Accelerated video test result	4.5	10.75	93.85

3.6.2 Influence of breathing rate perturbation on the estimation of respiratory rate

Because the RR of broilers is affected by age, health, and environment, the RR varies greatly. Since our data were obtained when the broiler were calm and no stress, their RR was stable. To verify the estimation effect of the proposed method in the case of fluctuation of RR, we randomly selected ten 1-min videos, twice accelerated the first and last 250 frames, and kept the other frames unchanged, to simulate the fluctuation of broiler RR, and then estimated it with the method we proposed. The RR estimation results are shown in Table 7. It can be seen from the table that the method proposed in this paper performed well on the accelerated video; accuracy was reduced by less than 1%. We deem that is because we extract each frame of the video, the sampling frequency is much greater than twice the upper limit of RR, which meets Shannon's sampling theorem. Therefore, the method proposed in this paper can be used to estimate the RR of broiler under special conditions, such as heat stress.

3.6.3 Analysis on the causes of poor estimation effect

According to the test result, Figure 7, it could be found that the estimation results of videos 12 and 13 were the worst, and the error reached 37.5%. By checking the original video, it was found that the broiler was too close to the camera, resulting in the broiler's body occupying almost the whole image. RR-D and RR-D-EVMGS had poor performance on video 33, with an error of 30%. Checking the original video, it emerged that part of the body walked out of the camera due to the movement of the broiler, and the complete image of the broiler could not be extracted. Therefore, the main factors affecting the estimation accuracy of the two methods were the distance between the broiler and the camera and whether the complete body contour of the broiler could be extracted. The method proposed in this study realizes the estimation of RR of broilers without contact and stress. It can

be used to remotely diagnose respiratory-related diseases and monitor the stress of broiler (such as heat stress). The method used in this study is portable and can be extended to different objects, such as ducks, geese, etc. And we will also try to verify the performance of this method on other objects in the future.

4 Conclusion

A non-stressful, contactless approach of RR estimate for broilers is presented in this research. Compared to the animal respiration rate detection methods proposed by Xie et al. [7] and Stewart et al. [8] and others, this study was aimed at a smaller subject with more complex applying environment, which means it was much more challenging to achieve respiration rate estimation. This results in a lack of contact-free RR estimate techniques for tiny birds like broilers. Using the semantic segmentation technique, the broiler pictures could be successfully retrieved from the complicated backdrop, with an extraction accuracy of 95%. We came to the conclusion that "Centroid Y" would be the ideal way to estimate broiler respiration and presented the RR-D-EVMGS and RR-D approaches. The performance of the two methods was compared in 50 videos, and in RR_{me}, RMSE, and RR_{acc}, RR-D-EVMGS performed better than RR-D. Through the Consistency evaluation with the manual measures, the results of the two methods were consistent with the manually measured results. The method proposed in this study can be applied to farming robots, such as the poultry health monitoring robot developed by Nanjing Agricultural University. And the method proposed in this study can be generalised to other small-sized birds for contactless RR estimation, such as ducks and geese. Because this study was still preliminary, there were some problems that needed to be further solved. For example, although this study used a single-channel Euler video magnification algorithm to improve the computing speed, it still took much longer time to achieve real-time detection. To address this matter, the algorithm requires further optimisation

in the future. Although the results obtained are still preliminary, we believe that this contactless detection of broiler RR has a promising prospect. It can provide technical support for broilers' respiratory diseases and heat stress monitoring.

Data availability statement

The datasets presented in this article are not readily available because this study is part of some ongoing projects, the datasets generated and/or analysed in the study are not publicly available at this time. Requests to access the datasets should be directed to 2018212012@njau.edu.cn.

Ethics statement

The animal study was reviewed and approved by the Biosafety Committee of Nanjing Agricultural University.

Author contributions

Conceptualization, JW; Methodology, JW, MS, CO, LL, and ML; Software, JW, CO, and LL; Formal analysis, JW, DL, CO,

and MG; Investigation, LL; Writing—original draft preparation, JW and CO; Writing—review and editing, JW, DL, MG, and CO; Supervision, MS, ML, and MG. All authors have read and agreed to the published version of the manuscript.

Conflict of interest

The authors declare that the research was conducted in the absence of any commercial or financial relationships that could be construed as a potential conflict of interest.

Publisher's note

All claims expressed in this article are solely those of the authors and do not necessarily represent those of their affiliated organizations, or those of the publisher, the editors and the reviewers. Any product that may be evaluated in this article, or claim that may be made by its manufacturer, is not guaranteed or endorsed by the publisher.

References

1. Fao. *Food and Agriculture Organization of the United Nations. The future of food and agriculture—alternative pathways to 2050*. Rome: Fao (2018).
2. United Nations. *World population prospects 2019*. Geneva: United Nations (2019).
3. Alexandratos N, Bruinsma J. *World agriculture towards 2030/2050: The 2012 revision*. Rome: FAO (2012).
4. Henchion M, McCarthy M, Resconi VC, Troy D. Meat consumption: Trends and quality matters. *Meat Sci* (2014) 98(3):561–8. doi:10.1016/j.meatsci.2014.06.007
5. Nascimento ST, Silva IJOD, Mourão GB, Castro ACD. Bands of respiratory rate and cloacal temperature for different broiler chicken strains. *R Bras Zootec* (2012) 41:1318–24. doi:10.1590/s1516-35982012000500033
6. El HH, Sykes AH. Thermal panting and respiratory alkalosis in the laying hen. *Br Poult Sci* (1982) 23(1):49–57. doi:10.1080/00071688208447928
7. Xie H, Ji B, Hu H, Yang P, Shen Y. A waveform model based on curvature radius for swine's abdominal breathing. *J Suzhou Univ Sci Technology (Natural Sci Edition)* (2016) 33 (3): 66–70. doi:10.3969/j.issn.1672-0687.2016.03.013
8. Stewart M, Wilson MT, Schaefer AL, Huddart F, Sutherland MA. The use of infrared thermography and accelerometers for remote monitoring of dairy cow health and welfare. *J Dairy Sci* (2017) 100(5):3893–901. doi:10.3168/jds.2016-12055
9. Zhao K, He D, Wang E. Detection of breathing rate and abnormality of dairy cattle based on video analysis. *Nongye Jixie Xuebao= Trans Chin Soc Agric Machinery* (2014) 45(10):258–63. doi:10.6041/j.issn.1000-1298.2014.10.040
10. Song HB, Wu DH, Yin XQ, Jiang B, He DJ. Respiratory behavior detection of cow based on Lucas-Kanade sparse optical flow algorithm. *Trans Chin Soc Agric Eng* (2019) 35(17):215–24. doi:10.11975/j.issn.1002-6819.2019.17.026
11. Okinda C, Lu M, Liu L, Nyalala I, Muneri C, Wang J, et al. A machine vision system for early detection and prediction of sick birds: A broiler chicken model. *Biosyst Eng* (2019) 188:229–42. doi:10.1016/j.biosystemseng.2019.09.015
12. Wang J, Shen M, Liu L, Xu Y, Okinda C. Recognition and classification of broiler droppings based on deep convolutional neural network. *J Sensors* (2019) 2019:1–10. doi:10.1155/2019/3823515
13. Otsu N. A threshold selection method from gray-level histograms. *IEEE Trans Syst Man Cybern* (1979) 9(1):62–6. doi:10.1109/tsmc.1979.4310076
14. Beucher S, Meyer F. Segmentation: The watershed transformation. Mathematical morphology in image processing. *Opt Eng* (1993) 34:433–81. doi:10.1007/978-94-011-1040-2_10
15. Canny J. A computational approach to edge detection. *Ieee Trans Pattern Anal Machine Intelligence* (1986) 6:679–98. doi:10.1109/TPAMI.1986.4767851
16. He K, Gkioxari G, Dollár P, Girshick R. Mask R-CNN. *IEEE Trans Pattern Anal Mach Intell* (2020) 42(2):386–97. doi:10.1109/TPAMI.2018.2844175
17. Bolya D, Zhou C, Xiao F, & Lee YJ. Yolact: Real-time instance segmentation. In: *Proceedings of the 2019 IEEE/CVF International Conference on Computer Vision (ICCV)*; October 2019; Seoul, Korea (South) (2019). p. 9157–66.
18. Wu H, Rubinstein M, Shih E, Guttag J, Durand F, Freeman W. Eulerian video magnification for revealing subtle changes in the world. *ACM Trans Graph* (2012) 31(4):1–8. doi:10.1145/2185520.2185561

19. Lucas BD, Kanade T. An iterative image registration technique with an application to stereo vision. In: Proceedings of the 7th international joint conference on Artificial intelligence; August 1987; Vancouver Canada (1981). p. 674–9.
20. Cooley JW, Tukey JW. An algorithm for the machine calculation of complex Fourier series. *Mathematics Comput* (1965) 19(90):297–301.
21. Howard RM. *Principles of random signal analysis and low noise design: The power spectral density and its applications*. Hoboken, NY, USA: John Wiley & Sons (2004).
22. Pereira DF, Miyamoto BC, Maia GD, Sales GT, Magalhães MM, Gates RS. Machine vision to identify broiler breeder behavior. *Comput Electronics Agric* (2013) 99:194–9. doi:10.1016/j.compag.2013.09.012
23. Kristensen HH, Prescott NB, Perry GC, Ladewig J, Ersbøll AK, Overvad KC, et al. The behaviour of broiler chickens in different light sources and illuminances. *Appl Anim Behav Sci* (2007) 103(1-2):75–89. doi:10.1016/j.applanim.2006.04.017
24. Tarvainen MP, Ranta-Aho PO, Karjalainen PA. An advanced detrending method with application to HRV analysis. *IEEE Trans Biomed Eng* (2002) 49(2):172–5. doi:10.1109/10.979357
25. Bernardo F, Luis ES. Broiler production. *Poult Prod Tropics* (2012) 103.
26. Altman DG, Bland JM. Measurement in medicine: The analysis of method comparison studies. *J R Stat Soc Ser D (The Statistician)* (1983) 32(3):307–17. doi:10.2307/2987937



OPEN ACCESS

EDITED BY

Julio Nogales-Bueno,
Universidad de Sevilla, Spain

REVIEWED BY

Boris Lazarević,
University of Zagreb, Croatia
Thinal Raj,
Sime Darby Plantation, Malaysia

*CORRESPONDENCE

Leizi Jiao
✉ jiaoleizi@126.com

SPECIALTY SECTION

This article was submitted to
Technical Advances in Plant Science,
a section of the journal
Frontiers in Plant Science

RECEIVED 25 October 2022

ACCEPTED 23 December 2022

PUBLISHED 12 January 2023

CITATION

Gao Z, Zhao C, Dong D, Liu S, Wen X, Gu Y
and Jiao L (2023) Visualizing changes of
metabolites during iron deficiency
chlorosis in field-grown pear leaves using
micro-Raman spectral imaging.
Front. Plant Sci. 13:1079660.
doi: 10.3389/fpls.2022.1079660

COPYRIGHT

© 2023 Gao, Zhao, Dong, Liu, Wen, Gu and
Jiao. This is an open-access article
distributed under the terms of the [Creative
Commons Attribution License \(CC BY\)](#). The
use, distribution or reproduction in other
forums is permitted, provided the original
author(s) and the copyright owner(s) are
credited and that the original publication in
this journal is cited, in accordance with
accepted academic practice. No use,
distribution or reproduction is permitted
which does not comply with these terms.

Visualizing changes of metabolites during iron deficiency chlorosis in field-grown pear leaves using micro-Raman spectral imaging

Zhen Gao^{1,2}, Chunjiang Zhao^{1,2}, Daming Dong², Songzhong Liu³,
Xuelin Wen^{2,4}, Yifan Gu² and Leizi Jiao^{2*}

¹College of Information and Electrical Engineering, China Agricultural University, Beijing, China,

²National Research Center of Intelligent Equipment for Agriculture, Beijing Academy of Agriculture and Forestry Sciences, Beijing, China, ³Institute of Forestry & Pomology, Beijing Academy of Agriculture & Forestry Sciences, Beijing, China, ⁴Wuhan National Laboratory for Optoelectronics (WNLO), Huazhong University of Science and Technology, Wuhan, Hubei, China

Owing to iron chlorosis, pear trees are some of the most severely impacted by iron deficiency, and they suffer significant losses every year. While it is possible to determine the iron content of leaves using laboratory-standard analytical techniques, the sampling and analysis process is time-consuming and labor-intensive, and it does not quickly and accurately identify the physiological state of iron-deficient leaves. Therefore, it is crucial to find a precise and quick visualization approach for metabolites linked to leaf iron to comprehend the mechanism of iron deficiency and create management strategies for pear-tree planting. In this paper, we propose a micro-Raman spectral imaging method for non-destructive, rapid, and precise visual characterization of iron-deficiency-related metabolites in pear leaves. According to our findings, iron deficiency significantly decreased the Raman peak intensities of chlorophylls and lipids in leaves. The spatial distributions of chlorophylls and lipids in the leaves changed significantly as the symptoms of iron insufficiency worsened. The technique offers a new, prospective tool for rapid recognition of iron deficiency in pear trees because it is capable of visual detection of plant physiological metabolites induced by iron deficiency.

KEYWORDS

iron deficiency, pear tree, Raman spectroscopy, spectral imaging, chlorosis

1 Introduction

By the middle of this century, there will be significant food shortages as the world's population expands. To meet rising demands for food, agricultural yields must be increased (Pretty et al., 2010). Meanwhile, 30% of the global population suffers from iron-deficiency anemia, which is induced by inadequate iron consumption and low iron bioavailability (Kassebaum et al., 2014). Iron is a crucial trace metal for plants and is necessary for both

photosynthesis and chlorophylls synthesis. A substantial decline in fruit productivity and quality will be caused by iron deficiency because it will cause chlorosis, lower photosynthesis and respiration rates, and inefficient water use (Larbi et al., 2006). Pear trees are some of the most severely affected by iron deficiency, and large losses occur each year because of chlorosis (Sanz et al., 1993; Therby-Vale et al., 2022). Therefore, timely detection of iron deficiency in pear trees is crucial for improving the healthy growth of pear trees, fruit quality, and planting efficiency.

The standard approaches for the detection of iron content in leaves, atomic absorption spectroscopy and inductively coupled plasma-emission spectrometry, can accurately measure the total iron content in leaves, but these operations are complicated, time-consuming, and labor-intensive (Kucukbay and Kuyumcu, 2014; Elango et al., 2021). Furthermore, there are limitations to using the total iron content of leaves to discriminate the iron deficiency status of plants. Studies have shown that iron-deficient leaves with intervein chlorosis have total iron contents similar to those of iron-sufficient leaves, which is known as the “chlorosis paradox” (Morales et al., 1998; Romheld, 1998; Jimenez et al., 2009). Therefore, using the total iron content to determine whether leaves are iron deficient is inaccurate.

A chlorotic effect is caused by changes in metabolites, such as pigments in the veins and leaf mesophyll, which are driven by iron deficiency. As a result, occurrences of leaf iron deficiency can be quickly determined using the quantity of chlorophylls and other leaf metabolites (Li et al., 2006). Therefore, some researchers have investigated the use of spectral reflectance to assess the concentrations of leaf metabolites in plants. They discovered that plant chlorosis is more strongly related to active iron content than total iron content (Basayigit et al., 2015). Although reflectance spectroscopy may identify iron deficiency in plant leaves quickly, the wavelength band used is in the visible–near-infrared range. Molecular compounds like chlorophylls have no fingerprints in this spectral range. Therefore, this technology cannot specifically identify molecules such as chlorophylls; instead, it relies on stoichiometric algorithms for modeling and identification, which are low-migration and imprecise.

As a next-generation detection technology for agricultural applications, Raman spectroscopy is advantageous because it allows specific, multi-component analysis, is non-destructive, and rapidly detects molecular compounds (Lew et al., 2020). Obvious physiological changes caused by iron deficiency are significant decreases in the content of leaf metabolites, such as chlorophylls and lipids (Morales et al., 1991). The water-insensitive nature of Raman spectroscopy enables the detection of these metabolites without pre-processing in plant leaves. More importantly, Raman spectroscopy can be integrated with a microscope to form a micro-Raman spectrometer, which can generate maps of relative content distributions of relevant leaf metabolites at a microscopic scale (Baranski et al., 2005; Gierlinger et al., 2008; Heiner et al., 2018; Zhang et al., 2020; Sasani et al., 2021).

In this paper, we conducted micro-Raman spectroscopy on iron-deficient pear leaves. The variation of metabolites, including chlorophylls and Lipids, in leaves affected by iron-deficiency was studied, providing a novel approach for revealing patterns of spatio-temporal variation and mechanisms of changes in metabolites accompanying iron deficiency.

2 Materials and methods

2.1 Materials and instruments

In North China, we discovered that a high-quality pear cultivar (*Pyrus bretschneideri* Rehd.) grafted to quince A (Hardy as interstock) suffered from iron deficiency chlorosis in calcareous soil in early spring, and that the condition was even worse in late spring to early summer. As a result, a high-density training system has been developed in Beijing research and demonstration pear orchard since 2016. This orchard is located in Beijing, China, 40 meters above sea level in the continental monsoon climate zone. The annual average temperature is 10°C, and rainfall occurs mainly from July to September, with an annual average precipitation of 550 mm. The soil is a silt loam consisting of clay, silt, and sand in proportions of 5.4%, 64.7%, and 29.9%, respectively (Zhao et al., 2020).

When iron fertilizer is sprayed on the leaves of yellow pear trees, the leaves can partially return to green, indicating that the yellow symptoms are caused by iron deficiency. To test the feasibility of Raman spectroscopy for visual characterization of iron-deficient leaf metabolites, basal leaves, young leaves, and apical leaves were picked from the same branch of Huangguan (*Pyrus bretschneideri* Rehd) pears with iron-deficiency symptoms, representing healthy, mildly iron-deficient, and severely iron-deficient leaves, respectively (Rustioni et al., 2018). This is because the degree of leaf iron deficiency varies at different positions on a branch, with iron deficiency first occurring on the youngest leaves at the top (Bertamini et al., 2002; Tremblay et al., 2012). The experiment included three groups of biological repetitions, totaling nine leaf samples.

Chlorophylls content within plant leaves is often characterized by soil–plant analysis development (SPAD) values. We used a handheld SPAD meter (SPAD-502, Konica Minolta Sensing, Inc., Osaka, Japan) to measure the SPAD values of healthy, mildly iron-deficient, and severely iron-deficient leaves to provide a reference for the analysis of the Raman spectral results. SPAD was measured three times per leaf.

The micro-Raman spectrometer (HORIBA HR Evolution, Horiba, Japan) can acquire high-resolution Raman spectra from leaves, because of its 800-mm focal length. During the experiment, a 532-nm continuous laser (100-mW power) was the excitation light source, the grating was set to 600 l/mm, the ND filter was set to 3.2%, the single-point integration time was set to 0.5 s, and the single-point accumulation number was set to 1. For the mapping, an area of 500µm by 500µm and 25µm steps were chosen, and every pixel corresponds to one scan. These settings ensure non-destructive Raman spectroscopic measurements of plant leaves.

2.2 Data acquisition and analysis methods

The Raman spectroscopic measurement process for pear leaves is shown in Figure 1. Leaves picked from the pear orchard were placed in a portable refrigerator and sent to the laboratory for micro-Raman spectroscopic analysis within 1 hour. Two regions, the midrib and vein, were selected for Raman spectral imaging in each of the healthy, mildly iron-deficient, and severely iron-deficient leaves. Through the displacement of the x-axis and y-axis of the object platform, the Raman hyperspectral data were acquired for the leaf regions. Using a simple

characteristic band-spectral imaging method, pseudo-color maps of the content distributions of specific substances in leaves can be obtained quickly. All spectral data were processed using Python. The resulting graph was drawn with origin software and PowerPoint (PPT).

To analyze the Raman spectra, cosmic rays were removed firstly. Because the leaf is a complex matrix, it contains many fluorescent substances. Therefore, under the excitation by visible light (532 nm), interference by fluorescence signals caused a baseline shift of the Raman spectrum of the leaves. For data analysis, we used adaptively iteratively reweighted penalized least squares (airPLS) for baseline correction (Zhang et al., 2010). The corrected Raman spectra were then filtered using the Savitzky-Golay filter method with an order of 1 and a number of points of 3. The relative concentration analysis was based on baseline-corrected, smoothed spectra. All spectrum was maximum normalized. In order to evaluate the variability in intensity of the Raman features of the spectra of the leaves (healthy, mildly iron-deficient and severely iron-deficient), pseudo-color maps based on the intensity of the Raman band was generated using Python. Statistical analysis was carried out with Excel. ANOVA was used to compare individual peaks between iron-deficient and healthy leaves.

3 Results

3.1 Raman spectral characteristics of metabolites in leaves with different degrees of iron deficiency

Figure 2A depicts the phenotype of the tested leaves. The healthy leaves are dark green in color and have white veins. Iron-deficient leaves are yellow-green in color overall and greenish near the veins. The chlorophylls pigment in leaves gradually decreased as iron deficiency worsened, and the leaves gradually changed from yellowish green to yellow, exhibiting severe symptoms of iron deficiency and chlorosis. Changes in leaf chlorophylls contents caused by iron deficiency were also confirmed by SPAD measurements (Figure 2B). The figure shows that the SPAD values of healthy, mildly iron-deficient, and severely iron-deficient leaves were approximately 35, 17, and 5, respectively. The results showed

that as iron deficiency worsened, the SPAD value of leaves decreased gradually, as did leaf chlorophylls contents (Yamamoto et al., 2002).

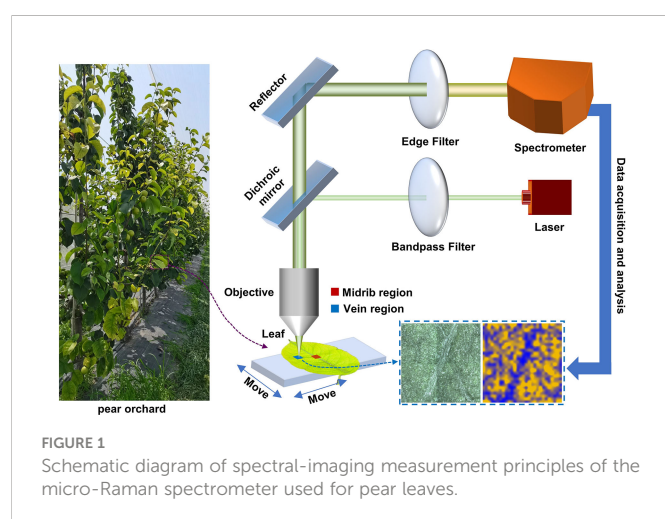
Figure 2C depicts the characteristic peaks analysis of the leaf Raman spectra. We found four spectral peaks in the average Raman spectrum of leaves: 1286cm^{-1} , 1353cm^{-1} , 1266cm^{-1} , and 1444cm^{-1} . Table 1 shows the attribution of peaks. The Raman peaks at 1286cm^{-1} and 1353cm^{-1} were assigned to chlorophylls (Cai et al., 2002; Mandrile et al., 2019), while those at 1266cm^{-1} and 1444cm^{-1} were assigned to lipids (Czamara et al., 2015). The intensities of the Raman peaks at 1286cm^{-1} and 1353cm^{-1} decreased sequentially in healthy, mildly iron-deficient, and severely iron-deficient leaves, as shown in Figure 2C, indicating that relative leaf chlorophylls content gradually decreased as the degree of iron-deficiency worsened. This result is consistent with the SPAD values shown in Figure 2B. Furthermore, the intensities of the Raman peaks at 1266cm^{-1} and 1444cm^{-1} gradually decreased with increasing severity of iron deficiency. This suggests that iron deficiency causes decreases in both chlorophylls and lipids. This is because iron deficiency reduces the soluble lipids content of the epidermis and also lipids in the vesicle membranes. The variations in characteristic chlorophylls and lipids peaks detected by Raman spectroscopy were correlated with the degree of iron deficiency in leaves according to cross-analyses with leaf phenotypes and SPAD values. Finally, Raman spectroscopy could detect physiological changes caused by iron deficiency in pear trees in a non-destructive and timely manner.

3.2 Spatial distribution of metabolites around the leaf midrib at different levels of iron deficiency

Figure 3 depicts the Raman spectral imaging results of metabolites in the regions near the midribs of leaves with varying degrees of iron deficiency. In mildly and severely iron-deficient leaves, the intervein was chlorotic, whereas the area near the midrib and the veins remained green, as seen in the microscopic images. This is consistent with symptoms of interveinal chlorosis associated with iron deficiency (Bertamini et al., 2002).

Based on the characteristic Raman peak of chlorophylls at 1353cm^{-1} , pseudo-color maps of relative chlorophylls content distributions near the midribs were generated. In Figure 3C, the chlorophylls content in the mesophyll region of healthy leaves is higher than in the region near the midrib. As a result, the midrib and mesophyll regions can be distinguished by chlorophylls distribution maps. When compared with healthy leaves, mildly and severely iron-deficient leaves had lower chlorophylls contents on the pseudo-color maps, making it more difficult to identify the positions of the midribs. Because of the difficulty of iron-ion transfer (Rustioni et al., 2018), the iron contents in venous regions of iron-deficient plant leaves are higher than in the inter-vein regions (Osório et al., 2014). This results in greater decreases in chlorophylls contents in the intervein regions because they are more susceptible to iron-deficiency stress than the midribs. In healthy leaves, the chlorophylls contents between veins are higher than those of the midrib and vein regions; iron deficiency causes lower chlorophylls contents between the veins. Consequently, chlorophylls distribution is uniform in Raman hyperspectral images, and veins cannot be identified.

The advantage of Raman spectroscopy is that it allows for single-spectrum, multi-component analysis. Simultaneously, a distribution map of the relative lipids content near the midrib was generated based



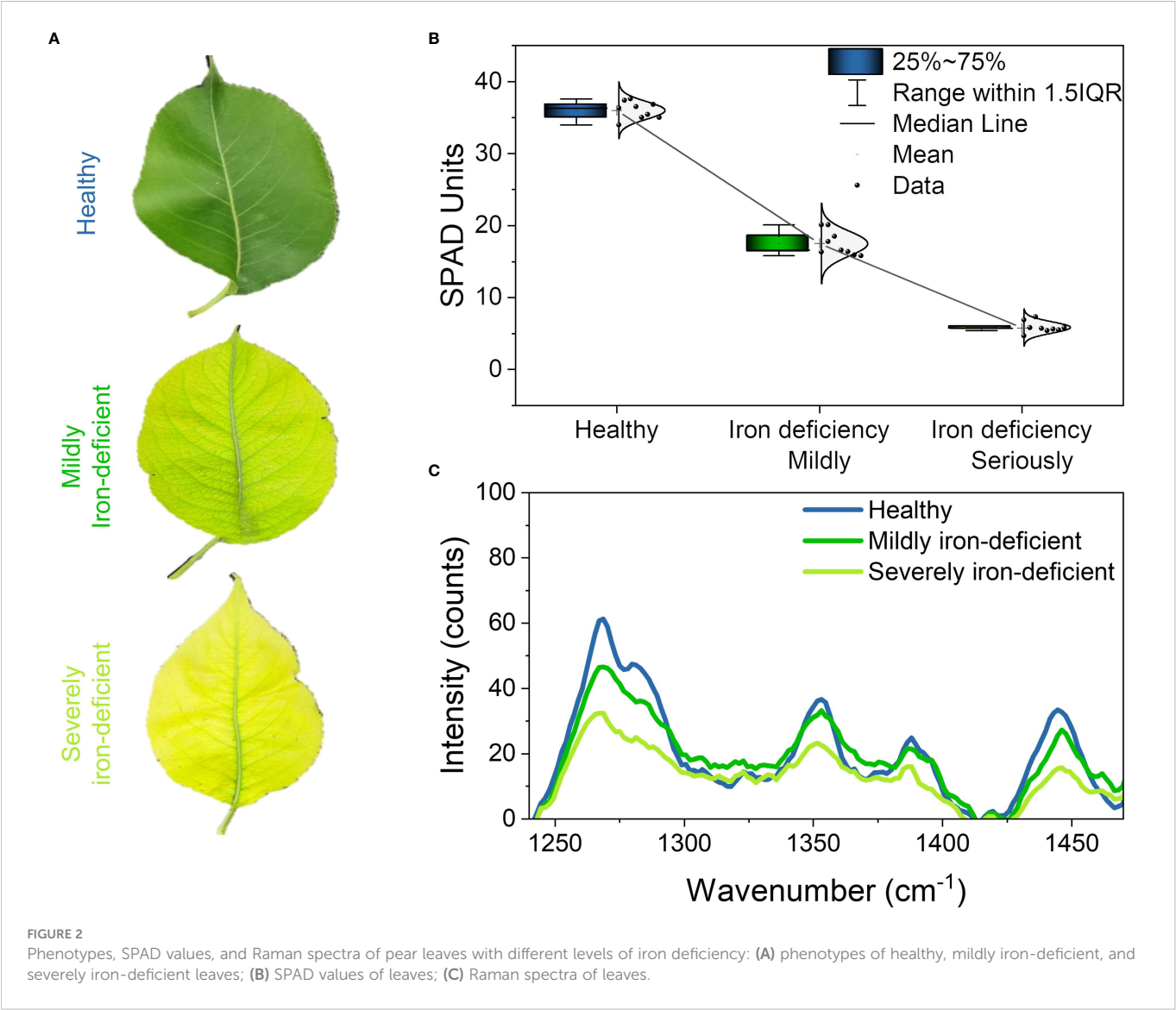


FIGURE 2 Phenotypes, SPAD values, and Raman spectra of pear leaves with different levels of iron deficiency: (A) phenotypes of healthy, mildly iron-deficient, and severely iron-deficient leaves; (B) SPAD values of leaves; (C) Raman spectra of leaves.

on the characteristic lipids peak at 1444cm⁻¹. Iron deficiency can cause a decrease in leaf lipids content, as shown in Figure 3D. There are two main reasons for this: iron stress reduces the soluble lipids content of the epidermis (Fernández et al., 2008); however, it also reduces the lipids content of the thylakoid membrane. Furthermore, the lipids content of the midrib was much lower than that of the mesophyll region. This could be because there are no chloroplasts in the midrib, resulting in reduced lipids contribution from thylakoid membranes. Consequently, in Figure 3D, there is a clear difference in lipids contents between the midrib and the mesophyll. This results in

the pseudo-color map of lipids exhibiting relatively consistent venation distribution in the visible light image in Figure 2B.

3.3 Spatial distribution of metabolites in the leaf-vein region

Figure 4 depicts the results of a similar pseudo-color map analysis of the area near the leaf veins. Like the midrib region, healthy leaves had higher chlorophylls contents in the mesophyll and lower contents in the veins. Because of differences in chlorophylls content distributions, it is

TABLE 1 Vibrational Bands and Their Assignments for Pear Leaf Samples.

band	vibrational assignment
1266	$\delta(=CH)$ (lipids) ^(Czamara et al., 2015)
1286	$\delta(\text{phenyl-OH})$ (phenolics) ^(Gill et al., 1970) + $-\delta(CH)-v(CN)$ (chlorophylls) ^(Cai et al., 2002)
1353	undefined (chlorophylls) ^(Cai et al., 2002; Mandrile et al., 2019)
1444	$\alpha(CH_2/CH_3)$ (lipids) ^(Czamara et al., 2015)

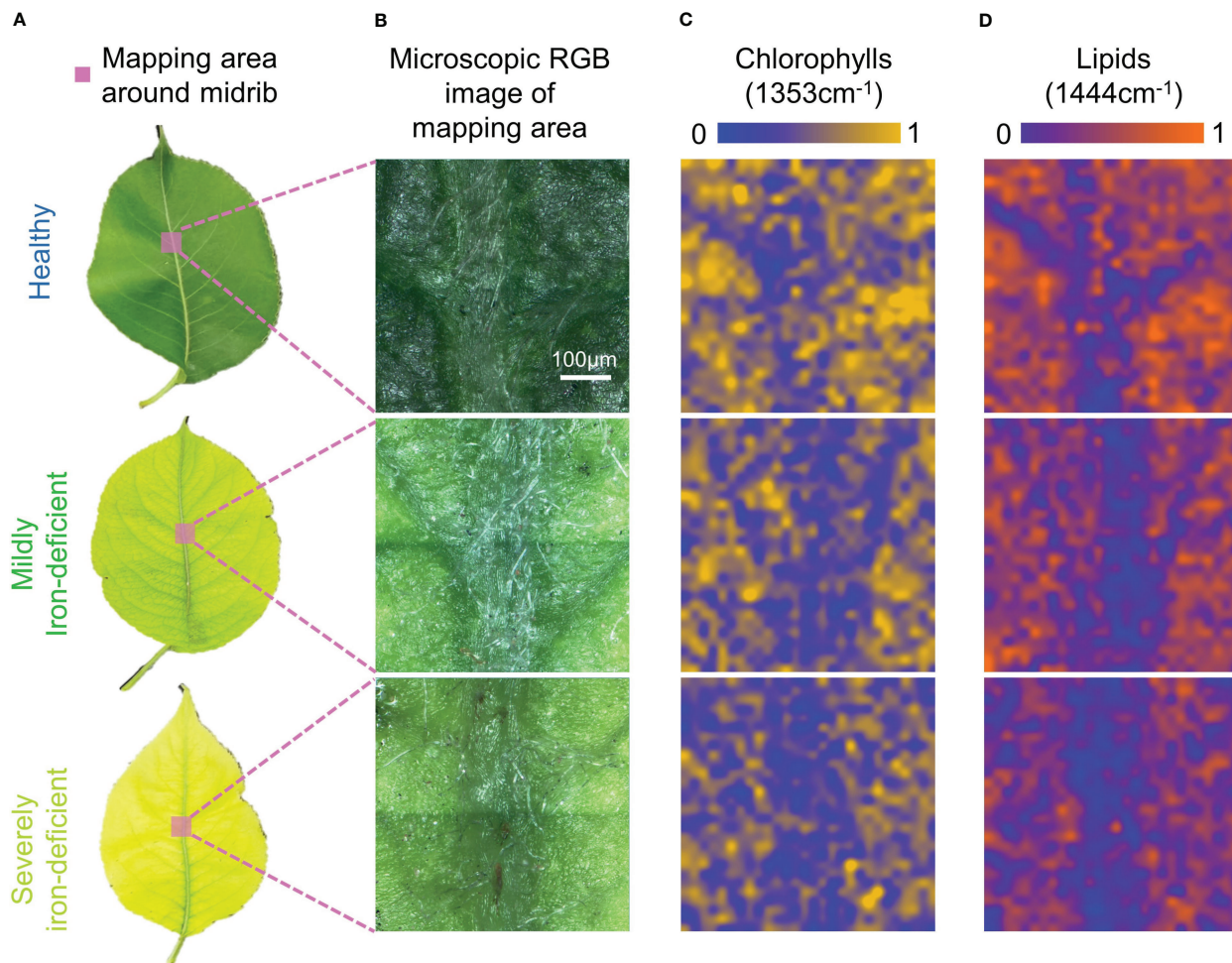


FIGURE 3

Visible light images and Raman spectral images of midrib components in leaves with differing degrees of iron deficiency. (A) Visible light images of healthy and iron-deficient leaves; (B) Microscopic visible light images of the midrib-mapping regions; (C) Pseudo-color maps of chlorophylls spatial distribution in the midrib-mapping regions; and (D) Pseudo-color maps of lipids spatial distribution in the midrib-mapping regions.

possible to see similar structural textures of the leaf in Figure 4C as in Figure 4B, allowing a clear distinction between the veins and mesophyll regions. In Figure 4C, the chlorophylls content of the mesophyll gradually decreases with the degree of iron deficiency in mildly and severely iron-deficient leaves. The difference in chlorophylls contents between mesophyll and veins in leaves was reduced as the degree of iron deficiency increased, resulting in an unclear chlorophylls distribution profile in Figure 4C. Consequently, a leaf texture structure similar to that shown in Figure 4B is not visible. Similarly, Figure 4D depicts the lipids content distribution in the vein-mapping region. The lipids content distributions in the vein-mapping areas of the three types of leaves were more uniform than in the midrib-mapping area. This could be because the veins are smaller in size, resulting in a higher proportion of mesophyll.

3.4 Normalized intensities of chlorophylls and lipids within the mapping area

The results of the preceding analyses show that micro-Raman maps can visualize the metabolites (detected chlorophylls and

lipids) in leaves with varying degrees of iron deficiency. The average normalized intensities of chlorophylls and lipids in the mapping areas in Figures 3, 4 were calculated to more clearly quantify changes in the relative contents of chlorophylls and lipids with respect to the degree of iron deficiency in the mapping area; these results are shown in Figure 5. In iron-deficient leaves, including mildly and severely iron-deficient ones, the two substances in the midrib and vein decreased significantly compared with those in healthy leaves.

The mapping method was also found to be more stable than the single-point acquisition method. The RSD of spectral characteristic peak intensity of all single points in each leaf scanning area represents the inaccuracy of single-point acquisition method. At the same time, the RSD of the characteristic peak intensity of the average spectrum of the scanning areas of the three samples in each category (healthy, mildly iron-deficient, and severely iron-deficient) represents the inaccuracy of mapping method. As shown in the Table 2, the RSD of mapping is much smaller than that of single-point acquisition measurement, so mapping method can improve the accuracy and consistency of the results.

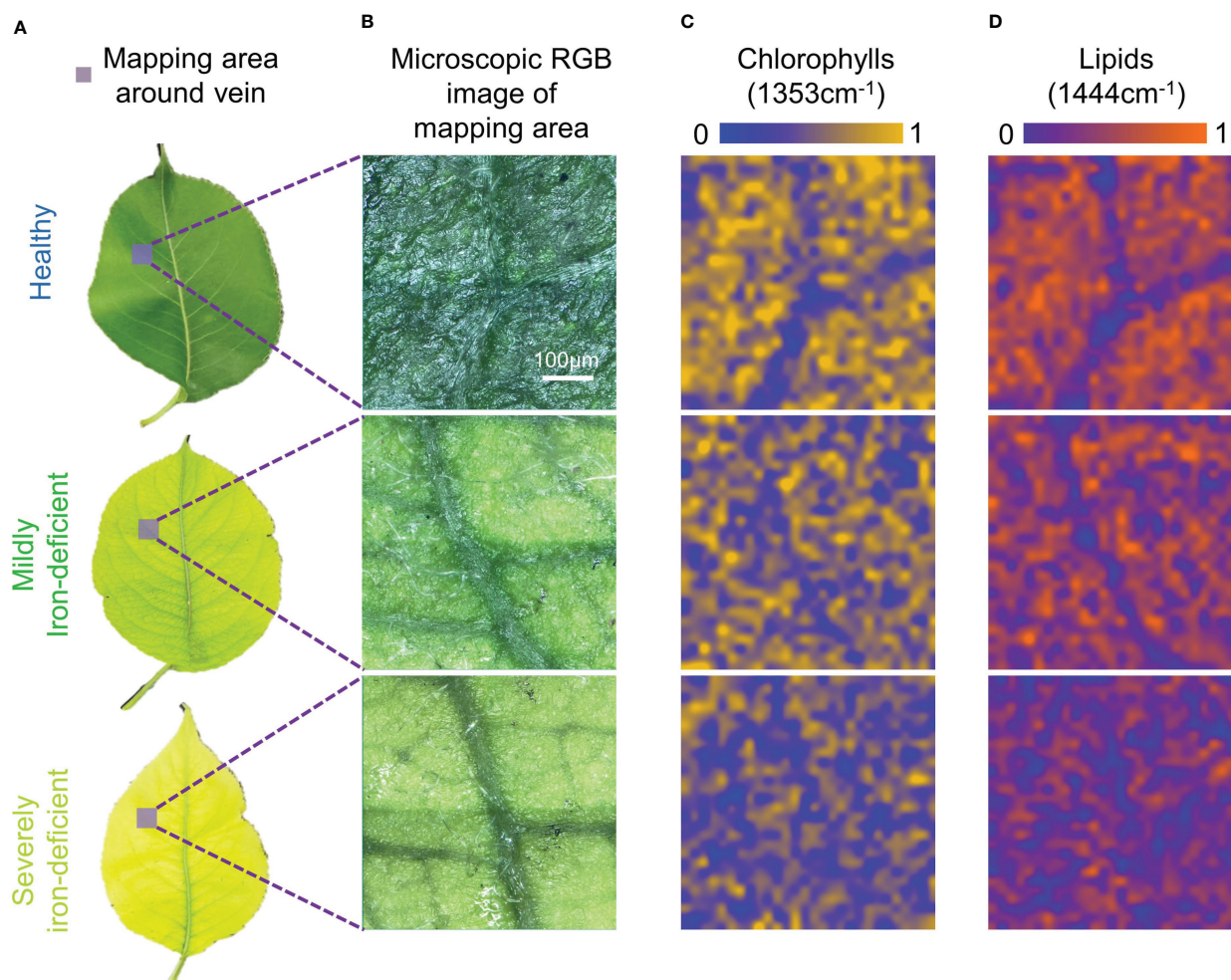


FIGURE 4

Visible light images and Raman spectral images of vein-region components of leaves with differing degrees of iron deficiency. (A) Visible light images of healthy and iron-deficient leaves; (B) Microscopic visible light images of the vein-mapping regions; (C) Pseudo-color maps of chlorophylls spatial distribution in the vein-mapping regions; (D) Pseudo-color maps of lipids spatial distribution in the vein-mapping regions.

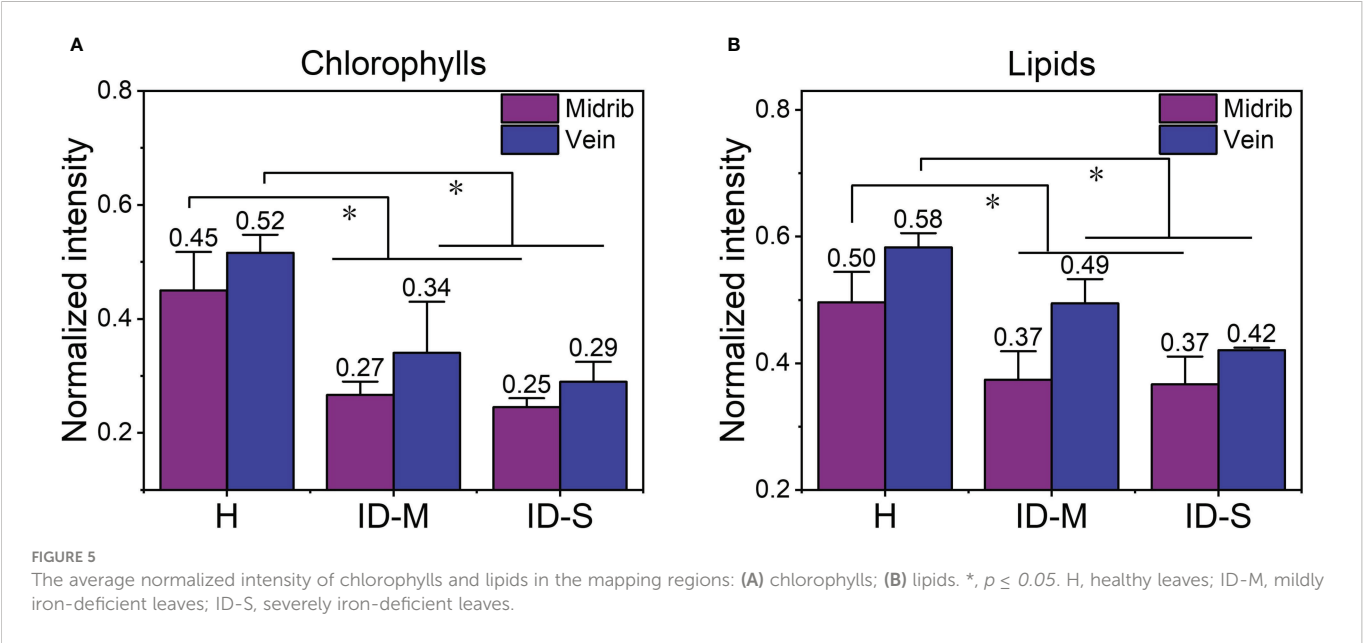
4 Discussion

In this paper, the feasibility of using the micro-Raman spectral imaging method for detecting metabolites in iron-deficient leaves was preliminarily explored, and visual detection of changes in the distribution of leaf metabolites caused by iron deficiency was discussed. Although the Raman spectral characteristics of chlorophylls and lipids were not robust, we could still identify them and relate temporal and spatial variations of their relative contents with the degree of iron deficiency by Raman spectroscopy. We found that iron deficiency resulted in decreased chlorophylls and lipids contents in leaves, which was more pronounced in the mesophyll regions.

Iron deficiency in pear trees can result in significant yield reductions and even death. As a result, it is critical to determine the physiological state of iron deficiency in pear leaves accurately and precisely. Existing measurement methods primarily focus on measurement of total iron content in leaves and reflectance spectroscopy. The “chlorosis paradox” suggests, however, that total iron content in leaves cannot accurately reflect the physiological state

of iron deficiency in plants, and the reflectance spectrum cannot specifically identify changes in leaf metabolites caused by iron deficiency. Compared with ICP-ES, the Raman spectral imaging method proposed in this paper can visualize the physiological state of iron deficiency in pear leaves with greater accuracy. It provides a method for visual characterization of specific substances for studying the mechanisms of plant responses to iron deficiency. Furthermore, the ability to recognize temporal and spatial variations in metabolite contents is expected to make different nutritional stresses distinguishable. Plant nutrients such as nitrogen, magnesium, and iron can cause leaf chlorosis, but there are subtle differences. The distribution of chlorophylls in leaves is expected to distinguish stress because of iron deficiency, magnesium deficiency, and nitrogen deficiency (Bertamini et al., 2002; Tremblay et al., 2012; Rustioni et al., 2018). These distinctions provide an opportunity for using Raman spectroscopy for nutrient stress discrimination. Future research will be focused on the use of Raman spectroscopy to diagnose specific nutrient stresses in plants.

Plants also contain many fluorescent chromophores. The weak Raman characteristics of many iron-deficiency-related substances



may be obscured because of strong background interference by fluorescence in leaf Raman spectra. Fortunately, we can detect changes in chlorophylls and lipids contents in pear leaves caused by iron deficiency. However, in the study of iron-deficiency mechanisms in leaves, providing only temporal and spatial variation of these two metabolites is insufficient; detection of variation in trace substances is also required. Determining how to reduce the strong fluorescence background and investigate high-resolution and high-sensitivity Raman mapping technology for iron-deficiency-related metabolite content maps is a critical and difficult task. In future work, shifted excitation Raman difference spectroscopy (SERDS) can be used to remove fluorescence interference by changing the acquisition method (Theurer et al., 2021); a Fourier-transform Raman spectrometer excited by near-infrared light at 1064 nm or an ultraviolet micro-Raman spectrometer can also be employed to avoid fluorescence background interference (Gallimore et al., 2018; Nazari and Holtz, 2018). However, increasing the spectral resolution of the micro-Raman spectrometer can improve its ability to detect more substances in one measurement. In terms of operation time, existing micro-Raman spectroscopy relies on the point-scanning mapping mode, which takes a long time. More advanced Raman techniques could be used to solve this problem. The spectral imaging

TABLE 2 The RSD calculated in the single-point and mapping acquisition methods.

	Method	Single-point			Mapping
	RSD Category	Sample 1	Sample 2	Sample 3	
Chlorophylls	Healthy	0.521133	0.265841	0.237239	0.061481
	Mildly iron-deficient	0.668272	0.428599	0.546086	0.263762
	Severely iron-deficient	0.435153	0.383717	0.412524	0.120858
Lipids	Healthy	0.343743	0.416906	0.361109	0.038703
	Mildly iron-deficient	0.356453	0.337559	0.343417	0.077702
	Severely iron-deficient	0.334797	0.141416	0.500061	0.009228

properties of coherent anti-Stokes Raman spectroscopy (CARS) and stimulated Raman spectroscopy are excellent (Hu et al., 2019; Xu et al., 2022). CARS is used to study anti-Stokes scattering, which not only reduces integration time but also significantly reduces the influence of fluorescence, improving mapping quality and speed. Similarly, because of the two-photon resonance effect, stimulated Raman spectroscopy increases the cross-section of Raman scattering and excitation efficiency, which can significantly improve the signal-to-noise ratio (SNR) and avoid fluorescence interference. High SNR means faster mapping speed, which is desirable when scanning larger areas. Using the techniques described above, it should be possible to detect more iron-deficiency-related metabolites in addition to chlorophylls and lipids and to fully utilize Raman single-spectrum, multi-component analysis.

5 Conclusion

Pear trees are grown widely and are valuable economic crops. Because the trees are iron-sensitive, iron deficiency is a common problem in pear cultivation, particularly in calcareous soils. Existing methods for determining iron deficiency in plants are destructive, necessitate complicated sample-preparation procedures, and do not accurately reflect the physiological state of plants suffering from iron deficiency. The Raman spectral imaging detection method proposed in this paper can detect iron deficiency on a microscopic scale without pre-processing and can accurately, non-destructively, and rapidly visualize changes in the relative content distributions of chlorophylls and lipids in pear leaves. To the best of our knowledge, this is the first use of Raman spectroscopy to investigate iron deficiency in pear trees. We have developed a new method of microscopic spectral image characterization for the study of physiological changes in pear leaves during iron deficiency. In the future, Raman spectroscopy could be used to study iron deficiency in other plant species. Additional characteristic peaks on the Raman spectrum for characterizing other substances will be mined with the advantage of single-spectrum, multi-component analysis. The metabolite-specific changes caused by iron deficiency in plants will then be studied in significant detail on a microscopic scale. It will be helpful to understand the mechanisms of plant responses to iron deficiency.

References

- Baranski, R., Baranska, M., and Schulz, H. (2005). Changes in carotenoid content and distribution in living plant tissue can be observed and mapped *in situ* using NIR-FT-Raman spectroscopy. *Planta* 222, 448–457. doi: 10.1007/s00425-005-1566-9
- Basayigit, L., Dedeoglu, M., and Akgul, H. (2015). The prediction of iron contents in orchards using VNIR spectroscopy. *Turk. J. Agric. For.* 39, 123–134. doi: 10.3906/tar-1406-33
- Bertamini, M., Muthuchelian, K., and Nedunchezian, N. (2002). Iron deficiency induced changes on the donor side of PS II in field grown grapevine (*Vitis vinifera* L. cv. pinot noir) leaves. *Plant Sci.* 162, 599–605. doi: 10.1016/S0168-9452(01)00604-5
- Cai, Z.-L., Zeng, H., Chen, M., and Larkum, A. W. D. (2002). Raman spectroscopy of chlorophyll d from *acaryochloris marina*. *Biochim. Biophys. Acta (BBA) - Bioenergetics* 1556, 89–91. doi: 10.1016/S0005-2728(02)00357-2
- Czamara, K., Majzner, K., Pacia, M. Z., Kochan, K., Kaczor, A., and Baranska, M. (2015). Raman spectroscopy of lipids: a review: Raman spectroscopy of lipids. *J. Raman Spectrosc.* 46, 4–20. doi: 10.1002/jrs.4607
- Elango, D., Kanatti, A., Wang, W., Devi, A. R., Ramachandran, M., and Jabeen, A. (2021). Analytical methods for iron and zinc quantification in plant samples. *Commun. Soil Sci. Plant Anal.* 52, 1069–1075. doi: 10.1080/00103624.2021.1872608
- Fernández, V., Eichert, T., Del Rio, V., López-Casado, G., Heredia-Guerrero, J. A., Abadía, A., et al. (2008). Leaf structural changes associated with iron deficiency chlorosis in field-grown pear and peach: physiological implications. *Plant Soil* 311, 161–172. doi: 10.1007/s11104-008-9667-4
- Gallimore, P. J., Davidson, N. M., Kalberer, M., Pope, F. D., and Ward, A. D. (2018). 1064 nm dispersive raman microspectroscopy and optical trapping of pharmaceutical aerosols. *Analytical Chem.* 90, 8838–8844. doi: 10.1021/acs.analchem.8b00817
- Gierlinger, N., Sapei, L., and Paris, O. (2008). Insights into the chemical composition of *equisetum hyemale* by high resolution raman imaging. *Planta* 227, 969–980. doi: 10.1007/s00425-007-0671-3
- Gill, D., Kilponen, R. G., and Rimai, L. (1970). Resonance raman scattering of laser radiation by vibrational modes of carotenoid pigment molecules in intact plant tissues. *Nature* 227, 743–744. doi: 10.1038/227743a0

Data availability statement

The raw data supporting the conclusions of this article will be made available by the authors, without undue reservation.

Author contributions

ZG: Conceptualization; Methodology; Software; Formal analysis; Investigation; Data Curation; Writing - Original Draft; Visualization; Project administration; CZ: Supervision; DD: Writing - Review & Editing; Funding acquisition; SL: Resources; XW: Investigation; YG: Data Curation; LJ: Writing - Review & Editing; Funding acquisition. All authors contributed to the article and approved the submitted version.

Funding

This research was financially supported by the National Natural Science Foundation of China (32101609), Distinguished Young Scientists Program of Beijing Natural Science Foundation (JQ19023) and Special financial Project of Beijing Academy of Agriculture and Forestry Sciences (CZZJ202204).

Conflict of interest

The authors declare that the research was conducted in the absence of any commercial or financial relationships that could be construed as a potential conflict of interest.

Publisher's note

All claims expressed in this article are solely those of the authors and do not necessarily represent those of their affiliated organizations, or those of the publisher, the editors and the reviewers. Any product that may be evaluated in this article, or claim that may be made by its manufacturer, is not guaranteed or endorsed by the publisher.

- Heiner, Z., Zeise, I., Elbaum, R., and Kneipp, J. (2018). Insight into plant cell wall chemistry and structure by combination of multiphoton microscopy with raman imaging. *J. Biophotonics* 11, e201700164. doi: 10.1002/jbio.201700164
- Hu, F., Shi, L., and Min, W. (2019). Biological imaging of chemical bonds by stimulated raman scattering microscopy. *Nat. Methods* 16, 830–842. doi: 10.1038/s41592-019-0538-0
- Jimenez, S., Morales, F., Abadia, A., Abadia, J., Moreno, M. A., and Gogorcena, Y. (2009). Elemental 2-d mapping and changes in leaf iron and chlorophyll in response to iron re-supply in iron-deficient GF 677 peach-almond hybrid. *Plant Soil* 315, 93–106. doi: 10.1007/s11104-008-9735-9
- Kassebaum, N., Jasrasaria, R., Naghavi, M., Wulf, S., Johns, N., Lozano, R., et al. (2014). A systematic analysis of global anemia burden from 1990 to 2010. *BLOOD* 123, 615–624. doi: 10.1182/blood-2013-06-508325
- Kucukbay, F. Z., and Kuyumcu, E. (2014). Determination of elements by atomic absorption spectrometry in medicinal plants employed to alleviate common cold symptoms. *Spectrosc. Spectr. Anal.* 34, 2548–2556. doi: 10.3964/j.issn.1000-0593(2014)09-2548-09
- Larbi, A., Abadia, A., Abadia, J., and Morales, F. (2006). Down co-regulation of light absorption, photochemistry, and carboxylation in fe-deficient plants growing in different environments. *Photosynth Res.* 89, 113–126. doi: 10.1007/s11120-006-9089-1
- Lew, T. T. S., Sarojam, R., Jang, I.-C., Park, B. S., Naqvi, N. I., Wong, M. H., et al. (2020). Species-independent analytical tools for next-generation agriculture. *Nat. Plants* 6, 1408–1417. doi: 10.1038/s41477-020-00808-7
- Li, B., Liew, O. W., and Asundi, A. K. (2006). Pre-visual detection of iron and phosphorus deficiency by transformed reflectance spectra. *J. Photochem. Photobiol. B: Biol.* 85, 131–139. doi: 10.1016/j.jphotobiol.2006.06.005
- Mandriale, L., Rotunno, S., Miozzi, L., Vaira, A. M., Giovannozzi, A. M., Rossi, A. M., et al. (2019). Nondestructive raman spectroscopy as a tool for early detection and discrimination of the infection of tomato plants by two economically important viruses. *Anal. Chem.* 91, 9025–9031. doi: 10.1021/acs.analchem.9b01323
- Morales, F., Abadia, A., and Abadia, J. (1991). Chlorophyll fluorescence and photon yield of oxygen evolution in iron-deficient sugar beet (*Beta vulgaris* L.) leaves. *Plant Physiol.* 97, 886–893. doi: 10.1104/pp.97.3.886
- Morales, F., Grasa, R., Abadia, A., and Abadia, J. (1998). Iron chlorosis paradox in fruit trees. *J. Plant Nutr.* 21, 815–825. doi: 10.1080/01904169809365444
- Nazari, M., and Holtz, M. W. (2018). Near-ultraviolet raman and micro-raman analysis of electronic materials. *Appl. Phys. Rev.* 5, 041303. doi: 10.1063/1.5054660
- Osório, J., Osório, M. L., Correia, P. J., de Varennes, A., and Pestana, M. (2014). Chlorophyll fluorescence imaging as a tool to understand the impact of iron deficiency and resupply on photosynthetic performance of strawberry plants. *Scientia Hort.* 165, 148–155. doi: 10.1016/j.scienta.2013.10.042
- Pretty, J., Sutherland, W., Ashby, J., Auburn, J., Baulcombe, D., Bell, M., et al. (2010). The top 100 questions of importance to the future of global agriculture. *Int. J. OF Agric. SUSTAINABILITY* 8, 219–236. doi: 10.3763/ijas.2010.0534
- Romheld, V. (1998). The chlorosis paradox: Fe inactivation in leaves as a secondary event in fe deficiency chlorosis. *J. Plant Nutr.* 23, 1971–1981.
- Rustioni, L., Grossi, D., Brancadoro, L., and Failla, O. (2018). Iron, magnesium, nitrogen and potassium deficiency symptom discrimination by reflectance spectroscopy in grapevine leaves. *Scientia Hort.* 241, 152–159. doi: 10.1016/j.scienta.2018.06.097
- Sanz, M., Montañés, L., and Carrera, M. (1993). The possibility of using floral analysis to diagnose the nutritional status of pear trees. *Acta Hort.* 367, 290–295. doi: 10.17660/ActaHortic.1994.367.41
- Sasani, N., Bock, P., Felhofer, M., and Gierlinger, N. (2021). Raman imaging reveals *in-situ* microchemistry of cuticle and epidermis of spruce needles. *Plant Methods* 17, 17. doi: 10.1186/s13007-021-00717-6
- Therby-Vale, R., Lacombe, B., Rhee, S. Y., Nussaume, L., and Rouached, H. (2022). Mineral nutrient signaling controls photosynthesis: focus on iron deficiency-induced chlorosis. *Trends Plant Sci.* 27, 502–509. doi: 10.1016/j.tplants.2021.11.005
- Theurer, L. S., Maiwald, M., and Sumpf, B. (2021). Shifted excitation raman difference spectroscopy: A promising tool for the investigation of soil. *Eur. J. Soil Sci.* 72, 120–124. doi: 10.1111/ejss.12928
- Tremblay, N., Wang, Z., and Cerovic, Z. G. (2012). Sensing crop nitrogen status with fluorescence indicators. a review. *Agron. Sustain. Dev.* 32, 451–464. doi: 10.1007/s13593-011-0041-1
- Xu, S., Camp, C. H. Jr., and Lee, Y. J. (2022). Coherent anti-stokes raman scattering microscopy for polymers. *J. Polymer Sci.* 60, 1244–1265. doi: 10.1002/pol.20210317
- Yamamoto, A., Nakamura, T., Adu-Gyamfi, J., and Saigusa, M. (2002). Relationship between chlorophyll content in leaves of sorghum and pigeonpea determined by extraction method and by chlorophyll meter (SPAD-502). *J. OF Plant Nutr.* 25, 2295–2301. doi: 10.1081/PLN-120014076
- Yeturu, S., Jentsch, P. V., Ciobotă, V., Guerrero, R., Garrido, P., and Ramos, L. A. (2016). Handheld raman spectroscopy for the early detection of plant diseases: Abutilon mosaic virus infecting abutilon sp. *Analytical Methods* 8, 3450–3457. doi: 10.1039/C6AY00381H
- Zhang, Z.-M., Chen, S., and Liang, Y.-Z. (2010). Baseline correction using adaptive iteratively reweighted penalized least squares. *Analyst* 135, 1138–1146. doi: 10.1039/b922045c
- Zhang, Y., Gao, W., Cui, C., Zhang, Z., He, L., Zheng, J., et al. (2020). Development of a method to evaluate the tenderness of fresh tea leaves based on rapid, *in-situ* raman spectroscopy scanning for carotenoids. *Food Chem.* 308, 125648. doi: 10.1016/j.foodchem.2019.125648
- Zhao, Y., Sun, M., Liang, Z., Li, H., Yu, F., and Liu, S. (2020). Analysis of contrast iron chlorosis tolerance in the pear cv. 'Huangguan' grafted onto pyrus betulifolia and quince a grown in calcareous soils. *Scientia Hort.* 271, 109488. doi: 10.1016/j.scienta.2020.109488



OPEN ACCESS

EDITED BY

Leizi Jiao,
Beijing Academy of Agriculture and
Forestry Sciences, China

REVIEWED BY

Dongyan Zhang,
Anhui University, China
Ce Yang,
University of Minnesota Twin Cities,
United States

*CORRESPONDENCE

Han Li

✉ cau_lihan@cau.edu.cn

SPECIALTY SECTION

This article was submitted to
Technical Advances in Plant Science,
a section of the journal
Frontiers in Plant Science

RECEIVED 21 November 2022

ACCEPTED 13 December 2022

PUBLISHED 24 January 2023

CITATION

Wang L, Miao Y, Han Y, Li H, Zhang M
and Peng C (2023) Extraction of 3D
distribution of potato plant CWSI
based on thermal infrared image and
binocular stereovision system.
Front. Plant Sci. 13:1104390.
doi: 10.3389/fpls.2022.1104390

COPYRIGHT

© 2023 Wang, Miao, Han, Li, Zhang and
Peng. This is an open-access article
distributed under the terms of the
[Creative Commons Attribution License
\(CC BY\)](https://creativecommons.org/licenses/by/4.0/). The use, distribution or
reproduction in other forums is
permitted, provided the original
author(s) and the copyright owner(s)
are credited and that the original
publication in this journal is cited, in
accordance with accepted academic
practice. No use, distribution or
reproduction is permitted which does
not comply with these terms.

Extraction of 3D distribution of potato plant CWSI based on thermal infrared image and binocular stereovision system

Liuyang Wang¹, Yanlong Miao², Yuxiao Han¹, Han Li^{1*},
Man Zhang² and Cheng Peng¹

¹Key Laboratory of Agricultural Information Acquisition Technology, Ministry of Agriculture and Rural Affairs, China Agricultural University, Beijing, China, ²Key Laboratory of Smart Agriculture System Integration Research, Ministry of Education, China Agricultural University, Beijing, China

As the largest component of crops, water has an important impact on the growth and development of crops. Timely, rapid, continuous, and non-destructive detection of crop water stress status is crucial for crop water-saving irrigation, production, and breeding. Indices based on leaf or canopy temperature acquired by thermal imaging are widely used for crop water stress diagnosis. However, most studies fail to achieve high-throughput, continuous water stress detection and mostly focus on two-dimension measurements. This study developed a low-cost three-dimension (3D) motion robotic system, which is equipped with a designed 3D imaging system to automatically collect potato plant data, including thermal and binocular RGB data. A method is developed to obtain 3D plant fusion point cloud with depth, temperature, and RGB color information using the acquired thermal and binocular RGB data. Firstly, the developed system is used to automatically collect the data of the potato plants in the scene. Secondly, the collected data was processed, and the green canopy was extracted from the color image, which is convenient for the speeded-up robust features algorithm to detect more effective matching features. Photogrammetry combined with structural similarity index was applied to calculate the optimal homography transform matrix between thermal and color images and used for image registration. Thirdly, based on the registration of the two images, 3D reconstruction was carried out using binocular stereo vision technology to generate the original 3D point cloud with temperature information. The original 3D point cloud data were further processed through canopy extraction, denoising, and k-means based temperature clustering steps to optimize the data. Finally, the crop water stress index (CWSI) of each point and average CWSI in the canopy were calculated, and its daily variation and influencing factors were analyzed in combination with environmental parameters. The developed system and the proposed method can effectively detect the water stress status of potato plants in 3D, which can provide support for analyzing the differences in the three-dimensional distribution and spatial and temporal variation patterns of CWSI in potato.

KEYWORDS

water stress, automation, photogrammetry, image registration, 3D distribution

1 Introduction

Global climate change and water scarcity lead to a severe negative impact on crop yield. Among the increasing research on crop precision irrigation, water stress detection has attracted increasing attention. Potato is the fourth most important food crop in the world after wheat, rice, and maize (FAOSTAT, 2020). Due to the relatively shallow root-zone depth coupled with the low to medium soil field capacity of the coarse-textured soils commonly used for their cultivation (Rud et al., 2014), the potato plant has a high sensitivity to water stress, which affects its growth and, in turn, its yield and quality. Therefore, it is crucial to improve potato yield and quality by effectively water stress status monitoring.

The immediate response of crop to water stress is to close leaf stomata, resulting in increasing canopy temperature. Stomatal conductance is a vital indicator of plant water stress, and canopy temperature is a surrogate indicator for stomatal conductance (Prashar and Jones, 2016). Idso et al. (1981) proposed the crop water stress index (CWSI) based on crop canopy temperature, which has been proved to effectively reflect the water stress status of the crop since it was proposed. This indicator can be calculated by three methods: empirical approach (Idso et al., 1981), analytical approach (Jackson et al., 1981), and direct approach (Jones, 1999). The CWSI calculated by the three methods can be abbreviated as CWSI_e, CWSI_a, and CWSI_d, respectively (Maes and Steppe, 2012). Among them, CWSI_e and CWSI_a rely on meteorological information such as ambient temperature, humidity, wind speed, etc. In the measurement process, CWSI_d only needs a thermal infrared image to simultaneously acquire the temperatures of the dry and wet reference surfaces (T_{dry} and T_{wet}), and the temperature of crop canopy or leaf (T_c). T_{dry} represents the temperature of a non-transpiring leaf with completely closed stomata, and T_{wet} represents the leaf temperature when stomata are fully open (undisturbed transpiring leaf). Due to the application of artificial reference surfaces (Poirier-Pocovi et al., 2020), the measurement based on thermal infrared images is further simplified. Moreover, the CWSI_d index showed a good correlation with stomatal conductance (Maes et al., 2016), leaf water potential (Rud et al., 2014), and stem water potential (Garcia-Tejero et al., 2017).

With the development of thermal imaging technology, especially the decrease in high-performance online thermal camera price, thermal infrared image has become increasingly widely used in the agricultural field (Qiu et al., 2018). CWSI (CWSI_d) calculation using the direct approach has become widely used. In addition to non-destructive temperature measurement, thermal infrared images can also be obtained continuously, online, and rapidly in high-resolution. Therefore, compared with other indicators such as stomatal conductance,

leaf water potential, and stem water potential, the CWSI calculation using the direct approach has the potential for high-throughput water stress detection, and can be applied to precise irrigation planning and drought resistance breeding (Prashar et al., 2013). Thermal image captured by thermal imaging equipment usually contains canopy temperature and background temperature. It is a vital issue to eliminate the background noise of thermal images. One method is to separate the canopy based on the temperature difference between the canopy and background. For example, Obidiegwu et al. (2015) assessed water stress by extracting the crop canopy in thermal images around noon under solar illumination. Because the pixel resolution of the thermal camera is very low, and a single pixel can detect thermal radiation from soil and leaf, a threshold based on temperature alone may create a high degree of uncertainty in estimating T_c . The other method is to collect thermal and color images of the canopy simultaneously for alignment and geometric registration, and then the canopy area can be extracted based on segmentation algorithms of color image processing (Amogi et al., 2020; Cucho-Padin et al., 2020; Elsherbiny et al., 2021). This method requires pre-calibration based on multiple sets of images from the thermal camera and color camera, to determine the horizontal and vertical displacement vectors between the two cameras. Manual selection of the relevant control points in the two images is often needed. Gan et al. (2018) proposed a photogrammetry-based multi-modal image registration method, which achieved an average accuracy of 3 pixels on citrus canopy images.

With the development of technology, high-throughput phenotyping methods using advanced sensors and robotic platforms have shown increasing efficiency over traditional manual phenotyping methods. Studies have shown that high-throughput phenotyping techniques have achieved good results in detecting and monitoring plant health, water and nutritional status using multi-sensor data (Pereyra-Irujo et al., 2012; Kipp et al., 2014). There are many high-throughput phenotyping platforms developed by organizations and institutions which are in use today (e.g., Scanalyzer Discovery platform, LemnaTec, Germany; Phenomobile, High Resolution Plant Phenomics Centre, Australia). However, these commercial platforms are expensive and unsuitable for large-scale deployment. Therefore, there is a need to develop a low-cost and lightweight system that can meet specific crop phenotyping needs. Zhang et al. (2016) developed a three-dimension (3D) motion robotic system for automated high-throughput phenotyping of cereal crops, which can extract 20 features from data acquired by onboard thermal and multispectral cameras. Precision irrigation and drought resistance breeding also require the large-scale automatic collection of crop water stress data.

The current methods for crop CWSI calculation is often based on temperature of random canopy parts or the entire

canopy, obtained on two-dimension (2D) thermal image. However, it fails to verify whether the water stress status of crops is affected by different leaf positions or different detection positions. Studies have shown that for potato plants, there are differences in different leaf positions of plants due to the transferability of chlorophyll. For example, Sun et al. (2018) took Atlantic cultivars at the flowering stage as the research object, drew a visual distribution map of chlorophyll in isolated potato leaves at different leaf positions, and found that the chlorophyll content increased from bottom to top. Also, Sun et al. (2019) analyzed the two-dimensional distribution of water content in isolated potato leaves by hyperspectral imaging, and found that water stress increased, and the leaves started to lose water from the edge and gradually spread to the middle of the leaves. The above research shows that the water stress status of potato plants may be affected by the leaf position and detection position, which reflects the necessity of studying the differences of potato CWSI in the 3D distribution. In general, there are many ways to acquire 3D point cloud data (PCD) of a plant. It has been reported that Narvaez et al. (2016) obtained thermal distribution of pear trees in 3D using LiDAR and thermal camera. However, the price of LiDAR is generally high. Rossi et al. (2022) proposed an algorithm to automatically collect plant structural parameters based on a phenotyping platform and structure-from-motion (SFM) method, and applied the algorithm to monitor the dynamic response of the plant to early water stress. The SFM is an offline algorithm for 3D reconstruction of a series of disordered images, which limits its commercial use. 3D reconstruction based on stereo vision technology, an image-based 3D information acquisition method, has low cost and simple equipment, and is one of the most commonly used reconstruction methods. Laguela et al. (2012)

used image matching and fusion techniques to combine thermal imaging and metric information to acquire 3D thermal models. Yang et al. (2018) developed an imaging system consisting of two smartphones and a low-cost thermal infrared camera, and the images captured by it were fused for 3D thermal model reconstruction.

This study aims to extract 3D distribution of potato plant CWSI at low cost using a thermal and a binocular camera. Firstly, a 3D motion robotic system integrated with a 3D thermal imaging system was developed for automated high throughput acquisition of potato plant thermal image, binocular images (a pair of color images), and temperature data. Then, specific methods for generating a 3D thermal model of the potato plant canopy were developed. The objectives of this study are to: (1) develop a low-cost 3D platform and an image acquisition control system, which has the function of positioning the image acquisition module at predefined position and triggering the control system to acquire images; (2) propose a method for fast pixel-level registration of thermal and color images, and (3) acquire the 3D CWSI distributions of the potato plant, and analyze its variation characteristics and influencing factors in time series.

2 Material and methods

2.1 3D motion robotic system

As shown in Figure 1A, the hardware of the 3D motion robotic system adopted a modular design, consisting of a 3D platform, an image acquisition module, and a host controller.

The 3D platform consists of an XYZ three-axis gantry aluminum frame, three stepper drive control integrated

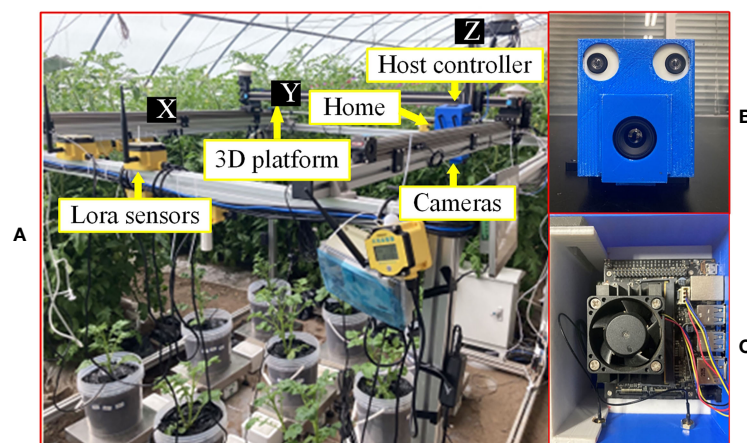


FIGURE 1
Equipment and apparatus used for experiments in this study: (A) overall experimental platform, (B) image acquisition module, and (C) host controller.

motors, and a single-chip microcomputer. The platform was designed as 1.8 m×1.8 m×1.5 m (L×W×H) in dimension. The sliders are driven by motors to move along the three axes. The single-chip microcomputer is a development board integrated with the STM32F103RCT6 (ST, Geneva, Switzerland) chip, which sends control signals to the motor. The maximum payload of the Z-axis for carrying the image acquisition module is 10 kg. The “Home” position or coordinate origin of the 3D platform is at one of the corners of the platform (Figure 1A).

The image acquisition module consists of a thermal camera (Wuhan Guide Infrared Co., Ltd, Wuhan, China) with a model of IPT384 and a binocular USB camera (Pixel XYZ, Wuhan, China). The thermal camera can capture thermal pseudo-color images with a resolution of 384×288 pixels, and save the temperature of each pixel (measurement resolution is 0.1°C) into a text file. The baseline of this binocular USB3.0 camera is 60 mm, and the left and right cameras can both capture color images in 1280×720-pixel resolution. As shown in Figure 1A, the image acquisition module was fixed on the slider of the Z-axis (indicated by Z in Figure 1A) of the 3D platform. For ease of installation, a camera frame was designed and 3D printed to mount the two cameras (Figure 1B).

The host controller is a Jetson Nano (NVIDIA Corporation, California, USA) running Ubuntu 18.04 system. The host controller sends commands to the single-chip microcomputer through the interface to control the 3D platform to move in three directions. Furthermore, the host controller controls the capturing of images of crop canopy by the cameras through communications with the image acquisition module. As shown in Figure 1A, the host controller and power module were fixed above the image acquisition module. To facilitate installation, a frame was designed and 3D printed to mount the host controller (Figure 1C).

The host controller uses the Robot Operating System (ROS) software architecture to write each functional module in the form of nodes, which are divided into “AxisMoveNode” (AMN), “IrCaramIpt384NodeV2016” (IrCN), and “RGBCaramNode” (RGBCN). Communication between the nodes is implemented in the form of publish/subscribe messages. The workflow of the 3D motion robotic system is shown in Figure 2. In the initial stage, the AMN controls the motors to drive the sliders to move to the origin position and return the coordinates to zero. Then, the AMN controls the motor to drive the slider to move to the preset target position, and judges whether the slider has reached the target position through the position coordinate information fed back in real-time. After reaching the target position, the IrCN and the RGBCN receive the message of reaching the target position published by the AMN, and then control the image acquisition module to capture the images of the crop canopy and the temperature data to the local folder, and publish the status

message of the folder at the same time. The AMN determines whether to go to the next target location by judging whether all images and temperature data are newly added to the folders. Until all the target positions are traversed, the AMN controls the motors to drive the sliders to move to the origin position. Hence, a round of inspection is completed.

2.2 Data collection

In the period from April 24th to May 1st (7 days), 2022, a water stress experiment on potato plants (Netherlands 15) was conducted in the No.9 greenhouse facilities of the National Precision Agriculture Research Base, Beijing, China (40°18′N, 116°45′E). Potatoes are grown in pots, with peat and coconut bran (at a volume ratio of 3:1) as the substrate, covered with a black plastic. There were two experimental groups (control and treatment groups, each has four potato plants), and the two groups were treated with the same irrigation from planting to the beginning of the experiment. After the first day of the experiment, the control group was fully irrigated, and the treatment group was not irrigated (Gerhards et al., 2016).

In this study, a wet reference surface was built following the steps proposed by Meron et al. (2013). The CWSI can be calculated by function (1) (Jones et al., 2002).

$$CWSI = \frac{T_c - T_{wet}}{T_{dry} - T_{wet}} \quad (1)$$

where T_c , T_{wet} , and T_{dry} are the potato plant canopy temperature, dry and wet reference surface temperatures, respectively. T_{dry} was replaced by air temperature T_{air} plus 7°C (Rud et al., 2014). The CWSI values are in the range of 0-1, and the larger the value, the greater the water shortage pressure.

In this experiment, the cameras acquired plant data perpendicular to the ground at a height of approximately 1.2m to 1.5m every day. The next day, the collection height were readjusted according to the natural growth of the potato to ensure that the entire canopy is included in the image as much as possible. When collecting thermal images, T_{air} and illumination were measured by LoRa sensors (IntelliFuture, Hebei, China). The real-time T_{air} and illumination were uploaded to the cloud platform through the LoRa communication gateway. From April 24th to May 1st, 20-25 datasets were collected from 8:00 to 17:00 every day, and the collected thermal data and images were stored in the onboard SD card of the host controller.

Using Visual studio 2019 as the platform, the point cloud library PCL1.10.0 and the computer vision library OpenCV3.1.0 (Open Source Computer Vision Library) were installed, and the C++ language for software programming was used to realize data processing.

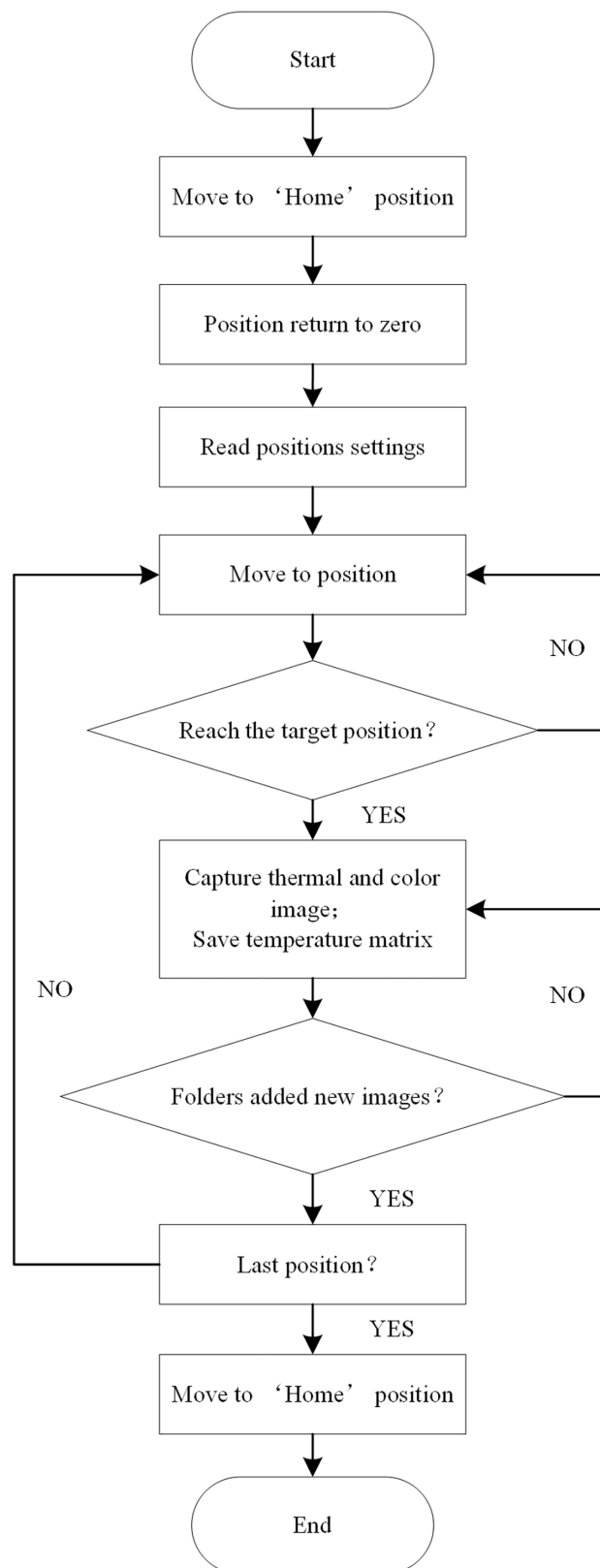


FIGURE 2
Workflow chart of the 3D robot system.

2.3 Data processing

2.3.1 Stereo-calibration of thermal and binocular cameras

Photogrammetry-based registration of thermal and binocular cameras requires stereo-calibration of the two cameras.

The checkerboard grid (Gan et al., 2018), was used in the experiment for stereo-calibration. The size of each square is 30×30 mm, as shown in Figure 3A. The resolutions and field of views of the color and thermal images are different. First, the checkerboard in the color image was resized to be the same as that in the thermal image by applying the bicubic interpolation algorithm, and then the color image was cropped to the same resolution as the thermal image to facilitate subsequent registration. The results are shown in Figures 3B, C. Next, stereo-calibration was implemented using the Stereo Camera Calibrator toolbox in MATLAB 2018a. The stereo-calibration gets two sets of parameters, the first set of parameters are the elements of interior orientation of the cameras (Wolf et al., 2014). The second set of parameters is named relative orientation between cameras (between the left and right cameras of the binocular camera; between the left color and the thermal cameras) (Gan et al., 2018). The calibrated parameters were saved for subsequent use. Finally, the interior orientation and relative orientation parameters of the left and right cameras of the binocular camera were loaded and the stereo rectification was applied, so that the left and right color images were aligned in parallel without distortion.

2.3.2 Coarse registration of thermal and color images

The registration between thermal and color images requires finding the geometric transformation relationship between them. This requires groups of homonymy points to be found correctly in two images. The process is shown in Figure 4A, and Figure 5 shows a specific example.

First, to quickly select the homonymy points as many as possible on the potato plants, the Laplacian algorithm was used to sharpen the left and right color images to enhance the contours/edges of the image (Ma et al., 2014). Then the sharpened images were converted into the HSV (Hue, Saturation, Value) color space. Compared with the RGB (Red, Green, Blue) model, the HSV model can express the brightness, hue, and saturation of the color very intuitively, and can effectively use the color space for segmentation (Hamuda et al., 2017). The mask parameters were obtained by setting the upper and lower thresholds of the H channel [HL, HU], S channel [SL, SU], and V channel [VL, VU] to extract the target image, which was the green channel image, through the 'and' operation (Li et al., 2020).

Second, speeded-up robust features (SURF) features were detected on the two target images and their descriptors were established. Then, the detected feature points were matched using the nearest neighbor distance ratio strategy and the matching results were displayed on the original images. Some mismatched points in the matching results may negatively affect the registration, filtered out using epipolar geometry constraints.

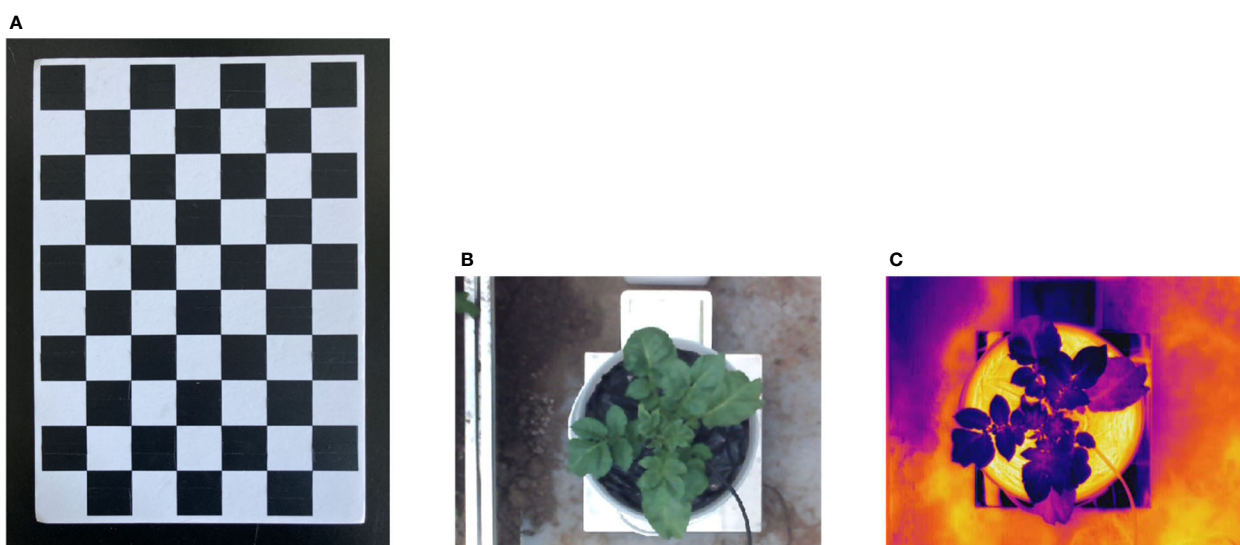
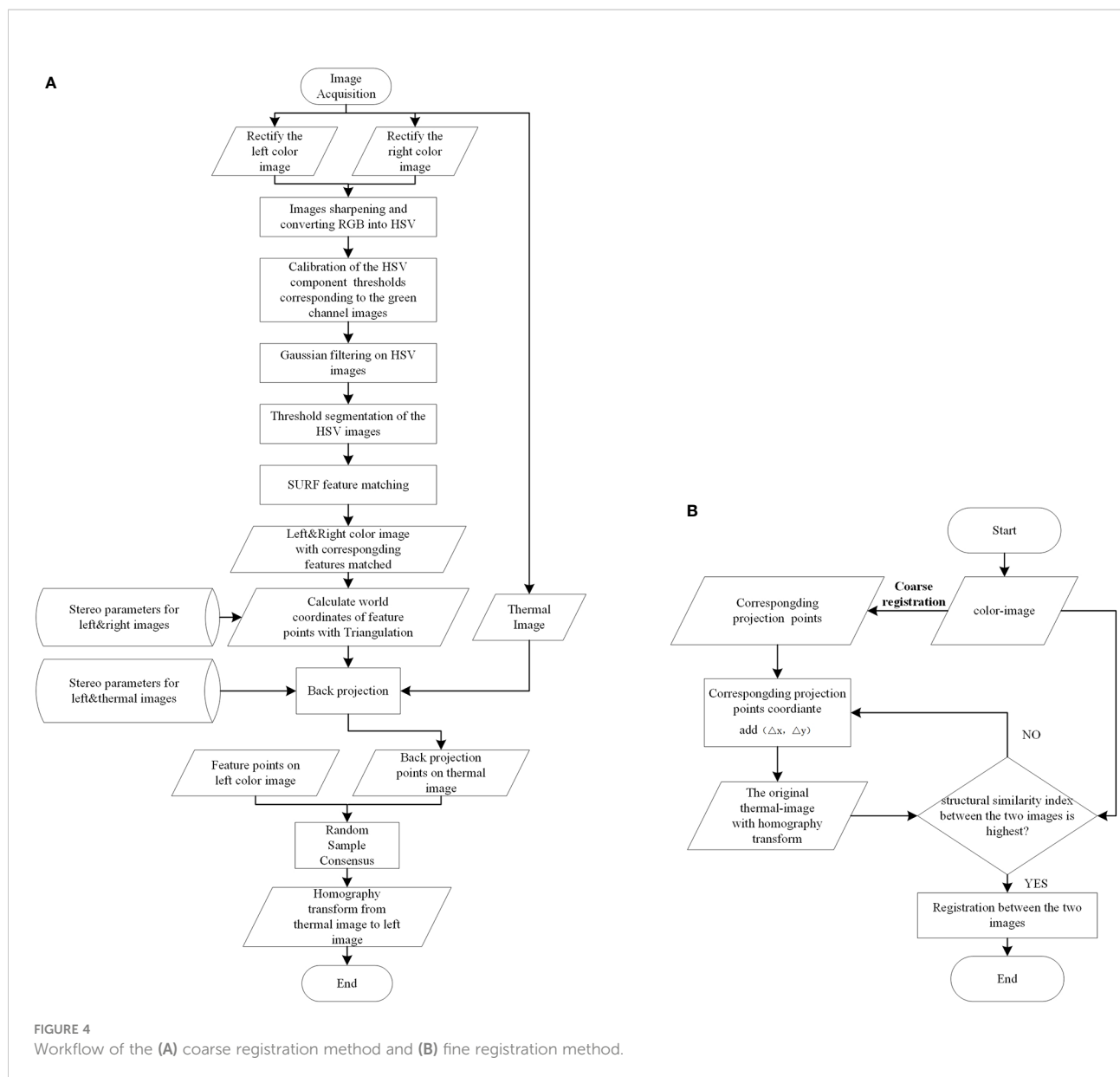


FIGURE 3
Images pre-processing and Checkerboard. (A) Checkerboard for stereo-calibration, (B) thermal image of the potato plant, (C) cropped and resized color image of the potato plant.



Third, the filtered feature point pairs were extracted, and the interior direction and relative direction parameters of the left and right cameras of the binocular camera were loaded. The triangulation principle was used for these point pairs to calculate the world coordinates. Back-projection was applied using function (2) to project those world coordinates onto the thermal image.

Lastly, taking the feature points in the left color image and the back-projected points on the thermal image as the input, Random Sample Consensus (RANSAC) algorithm was applied to compute the homography transformation that best describes the relationship between these point pairs. The calculation result of the RANSAC algorithm is the optimal solution in the sense of least squares error. The

thermal image was transformed using the resulting transformation matrix.

$$S \tilde{n}Coordinates_{thermal} = K \tilde{n} \begin{bmatrix} R & T \\ 0^T & 1 \end{bmatrix} \tilde{n}Coordinates_{world} \quad (2)$$

where, S is a non-zero scale factor, which is the z-component of the world coordinates, $Coordinates_{thermal}$ are the homogeneous coordinates of the back-projection points on the thermal image, and $Coordinates_{world}$ are the homogeneous coordinates of the world points. K , R , and T are the intrinsic matrix of the thermal camera, the rotation matrix, and the translation matrix of the thermal camera relative to the left camera of the binocular camera, respectively.

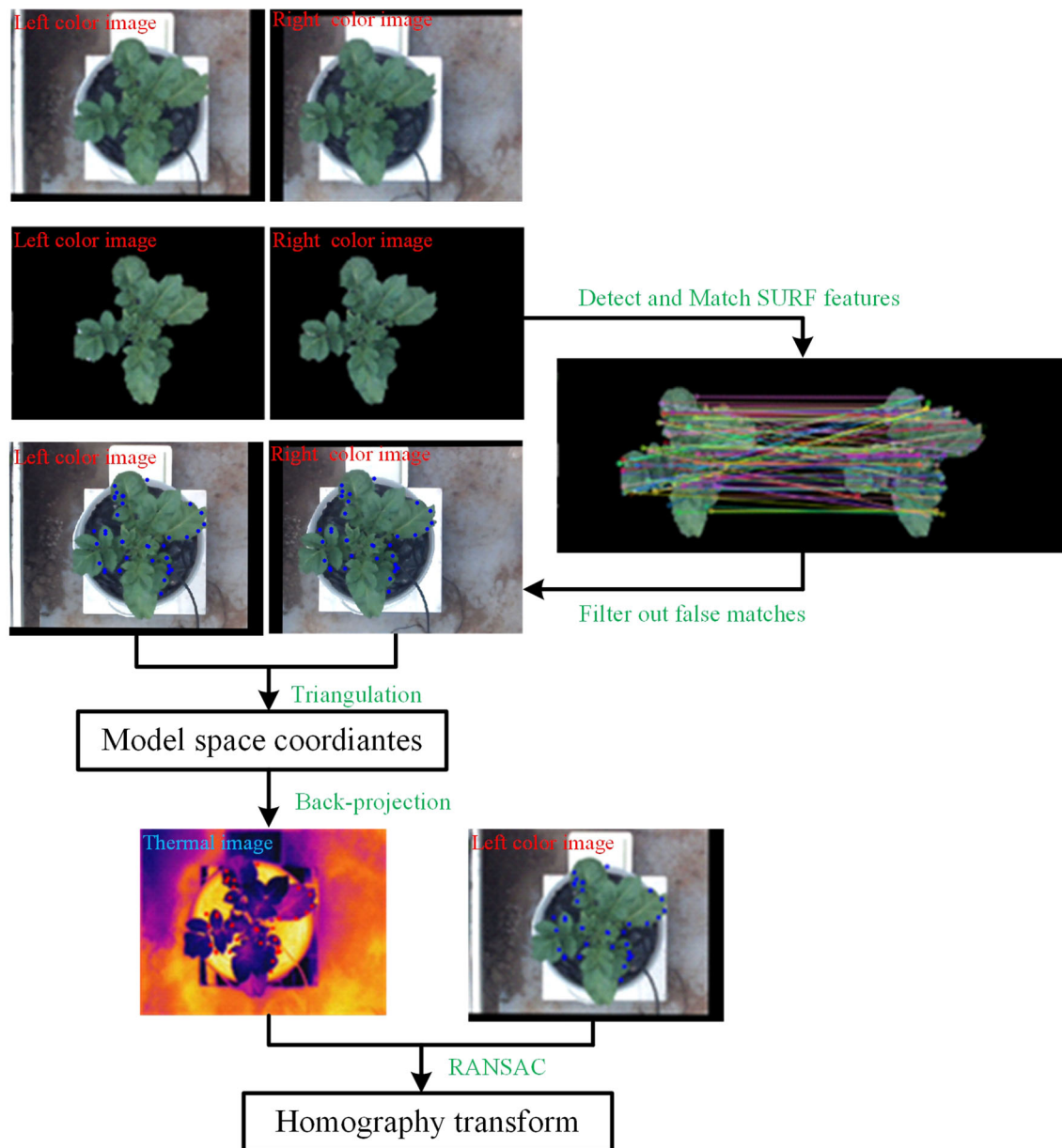


FIGURE 5
Example of coarse registration of color and thermal images.

2.3.3 Fine registration of thermal and color images

The premise of applying the coarse registration method to accurately register color and thermal images is that the photographed object is close to the plane. However, the surface structure of the potato plant canopy is complex and the depth varies greatly. Moreover, the error of the coarse registration is relatively large due to the error brought by the camera calibration. Therefore, when the coarse registration cannot meet the registration accuracy requirements, further

fine registration is required. The specific process is shown in Figure 4B.

Firstly, for any filtered feature point in the color image, its corresponding point in the thermal image can be obtained by applying the coarse registration method. For instance, if the coordinates of a feature point in the color image were (x_0, y_0) , the corresponding projection point coordinates in the thermal image were calculated by back-projection as $(x_{0_pro_thermal}, y_{0_pro_thermal})$. Secondly, it was assumed that $(x_{0_pro_thermal}, y_{0_pro_thermal})$ and the coordinates of the true corresponding points in the thermal image

$(x_{0_thermal}, y_{0_thermal})$ had a small position difference (Δ_x, Δ_y) , which had an initial value $(0, 0)$. Thirdly, the filtered feature points in the color image and the position-compensated corresponding points in the thermal image $(x_{0_pro_thermal} + \Delta_x, y_{0_pro_thermal} + \Delta_y)$ were retaken as input, and the RANSAC algorithm was used to calculate the homography matrix that can best describe the transformation relationship between them, and the original thermal image was transformed. Fourthly, the structural similarity (SSIM) index was used to measure the similarities between the transformed thermal image and the color image. The two images were first constrained to co-aligned regions by cropping and then used as input for measurement (Dandrisosse et al., 2021). Lastly, repeated the previous four steps by increasing the values (Δ_x, Δ_y) . Because the SSIM possesses the property of maximum uniqueness, the transformation with the largest SSIM value was chosen as the optimal transformation. The temperature matrix was acquired simultaneously with the thermal image was also transformed using the optimal homography transformation for subsequent use.

2.3.4 Generation of potato plant PCD with temperature

3D reconstruction based on stereo vision technology is one of the most commonly used reconstruction methods. Stereo matching technology based on image information to acquire depth information is a popular research topic in stereo vision. It is the process of finding the homonymy points in two images, then calculating the disparity value to acquire the depth information of the point in the three-dimensional space.

In this study, stereo vision technology was used to reconstruct the canopies of potato plants in 3D to generate point clouds. Based on the similar triangle principle, the depth of the world coordinate point can be calculated by the following function:

$$D = \frac{B \cdot f}{x_l - x_r} \quad (3)$$

where D is the depth value. B is the baseline, which is the distance between the principal points of the two cameras of the binocular camera. f is equal to the focal length multiplied by a coefficient representing the number of pixels per millimeter on the imaging plane. $d = x_l - x_r$ is called disparity, which is the difference between the x coordinates of the two corresponding pixels on the left and right images.

First, a variant of the semi-global matching algorithm (SGM), the semi-global block matching algorithm (SGBM) was applied, using the left and right color images with stereo rectification in section 2.3.1 to calculate the disparity map. Next, due to occlusion or uneven illumination, some disparity values in the disparity map are unreliable, and median filtering was used to filter out isolated noise points caused by mismatching. After removing false matches, the removed pixels will cause holes of invalid values, and the method of

multi-level mean filtering was used to fill the voids iteratively. Multi-level mean filtering is a variant of mean filtering, which is an algorithm that fills holes multiple times by changing the filter window size and using the integral map of the disparity map. It first performs mean filtering with a larger initial window and assigns values to the holes in a large area. Then in the subsequent filtering, the window size was reduced to half of the original size, and the original integral graph was used to filter again and assign values to the smaller holes (overwrite the original values). These steps were repeated until the window size became 3×3 , then the filtering stopped and the final result was obtained. Then, the similar triangle principle was applied using function (3) to calculate the depth value of a point in space, and the three-dimensional coordinate information of the point was calculated in combination with function (4) (Huang et al., 2020; Xie et al., 2020). Finally, based on the homography transformation between the color and thermal images in section 2.3.3, a new point cloud data type was defined by using the PCL library, which integrated the three-dimensional coordinate information, RGB color value, and temperature information of the potato plant canopy together. Thus, the original 3D points cloud data of the potato canopy containing both color information and temperature information has been generated.

$$\begin{cases} Z = D \\ X = \frac{x - x_0}{f} \frac{D}{n} \\ Y = \frac{y - y_0}{f} \frac{D}{n} \end{cases} \quad (4)$$

where (x, y) are the pixel coordinates of the image, and (x_0, y_0) are the pixel coordinates of the principal point.

2.3.5 Optimization of PCD and extraction of 3D distribution of CWSI

In section 2.3.4, the original PCD of the potato plant were acquired through stereo vision technology. The original PCD not only contained potato plant but also background point clouds such as soil and flower pots. The quality of PCD is not high due to the influence of environmental factors (e.g. illumination, wind speed) and image registration errors. Some methods need to be taken to optimize the original PCD to extract the potato plant canopy information. The specific steps are as follows.

Step one: the PCD of the canopy of the potato plant were extracted. Color is one of the most important features for distinguishing crops and backgrounds in a greenhouse environment (Tkalcic and Tasic, 2003). Philipp and Rath (2002) found that the HSV color space is one of the most reliable color spaces for distinguishing plant from the background. In order to extract the green canopy area of potato plant, a color model based on the HSV color space was used to segment the original PCD.

Step two: the scatter points were removed. The produced scatter points due to factors such as random measurement error and external environment when acquiring PCD was removed by using the statistical filtering algorithm.

Step three: the abnormal temperature points of the canopy were removed. Some ground areas were incorrectly matched to some of the leaves due to the registration errors of the thermal and color images, resulting in higher temperature values of the leaves than their true surface temperatures. To remove such incorrectly matched points, the k-means algorithm was used to classify all points into two classes according to their temperature, and the class with more points was saved as the optimized PCD of the potato plant canopy (Qiu et al., 2021).

Step four: the CWSI value of each point of the potato plant canopy was calculated and its 3D distribution was acquired. The temperature of the wet reference surface was acquired from the original PCD, and the temperature of the dry reference surface was replaced by the air temperature plus 7 °C. The CWSI of each point in the canopy can be obtained with these data through function (1) and the distributions of CWSI in 3D were obtained.

2.4 Performance evaluation

Evaluation of registration performance was conducted for thermal and color images. Because the true coordinates of the matching points on the thermal image corresponding to the color image cannot be determined, the accurate matching error between these point pairs cannot be calculated. However, the thermal image after the optimal homography transformation can be overlaid with the color image to show the performance of the registration. At the same time, the homography transformation errors between the matching feature points on the color image and transformed thermal image were calculated. Second, registration performance was also measured by computing the average distance between control points (control point error) on the color and thermal images (Dandrifosse et al., 2021). The control points were visually selected by a human operator on the potato plant. The points had to be selected on recognizable pixels (all locations of the canopy and leaves).

3 Results

3.1 Feature detection and matching results of the left and right color images

The image processing shows that illumination affects the specific settings of H, S, V thresholds, especially in the saturation, that is, the parameter S. When the sunlight hits the crop surface directly, it affects the color and brightness of the image, and the SL of the green reference color varies from 30 to

40. The SL of the green reference color varies from 45 to 65 when there is no direct sunlight. The images obtained at different times of the day were analyzed and compared, as shown in Figure 6. Figures 6A, B show the images when the sunlight directly on the surface of tomato plants. At this time, the effect is best when the SL is 35. Figures 6C, D show images of tomato plants in shadow or without direct sunlight. At this point, the best result is when the SL is 60. In the experiment, in order to reduce the interference of background such as soil, a black plastic was covered on the soil surface (Figure 1A). Under these conditions, the values of HU and HL were set to 100 and 35, respectively.

The feature detection results on the green channel image were compared with the feature detection results on the original color image. The number of good matching points acquired by filtering before and after extracting the canopy was used to characterize the comparison results (the feature detection, matching and filtering algorithms and parameter settings used before and after the canopy extraction remain the same), as shown in Figure 7. In this study, a total of 30 potato plant samples from different collection periods were randomly selected for verification, the results are shown in Table 1. It can be seen that the number of matching point pairs filtered from the extracted canopy images is 48% more than the number of point pairs filtered from the original images on average.

3.2 Results of registration for thermal and color images

The registration of thermal and color images was finished according to the procedures described in sections 2.3.2 and 2.3.3. The example in Figure 8 shows the performance of the proposed image registration method and it can be seen that even though some potato plants have a complex canopy structure and a wide range of depths, their color and thermal images can be well registered. Image registration performance was evaluated with the same set of randomly selected 30 potato plant samples. The homography transformation error and control point error of each potato plant sample was recorded. The statistical results are shown in Tables 2 and 3. The registered control point error is 2.8 pixels on average, indicating that the proposed SURF feature detection on the extracted canopy images and photogrammetry-based methods can effectively register the color and thermal images of potato plants.

3.3 Extraction of 3D distribution of potato plant CWSI

3.3.1 Results of generation and optimization of the PCD

When using the disparity map calculated by stereo matching for 3D reconstruction, the quality of the generated PCD is often

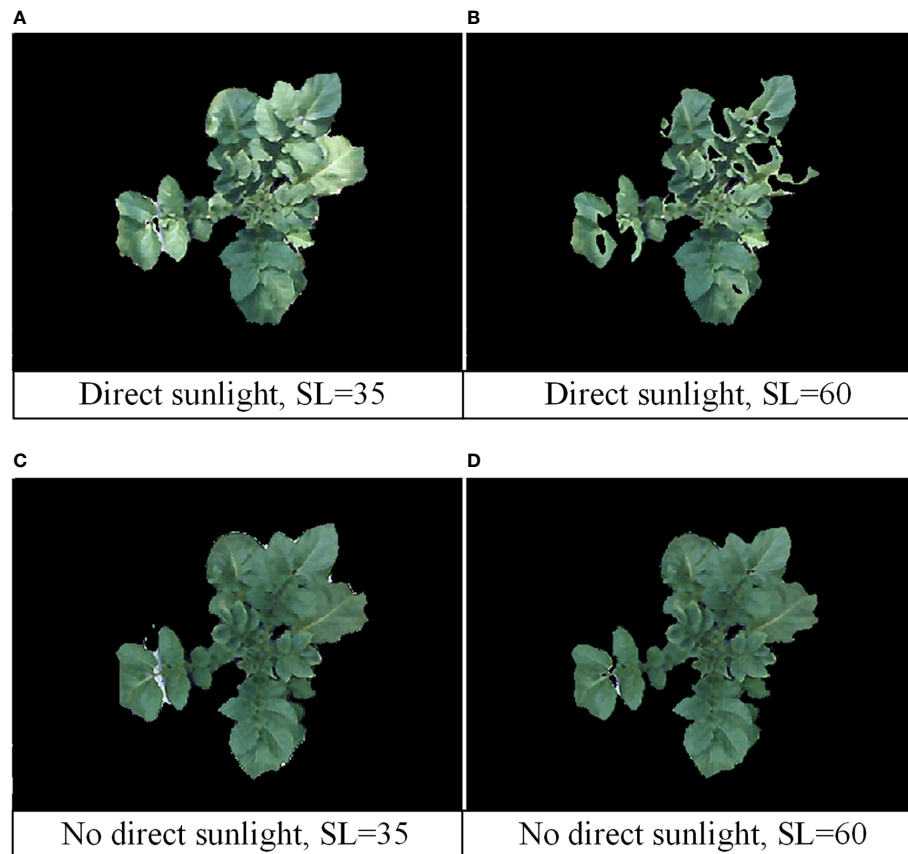


FIGURE 6
Image processing results under different sunlight and SL thresholds. (A) Direct sunlight, SL=35; (B) direct sunlight, SL=60; (C) no direct sunlight, SL=35; (D) no direct sunlight, SL=60.

not high due to the low quality of the disparity map. Therefore, some disparity refines operations can be performed to improve the quality of the disparity map. In this study, the SGBM algorithm used, in addition to its sub-pixel fitting and consistency check and other strategies to refine the disparity map, median filtering and multi-level mean filtering algorithms were also adopted to refine the disparity map further. Experiments show that setting the initial window size to 4×4 not only ensures that the holes were filled, but also ensures that the image is not over-smoothed.

The PCD were generated from the stereo-rectified left and right color images and the registration results of the color and thermal images, and contains both color information and temperature information. Firstly, a method based on HSV color space segmentation was used to extract the green canopy of the potato plant, and then only the canopy PCD were operated. However, the resulting PCD also contained many scatter points, which was filtered out by applying a statistical filtering algorithm. In this study, the number of neighbors

selected for statistical analysis was 50, and the threshold for identifying outliers was set to 0.5. Besides, the temperature values of some regions were much higher than the real surface temperature of the potato plant, mainly due to the miss matching of the canopy partial PCD and the ground caused by the image registration error. The difference between the temperature of the potato plant and the ground was significant. A clustering algorithm based on k-means was used to filter out abnormal temperature points caused by image registration errors, and the optimized PCD of the potato plant canopy were retained. The PCD of four potato plant samples (two well-watered and two water-stressed) of different sizes and qualities were selected from the treatment and control groups to demonstrate the results of this method. As the black circles shown in Figure 9, it can be seen that the temperatures in some edge regions of the canopy were significantly higher than that of other regions before the k-means clustering algorithm was adopted. Through the above treatments, the canopy PCD of the potato plant were relatively intact, as shown in Figure 10.

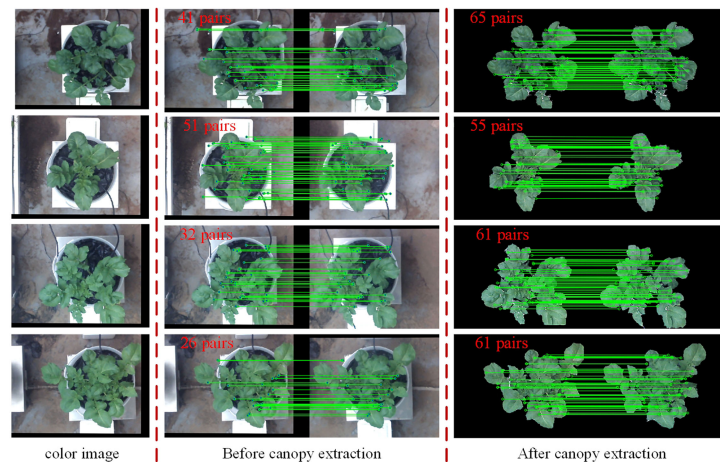


FIGURE 7

Comparison of the number of feature points obtained by detection, matching and filtering before and after canopy extraction.

3.3.2 Extraction of plant CWSI in 3D distribution—a case study

In this study, the PCD and temperature data of the potato plant were combined basing color and thermal images registration. The direct approach was used to calculate the CWSI value of each point of the potato plant canopy, and the 3D distributions of the CWSI were obtained.

After extraction of 3D distribution of CWSI, one potato plant sample was selected from each of the data of treatment and control acquired on April 26 (partly cloudy), and the PCD generated from 11:00–15:00 were processed to obtain their distributions of the temperature and 3D CWSI, and the results are shown in Figures 11A–C. It can be seen from the figure that the potato petiole and the area around the vein respond quickly to water stress, the temperatures were significantly higher than that of other areas, and the difference under different irrigation treatments was very large, which can provide a reference for the selection of the measurement position of potato plant water stress state. At the same time, the change curve of their average CWSI values of canopy were plotted, as shown in Figure 11D. It can be seen from the figure that each two peaks appeared in the CWSI (CWSI_{well} and CWSI_{stress}) of the potato plants under two different moisture treatments, and each time appeared at the same time. The first peak appeared at 11:30. At this time, the temperature in the greenhouse was 29.54 °C, which was in the rising stage, and the illumination intensity was the maximum value of 72.4 klx. The second peak appeared at 13:00. At this time, the CWSI of the potato plant under two different water treatments reached the maximum value, the temperature in the greenhouse was 31.05°C, which was the highest value in a day, and the illumination intensity was 69.4 klx. From the above statistical results, it can be seen that the water stress state of the potato plant was jointly affected by air temperature and

illumination intensity. The water stress degree of potato plant can be comprehensively evaluated in combination with soil moisture and environmental parameters.

4 Discussion

4.1 Feature detection and matching of the left and right color images

To quickly find the set of points that best represent the geometric transformation between color and thermal images, and to select these points from the potato plant canopy as much as possible. The RGB color space was converted to HSV color space and extracted the green channel image, by setting the upper and lower thresholds of the H, S, and V values, respectively. The purpose of this is to reduce the interference of background points when computing the homography transformation using the RANSAC algorithm. The results show that the method of feature detection by extracting the canopy provides more and effective candidate matches for computing the optimal homography transformation between color and thermal images.

4.2 Registration of thermal and color images

Although the method of extracting the canopy from the color image and then performing the SURF feature detection can provide more candidate matches for image registration, the thermal image after homography transformation sometimes cannot be well registered with the color image.

TABLE 1 Comparison of the results of feature detection before and after canopy extraction in ten samples.

Sample No.	Amounts of feature points		
	Before canopy extraction	After canopy extraction	Increase (%)
1	41	65	58.5
2	51	55	7.8
3	32	61	90.6
4	26	61	134.6
5	20	34	70
6	33	54	63.6
7	42	68	61.9
8	10	28	180
9	71	78	9.9
10	26	35	34.6
11	48	68	41.7
12	60	81	35.0
13	42	63	50.0
14	47	79	68.1
15	24	60	150.0
16	35	71	100.0
17	41	52	26.8
18	28	65	132.1
19	34	67	97.1
20	38	65	71.1
21	28	42	50.0
22	21	40	90.5
23	46	38	-17.4
24	29	35	66.7
25	66	81	22.7
26	47	66	40.4
27	34	49	44.1
28	75	89	18.7
29	31	42	35.5
30	51	49	-3.9
average	39.2	58.0	48.0

In this study, a similarity index was selected to evaluate the structural similarity between images, and the optimal homography transformation matrix that could ensure more canopy pixel overlap was obtained by finding its maximum value. Nonetheless, some areas in the potato plant canopy

were less affected by the homography transformation because no feature points were detected in these areas due to the influence of illumination changes and the weak texture of the canopy surface, as the blue circles shown in [Figure 12A](#). It was also because even if feature points were detected in this part of

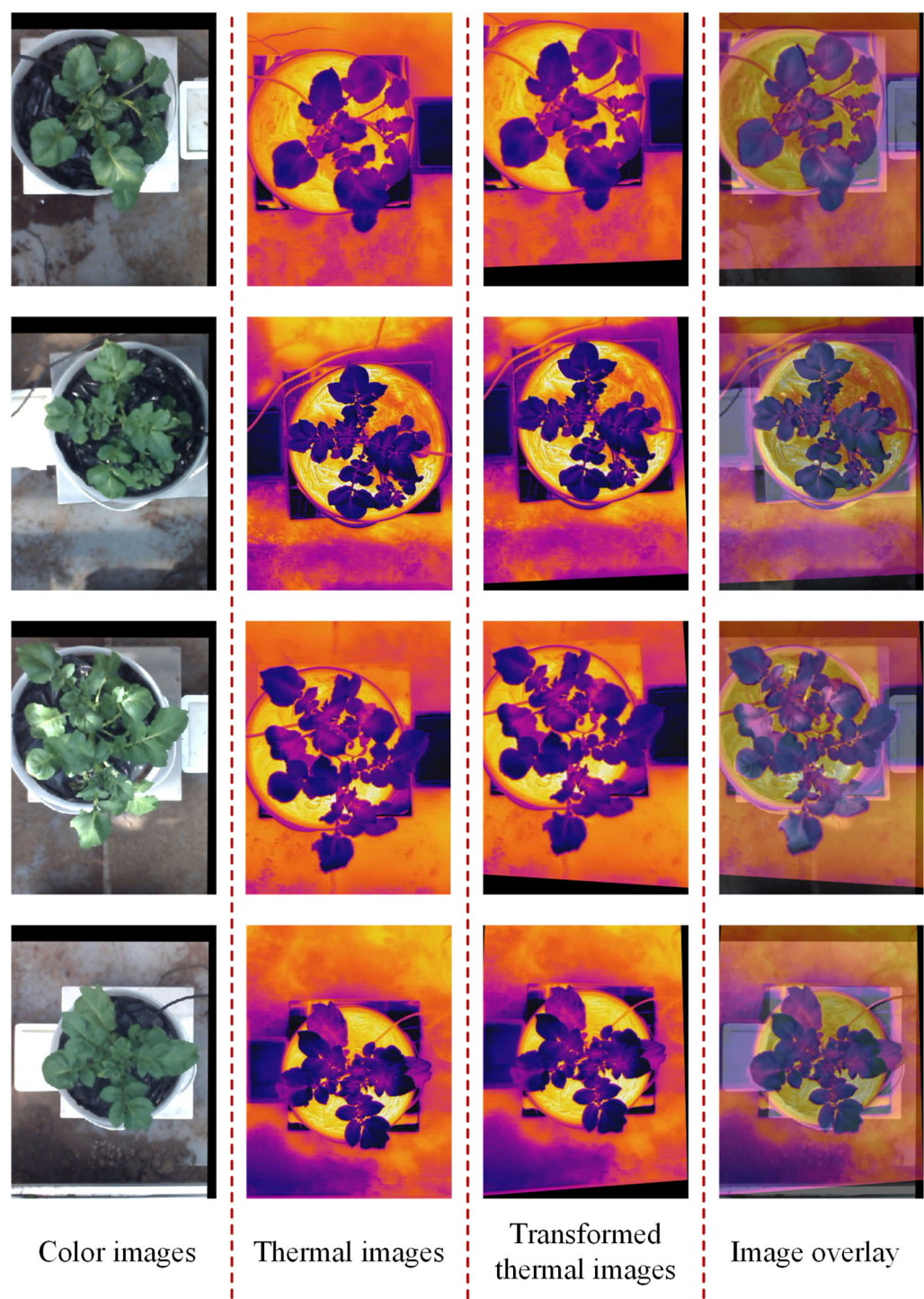


FIGURE 8
Registration results of the thermal and color images of potato plant.

the region, they will finally be filtered out by the RANSAC algorithm due to their low quality, which also caused this part of the region to be less affected by the homography transformation, as the blue circles shown in Figure 12B.

These situations resulted in some regions cannot be perfectly aligned, increasing the registration error.

As the blue circles shown in Figure 12C, it can be seen that some regions in the color and thermal images have large

TABLE 2 Homography transformation errors between color image and transformed thermal image.

Images No.	1	2	3	4	5	6	7	8	9	10
Error (pixel)	0.4	0.5	1.0	0.3	0.3	0.5	0.3	0.8	0.9	0.5
Images No.	11	12	13	14	15	16	17	18	19	20
Error (pixel)	0.3	0.6	0.7	1.0	0.7	0.5	0.4	0.3	0.6	0.6
Images No.	21	22	23	24	25	26	27	28	29	30
Error (pixel)	0.4	0.5	0.3	0.3	0.4	0.6	0.5	0.5	0.3	0.7
Bold values represent image sequences.										

TABLE 3 Control Points Error between color image and transformed thermal image.

Images No.	1	2	3	4	5	6	7	8	9	10
Control Points Error (pixel)	3.3	2.8	3.5	2.1	2.7	1.9	2.0	3.1	3.3	2.2
Images No.	11	12	13	14	15	16	17	18	19	20
Control Points Error (pixel)	1.8	3.3	3.7	3.3	4.2	2.7	4.0	2.6	2.4	1.9
Images No.	21	22	23	24	25	26	27	28	29	30
Control Points Error (pixel)	4.5	2.2	3.5	2.8	3.1	2.6	3.4	2.5	2.2	2.3
Bold values represent image sequences.										

differences in shape, and some edge regions are not absolutely overlapping. One reason for the differences was that the different resolutions of the thermal and color cameras resulted in the cropped color image not being exactly the same size as the potato plant in the thermal image. The other reason was that the thermal and binocular camera were fixed at different positions of the image acquisition module resulting in the potato plant in the captured images having different shape characteristics in some areas. Lastly, although the experiments were conducted in a relatively closed greenhouse environment, ventilation was applied during the day, causing the leaves of the potato plant to swing in the wind sometimes. The differences in the shape of the potato plants in the two images caused by all these factors lead to inevitable registration errors.

4.3 Extraction and analysis of 3D distribution of potato plant CWSI

When filtering out abnormal temperature points caused by thermal image and color image registration errors, the k-means algorithm sometimes clustered leaves and soil background points into one class, resulting in false segmentation of some leaves point clouds. This was most likely to occur in the near-ground leaves of potato plants under water stress. The near-ground potato plant leaves under water stress conditions were affected by high-temperature radiation from the soil, and their temperatures were close to or even the same as the ground temperature. When the temperature clustering method based on k-means was applied, this

part of the point clouds and the soil point clouds will be clustered into one class, resulting in the false segmentation of canopy point clouds. In this case, the method of accurately extracting the canopy point clouds needs further improvement.

The experimental period of this study was the seedling stage of potato, which was mainly the period for stem and leaf growth and root system development, and the growing amount accounted for about 1/5 of the whole growth period. Most of the leaves in this period were in the early stage of function, and various physiological activities were very vigorous. Therefore, the detection of water stress status in this period can be considered using the entire canopy. However, at the stage of tuber expansion, the growth of shoots and leaves on the ground stopped, and the growth of tuber volume and weight were the main factors. At this time, the potato is most sensitive to water and needs the most water, and the water demand accounts for more than 50% of the water demand in the whole growth period. Therefore, accurate detection of water stress status during this period directly determines tuber size and yield. During this period, the plant canopy size was large, and the leaves at different depths responded differently to water stress due to the difference in chlorophyll content and the length of the functional period. To analyze the water status of potato plant more accurately, some point clouds segmentation techniques to extract a single leaf from the PCD of the potato plant canopy can be considered. A leaf-scale-based water stress status analysis method based on the 3D motion robotic system proposed in this study will be further studied in the future.

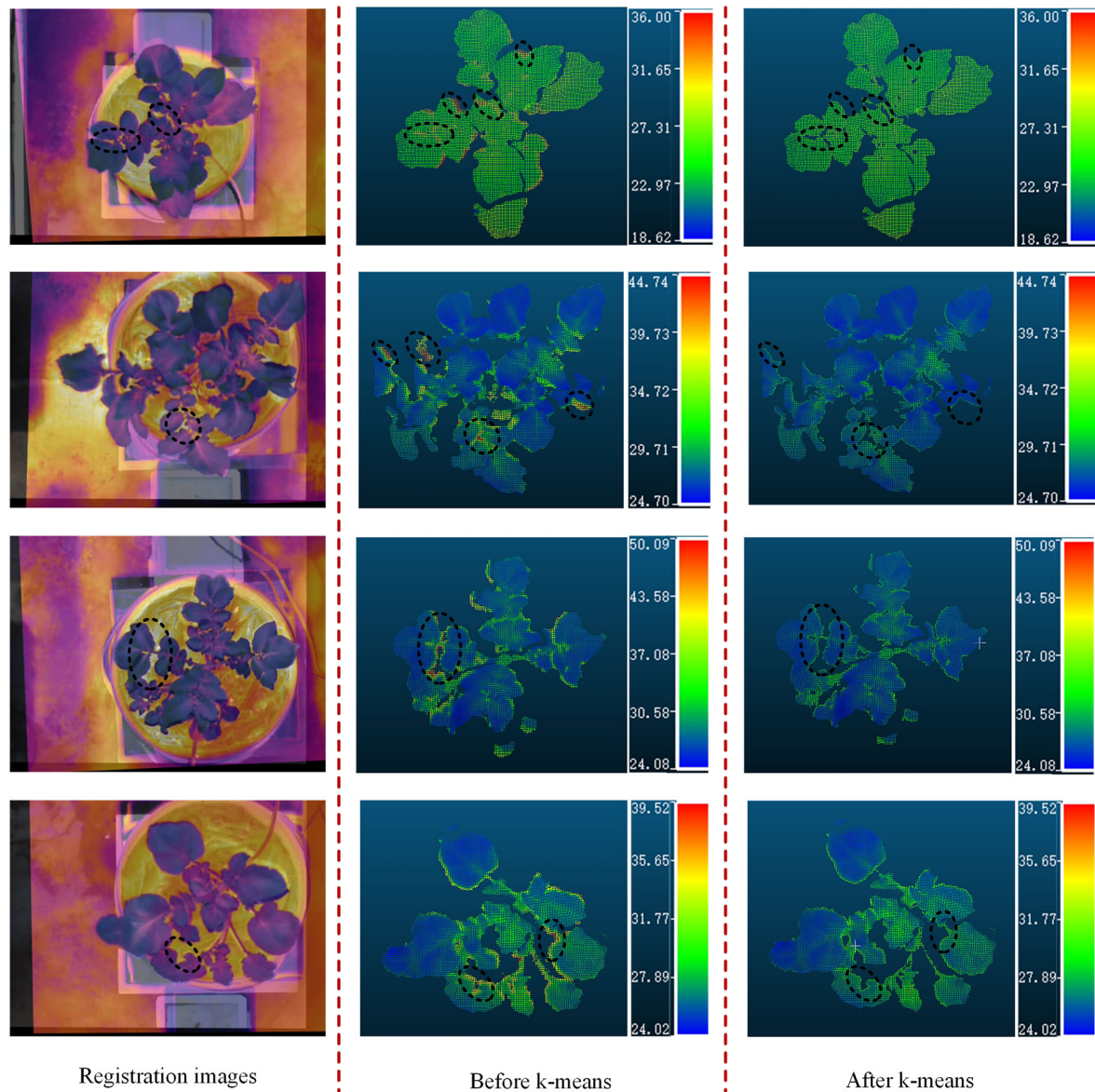


FIGURE 9

Four examples of the processed PCD of potato plant. PCD of potato plant before the k-means and the PCD of potato after the k-means. (unit: °C).

5 Conclusion

A low-cost 3D motion robotic system for automated high-throughput phenotyping detection of potato plant was developed and demonstrated in this study. The system can continuously acquire potato plant canopy image and thermal data through timing triggering, providing data support for potato plant water status analysis in both space and time scale. The efficiency of data collection using this system was much higher than that done manually.

With the help of this 3D motion robotic system platform, a cost-effective method was proposed to realize the detection of potato plant CWSI in 3D. The green canopy was extracted from a color image of potato plant based on the HSV color space, and the thermal and color images were registered using the SURF algorithm and photogrammetry. The results show that extracting the green canopy from the color image and then performing feature detection can provide more candidate point pairs for computing the homography transformation. The filtered feature points on the color images were projected as world coordinate points, and back-projected onto the thermal image, and then accuracy of these back-

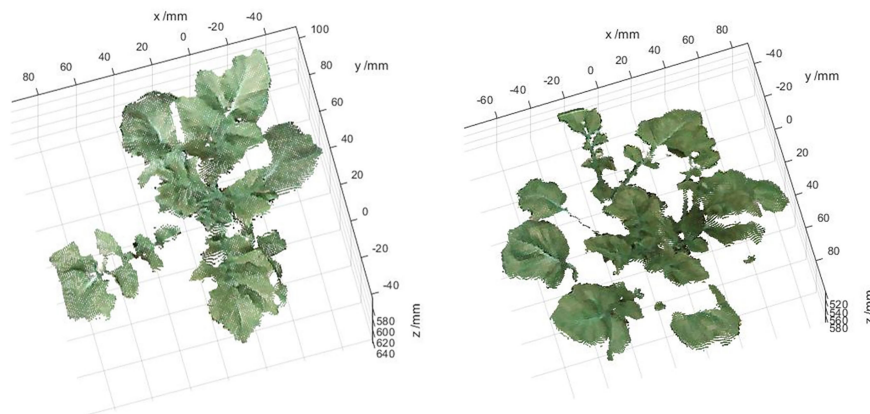


FIGURE 10

Two examples of the optimized PCD of potato plant. (unit: mm).

projected points was improved to through position-compensated method. Finally, taking the points on the thermal and left color images as input, the optimal homography transformation for each set of images was calculated by the RANSAC algorithm. The average error of the homography transformation was 0.52 pixels, and the average error of the registered control points was 2.8 pixels, indicating that the used method was suitable for registering thermal and color images of potato plants. In addition, the temperature clustering method based on k-means can effectively eliminate the

interference of background point clouds. However, for the accurate extraction of point cloud of potato plant canopy under partial water stress, the k-means algorithm needs to be further optimized to improve the segmentation accuracy.

This paper also provided a case study for 3D distribution extraction of CWSI analysis based on the provided 3D motion robotic system. By analyzing the diurnal variation and influencing factors of CWSI, data support can be provided for accurate detection of potato water stress. In the future, the performance of

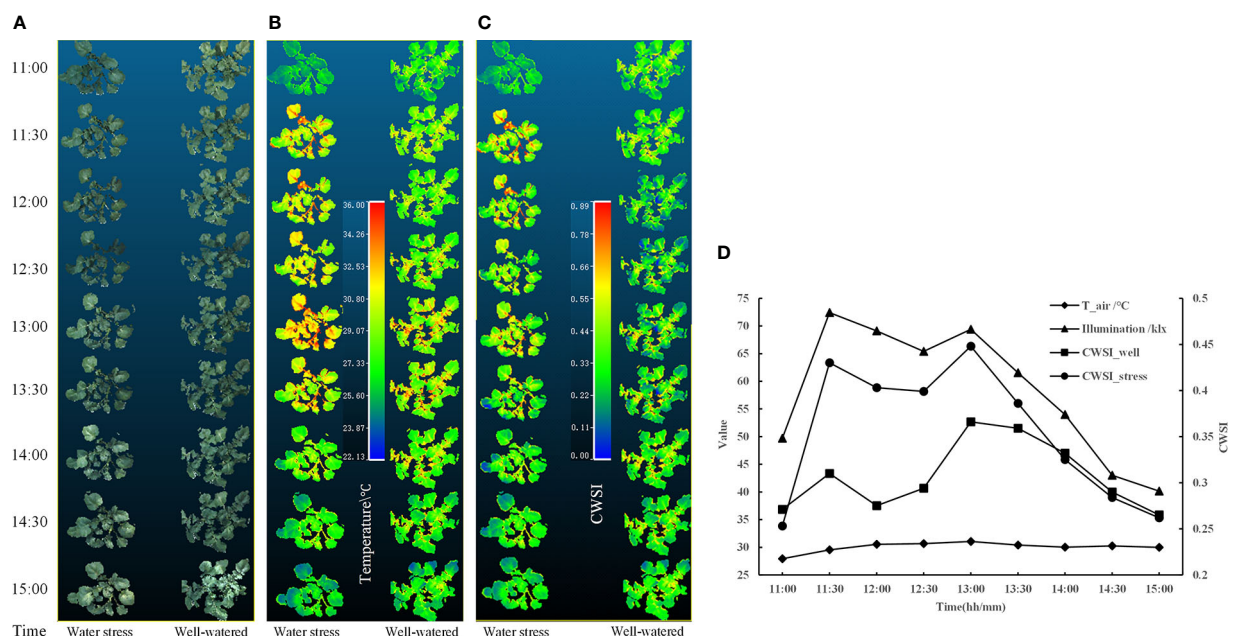


FIGURE 11

At the conditions of under well-watered and water stress, the distributions of the (A) color, (B) temperature, (C) CWSI of two potato samples in 3D, and (D) variation curves of air temperature, illumination intensity, and CWSI of two potato samples.

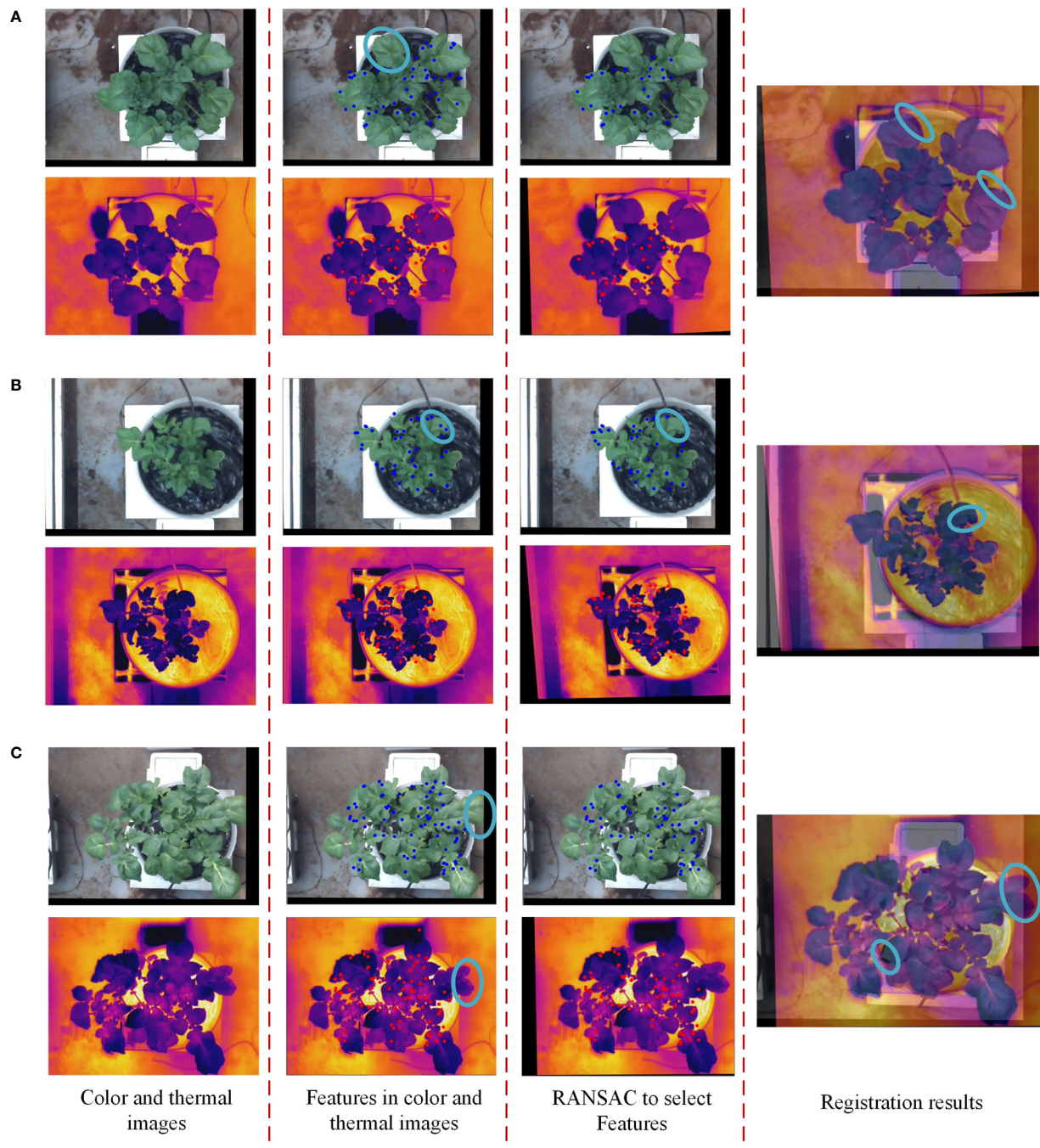


FIGURE 12

Three examples of potato plants that were not perfectly registered. (A) No feature points can be detected in the blue circled area, (B) feature points with low intensity in the blue circled region are filtered out, and (C) different plant sizes in the blue circled area..

the proposed method will be verified in different growth stages of potato. And the changing of the CWSI 3D distribution in both leaf scale and canopy scale with the continuous changing time under different water stress levels will be studied, which will provide data support for precision irrigation strategy making both in the field and in the greenhouse.

Data availability statement

The raw data supporting the conclusions of this article will be made available by the authors, without undue reservation.

Author contributions

LW and HL: Methodology, Software, Writing – original draft, Writing – review and editing. YM: Writing – review and editing. YH, CP: Performed the experimental work, and acquired data. MZ: Supervision, Writing – review and editing. All authors contributed to the article and approved the submitted version.

Funding

This work was supported by National Natural Science Foundation of China (32171893), the National Natural Science Foundation of China (31971786), and the 2115 Talent Development Program of China Agricultural University.

Acknowledgments

The authors would like to thank Dr. Ruicheng Qiu, Mr. Yida Li at China Agricultural University for their assistance in this study.

References

- Amogi, B. R., Chandel, A. K., Khot, L. R., and Jacoby, P. W. (2020). "A mobile thermal-RGB imaging tool for mapping crop water stress of grapevines," in *2020 IEEE International Workshop on Metrology for Agriculture and Forestry (MetroAgriFor)*. p. 293–297. doi: 10.1109/MetroAgriFor50201.2020.9277545
- Cucho-Padin, G., Rinza, J., Ninanya, J., Loayza, H., Quiroz, R., and Ramirez, D. A. (2020). Development of an open-source thermal image processing software for improving irrigation management in potato crops (*Solanum tuberosum* L.). *Sensors* 20, 472. doi: 10.3390/s20020472
- Dandridge, S., Carlier, A., Dumont, B., and Mercatoris, B. (2021). Registration and fusion of close-range multimodal wheat images in field conditions. *Remote Sens.* 13, 1380. doi: 10.3390/rs13071380
- Elsherbiny, O., Zhou, L., Feng, L., and Qiu, Z. J. (2021). Integration of visible and thermal imagery with an artificial neural network approach for robust forecasting of canopy water content in rice. *Remote Sens.* 13 (9). doi: 10.3390/rs13091785
- FAOSTAT (2020) *Food and agriculture organization of the united nations statistics division (FAOSTAT)*. Available at: <http://faostat.fao.org>.
- Gan, H., Lee, W. S., and Alchanatis, V. (2018). A photogrammetry-based image registration method for multi-camera systems – with applications in images of a tree crop. *Biosyst. Engineer.* 174, 89–106. doi: 10.1016/j.biosystemseng.2018.06.013
- Garcia-Tejero, I. F., Hernandez, A., Padilla-Diaz, C. M., Diaz-Espejo, A., and Fernandez, J. E. (2017). Assessing plant water status in a hedgerow olive orchard from thermography at plant level. *Agric. Water Manage.* 188, 50–60. doi: 10.1016/j.agwat.2017.04.004
- Gerhards, M., Rock, G., Schlerf, M., and Udelhoven, T. (2016). Water stress detection in potato plants using leaf temperature, emissivity, and reflectance. *Int. J. Appl. Earth Observation Geoinformation* 53, 27–39. doi: 10.1016/j.jag.2016.08.004
- Hamuda, E., Mc Ginley, B., Glavin, M., and Jones, E. (2017). Automatic crop detection under field conditions using the HSV colour space and morphological operations. *Comput. Electron. Agricult.* 133, 97–107. doi: 10.1016/j.compag.2016.11.021
- Huang, K. W., Li, Y. J., Suo, F. Y., and Xiang, J. (2020). "Stereo vision and mask-RCNN segmentation based 3D points cloud matching for fish dimension measurement," in *2020 39th Chinese Control Conference (CCC)*. p. 6345–6350. doi: 10.23919/CCC50068.2020.9188604
- Idso, S. B., Jackson, R. D., Pinter, P. J., Reginato, R. J., and Hatfield, J. L. (1981). Normalizing the stress-Degree-Day parameter for environmental variability. *Agr. Meteorol.* 24 (1), 45–55. doi: 10.1016/0002-1571(81)90032-7
- Jackson, R. D., Idso, S. B., Reginato, R. J., and Pinter, P. J. (1981). Canopy temperature as a crop water-stress indicator. *Water Resour. Res.* 17 (4), 1133–1138. doi: 10.1029/WR017i004p01133
- Jones, H. G. (1999). Use of thermography for quantitative studies of spatial and temporal variation of stomatal conductance over leaf surfaces. *Plant Cell Environ.* 22 (9), 1043–1055. doi: 10.1046/j.1365-3040.1999.00468.x
- Jones, H. G., Stoll, M., Santos, T., Sousa, C. D., Chaves, M. M., and Grant, O. M. (2002). Use of infrared thermography for monitoring stomatal closure in the field: application to grapevine. *J. Exp. Bot.* 53 (378), 2249–2260. doi: 10.1093/jxb/erf083
- Kipp, S., Mistele, B., Baresel, P., and Schmidhalter, U. (2014). High-throughput phenotyping early plant vigour of winter wheat. *Eur. J. Agron.* 52, 271–278. doi: 10.1016/j.eja.2013.08.009
- Lagueta, S., Armesto, J., Arias, P., and Herraez, J. (2012). Automation of thermographic 3D modelling through image fusion and image matching techniques. *Automat. Constr.* 27, 24–31. doi: 10.1016/j.autcon.2012.05.011
- Li, L., Chen, S. W., Yang, C. F., Meng, F. J., and Sigrimis, N. (2020). Prediction of plant transpiration from environmental parameters and relative leaf area index using the random forest regression algorithm. *J. Cleaner Production* 261. doi: 10.1016/j.jclepro.2020.121136
- Maes, W. H., Baert, A., Huete, A. R., Minchin, P. E. H., Snelgar, W. P., and Steppe, K. (2016). A new wet reference target method for continuous infrared thermography of vegetations. *Agric. For. Meteorology*. 226, 119–131. doi: 10.1016/j.agrformet.2016.05.021
- Maes, W. H., and Steppe, K. (2012). Estimating evapotranspiration and drought stress with ground-based thermal remote sensing in agriculture: a review. *J. Exp. Botany*. 63 (13), 4671–4712. doi: 10.1093/jxb/ers165
- Ma, T. H., Li, L., Ji, S., Wang, X., Tian, Y., Al-Dhelaan, A., et al. (2014). Optimized laplacian image sharpening algorithm based on graphic processing unit. *Physica A*. 416, 400–410. doi: 10.1016/j.physa.2014.09.026

Conflict of interest

The authors declare that the research was conducted in the absence of any commercial or financial relationships that could be construed as a potential conflict of interest.

Publisher's note

All claims expressed in this article are solely those of the authors and do not necessarily represent those of their affiliated organizations, or those of the publisher, the editors and the reviewers. Any product that may be evaluated in this article, or claim that may be made by its manufacturer, is not guaranteed or endorsed by the publisher.

Supplementary material

The Supplementary Material for this article can be found online at: <https://www.frontiersin.org/articles/10.3389/fpls.2022.1104390/full#supplementary-material>

SUPPLEMENTARY VIDEO 1

The workflow of the 3D motion robotic system.

- Meron, M., Sprintsins, M., Tsipris, J., Alchanatis, V., and Cohen, Y. (2013). Foliage temperature extraction from thermal imagery for crop water stress determination. *Precis. Agricult.* 14 (5), 467–477. doi: 10.1007/s11119-013-9310-0
- Narvaez, F. J. Y., del Pedregal, J. S., Prieto, P. A., Torres-Torriti, M., and Cheein, F. A. A. (2016). LiDAR and thermal images fusion for ground-based 3D characterisation of fruit trees. *Biosyst. Engineer.* 151, 479–494. doi: 10.1016/j.biosystemseng.2016.10.012
- Obidiegwu, J. E., Bryan, G. J., Jones, H. G., and Prashar, A. (2015). Coping with drought: stress and adaptive responses in potato and perspectives for improvement. *Front. Plant Sci.* 6. doi: 10.3389/fpls.2015.00542
- Pereyra-Irujo, G. A., Gasco, E. D., Peirone, L. S., and Aguirrez Bal, L. A. N. (2012). Glyph: a low-cost platform for phenotyping plant growth and water use. *Funct. Plant Biol.* 39 (11), 905–913. doi: 10.1071/FP12052
- Philipp, I., and Rath, T. (2002). Improving plant discrimination in image processing by use of different colour space transformations. *Comput. Electron. Agricult.* 35 (1), 1–15. doi: 10.1016/S0168-1699(02)00050-9
- Poirier-Pocovi, M., Volder, A., and Bailey, B. N. (2020). Modeling of reference temperatures for calculating crop water stress indices from infrared thermography. *Agric. Water Manage.* 233, 106070. doi: 10.1016/j.agwat.2020.106070
- Prashar, A., and Jones, H. G. (2016). Assessing drought responses using thermal infrared imaging. *Methods Mol. Biol.* 1398, 209–219. doi: 10.1007/978-1-4939-3356-3_17
- Prashar, A., Yildiz, J., McNicol, J. W., Bryan, G. J., and Jones, H. G. (2013). Infra-red thermography for high throughput field phenotyping in solanum tuberosum. *PLoS One* 8 (6), e65816. doi: 10.1371/journal.pone.0065816
- Qiu, R. C., Miao, Y. L., Zhang, M., and Li, H. (2021). Detection of the 3D temperature characteristics of maize under water stress using thermal and RGB-d cameras. *Comput. Electron. Agric.* 191. doi: 10.1016/j.compag.2021.106551
- Qiu, R. C., Wei, S., Zhang, M., Li, H., Sun, H., Liu, G., et al. (2018). Sensors for measuring plant phenotyping: A review. *Int. J. Agr. Biol. Eng.* 11 (2), 1–17. doi: 10.25165/ijabe.20181102.2696
- Rossi, R., Costafreda-Aumedes, S., Leolini, L., Leolini, C., Bindi, M., and Moriondo, M. (2022). Implementation of an algorithm for automated phenotyping through plant 3D-modeling: A practical application on the early detection of water stress. *Comput. Electron. Agric.* 197, 1–15. doi: 10.1016/j.compag.2022.106937
- Rud, R., Cohen, Y., Alchanatis, V., Levi, A., Brikman, R., Shenderey, C., et al. (2014). Crop water stress index derived from multi-year ground and aerial thermal images as an indicator of potato water status. *Precis. Agricult.* 15 (3), 273–289. doi: 10.1007/s11119-014-9351-z
- Sun, H., Liu, N., Wu, L., Zheng, T., Li, M. Z., and Wu, J. S. (2019). Visualization of water content distribution in potato leaves based on hyperspectral image. *Spectrosc. Spectral Analysis* 39 (03), 910–916. doi: 10.3964/j.issn.1000-0953(2019)03-0910-07
- Sun, H., Zheng, T., Liu, N., Cheng, M., Li, M. Z., and Zhang, Q. (2018). Vertical distribution of chlorophyll in potato plants based on hyperspectral imaging. *Trans. Chin. Soc. Agric. Engineer.* 34 (01), 149–156. doi: 10.11975/j.issn.1002-6819.2018.01.020
- Tkalcic, M., and Tasic, J. F. (2003). “Colour spaces: Perceptual, historical and applicational background,” in *The IEEE Region 8 EUROCON 2003. Computer as a Tool*. 1, 304–308. doi: 10.1109/EURCON.2003.1248032
- Wolf, P. R., Dewitt, B. A., and Wilkinson, B. E. (2014). *Elements of photogrammetry with applications in GIS, fourth edition. ed* (New York: McGraw-Hill Education). Available at: <https://www.accessengineeringlibrary.com/content/book/9780071761123>.
- Xie, R. D., Yang, H. C., Yi, Y. M., Shi, Q. M., Wang, K. Y., and Fan, X. L. (2020). Volume measuring method for forming additive manufacturing based on SGBM. *Chin. Autom. Congr.* 2020, 129–132. doi: 10.1109/Cac51589.2020.9327209
- Yang, M. D., Su, T. C., and Lin, H. Y. (2018). Fusion of infrared thermal image and visible image for 3D thermal model reconstruction using smartphone sensors. *Sensors* 18, 2013. doi: 10.3390/s18072003
- Zhang, C. Y., Gao, H. H., Zhou, J. F., Cousins, A., Pumphrey, M. O., and Sankaran, S. (2016). 3D robotic system development for high-throughput crop phenotyping. *Ifac Papersonline*. 49 (16), 242–247. doi: 10.1016/j.ifacol.2016.10.045



OPEN ACCESS

EDITED BY

Leizi Jiao,
Beijing Academy of Agriculture and
Forestry Sciences, China

REVIEWED BY

Jiangbo Li,
Beijing Academy of Agriculture and
Forestry Sciences, China
Jinming Pan,
Zhejiang University, China

*CORRESPONDENCE

Huishan Lu,
✉ 13934597379@139.com

SPECIALTY SECTION

This article was submitted to
Optics and Photonics,
a section of the journal
Frontiers in Physics

RECEIVED 08 January 2023

ACCEPTED 09 February 2023

PUBLISHED 22 February 2023

CITATION

Wang F, Cui J, Xiong Y and Lu H (2023),
Application of deep learning methods in
behavior recognition of laying hens.
Front. Phys. 11:1139976.
doi: 10.3389/fphy.2023.1139976

COPYRIGHT

© 2023 Wang, Cui, Xiong and Lu. This is
an open-access article distributed under
the terms of the [Creative Commons
Attribution License \(CC BY\)](#). The use,
distribution or reproduction in other
forums is permitted, provided the original
author(s) and the copyright owner(s) are
credited and that the original publication
in this journal is cited, in accordance with
accepted academic practice. No use,
distribution or reproduction is permitted
which does not comply with these terms.

Application of deep learning methods in behavior recognition of laying hens

Fujie Wang, Jiquan Cui, Yingying Xiong and Huishan Lu*

School of Mechanical Engineering, North University of China, Taiyuan, China

Poultry behaviors reflect the health status of poultry. For four behaviors of laying hens, such as standing, lying, feeding, and grooming, four deep learning methods for recognition were compared in this paper, as Efficientnet-YoloV3, YoloV4-Tiny, YoloV5, and Faster-RCNN. First, the behavior detection dataset was produced based on the monitoring video data. Then, four algorithms, Efficientnet-YoloV3, YoloV4-Tiny, YoloV5, and Faster-RCNN, were used for training respectively. Finally, using the validation set for recognition, we got the mAP values for the four algorithms: Efficientnet-YoloV3 had mAP values of 81.82% (standing), 88.36% (lying), 98.20% (feeding), 77.30% (grooming), and its FPS values were 9.83 in order; YoloV4-Tiny had mAP values of 65.50% (standing), 78.40% (lying), 94.51% (feeding), 62.70% (grooming), and their FPS values were 14.73 successively; YoloV5 had mAP values of 97.24% (standing), 98.61% (lying), 97.43% (feeding), 92.33% (grooming), and their FPS values were 55.55 successively; Faster-RCNN had mAP values were 95.40% (standing), 98.50% (lying), 99.10% (feeding), and 85.40% (grooming), and their FPS values were 3.54 respectively. The results showed that the YoloV5 algorithm was the optimal algorithm among the four algorithms and could meet the requirements for real-time recognition of laying hens' behavior.

KEYWORDS

behavior detection, deep learning, poultry behaviors, faster-RCNN, YoloV5

1 Introduction

With the increasing demand for poultry meat and eggs, the poultry farming industry is rapidly developing towards industrialization and scale. The information level of modern poultry breeding has been continuously improved and enhanced [1]. The welfare level of poultry under large-scale breeding has gradually attracted the attention of various countries [2], and standardized farming conditions have been proposed in various countries to improve the welfare level of poultry breeding [3]. There are many factors affecting the welfare breeding of poultry. The significant issue is the factor of the breeding environment [4], and the behavioral information of poultry can be a good reflection of the welfare level and health status of poultry.

Traditional manual observation and statistics of poultry behavior are easily influenced by farmers' experience, time-consuming, and easy to miss detection. With the development of science and technology, artificial intelligence breeding and non-invasive precision breeding technology have gradually emerged [5, 6]. Artificial intelligence breeding has good potential in solving poultry behavior detection. The combination of sensor and AI model-driven to well detect poultry behavior [5], and sensor monitoring for harmless sensing of poultry behavior, image monitoring, and

sound monitoring technologies are also widely used in the poultry breeding industry [6]. The application of the Internet of Things and data analysis in monitoring the welfare of chickens on poultry farms was studied using radio frequency identification (RFID) technology [7]. RFID transponders were attached to chicken legs to compose feedback with weighing sensors to establish an automatic monitoring system for identifying poultry roosting behavior [8]. It is difficult to assess behavioral changes in chickens when humans are present, and the use of an Internet-based camera to monitor and record chicken behavior can be effective in assessing the level of chicken welfare [9]. The monitoring adaptability of different vision systems and image processing algorithms for poultry activity on breeding farms was tested [10]. The study proposed machine vision to test broiler health, which allows early warning and prediction of broiler disease [11]. The sound of poultry eating has obvious differences from normal vocalization and based on the analysis of the combination of timbre and time change, there are proposed 3 types of poultry feeding vocal networks, which were experimentally tested for a high recognition rate [12]. Researchers experimented on the relationship between animal vocalization and body weight, and the results showed that the method can be used for early warning [13]. The monitoring analysis of nocturnal vocalizations of poultry can provide a practical method for poultry abnormal status judgment [14]. With the development of the computer vision method of Convolutional Neural Network (CNN), deep learning computer vision analysis has been continuously used for behavior detection of animals to improve the welfare level of rural animals [15]. The pose analysis of broilers is the basis of poultry behavior prediction. The deep neural network is used for pose research, and the Naive Bayes model (NBM) is used to classify and identify the pose of broilers. The experimental method has a high recognition accuracy for the pose of broilers [16]. Deep learning models of convolutional neural networks (CNN) were used to identify rumination behavior in cattle [17]. The researchers used a convolutional neural network (CNN) to extract the feeding features of pigs, used an image processing algorithm to determine the situation of pigs and the feeding areas, and identify the feeding time of single pigs [18]. The researchers proposed the use of convolutional neural networks to identify three important activities in sheep and demonstrate the importance of the method in the case of data capture, and data tagging [19]. Experts used a deep convolutional neural network to detect the walking key points of broilers, and the extracted key point information is input into the model for classification, and the model provided an effective detection method for the clinical symptoms of claudication in poultry [20]. The Kinect sensor combined with the convolutional neural network approach was effective in identifying the behavior of chickens [21]. Yolo detection models are also commonly used in animal behavior recognition. The researchers used the deep learning model YoloV3 to identify six behaviors of laying hens and analyzed the frequency of each behavior [22]. Comparison of the training detection of the deep learning model YoloV4 with YoloV5 provided data support for poultry embryo detection [23]. Researchers trained and tested the YoloV5 deep learning model to identify domesticated chickens, using the Kalman filter

principle to propose a model to track multiple chickens, and thus improve the welfare level of chickens in animal breeding [24].

In order to achieve the real-time accurate identification of the behavior of the laying layer, this paper analyzed and compared through different first-and second-order target detection algorithms, which better verified the applicability of the target detection algorithm for poultry behavior identification and provided experimental support for further real-time monitoring of poultry health.

2 Materials and methods

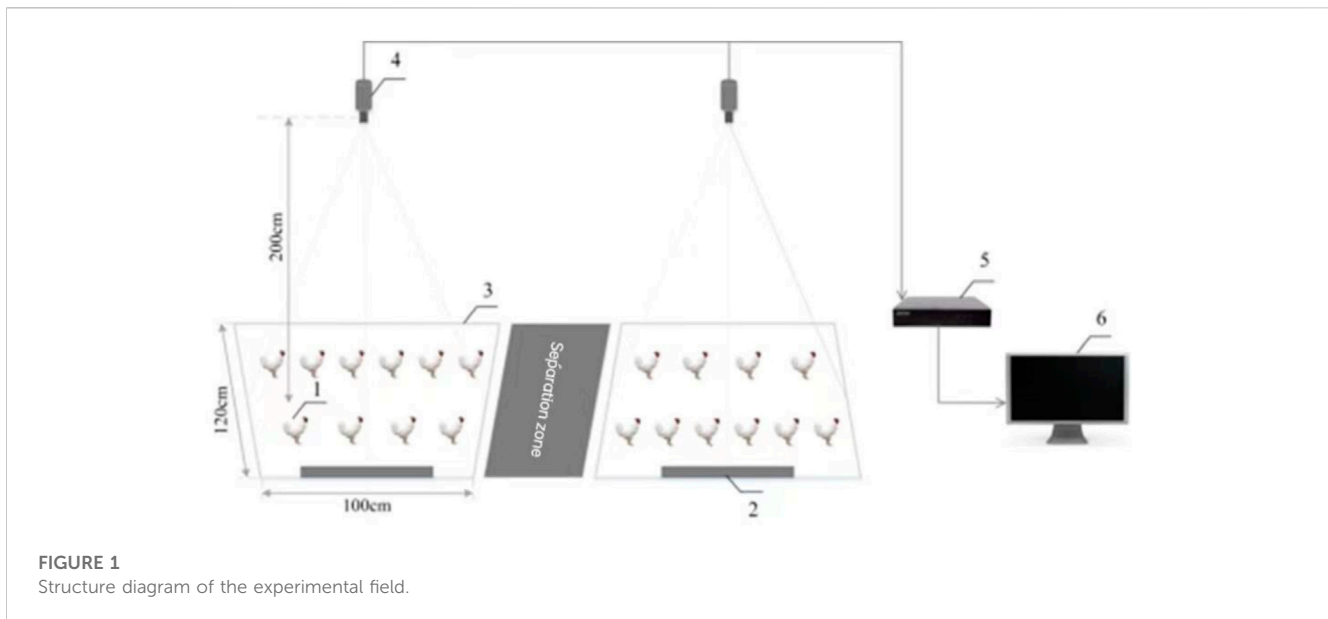
2.1 Experimental environment

The experiment was conducted at Huixin Breeding Co., LTD., Lingqiu County, Datong City, Shanxi Province. The white-green-shell laying hens in the chicken house were pure white, 7 weeks of age, and their body weight was 750 g–1100 g. During the experiment, two 100 cm × 120 cm × 150 cm wire mesh fences were built in the chicken house. The feed trough was fixed on the long side of the fence, and 1/3 of the trough was for drinking and the remaining 2/3 was for feeding. The fence is 15 cm above the ground to facilitate the cleaning of manure on the ground, and a webcam is installed 200 cm from the center of the fence. The camera is connected to the hard disk video recorder to record and save experimental videos, and a monitor is connected to facilitate observation. Ten white-green-shelled hens are placed in each enclosure. The laying hens are kept with natural lighting inside, with vents and a temperature and hygrometer inside, to keep the chicken house comfortable. The structure diagram of the experimental field is shown in Figure 1.

2.2 Data processing and labeling

The experiment was recorded by Hikvision webcam with an image resolution of 1920 × 1,080 and a frame rate of 25 fps. The recording time was set at 7:00–22:00 per day, the experiment was conducted for 15 days, and the video files in the hard disk video recorder were sorted and saved daily. After the experiment, VSPlayer software was used to intercept the content in the video to obtain suitable single-frame pictures, and 1,500 pictures with different light intensities were selected. The selected images were labeled using the Labellmg software to generate files in XML format. Four behaviors were labeled as eating, standing, lying, and grooming. After the labeling was completed: eating (2,800), lying (5,000), standing (3,000), and grooming (600) were obtained. The data set was divided into validation sets and training sets in a 1: 9 ratio.

The computer system used for this experiment was Windows 10 Home Edition system Intel (R) Core (TM) i7-10750H CPU @ 2.60 GHz 2.59 GHz processor with 16G RAM and NVIDIA GeForce GTX 1650Ti graphics card. Installed the Anaconda3 version loaded with Python 3.7 environment, trained and predicted the algorithm on PyCharm integrated development environment. The epoch of all four object detection algorithms was 300, and the optimal training weight in each algorithm was finally selected for prediction. Both



Efficientnet-YoloV3 and YoloV4-tiny algorithms were trained 100 times, with an uninterrupted training process, the batch size is 8, and the thawing training batch size is 4, using 4 threads. The Faster-RCNN algorithm is complex and occupies large memory, the epoch of freezing training is set to 50, batch size to 4, and the batch size of thawing training is 2, trained using 2 threads. The batch size of the YoloV5 algorithm was set to 4 and 4 threads are used for training.

2.3 Algorithmic network structure

In this paper, four target detection algorithms are used, and three first-order target detection algorithms, namely, Efficientnet-YoloV3, YoloV4-tiny, and YoloV5. The second-order target detection algorithm is Faster-RCNN. The first-order algorithm directly locates the target border to do regression processing, while the second-order algorithm generates sample candidate frames for convolution classification processing. Among the two algorithms, the first-order algorithm has the advantage of high detection speed, while the second-order algorithm has high detection accuracy. In this paper, in order to realize real-time detection of laying hens' behavior, a faster algorithm is needed, so a variety of first-order algorithms are selected; at the same time, second-order algorithms are selected to compare and verify the detection accuracy of first-order algorithms.

2.3.1 Efficientnet-YoloV3

The YoloV3 algorithm has made some improvements on the basis of YoloV1 and YoloV2, which in turn improves its detection speed and has an outstanding performance in small object detection [25]. The backbone feature extraction network of YoloV3 is Darknet53, which contains a residual structure. The convolution of multiple residual structures in the Darknet53 network deepens the network and improves detection accuracy. The FPN (Feature Pyramid) structure strengthens the feature extraction of the three feature layers after the

convolution of the backbone feature network to obtain these three effective feature layers, and finally predict the three effective feature layers. In the Efficientnet-YoloV3 detection algorithm, the main purpose is to change the backbone feature extraction network to the Efficientnet model. Efficient net is an efficient and small-parameter model proposed by Google, which improves the efficiency of detection while retaining detection accuracy. The Efficientnet model consists of the Stem part for preliminary feature extraction, the Blocks part for further extraction, and the classification head. The Efficientnet-YoloV3 network structure is shown in Figure 2.

2.3.2 YoloV4-tiny

The YoloV4 target detection algorithm is improved based on YoloV3 [26]. The main improvements are: the backbone feature extraction network YoloV4 uses the CSPDarkNet53 structure, the activation function in the backbone network is replaced by the Mish function from YoloV3's LeakyReLU, while the CSPnet structure is also used in the backbone network to optimize the residual structure. The feature pyramid uses the SPP and PANet structures, The SPP structure performs the maximum pooling operation on the features extracted from the backbone at four different scales to increase the perceptual field, and the PANet structure extracts the features from top to bottom after SPP processing to achieve iterative feature, boosted and enhanced the feature structure of the feature layer. The YoloV4-tiny is simplified based on the YoloV4 structure, and the partial structure is deleted to improve the detection speed of the target detection algorithm. In the YoloV4-tiny structure, the deleted CSPDarkNet53-tiny structure is used to replace the activation function with LeakyReLU to increase the operation speed. Firstly, we perform the second convolution to compress the image, obtain the effective feature layer through the Resblock-body residual structure, and finally obtain the effective feature layer of two arrays, and use a feature pyramid structure for the effective features extracted by the backbone after convolution, the last sample is convolved with the last array. The CSPnet network structure is shown in Figure 3.

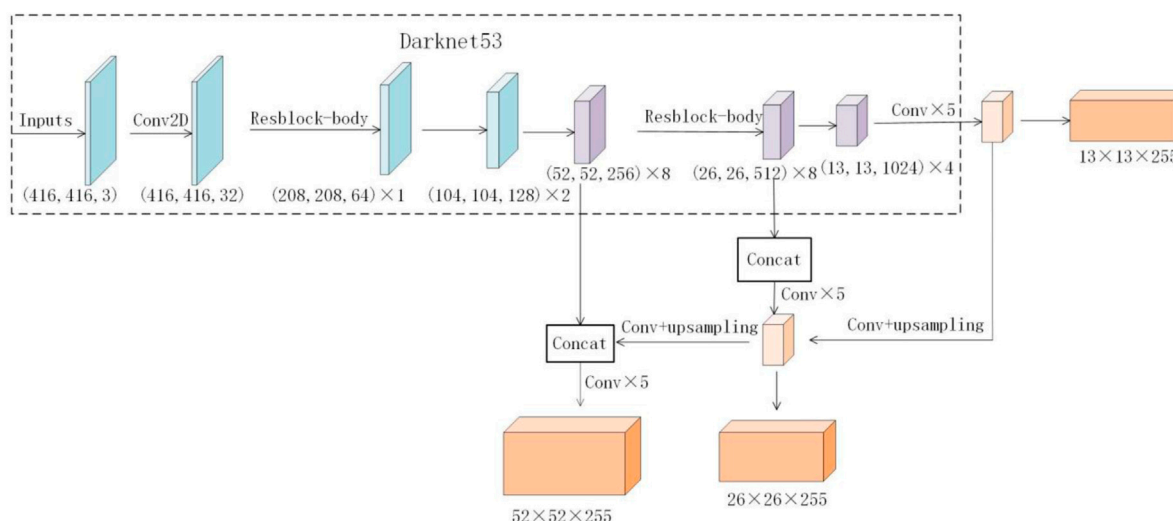


FIGURE 2
Efficientnet-YoloV3 network structure.

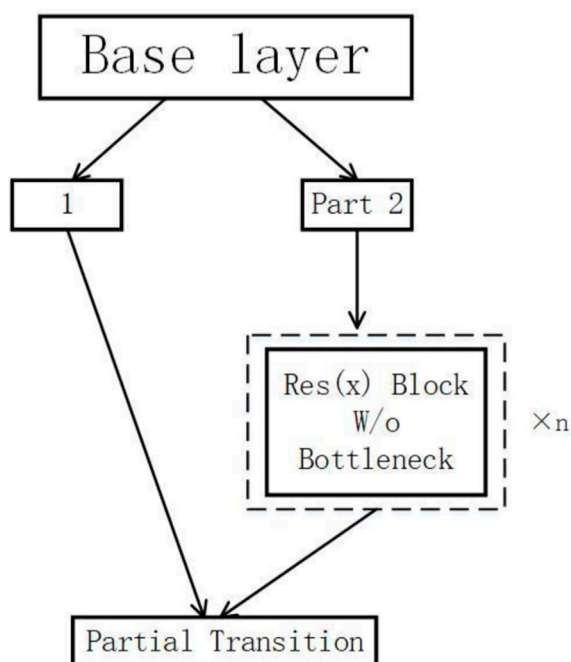


FIGURE 3
CSPnet network structure.

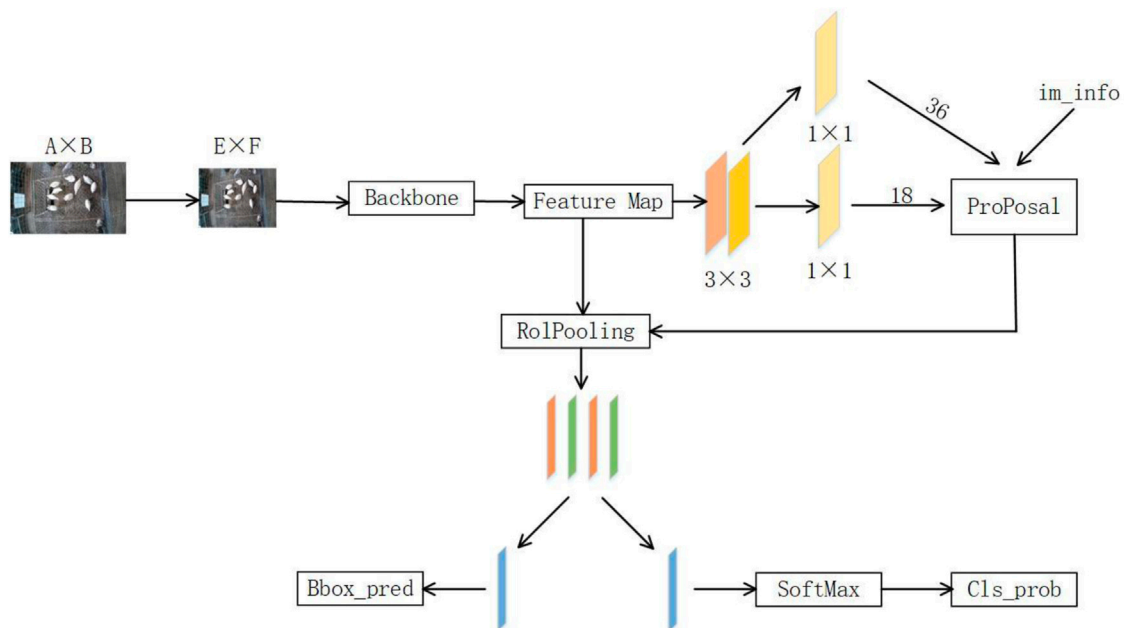
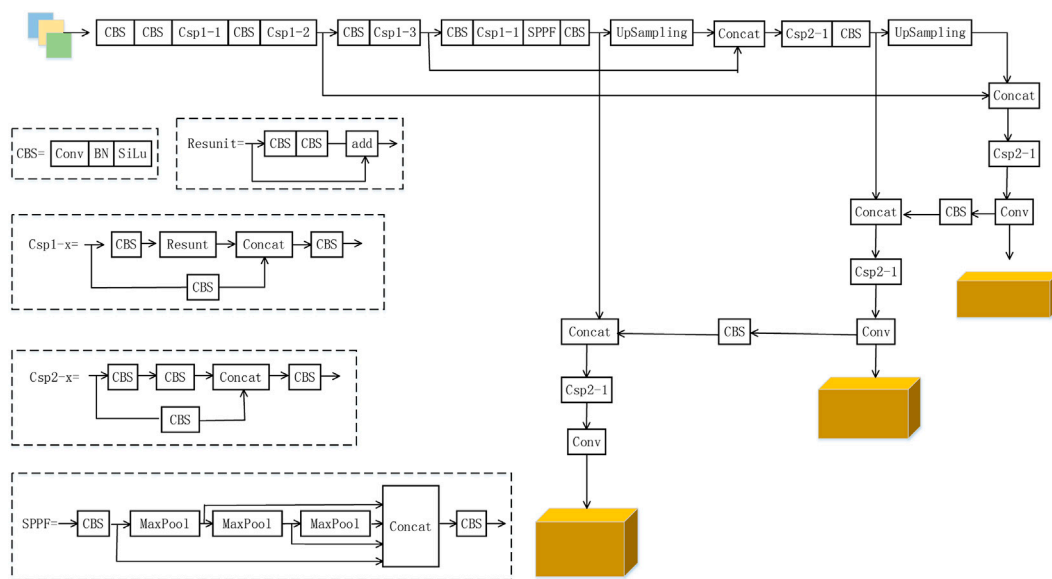
2.3.3 YoloV5

In this paper, version 6.0 of YoloV5 is used for training and prediction during the experiments [27]. The network results of YoloV5 mainly consist of four structures: the input side, Backbone, Neck, and Prediction. The input side, like YoloV4, uses the data enhancement function, which can be adjusted by modifying program parameters. The data enhancement is mainly to re-stitch the randomly scaled, cropped, or arranged

images to improve the robustness and generalization of the network training. Meanwhile, the input side of YoloV5 integrates the initial anchor frame algorithm directly into the program to realize adaptive calculation. The YoloV5's Backbone (backbone network) consists of the Focus structure and the CSP structure while using the more effective SiLU activation function. The Focus structure mainly performs a slicing operation on the input picture, compressing the length and width of the picture to increase the number of channels. The CSP structure is also used in YoloV5, one is the CSP1_X structure in the Backbone, and the other is the CSP2_X structure in the Neck. The FPN + PAN structure is used in constructing the construction feature pyramid structure, while the SPP structure used in YoloV4 is directly applied to the backbone feature extraction network. The YoloV5 network structure is shown in Figure 4.

2.3.4 Faster-RCNN

The second-order algorithm has high detection accuracy and has a good effect on small target detection. The Faster-RCNN in the second-order algorithm is selected for training and testing to compare with the test results of various Yolo algorithms [28]. The Faster-RCNN algorithm consists of four parts: conv layers (backbone feature extraction), RPN network, ROI Pooling structure, and Classification and regression (classification and regression). Faster-RCNN has multiple backbone feature extraction networks, and this paper uses Resnet50 as the backbone network, which contains two residual structure blocks, Conv Block and identity Block. The common feature layer acquired by the backbone feature network has two functions. One is to generate a check box after the RPN structure, and the other is to act on the ROI Pooling structure to obtain the feature layer of the same size and send the results to the full connected layer for classification and regression. The Faster-RCNN network structure is shown in Figure 5.



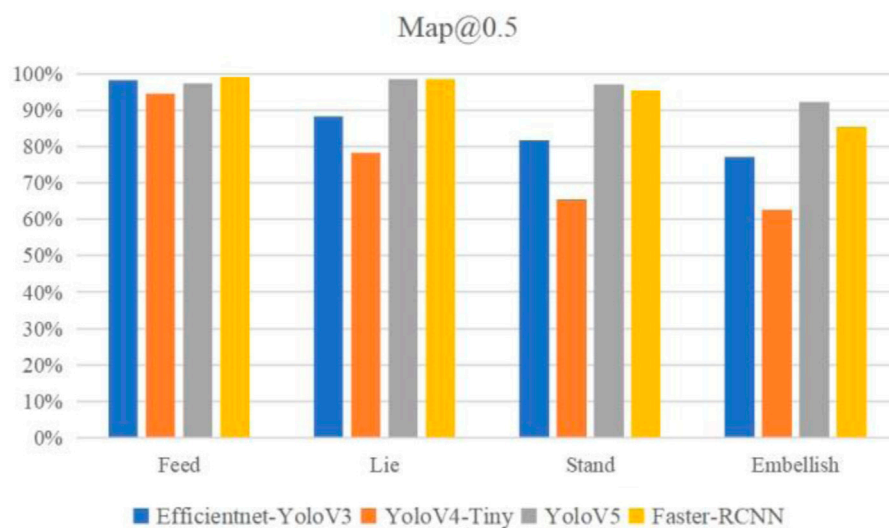


FIGURE 6

Map comparison diagram of different behaviors.

TABLE 1 Comparison of Map values of different algorithms.

Behavior	Feed	Lie	Stand	Embellish
Algorithm				
Efficientnet-YoloV3	0.982	0.8836	0.8182	0.773
YoloV4-Tiny	0.9451	0.784	0.655	0.627
YoloV5	0.9743	0.9861	0.9724	0.9233
Faster-RCNN	0.991	0.985	0.954	0.854

$$\text{Recall} = \frac{TP}{TP + FN} \quad (2)$$

$$\text{Accuracy} = \frac{TP + TN}{TP + FN + FP + TN} \quad (3)$$

$$F_1\text{score} = \frac{2 \times \text{Precision} \times \text{Recall}}{\text{Precision} + \text{Recall}} \quad (4)$$

In the formula, TP (True Positives) means that the sample is determined as positive and correct, TN (True Negatives) means that the sample is determined as negative and correct, and FP (False Positives) means that the sample is determined as positive but incorrect. FN (False Negatives) means that the sample is judged negative but incorrect. Precision refers to the ratio of the number of correctly determined positive samples to the total number of determined positive samples, Recall (recall) refers to the ratio of the number of correctly determined positive samples to the total number of determined positive samples, the average of mAP (mean Average Precision), the calculation method uses the difference average, that is, the area under the Precision-Recall curve.

After the experimental training, the evaluation file was generated, and the nms_iou used for non-maximum inhibition was set to 0.5 to obtain the evaluation indexes of the four

algorithms. The following Figure 6 shows the results diagram of the various algorithms at mAP@0.5, and the detailed data analysis is shown in Table 1.

The following Figure 7 and Table 2 show the comparison of the Precision of the four different algorithms. Which shows the detection accuracy of each type of algorithm after training under different behaviors of laying hens.

The following Figure 8 and Table 3 show the comparison of the four different algorithms Recall (recall).

After the comparison of the evaluation indicators, the pictures of the layers in two different environments of day and night were selected and verified by different target detection algorithms, and the results are shown in Figure 9. Figure (A) to Figure (D) verifies the behavior of a laying hen in the daytime environment using YoloV3, YoloV4, YoloV5, and Faster-RCNN respectively, and Figure (E) to Figure (H) identify a picture of a laying hen in the night environment. The identification accuracy of all kinds of algorithms can be seen in the figure below.

The experiment also compared the FPS values of various algorithms. The video images were intercepted to obtain 9 s of test video and tested using different target detection algorithms. Figure 10 shows the real-time FPS values of the different target detection algorithms, where (A) to (D) are the FPS values when detected using YoloV3, YoloV4, YoloV5, and Faster-RCNN, respectively. The results are shown in Figure 11.

4 Discussion

In this paper, four target detection algorithms of YoloV3, YoloV4, YoloV5, and Faster-RCNN were selected for the training and detection of four behaviors of laying hens. From the analysis of the three evaluation indexes selected, the YoloV5 target detection algorithm has a very good detection effect in this

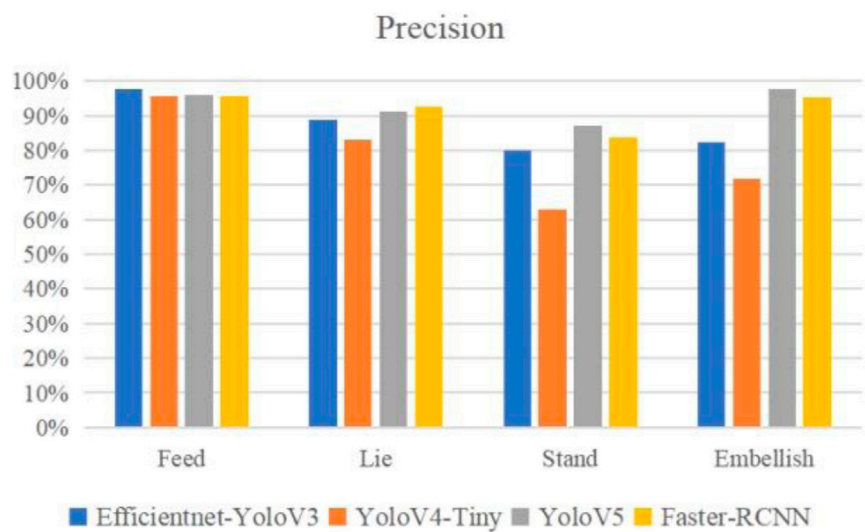


FIGURE 7
Comparison of the different algorithm Precision s for different behaviors.

TABLE 2 Comparison of Precision values of different algorithms.

Behavior	Feed	Lie	Stand	Embellish
Algorithm				
Efficientnet-YoloV3	0.9769	0.8891	0.7994	0.823
YoloV4-Tiny	0.9554	0.8289	0.6298	0.719
YoloV5	0.9612	0.9134	0.8697	0.9778
Faster-RCNN	0.9561	0.9251	0.8363	0.9524

TABLE 3 Comparison of Recall values of different algorithms.

Behavior	Feed	Lie	Stand	Embellish
Algorithm				
Efficientnet-YoloV3	0.9221	0.8369	0.7972	0.7362
YoloV4-Tiny	0.8	0.7194	0.6806	0.5463
YoloV5	0.9821	0.9815	0.9412	0.8645
Faster-RCNN	0.9778	0.9542	0.932	0.8337

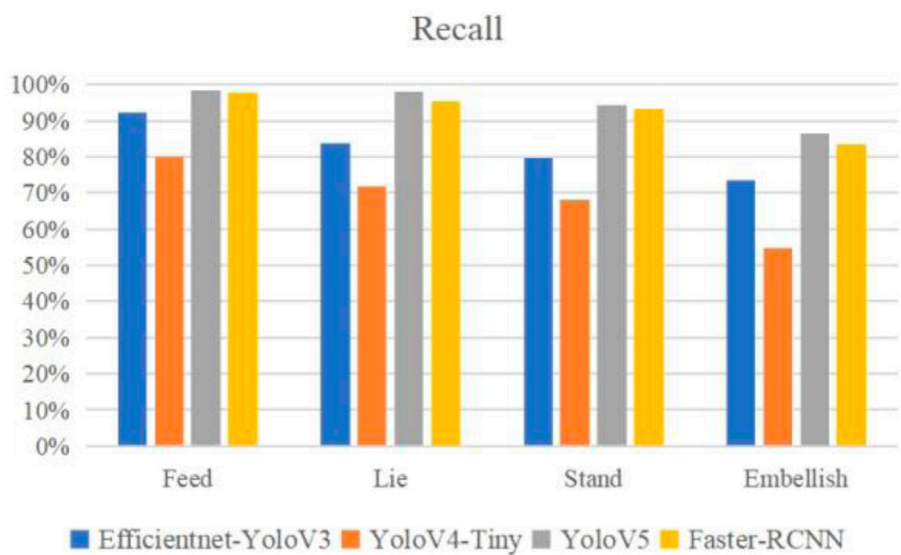


FIGURE 8
Comparison of the different algorithm Recall s for different behaviors.

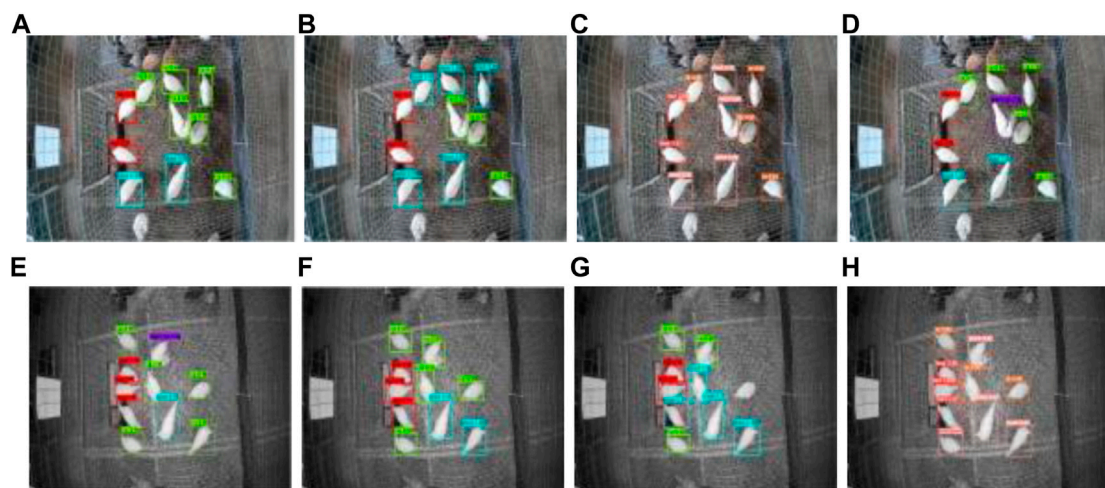


FIGURE 9
Detection effect of various algorithms in different environments (A) YoloV3 Day; (B) YoloV4 Day; (C) YoloV5 Day; (D) Faster-RCNN Day; (E) YoloV3 Night; (F) YoloV4 Night; (G) Faster-RCNN Night; (H) YoloV5 Night.

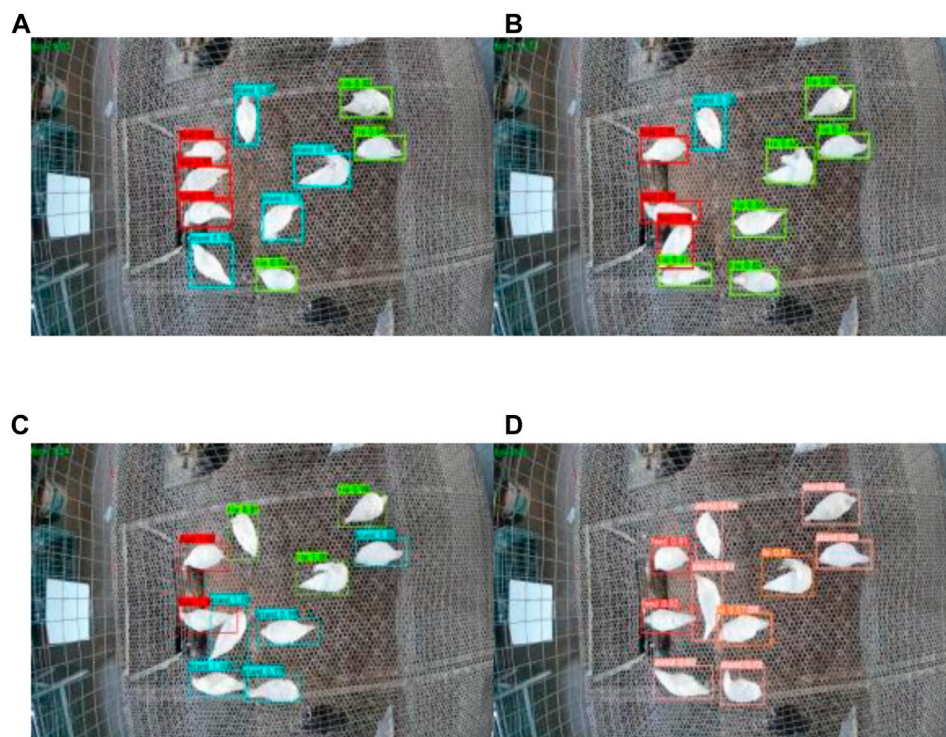


FIGURE 10
Video detection of the FPS values of various algorithms (A) YoloV3 FPS; (B) YoloV4 FPS; (C) Faster-RCNN FPS; (D) YoloV5 FPS.

experiment. From Figure 6, the Map value of YoloV5 is significantly higher than that of YoloV3 and YoloV4, and it is better than the Map value of Faster-RCNN. In particular, the modification (Embellish) behavior of laying hens has a Map value of 92.33%. In Figures 7, 8, the precision and recall values of

YoloV5 are 91.34% and 98.15%, respectively, higher than the tested values of the other three detection algorithms for this behavior of lying. Experiments with the same size data set and experimental equipment showed that YoloV5 and Faster-RCNN were able to accurately identify various types of laying hens'

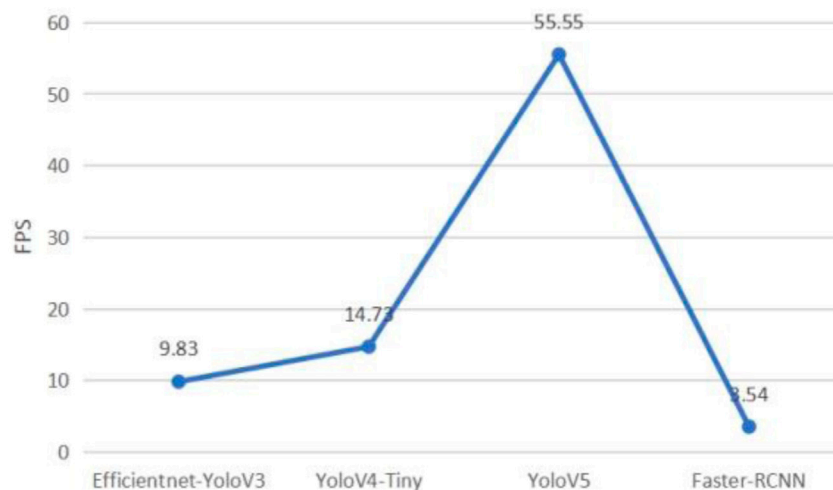


FIGURE 11
The FPS data comparison diagram.

behaviors, while YoloV3 and YoloV4 had lower detection effects and there were missing detection and judgment errors. Meanwhile, two environments of day and night were selected for detection in this paper. From Figure 9, the detection confidence of YoloV3, YoloV4, YoloV5, and Faster-RCNN in the behavior of stand in the daytime environment is 91%, 91%, 96%, 100%, and in the dark environment, its detection confidence is 81%, 77%, 93%, and 99%. In the day and night environment, we can see that the detection confidence of YoloV5 and Faster-RCNN was very high, in particular, Faster-RCNN, which reached 100% in the detection of the day environment, while YoloV3 and YoloV4 found a reduced detection accuracy obviously in the night environment. In Figures 10, 11, we can analyze that YoloV5 has a better detection speed under the same hardware conditions and its FPS value can reach 55, while the Faster-RCNN FPS is 3.54, YoloV5 can fully meet the needs of real-time detection of farms. In subsequent studies, the YoloV5 detection accuracy can be further improved by increasing the training data set and enhancing the data effect.

5 Conclusion

The comparative experimental results of four different target detection algorithms show that the detection accuracy and detection speed of the YoloV5 are better than YoloV3 and YoloV4. Faster-RCNN and YoloV5 detection accuracy are similar, but Faster-RCNN has a low detection speed and occupies more memory. The precision values of the YoloV5 target detection algorithm were 96.12%, 91.34%, 86.97%, and 97.78% for the four behaviors: feed, stand, lie, and embellish, respectively; the recall values were 98.21%, 98.15%, 94.12%, and 86.45%, respectively. YoloV5 can effectively identify four different behaviors of laying hen in a day and night environment, and its detection speed is fast enough to meet the needs of real-time detection. It can be used to realize

the real-time detection of laying hens' behavior in breeding farms and provide data support for the health assessment of laying hens. Its characteristics of high detection accuracy and fast detection speed are easy to be deployed in the embedded intelligent front-end detection equipment. In the experimental link of this paper, the breeding density of the experimental environment needs to be improved. In the future, we will strengthen the research on the breeding farm to improve the breeding density.

Data availability statement

The original contributions presented in the study are included in the article/supplementary material, further inquiries can be directed to the corresponding author.

Author contributions

FW and JC: Investigation, formal analysis, and prepare draft; YX: Writing, review and editing; and HL: Conceptualization, methodology, review and editing, project administration.

Funding

This paper is supported by Fundamental Research Program of Shanxi Province (20210302123054).

Conflict of interest

The authors declare that the research was conducted in the absence of any commercial or financial relationships that could be construed as a potential conflict of interest.

Publisher's note

All claims expressed in this article are solely those of the authors and do not necessarily represent those of their affiliated

organizations, or those of the publisher, the editors and the reviewers. Any product that may be evaluated in this article, or claim that may be made by its manufacturer, is not guaranteed or endorsed by the publisher.

References

1. Wu D, Cui D, Zhou M, Ying Y. Information perception in modern poultry farming: A review. *Comput Electron Agric* (2022) 199:107131. doi:10.1016/j.compag.2022.107131
2. Hartung J, Nowak B, Springorum AC. Animal welfare and meat quality. In: J Kerry, editor. *Improving the sensory and nutritional quality of fresh meat*. Netherlands: Elsevier (2009). p. 628–646.
3. Silva RTBR, Nääs IA, Neves DP. Selecting the best norms for broiler rearing welfare legislation. In: Precision Livestock Farming 2011 - Papers Presented at the 5th European Conference on Precision Livestock Farming, ECPLF 2011 (2011). p. 522–527.
4. Li B, Wang Y, Zheng W, Tong Q. Research progress in environmental control key technologies, facilities and equipment for laying hen production in China. *Nongye Gongcheng Xuebao/Transactions Chin Soc Agric Eng* (2020) 36(16):212–221. doi:10.11975/j.issn.1002-6819.2020.16.026
5. Bao J, Xie Q. Artificial intelligence in animal farming: A systematic literature review. *J Clean Prod* (2022) 331:129956. doi:10.1016/j.jclepro.2021.129956
6. Wang K, Zhao X, He Y. Review on noninvasive monitoring technology of poultry behavior and physiological information. *Nongye Gongcheng Xuebao/Transactions Chin Soc Agric Eng* (2017) 33(20):197–209. doi:10.11975/j.issn.1002-6819.2017.20.025
7. Gridaphat S, Phakkaphong K, Kraivit W. Toward IoT and data analytics for the chicken welfare using RFID technology. In: 19th International Conference on Electrical Engineering/Electronics, Computer, Telecommunications and Information Technology, ECTI-CON; 24–27 May 2022; Prachuap Khiri Khan, Thailand (2022).
8. Wang K, Liu K, Xin H, Chai L, Wang Y, Fei T, et al. An RFID-based automated individual perching monitoring system for group-housed poultry. *Trans ASABE* (2019) 62(3):695–704. doi:10.13031/trans.13105
9. Dan H, John B. Video recording system to assess animal welfare impact of environmental changes in barns. In: 2022 ASABE Annual International Meeting; 17–20 Jul 2022; Houston, USA (2022).
10. Carlos G, Ricardo P, José F, María D V. Real-time monitoring of poultry activity in breeding farms. In: Proceedings IECON 2017 - 43rd Annual Conference of the IEEE Industrial Electronics Society; 29 October 2017 - 01 November 2017; Beijing, China (2017). p. 3574–3579.
11. Okinda C, Lu M, Liu L, Nyalala I, Muneri C, Wang J, et al. A machine vision system for early detection and prediction of sick birds: A broiler chicken model. *Biosyst Eng* (2019) 188:229–42. doi:10.1016/j.biosystemseng.2019.09.015
12. Huang J, Zhang T, Cuan K, Fang C. An intelligent method for detecting poultry eating behaviour based on vocalization signals. *Comput Electron Agric* (2021) 180:105884. doi:10.1016/j.compag.2020.105884
13. Fontana I, Tullo E, Butterworth A, Guarino M. An innovative approach to predict the growth in intensive poultry farming. *Comput Electron Agric* (2015) 119:178–83. doi:10.1016/j.compag.2015.10.001
14. Du X, Lao F, Teng G. A sound source localisation analytical method for monitoring the abnormal night vocalisations of poultry. *Sensors* (2018) 18(9):2906. doi:10.3390/s18092906
15. Li G, Huang Y, Chen Z, Chesser GD, Purswell JL, Linhoss J, et al. Practices and applications of convolutional neural network-based computer vision systems in animal farming: A review. *Sensors* (2021) 21(4):1492. doi:10.3390/s21041492
16. Fang C, Zhang T, Zheng H, Huang J, Cuan K. Pose estimation and behavior classification of broiler chickens based on deep neural networks. *Comput Electron Agric* (2021) 180:105863. doi:10.1016/j.compag.2020.105863
17. Ayadi S, Said A, Jabbar R, Aloulou C. Dairy cow rumination detection: A deep learning approach (2021) arXiv.
18. Chen C, Zhu W, Steibel J, Siegford J, Han J, Norton T. Recognition of feeding behaviour of pigs and determination of feeding time of each pig by a video-based deep learning method. *Comput Electron Agric* (2020) 176:105642. doi:10.1016/j.compag.2020.105642
19. Kleanthous N, Hussain A, Khan W, Sneddon J, Liatsis P. Deep transfer learning in sheep activity recognition using accelerometer data. *Expert Syst Appl* (2022) 207:117925. doi:10.1016/j.eswa.2022.117925
20. Nasiri A, Yoder J, Zhao Y, Hawkins S, Prado M, Gan H. Pose estimation-based lameness recognition in broiler using CNN-LSTM network. *Comput Electron Agric* (2022) 197:106931. doi:10.1016/j.compag.2022.106931
21. Pu H, Lian J, Fan M. Automatic recognition of flock behavior of chickens with convolutional neural network and kinect sensor. *Int J Pattern Recognition Artif Intelligence* (2018) 32(07):1850023. doi:10.1142/s0218001418500234
22. Wang J, Wang N, Li L, Ren Z. Real-time behavior detection and judgment of egg breeders based on YOLO v3. *Neural Comput Appl* (2019) 32:5471–81. doi:10.1007/s00521-019-04645-4
23. Nakaguchi VM, Ahamed T. Development of an early embryo detection methodology for quail eggs using a thermal micro camera and the YOLO deep learning algorithm. *Sensors* (2022) 22(15):5820. doi:10.3390/s22155820
24. Neethirajan S. ChickTrack – a quantitative tracking tool for measuring chicken activity. *Measurement* (2022) 191:110819. doi:10.1016/j.measurement.2022.110819
25. Jia Y, Liu L, Zhang L, Li H. Target detection method based on improved YOLOv3. In: 2022 3rd International Conference on Computer Vision, Image and Deep Learning and International Conference on Computer Engineering and Applications. CVIDL and ICCEA; 20–22 May 2022; Changchun, China (2022).
26. Jiang Z, Zhao L, Li S, Jia Y. Real-time object detection method based on improved YOLOv4-tiny (2020) arXiv.
27. Cao C, Chen C, Kong X, Wang Q, Deng Z. A method for detecting the death state of caged broilers based on improved Yolov5. *SSRN Electron J* (2022). doi:10.2139/ssrn.4107058
28. Mu L, Shen Z, Liu J, Gao J. Small scale dog face detection using improved Faster RCNN. In: 2022 3rd International Conference on Electronic Communication and Artificial Intelligence (IWECAT); 14–16 January 2022; Zhuhai, China. IEEE (2022).



OPEN ACCESS

EDITED BY

Leizi Jiao,
Beijing Academy of Agriculture and
Forestry Sciences, China

REVIEWED BY

Leiqing Pan,
Nanjing Agricultural University, China
Seyed Ahmad Mireei,
Isfahan University of Technology, Iran

*CORRESPONDENCE

Guohui Han
✉ hghui2007@126.com

SPECIALTY SECTION

This article was submitted to
Technical Advances in Plant Science,
a section of the journal
Frontiers in Plant Science

RECEIVED 04 January 2023

ACCEPTED 06 March 2023

PUBLISHED 27 March 2023

CITATION

Li X, Wei Z, Peng F, Liu J and Han G (2023)
Non-destructive prediction and
visualization of anthocyanin
content in mulberry fruits using
hyperspectral imaging.
Front. Plant Sci. 14:1137198.
doi: 10.3389/fpls.2023.1137198

COPYRIGHT

© 2023 Li, Wei, Peng, Liu and Han. This is an
open-access article distributed under the
terms of the [Creative Commons Attribution
License \(CC BY\)](#). The use, distribution or
reproduction in other forums is permitted,
provided the original author(s) and the
copyright owner(s) are credited and that
the original publication in this journal is
cited, in accordance with accepted
academic practice. No use, distribution or
reproduction is permitted which does not
comply with these terms.

Non-destructive prediction and visualization of anthocyanin content in mulberry fruits using hyperspectral imaging

Xunlan Li, Zhaoxin Wei, Fangfang Peng, Jianfei Liu
and Guohui Han*

Research Institute of Pomology, Chongqing Academy of Agricultural Sciences, Chongqing, China

Being rich in anthocyanin is one of the most important physiological traits of mulberry fruits. Efficient and non-destructive detection of anthocyanin content and distribution in fruits is important for the breeding, cultivation, harvesting and selling of them. This study aims at building a fast, non-destructive, and high-precision method for detecting and visualizing anthocyanin content of mulberry fruit by using hyperspectral imaging. Visible near-infrared hyperspectral images of the fruits of two varieties at three maturity stages are collected. Successive projections algorithm (SPA), competitive adaptive reweighted sampling (CARS) and stacked auto-encoder (SAE) are used to reduce the dimension of high-dimensional hyperspectral data. The least squares-support vector machine and extreme learning machine (ELM) are used to build models for predicting the anthocyanin content of mulberry fruit. And genetic algorithm (GA) is used to optimize the major parameters of models. The results show that the higher the anthocyanin content is, the lower the spectral reflectance is. 15, 7 and 13 characteristic variables are extracted by applying CARS, SPA and SAE respectively. The model based on SAE-GA-ELM achieved the best performance with R^2 of 0.97 and the RMSE of 0.22 mg/g in both the training set and testing set, and it is applied to retrieve the distribution of anthocyanin content in mulberry fruits. By applying SAE-GA-ELM model to each pixel of the mulberry fruit images, distribution maps are created to visualize the changes in anthocyanin content of mulberry fruits at three maturity stages. The overall results indicate that hyperspectral imaging, in combination with SAE-GA-ELM, can help achieve rapid, non-destructive and high-precision detection and visualization of anthocyanin content in mulberry fruits.

KEYWORDS

hyperspectral imaging, mulberry fruit, anthocyanin content, SAE, ELM

1 Introduction

Mulberry (*Morus* L.) is widely planted around the world. Tender, juicy and delicious mulberry fruits have long been used as traditional medicine as well as edible fruits in countries such as China, India and Turkey (Jan et al., 2021). Modern researches show that black and red mulberry fruits are rich in anthocyanins, which, with the properties of antioxidant, anti-inflammatory and chemical protection, play a positive role in reducing the risk of cardiovascular diseases and cancers (Chen et al., 2006; Krishna et al., 2018). Anthocyanins are considered to be one of the most important indicators for mulberry fruits of good quality by researchers and consumers.

Anthocyanin contents are usually determined by adopting wet chemical methods, such as spectrophotometry (Jiang and Nie, 2015) and high-performance liquid chromatography (Zou et al., 2012). The samples need to be ground and extracted with the use of chemical reagents such as ethanol or acetone. These methods are destructive and will produce chemical residues. And only a small number of samples can be analyzed at a time. It is difficult to detect anthocyanin content in mulberry fruits on a large scale by applying the existing time-consuming and inefficient detecting methods. For efficient agricultural management and production, it is necessary to find a reliable, fast and non-destructive method for anthocyanin content detection.

Hyperspectral imaging (HSI) can obtain the spectral data of each pixel in the sample image simultaneously. This is of potential value in non-destructive detection of uneven distribution of quality indicators. There are reports about visualizing anthocyanin contents of purple sweet potato (Liu et al., 2017), lychee pericarp (Yang et al., 2015), and grape (Chen et al., 2015) by using HSI. The research by Huang et al. (2017) has shown that 400–1000 nm and 900–1700 nm HSI, in combination with least squares support vector machine (LS-SVM), has great potential in evaluating total anthocyanin content and antioxidant activity of mulberry fruits. This is the only study on determining anthocyanin of mulberry by using HSI. And further research endeavors to visualize anthocyanin content of mulberry fruit have not been reported yet.

The variable selection is an essential step for modeling. From previous researches, variable selection methods, such as interval partial least square, successive projections algorithm (SPA) and competitive adaptive reweighted sampling (CARS) are often used to reduce the number of input variables before modeling (Zhu et al., 2017; Silva and Melo-Pinto, 2021). When using these variable selection methods, the average spectrum of all pixels in the hyperspectral image is applied, while efficient big data analysis of each pixel spectrum is ignored. Depth feature extraction and dimension reduction can be conducted by using the stacked auto-encoder (SAE), a nonlinear unsupervised neural network, which is capable of effectively analyzing the spectral data of all pixels of the hyperspectral image and then select variables (Yu et al., 2018). In terms of modeling, the LS-SVM has been shown to be of good potential in non-destructive detection. Research reports show that the extreme learning machine (ELM), a single hidden layer

feedforward neural network model, is able to achieve similar or much better performance at a much faster learning speed than traditional LS-SVM (Huang et al., 2011; Zheng et al., 2014).

This study is meant for developing a rapid, non-destructive, high-precision method to detect and visualize the anthocyanin content of mulberry fruit. The main research objects are as follows: (1) analyzing the differences in anthocyanin content and corresponding spectral data between two mulberry varieties at different maturity stages; (2) reducing the dimension of high-dimensional spectral data by using SPA, CARS and SAE, and selecting the most effective feature variables; (3) using LS-SVM and ELM to build the models for predicting mulberry anthocyanin and selecting the best prediction model so as to achieve rapid, non-destructive and high-precision prediction of the anthocyanin content of mulberry fruit; (4) mapping distribution of anthocyanin content in mulberry fruit.

2 Materials and methods

2.1 Materials

The sampled varieties, Dashi (*Morus nigra* L.) and Siji (*Morus nigra* L.) were collected from the mulberry resource conservation nursery of Chongqing Academy of Agricultural Sciences on April 23, 2020. Disease-free fruits at three maturity stages (S1: red maturity, S2: red to purple maturity and S3: full maturity) were randomly picked, then stored in ice boxes. They were brought back to the laboratory for hyperspectral image collection and anthocyanin content detection (Figure 1). Six fruits at the same maturity stage were randomly selected as one sample for anthocyanin content detection. A total of 180 samples were obtained, and the numbers of Dashi and Siji were 90 respectively. The samples were randomly divided into the training set and the testing set at a ratio of 7:3.

2.2 Collection and calibration hyperspectral images

The hyperspectral imaging system was used to collect hyperspectral images of mulberry fruits (Figure 2). The hyperspectral imaging system consists of a spectrograph (ImSpector V10E, SPECIM, Finland), an EMCCD camera (DL-604E, Andor Technology plc., N. Ireland), two halogen light sources (150 W/21 V halogen lamp, Illuminator Technologies, Inc, USA), an electric mobile platform and controller (SC30021A, Zolix, China), and a laptop. The wavelength range of the spectrum collected was 305–1 090 nm. The two light sources were at an angle of 45° with the mobile platform respectively. The camera exposure time was 60 ms. The spectral resolution was 2.8 nm. The platform moving speed was 1.87 mm/s. The distance between the objective lens and the platform was 40 cm. After preheating for half an hour by the light source, the mulberry fruits were placed on the black cardboard for hyperspectral image collection.

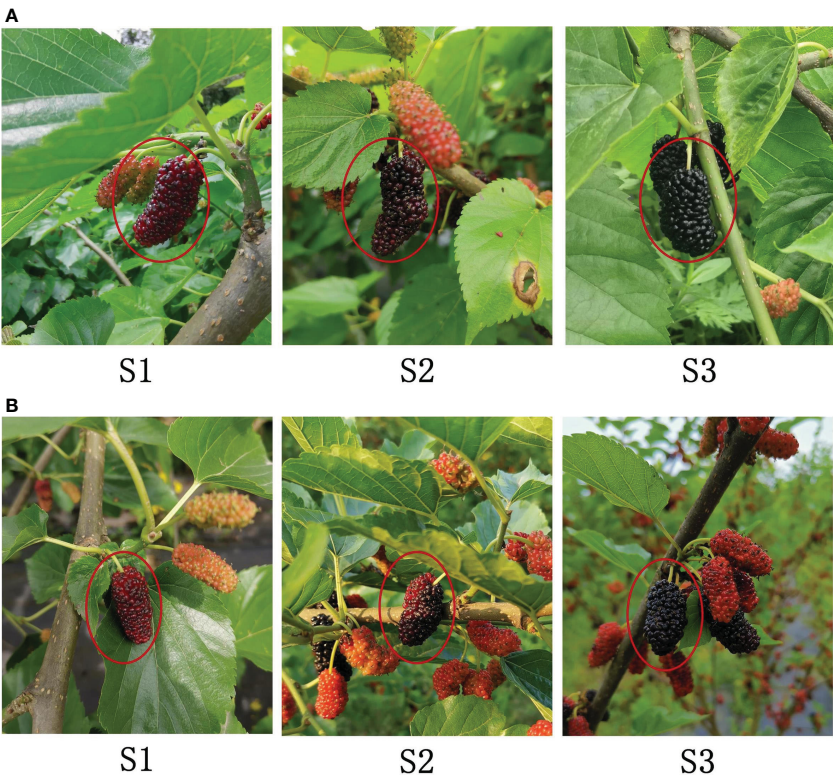


FIGURE 1
Fruit images of Dashi (A) and Siji (B) at three maturity stages: (S1) red maturity; (S2) red to purple maturity; (S3) full maturity.

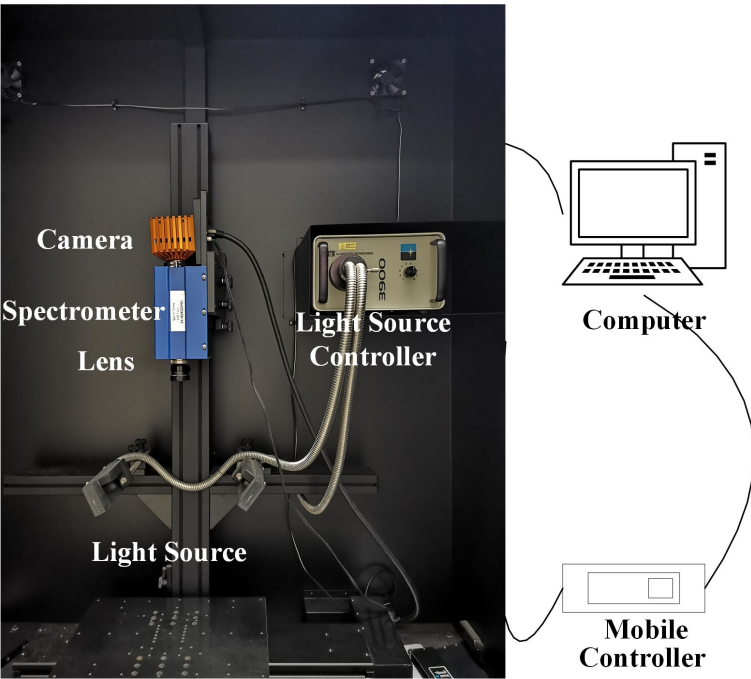


FIGURE 2
The hyperspectral imaging system.

The collected hyperspectral images need to be calibrated so as to avoid the effect caused by uneven light source intensity distribution and dark current during the image collecting process. Under the same conditions as the sample images were collected, the white reference image W was obtained by scanning the standard white reference panels. The dark reference image D was obtained by scanning with the lens covered. And the image calibration was completed on the basis of formula (1),

$$R_{\lambda} = \frac{I_{\lambda} - D_{\lambda}}{W_{\lambda} - D_{\lambda}} \quad (1)$$

where R_{λ} is the calibrated image, I_{λ} is the raw image, W_{λ} is the white reference image, and D_{λ} is the dark reference image.

2.3 Anthocyanin content extraction

Anthocyanin content was detected by pH-differential spectrophotometry (Lee et al., 2005). 0.5 ± 0.001 g of grinded fresh mulberry fruits was added to 10 ml of acidified ethanol (95% ethanol and 1% concentrated hydrochloric acid, the volume ratio of ethanol to hydrochloric acid was 60:40) for 1 h ultrasound extraction and 2 min centrifugation at 8000 r·min⁻¹. 1 ml of supernatant was taken and the volume was fixed to 25 ml by adding buffer solutions of pH 1.0 and pH 4.5 respectively. The absorbance was measured at 520 nm and 700 nm after letting it stand for 15 min with an ultra-violet-visible spectrophotometer (UV-6000PC ShanghaiMetash. Co. Ltd, China). The anthocyanin content was calculated by the formula (2) and (3).

$$A = (A_{520nm} - A_{700nm}) \text{ at PH } 1.0 - (A_{520nm} - A_{700nm}) \text{ at PH } 4.5 \quad (2)$$

$$\begin{aligned} &\text{Total anthocyanin content(mg/g)} \\ &= (A * MW * DF * V) / (\epsilon * 1 * M) \end{aligned} \quad (3)$$

Where is the absorbance, A_{520nm} and A_{700nm} are the absorbance at the 520 nm and 700 nm respectively. MW (molecular weight) = 449.2 g/mol for cyanidin-3-glucoside (cyd-3-glu). DF (Dilution factor) = 25. V is the original volume of 10 ml. The molar extinction coefficient ϵ =26900. M is the weight of the sample.

2.4 Region of interest and spectral data extraction

In this study, the whole fruit with the fruit stalk removed was treated as the region of interest (ROI). The whole mulberry fruit and the collection background plate were segmented at 800 nm, with the reflectance of 0.2 as the minimum value. The petiole was removed from the whole fruit at 550 nm and 670 nm, with the difference value of 0.04 as the maximum value. Then the ROI was obtained by conducting mask processing. The average spectrum of ROI at each wavelength was calculated for subsequent SPA and CARS feature wavelength extraction. To create a data set for deep learning, 400

pixels (20 * 20) corresponding to spectral data were randomly selected from the ROI of each sample, totaling 72,000, for SAE training.

2.5 Spectral data processing

2.5.1 Spectral data pretreatment

Owing to the existence of strong noises in the beginning and ending bands of the raw spectral data, spectral data within the range of 450-1050 nm, a total of 379 variables were selected for subsequent analysis. In this study, standard normal variate transform (SNV) was used to preprocess the spectral data, to eliminate the scattering caused by uneven particle distribution and different particle sizes, and the influence of optical path change on the spectral data.

2.5.2 Feature extraction

Successive projections algorithm (SPA), Competitive adaptive reweighted sampling (CARS) and Stacked auto-encoder (SAE) were respectively used in this study to extract spectral data features for the purpose of reducing the number of input variables, improving model efficiency, eliminating redundant information of spectral data, and improving the prediction accuracy of the model.

Successive projections algorithm (SPA) is a forward variable selection algorithm. By this method, the cycle of forward is conducted with a wavelength initially selected and the projection value of the remaining wavelength calculated. Then the projection vector is combined with the wavelength corresponding to the maximum projection value until the cycle ends. The minimum variable group can be effectively obtained by calculating the band projection value, thus minimizing the collinearity between variables (Araújo et al., 2001).

Competitive adaptive reweighted sampling (CARS) is a method based on Monte Carlo sampling and the PLS regression coefficient. By this method, characteristic variables are primarily screened out by using the PLS regression coefficient in combination with the exponential decline function. Then the initially selected characteristic variables are competitively screened out by using adaptive reweighted sampling. And the final characteristic variables are screened out from the wavelength combinations according to the cross-validation root mean square error. The detailed algorithm of CARS can be found in reference (Li et al., 2009). In this study, the number of CARS samples was set to 50, and the ten-fold cross-validation method was used.

Stacked auto-encoder (SAE) is a deep neural network consisting of multilayer auto-encoders (AE), by which better feature extraction is obtained with the hidden layers added to the simple auto-encoders. AE consists of encoders and decoders. The input layers map the input data to the hidden layers through the activation function to obtain the encoding features, which is called encoding. Through the same steps, the encoding features are mapped to the output layers by using the activation function to obtain the decoding features, which is called decoding. In terms of SAE, the decoding features of the previous AE are used as the input of

the next hidden layer of AE, and code and decode the next layer of AE. By analogy, these hidden input layers are connected to form SAE (Xu et al., 2022).

2.5.3 Model construction and evaluation

Least squares support vector machine (LS-SVM) is a machine learning algorithm based on SVM, boasting good generalization ability and nonlinear regression processing ability (Suykens and Vandewalle, 1999). The fitting ability of LS-SVM mainly depends on the selection of kernel parameters (C and γ). Kernel parameter C affects the fitting accuracy and generalization ability of the model, and kernel parameter γ directly determines the calculation amount and efficiency of the model.

Extreme learning machine (ELM) is a feedforward neural network with a single hidden layer, which has a fast learning ability and strong nonlinear approximation ability (Huang et al., 2006). Compared with traditional neural network learning algorithms, such as back propagation neural network, ELM presents the advantages of strong generalization ability and fast calculation speed (Ye et al., 2022). Over-fitting is liable to occur, since the weight and offset of ELM are randomly determined.

Genetic algorithm (GA) is a search algorithm for obtaining the global optimal solution based on the biological evolution mechanism of “survival of the fittest” (Mirjalili, 2019). In this study, GA is used to optimize the important parameters of the RBF kernel function and the offset and weight of ELM. In this case, the value ranges of kernel parameters (C and γ) were set to 0.01–100, the population size was set to 20, and the number of maximum evolution times was set to 200. When GA was used to optimize ELM, the population size was set to 20, the maximum number of evolutions was set to 300, and the number of neurons in the hidden layer of ELM was set to 90.

The training set determination coefficient (R^2_c), testing set determination coefficient (R^2_p), training set root mean square error (RMSEC), and testing set root mean square error (RMSEP) were used as indicators to evaluate the performance of models. The closer to 1 the determination coefficient (R^2) is, the better the model

fitting effect is. And the smaller RMSEC and RMSEP are, the higher the precision of the model is.

The hyperspectral image calibration in this study was completed by the software of the hyperspectral image acquisition system. ROI segmentation, spectral data extraction and processing were completed by using MATLAB 2022a, with SPA, CARS, GA, SAE, and LS-SVM realized by using SPA_GUI, Lib PLS1.98, GATBX, Deep Learning toolbox, and LS-SVMlab v1.8 toolbox. The overall flow is shown in Figure 3.

3 Results and analysis

3.1 Anthocyanin content and spectral characteristics of mulberry fruits

The anthocyanin contents of two mulberry varieties at three maturity stages were analyzed and measured, and the mean anthocyanin content and corresponding spectral reflectance of two mulberry varieties at different maturity stages were calculated (Figure 4). It was shown in Figure 4A that the higher the maturity of mulberry fruits was, the higher the anthocyanin content was, which followed the description of the report of Saracoglu (Saracoglu, 2018). The anthocyanin content of Dashi was higher than that of Siji at the same maturity stage. Anthocyanins are the main reasons why mulberry has red and purple (Li et al., 2020). From the analysis of the spectrum reflection curve of mulberry fruit, it can be seen that the spectral reflection value in the range from 500 to 700 nm was very low. According to Qin and Lu (Qin and Lu, 2008), the maximum absorbance of anthocyanin pigments is about 535 nm. However, the difference between the mulberry fruits of different maturity was not obvious at 535 nm in Figure 4B. This may be because the black substances have strong absorption in the visible light area, and the reflectance value is not attributed to a single compound, the spectra are the sum of the major mulberry fruit composition spectra (Cozzolino et al., 2004). A small reflective valley could be seen near 680 nm in red maturity fruits, which is related to the existence of

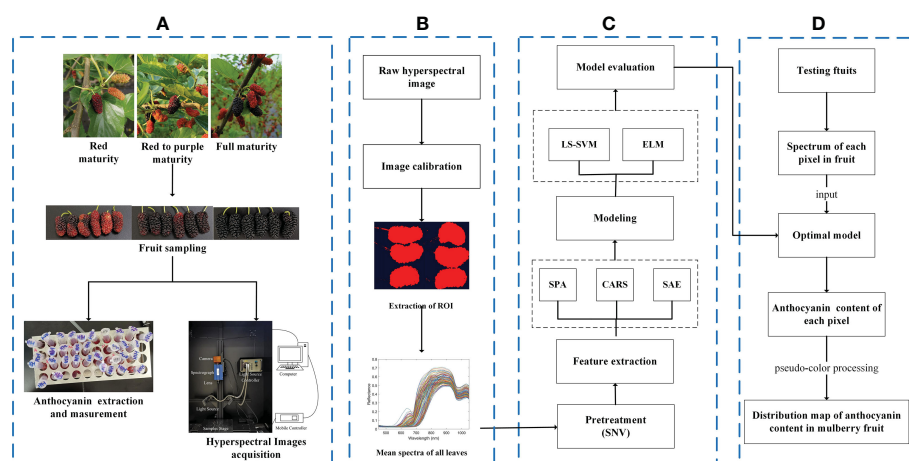


FIGURE 3

Overall flow chart. (A) Acquisition of data; (B) hyperspectral image processing; (C) analysis of spectral data; (D) visualization of anthocyanin content.

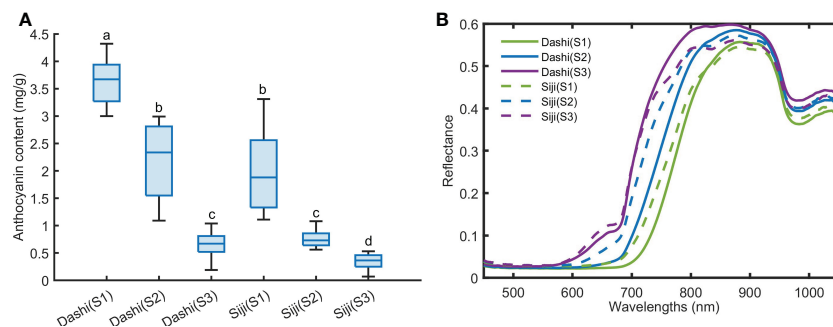


FIGURE 4

The anthocyanin content (A) and average spectra (B) of mulberry fruit at three maturity stages. Values with the same letter (i.e. a, b, c or d) are not significantly different ($p < 0.05$).

chlorophyll. The spectral reflectance was lower with the increase of maturity and anthocyanin content within the range of 590–800 nm. The two varieties showed obvious absorption peaks near 970 nm and 840 nm. This is speculated to be related to water and sugar absorption (ElMasry et al., 2008; Zheng et al., 2008). The differences in spectral characteristics of the mulberry fruits above show that hyperspectral imaging has the potential to distinguish the mulberry fruits of different anthocyanin contents.

3.2 The results of feature extraction

When hyperspectral imaging is used to detect the anthocyanin contents of mulberry fruits, the redundant information is often eliminated and the amount of calculation is compressed by screening out the characteristic wavelengths to improve the accuracy and robustness of the diagnostic models. In this paper, SPA, CARS and SAE were used to extract feature variables from the 379 variables.

SPA was used to screen characteristic wavelengths from spectral data of SNV pretreatment in 450–1,050 nm region, and the results were shown in Figure 5. It can be seen from Figure 5A that when the number of characteristic wavelengths increased from 1 to 7, the value of RMSE decreased in a ladder shape and then leveled off. And 7 characteristic wavelengths at 684.88, 703.98, 747.15, 798.58, 842.15, 923.11 and 962.05 nm were obtained.

The process of screening wavelengths by using CARS was shown in Figure 6. With the increase in sampling times, the number of selected wavelengths decreased gradually at the speed from fast to slow. This reflected the two stages, preliminary screening and fine screening, of using CARS to screen out key variables. With the increase in sampling times, the root mean squares error of cross-validation (RMSECV) value gradually decreased. And the RMSECV value obtained was the lowest when the 31st sampling was conducted. This is an indication that some irrelevant variables are removed during the sampling process. After the 31st sampling, the RMSECV value presented a stepwise progression, indicating the removal of some key information. Therefore, the wavelengths obtained at the 31st sampling were

the characteristic wavelengths. Fifteen characteristic wavelengths, 450.08, 451.59, 601.16, 703.98, 707.17, 708.77, 743.95, 795.36, 796.97, 798.58, 832.45, 963.67, 965.29, 1038.29 and 1046.39 nm, were screened out by using CARS.

Based on the analysis of the characteristic wavelengths, the positions and numbers of characteristic wavelengths screened out by using SPA and CARS were found to be different. And the wavelength positions are concentrated within the ranges of 703–835 nm and 963–1046 nm.

The feature variables of SAE screening are shown in Figure 7. When it comes to SAE, it is not necessarily the case that the more hidden layers are, the better the effect is. In this study, 379–300–150–h–150–300–379 was set to be the basic network. h denotes the number of neurons in the last coding layer, and it is also the number of feature variables extracted. Based on experience and many previous attempts, sigmoid was set as the activation function, iterate was set to 40 times, the batch size was set to 200, the initial learning rate was set to 0.001, and h was set to 13. From the results shown in Figure 7A, the reconstructed spectral reflectance curve is highly coincident with the original spectral curve, indicating that the original spectral data can be perfectly reconstructed by using SAE. The last coding layer was extracted as the spectral feature variables (Figure 7B). It can be seen that the corresponding values of the 13 feature variables of samples at different maturity stages are obviously different.

3.3 The results of modeling

All wavelengths and feature variables extracted by using SPA, CARS and SAE were used as the model inputs. Regression models of mulberry anthocyanin contents were built based on GA-LS-SVM and GA-ELM respectively. And the regression results were evaluated (Figure 8). Models were constructed by using the two non-linear regression methods that achieved good performance, R^2 values of the training sets and those of the testing sets of GA-LS-SVM and GA-ELM models built on the basis of full wavelengths and variables extracted by using SPA, CARS and SAE were greater than 0.90, RMSE was less than 0.38 mg/g. The models based on

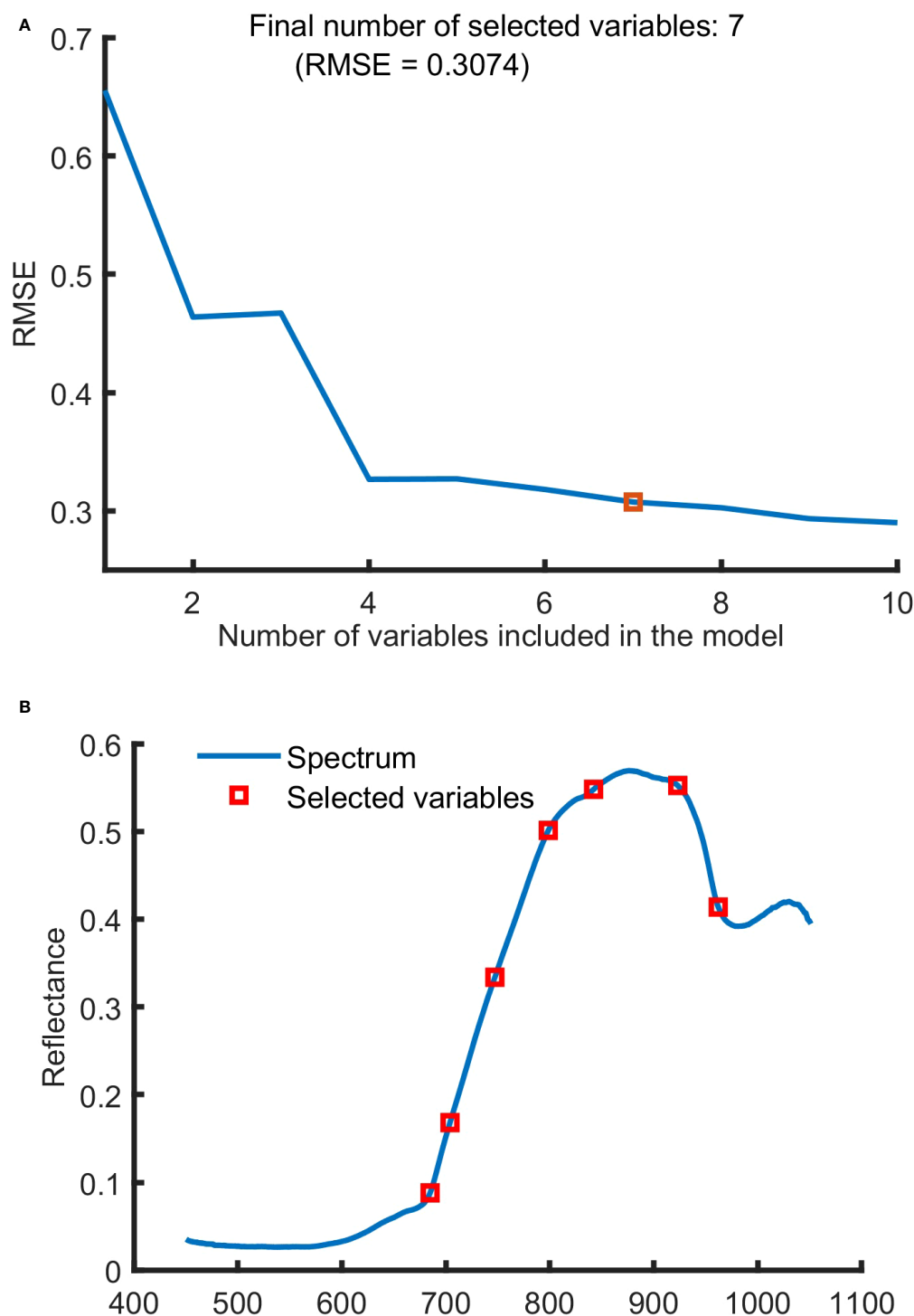


FIGURE 5

The characteristic wavelengths selected by SPA. (A) Variation of RMSE with the number of variables, (B) the selected wavelengths.

variables selected by SPA, CARS and SAE achieved better performances than those based on full-band spectral data, indicating that SPA, CARS and SAE can reduce the redundancy of model input variables and help improve the accuracy of the model. Many researches show that ELM has the advantages of fast

learning speed and good generalization ability (Wong et al., 2013; Huang et al., 2014). In this study, The SAE-GA-ELM models, requiring only 13 input variables, has achieved the best predictive performance, with the values of R^2_c and R^2_p reaching 0.97, and RMSEC and RMSEP being only 0.22 mg/g, obtained.

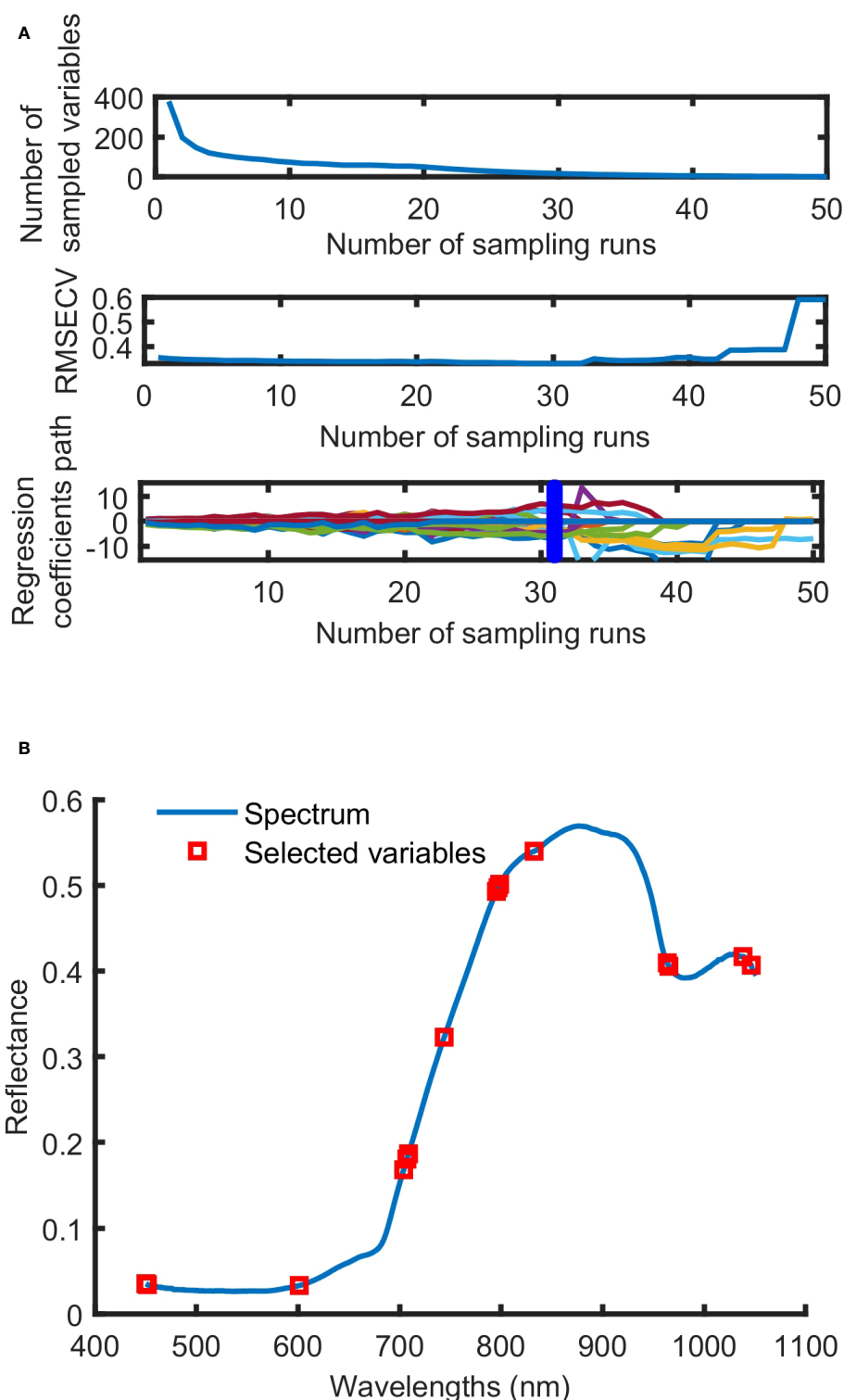


FIGURE 6
The process (A) and result (B) of characteristic wavelength selection by CARS.

3.4 Visualization of anthocyanin content

The visualization of anthocyanin content distribution in mulberry fruits is needed for more intuitively observing the changes in anthocyanin contents of mulberry fruits at different

maturity levels. One of the advantages of hyperspectral imaging is that spectral data of each pixel can be obtained by using hyperspectral imaging. This makes it possible for the prediction about each pixel to be made, thus helping create distribution prediction maps. The visualization can be achieved with the average spectra applied for

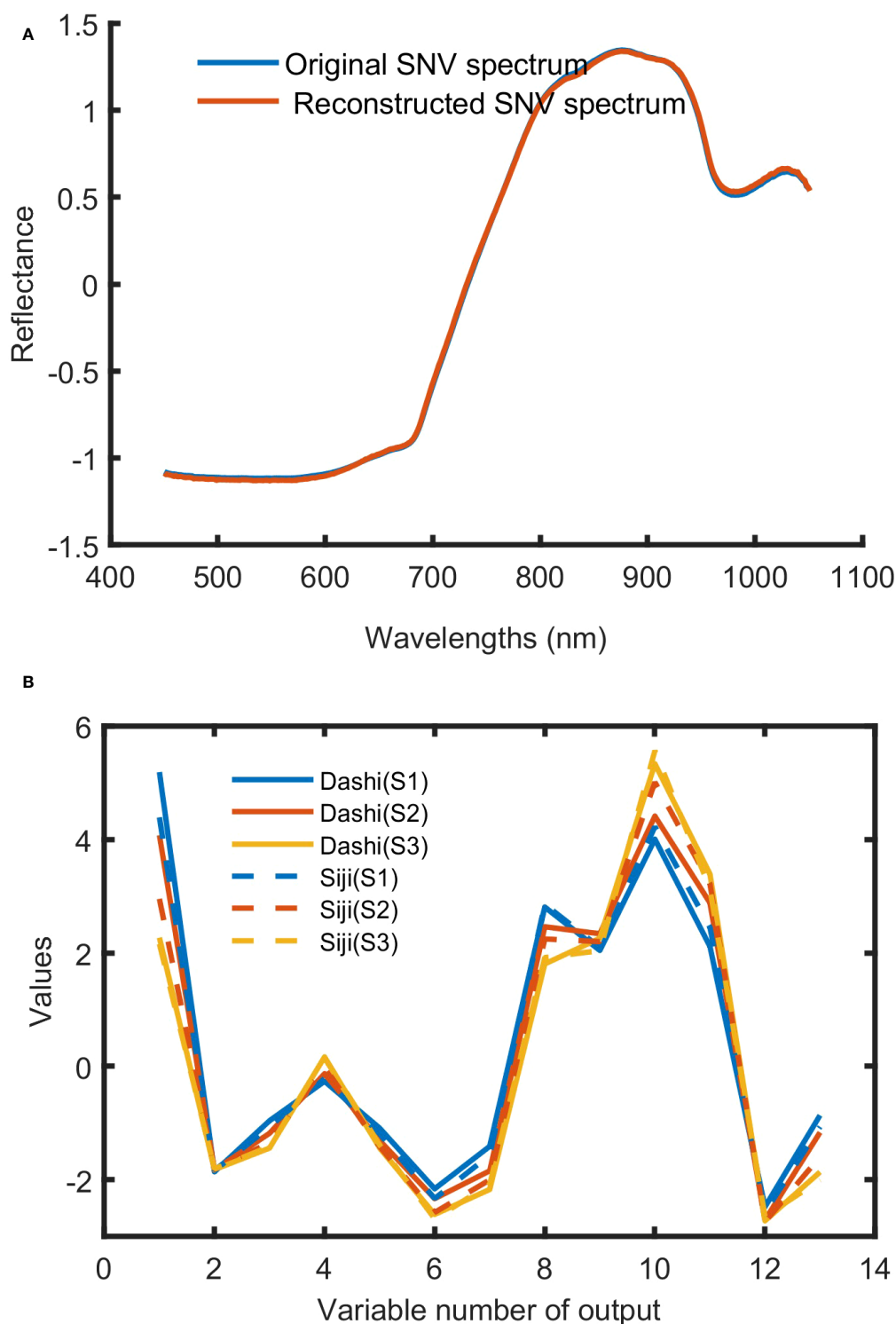


FIGURE 7

The training results of SAE. (A) Original SNV spectrum and reconstructed SNV spectrum; (B) deep spectral features of Dashi and Siji.

modeling and all of the single-pixel spectra in the hyperspectral image used for the best prediction model (Sun et al., 2019; Xiao et al., 2020). In this study, SAE-GA-ELM, the best model for anthocyanin content detection, was applied to visualize anthocyanin content distribution. All the single-pixel spectrum was processed by the same treatment used in the modeling. Figure 9 shows the visualization maps of

eighteen samples representing different maturity levels of two varieties. we can see from Figure 9 that the higher the maturity level of mulberry fruits is, the higher the anthocyanin content is, and that the anthocyanin content of Dashi is higher than that of Siji at the same maturity stage, which is consistent with the results shown in Figure 4A. It can be seen that the distribution of anthocyanin content

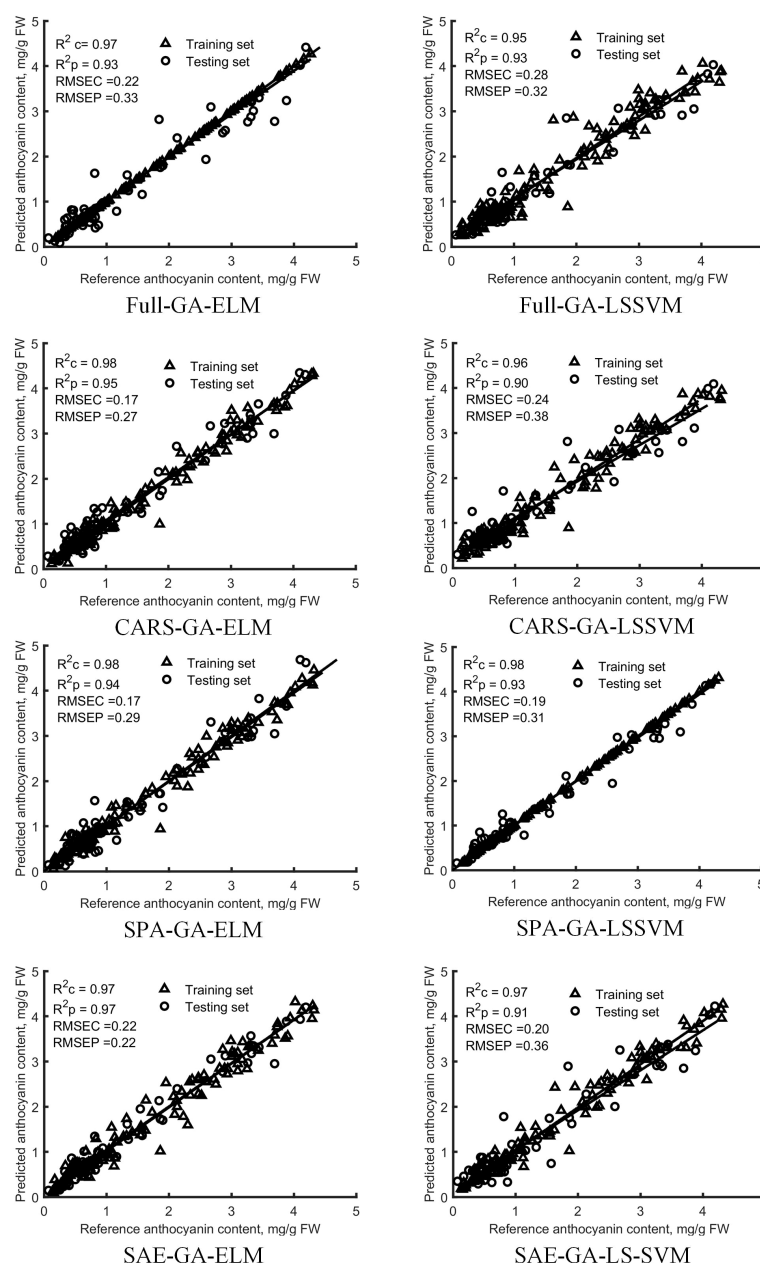


FIGURE 8

Diagnosis results of anthocyanin content in the training set and testing set by GA-ELM and GA-LS-SVM models based on all-band and feature variables.

of the mulberry fruits at the red maturity stage is not consistent with that of the content of the mulberry fruits at the red to purple maturity stage, which is speculated to be the result of the uneven distribution of such anthocyanin synthesis regulators as sugars and hormones in the fruits (Aramwit et al., 2010; Mo et al., 2022).

4 Conclusions

In this study, with Dashi and Siji mulberry varieties selected as research objects, and SPA, CARS and deep learning methods

SAE used to screen out feature variables, models for predicting anthocyanin content in mulberry fruits are built based on GA-LS-SVM and GA-ELM. The SAE-GA-ELM has achieved the best performance with R^2_c and R^2_p reaching the value of 0.97 under the condition of RMSEC and RMSEP being only 0.22 mg/g. By applying this best model to each pixel of the mulberry fruit images, distribution maps are created for visualizing the changes in anthocyanin content of mulberry fruits at three maturity stages. The results indicate that the hyperspectral imaging, in combination with SAE-GA-ELM could realize the fast, non-destructive, and high-precision detection of

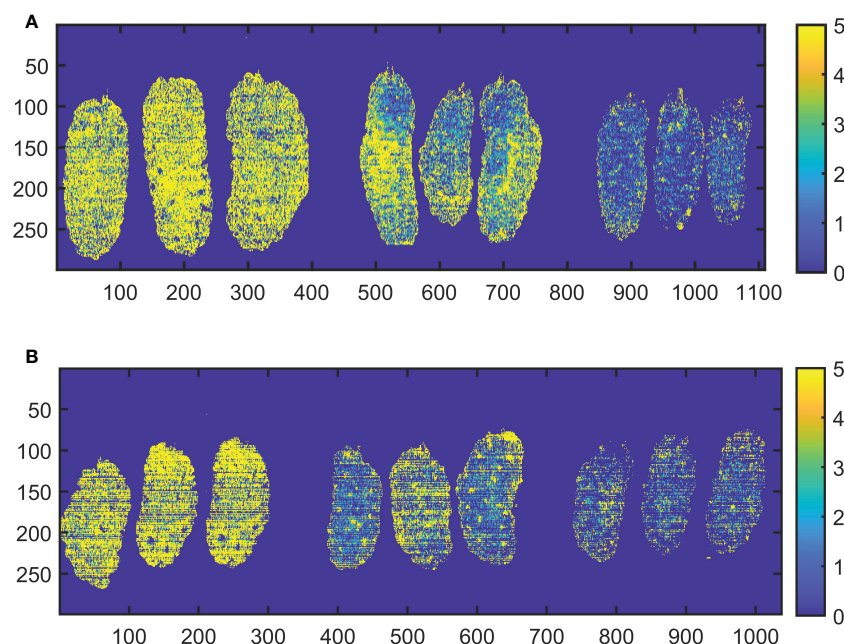


FIGURE 9

Visualization of anthocyanin content in mulberry fruits of Dashi (A) and Siji (B) at three maturity stages.

anthocyanin content of mulberry fruits, which means a new reference for rapid and nondestructive evaluation of physiological traits for the breeding, cultivation, harvesting and selling of the fruits.

Data availability statement

The raw data supporting the conclusions of this article will be made available by the authors, without undue reservation.

Author contributions

XL completed data collection, model construction, and paper writing. ZW and FP helped to collect data and provided comments and suggestions to improve the manuscript. JL edited the manuscript. GH directed the paper revision and provided the main idea. All authors contributed to the article and approved the submitted version.

Funding

This research was funded by Youth Innovation Team Project of Chongqing Academy of Agricultural Sciences (Grant No. NKY-

2019QC08), Performance Incentive and Guidance Special Project of Chongqing Research Institute (Grant No. cqaas2021jxjl08) and Excellent Germplasm Innovation Project of Chongqing (Grant No. NKY-2021AB019).

Conflict of interest

The authors declare that the research was conducted in the absence of any commercial or financial relationships that could be construed as a potential conflict of interest.

Publisher's note

All claims expressed in this article are solely those of the authors and do not necessarily represent those of their affiliated organizations, or those of the publisher, the editors and the reviewers. Any product that may be evaluated in this article, or claim that may be made by its manufacturer, is not guaranteed or endorsed by the publisher.

References

- Aramwit, P., Bang, N., and Srichana, T. (2010). The properties and stability of anthocyanins in mulberry fruits. *Food Res Int* 43, 4, 1093–1097. doi: 10.1016/j.foodres.2010.01.022
- Araújo, M. C. U., Saldanha, T. C. B., Galvao, R. K. H., Yoneyama, T., Chame, H. C., Visani, V. J. C., et al. (2001). The successive projections algorithm for variable selection in spectroscopic multicomponent

analysis. *Chemom. Intell. Lab. Syst. 57* (2), 65–73. doi: 10.1016/S0169-7439(01)00119-8

Chen, P.-N., Chu, S.-C., Chiou, H.-L., Kuo, W.-H., Chiang, C.-L., and Hsieh, Y.-S. (2006). Mulberry anthocyanins, cyanidin 3-rutinoside and cyanidin 3-glucoside, exhibited an inhibitory effect on the migration and invasion of a human lung cancer cell line. *Cancer Lett.* 235, 2, 248–259. doi: 10.1016/j.canlet.2005.04.033

Chen, S., Zhang, F., Ning, J., Liu, X., Zhang, Z., and Yang, S. (2015). Predicting the anthocyanin content of wine grapes by NIR hyperspectral imaging. *Food Chem.* 172, 788–793. doi: 10.1016/j.foodchem.2014.09.119

Cozzolino, D., Esler, M., Damberg, R., Cynkar, W., Boehm, D., Francis, I., et al. (2004). Prediction of colour and pH in grapes using a diode array spectrophotometer (400–1100 nm). *J. Near Infrared Spectrosc.* 12, 2, 105–111. doi: 10.1255/jnirs.414

ElMasry, G., Wang, N., Vigneault, C., Qiao, J., and ElSayed, A. (2008). Early detection of apple bruises on different background colors using hyperspectral imaging. *LWT - Food Sci. Technol.* 41, 2, 337–345. doi: 10.1016/j.lwt.2007.02.022

Huang, M., Wang, Q., Zhang, M., and Zhu, Q. (2014). Prediction of color and moisture content for vegetable soybean during drying using hyperspectral imaging technology. *J. Food Eng.* 128, 24–30. doi: 10.1016/j.jfoodeng.2013.12.008

Huang, G.-B., Zhou, H., Ding, X., and Zhang, R. (2011). Extreme learning machine for regression and multiclass classification. *IEEE Transactions on Systems, Man, and Cybernetics, Part B (Cybernetics)* 42, 2, 513–529. doi: 10.1109/TSMCB.2011.2168604

Huang, L., Zhou, Y., Meng, L., Wu, D., and He, Y. (2017). Comparison of different CCD detectors and chemometrics for predicting total anthocyanin content and antioxidant activity of mulberry fruit using visible and near infrared hyperspectral imaging technique. *Food Chem.* 224, 1–10. doi: 10.1016/j.foodchem.2016.12.037

Huang, G.-B., Zhu, Q.-Y., and Siew, C.-K. (2006). Extreme learning machine: Theory and applications. *Neurocomputing* 70, 1–3, 489–501. doi: 10.1016/j.neucom.2005.12.126

Jan, B., Parveen, R., Zahiruddin, S., Khan, M. U., Mohapatra, S., and Ahmad, S. (2021). Nutritional constituents of mulberry and their potential applications in food and pharmaceuticals: A review. *Saudi J. Biol. Sci.* 28, 7, 3909–3921. doi: 10.1016/j.sjbs.2021.03.056

Jiang, Y., and Nie, W.-J. (2015). Chemical properties in fruits of mulberry species from the xinjiang province of China. *Food Chem.* 174, 460–466. doi: 10.1016/j.foodchem.2014.11.083

Krishna, P. G. A., Sivakumar, T. R., Jin, C., Li, S.-H., Weng, Y.-J., Yin, J., et al. (2018). Antioxidant and hemolysis protective effects of polyphenol-rich extract from mulberry fruits. *Pharmacognosy Magazine* 14, 53, 103. doi: 10.4103/pm.pm_491_16

Lee, J., Durst, R. W., Wrolstad, R. E., and Kupina, C. (2005). Determination of total monomeric anthocyanin pigment content of fruit juices, beverages, natural colorants, and wines by the pH differential method: Collaborative study. *J. AOAC Int.* 88, 5, 1269–1278. doi: 10.1093/jaoac/88.5.1269

Li, H., Liang, Y., Xu, Q., and Cao, D. (2009). Key wavelengths screening using competitive adaptive reweighted sampling method for multivariate calibration. *Analytica Chimica Acta* 648, 1, 77–84. doi: 10.1016/j.aca.2009.06.046

Li, H., Yang, Z., Zeng, Q., Wang, S., Luo, Y., Huang, Y., et al. (2020). Abnormal expression of bHLH3 disrupts a flavonoid homeostasis network, causing differences in pigment composition among mulberry fruits. *Horticult. Res.* 7, 83. doi: 10.1038/s41438-020-0302-8

Liu, Y., Sun, Y., Xie, A., Yu, H., Yin, Y., Li, X., et al. (2017). Potential of hyperspectral imaging for rapid prediction of anthocyanin content of purple-fleshed sweet potato slices during drying process. *Food Anal. Methods* 10, 3836–3846. doi: 10.1007/s12161-017-0950-y

Mirjalili, S. (2019). “Genetic algorithm,” in *Evolutionary algorithms and neural networks* (Springer), 43–55.

Mo, R., Han, G., Zhu, Z., Essemine, J., Dong, Z., Li, Y., et al. (2022). The Ethylene Response Factor ERF5 Regulates Anthocyanin Biosynthesis in ‘Zijin’ Mulberry Fruits by Interacting with MYBA and F3H Genes. *Int. J. Mol. Sci.* doi: 10.3390/ijms23147615

Qin, J., and Lu, R. (2008). Measurement of the optical properties of fruits and vegetables using spatially resolved hyperspectral diffuse reflectance imaging technique. *Postharvest Biol. Technol.* 49, 3, 355–365. doi: 10.1016/j.postharvbio.2008.03.010

Saracoglu, O. (2018). Phytochemical accumulation of anthocyanin rich mulberry (*Morus laevigata*) during ripening. *Food Measure.* 12, 3, 2158–2163. doi: 10.1007/s11694-018-9831-3

Silva, R., and Melo-Pinto, P. (2021). A review of different dimensionality reduction methods for the prediction of sugar content from hyperspectral images of wine grape berries. *Appl. Soft Comput.* 113, 107889. doi: 10.1016/j.asoc.2021.107889

Sun, J., Zhou, X., Hu, Y., Wu, X., Zhang, X., Wang, P. J. C., et al. (2019). Visualizing distribution of moisture content in tea leaves using optimization algorithms and NIR hyperspectral imaging. *Comput. Electron. Agric.* 160, 153–159. doi: 10.1016/j.compag.2019.03.004

Suykens, J. A., and Vandewalle, J. (1999). Least squares support vector machine classifiers. *Neural Process. Lett.* 9, 3, 293–300. doi: 10.1023/A:1018628609742

Wong, K. I., Wong, P. K., Cheung, C. S., and Vong, C. (2013). Modeling and optimization of biodiesel engine performance using advanced machine learning methods. *LWT - Food Sci. Technol.* 55, 519–528. doi: 10.1016/j.lwt.2007.02.022

Xiao, Q., Bai, X., and He, Y. (2020). Rapid screen of the color and water content of fresh-cut potato tuber slices using hyperspectral imaging coupled with multivariate analysis. *Foods.* 9, 1, 94. doi: 10.3390/foods9010094

Xu, M., Sun, J., Yao, K., Cai, Q., Shen, J., Tian, Y., et al. (2022). Developing deep learning based regression approaches for prediction of firmness and pH in kyoho grape using Vis/NIR hyperspectral imaging. *Infrared Phys. Technol.* 120, 104003. doi: 10.1016/j.infrared.2021.104003

Yang, Y.-C., Sun, D.-W., Pu, H., Wang, N.-N., and Zhu, Z.-W. (2015). Rapid detection of anthocyanin content in lychee pericarp during storage using hyperspectral imaging coupled with model fusion. *Postharvest Biol. Technol.* 103, 55–65. doi: 10.1016/j.postharvbio.2015.02.008

Ye, A., Zhou, X., and Miao, F. (2022). Innovative hyperspectral image classification approach using optimized CNN and ELM. *Electronics.* 11, 5, 775. doi: 10.3390/electronics11050775

Yu, X., Lu, H., and Wu, D. (2018). Development of deep learning method for predicting firmness and soluble solid content of postharvest korla fragrant pear using Vis/NIR hyperspectral reflectance imaging. *Postharvest Biol. Technol.* 141, 39–49. doi: 10.1016/j.postharvbio.2018.02.013

Zheng, W., Fu, X., and Ying, Y. (2014). Spectroscopy-based food classification with extreme learning machine. *Chemom. Intell. Lab. Syst.* 139, 42–47. doi: 10.1016/j.chemolab.2014.09.015

Zheng, Y., Lai, X., Bruun, S. W., Ipsen, H., Larsen, J. N., Lföwenstein, H., et al. (2008). Determination of moisture content of lyophilized allergen vaccines by NIR spectroscopy. *J. Pharm. Biomed. Anal.* 46, 3, 592–596. doi: 10.1016/j.jpba.2007.11.011

Zhu, H., Chu, B., Fan, Y., Tao, X., Yin, W., and He, Y. (2017). Hyperspectral imaging for predicting the internal quality of kiwifruits based on variable selection algorithms and chemometric models. *Sci. Rep.* 7, 1, 1–13. doi: 10.1038/s41598-017-08509-6

Zou, T., Wang, D., Guo, H., Zhu, Y., Luo, X., Liu, F., et al. (2012). Optimization of microwave-assisted extraction of anthocyanins from mulberry and identification of anthocyanins in extract using HPLC-ESI-MS. *J. Food Sci.* 77, 1, C46–C50. doi: 10.1111/j.1750-3841.2011.02447



OPEN ACCESS

EDITED BY

Jinchang Ren,
Robert Gordon University, United Kingdom

REVIEWED BY

Zhiming Guo,
Jiangsu University, China
Liu Xiangjiang,
Zhejiang University, China

*CORRESPONDENCE

Guiyan Yang
✉ yanggy@nrcita.org.cn

SPECIALTY SECTION

This article was submitted to
Technical Advances in Plant Science,
a section of the journal
Frontiers in Plant Science

RECEIVED 27 February 2023

ACCEPTED 22 March 2023

PUBLISHED 03 April 2023

CITATION

Jin Y, Tian H, Gao Z, Yang G and Dong D
(2023) Oil content analysis of corn
seeds using a hand-held Raman
spectrometer and spectral peak
decomposition algorithm.
Front. Plant Sci. 14:1174747.
doi: 10.3389/fpls.2023.1174747

COPYRIGHT

© 2023 Jin, Tian, Gao, Yang and Dong. This
is an open-access article distributed under
the terms of the [Creative Commons
Attribution License \(CC BY\)](#). The use,
distribution or reproduction in other
forums is permitted, provided the original
author(s) and the copyright owner(s) are
credited and that the original publication in
this journal is cited, in accordance with
accepted academic practice. No use,
distribution or reproduction is permitted
which does not comply with these terms.

Oil content analysis of corn seeds using a hand-held Raman spectrometer and spectral peak decomposition algorithm

Yuan Jin^{1,2,3}, Hongwu Tian^{2,3}, Zhen Gao^{2,3,4}, Guiyan Yang^{2,3,5*}
and Daming Dong^{2,3}

¹School of Computer, Electronics and Information, Guangxi University, Nanning, China, ²Key Laboratory of Agricultural Sensors, Ministry of Agriculture and Rural Affairs, Beijing, China, ³Research Center of Intelligent Equipment, Beijing Academy of Agriculture and Forestry Sciences, Beijing, China, ⁴College of Information and Electrical Engineering, China Agricultural University, Beijing, China, ⁵College of Plant Science and Technology, Huazhong Agricultural University, Wuhan, China

Rapid, non-destructive and reliable detection of the oil content of corn seeds is important for development of high-oil corn. However, determination of the oil content is difficult using traditional methods for seed composition analysis. In this study, a hand-held Raman spectrometer was used with a spectral peak decomposition algorithm to determine the oil contents of corn seeds. Mature and waxy Zhengdan 958 corn seeds and mature Jingke 968 corn seeds were analyzed. Raman spectra were obtained in four regions of interest in the embryo of the seed. After analysis of the spectra, a characteristic spectral peak for the oil content was identified. A Gaussian curve fitting spectral peak decomposition algorithm was used to decompose the characteristic spectral peak of oil at 1657 cm^{-1} . This peak was used to determine the Raman spectral peak intensity for the oil content in the embryo and differences in the oil contents among seeds of varying maturity and different varieties. This method is feasible and effective for detection of corn seed oil.

KEYWORDS

Raman spectroscopy, spectral peak decomposition, Gaussian curve fitting, corn seed, oil content

1 Introduction

Corn is a leading food crop in China. Corn kernel is mainly composed of seed coat, endosperm and embryo, which contains starch, oil, protein, cellulose, lignin, and soluble sugar (Chen, 2009). Corn is a major source of human food, animal feed, and industrial raw materials (Abbassian, 2006). Corn oil is extracted from the germ of the corn kernel and is rich in unsaturated fatty acids and vitamin E, which are essential in the human body (Aksoz et al., 2020; Zhao et al., 2020). This oil is a popular, high-quality edible oil. The oil content of common corn is approximately 4%, while the oil content of high-oil corn is greater than

8% (Barrera-Arellano et al., 2019). Therefore, increasing the oil content and quality in corn is crucial for improving its value. At the same time, determining the oil content in corn is important for selective breeding of high-oil corn and transgenic engineering (Barrera-Arellano et al., 2019). However, traditional analytical methods (Matthäus et al., 2001), such as solvent extraction, accelerated solvent extraction, supercritical fluid extraction, microwave-assisted extraction, and Soxtherm extraction, are destructive, time-consuming, labor-intensive and use many chemical reagents. These methods are not suitable for rapid and non-destructive quality evaluation of mass-produced corn seeds. Consequently, it is necessary to develop rapid and non-destructive techniques for quality evaluation of corn seeds.

Spectroscopy is a rapid and non-destructive detection method (Huang et al., 2015), and has been successfully applied to the quality evaluation of agricultural products. Among them, near infrared spectroscopy (NIR) is an absorption spectrum that has been used to rapidly determine the compositions of grain seeds, including the oil content (Fassio et al., 2015), total starch content of corn seeds (Liu et al., 2020), and protein content of cowpeas (Weng et al., 2017). However, NIR is mainly related to frequency doubling and combined vibrations of hydrogen-containing chemical groups (e.g., C-H, O-H, and N-H) in organic molecules (Beć et al., 2020). Consequently, this technique suffers from serious overlap of spectral peaks, low sensitivity, and is susceptible to interference from water. It is difficult to directly analyze the chemical compositions of seeds using the absorption peak characteristics of a NIR spectrum, and this has resulted in a dependence on chemometrics for analysis.

Raman spectroscopy is an analytical technique that is based on Raman scattering, which originates from the vibration and rotation of molecules (Jones et al., 2019). The positions, intensities and shapes of the spectral peaks can reflect the characteristic fundamental frequency vibrations of the functional groups or chemical bonds in molecule of the target substance. Compared with NIR, Raman spectroscopy has high sensitivity, produces clear and sharp spectral peaks, and provides strong recognition ability, which makes the analysis of chemical composition more intuitive and concise. Wu X. et al. (2022) established a quantitative model based on Raman spectra and one-dimensional convolutional neural network (1D CNN) to identify the amount of olive oil in a corn-olive oil blend, providing a new analytical method for the quantitative identification of vegetable oils. Yang et al. (2018) showed that characteristic peaks related to corn starch, an oil-starch mixture, zeaxanthin, lignin, and oil were located at 477, 1443, 1522, 1596, and 1654 cm^{-1} , respectively. They realized rapid visual detection of the chemical composition of corn seeds using a line-scanning Raman hyperspectral imaging system. These studies indicate that Raman spectroscopy can be used to analyze the composition of corn seeds.

In recent years, because of continuous improvement in the performance of optical devices and other components, hand-held Raman spectrometers, which are small, flexible to use, simple to operate, and provide stable performance, have been favored by

researchers. Farber and Kurouski (2018) analyzed the Raman spectra of corn seeds before and after pathogen infection using a hand-held Raman spectrometer. After infection, a peak at 1633 cm^{-1} for C=C vibration in the aromatic ring of lignin disappeared, which indicating that the lignin degraded. Furthermore, a peak at 1658 cm^{-1} belonging to the protein amide I band became stronger, which showed that growth of the pathogen was closely related to deposition of protein in corn. Additionally, spectral peaks related to the -C=C-plane vibration of carotenoid shifted and increased in intensity. Therefore, the growth of pathogens may be related to degradation and breaking of bonds in carotenoid. These studies show that a hand-held Raman spectrometer may be feasible for seed composition analysis. Although Raman spectroscopy can be used simultaneous measurement of various compositions of seeds, the Raman characteristic peaks of oil in corn seeds suffer from interference from starch, protein, lignin, and other compositions (Yang et al., 2018). To overcome this issue, Raman spectroscopy could be combined with a spectral peak decomposition algorithm to realize the identification, classification, and quantification of composition (Postnikov et al., 2021). Sadat and Joye (2020) used a peak decomposition method based on the second derivative of the original spectrum and the curve fitting of the Voigt function to identify, separate and quantify hidden peaks of the amide I band in the infrared and Raman spectra of globular proteins, hydrated zein and gluten proteins. Wu T. et al. (2022) proposed an optimal multi-peak fitting model for the first-order and second-order Raman spectra of high-strength carbon fibers (T-series) and high-strength and high-modulus carbon fibers (MJ series), and quantitatively analyzed the structure of the carbon fiber.

The primary aim of this study was to realize the oil content analysis of corn seeds using a hand-held Raman spectroscopy combined with a peak decomposition algorithm. The Raman spectral characteristics of the corn seed embryo were studied, and spectral information for the oil content in the corn seeds was extracted and analyzed using a spectral peak decomposition algorithm. Differences in the oil content for corn seeds of different varieties and maturities were compared and analyzed.

2 Materials and methods

2.1 Experimental materials

Corn seeds of the Zhengdan 958 and Jingke 968 varieties were obtained from a seed company in Beijing, China. Fifty seeds of the Zhengdan 958 variety were selected and divided into two groups according to the milk line of endosperm. 25 of the seeds were mature and the others were waxy. For the Jingke 968 variety, 25 mature seeds were selected. Standard samples, including corn starch (reagent grade, Aladdin Reagent Co., Ltd., Shanghai, China), corn oil (reagent grade, Aladdin Reagent Co., Ltd., Shanghai, China), cellulose (reagent grade, Aladdin Reagent Co., Ltd., Shanghai, China), and corn hulls, were obtained for analyzing the Raman characteristics of the corn seeds.

2.2 Instruments

Raman spectra of the standard samples were collected using a high-resolution benchtop Raman spectrometer (DXR Smart Raman System, Thermo Fisher Scientific). The spectrometer was equipped with a 780 nm diode laser with a maximum power of 150 mW. The spectral resolution was 3.0–4.1 cm^{-1} , and the spectral range was 50–1800 cm^{-1} . The optical power was 100 mW and the integration time was 10 s.

Raman spectra of the corn seeds were collected using a hand-held Raman spectrometer (785 hand-held Raman spectrometer, Beijing Yunduan Optical Technology Co., Ltd.). The hand-held Raman spectrometer was equipped with a 785 nm laser. The laser power was continuously adjustable from 1 to 500 mW. The spectral resolution was approximately 8.0 cm^{-1} , and the spectral range is 200–1800 cm^{-1} . The optical power was 150 mW and the integration time was 10 s.

2.3 Spectral data acquisition

Standard samples (corn starch, corn oil, cellulose, and hulls) were placed on a quartz plate, which was set on the sampling platform of DXR Smart Raman System for spectral acquisition. For the Zhengdan 958 seeds, the mature seeds were labeled as group D1 and the waxy seeds as group D2. The Jingke 968 seeds were labeled as group D3. Four regions of interest (ROIs) for detection (P1, P2, P3, and P4) were set from the top to bottom along the midline of the embryo of the corn seed (Figure 1A). The Raman spectra of the ROIs were collected by the acquisition system shown in Figure 1B. The acquisition system consisted of a hand-held Raman spectrometer, a movable platform, a sample rack, and an optical breadboard. The hand-held Raman spectrometer was placed horizontally on the left of the mobile platform. The seed sample was placed vertically on the right of the mobile platform, with the P1 end of the seed facing down and the tip of the embryo facing up. The embryonic surface of the seed faced the Raman probe. First, the laser was focused on P1 and Raman spectral data were collected. Then, the movable platform was adjusted to move the sample downward, and spectral data were collected at P2. This process was repeated for P3 and P4. During spectral collection, the four ROIs of each seed were as similar as possible. The spectra of the standard samples were used as reference data for the spectral analysis of the seeds.

2.4 Spectral data preprocessing

Firstly, the Savitzky–Golay smoothing algorithm was used to remove noise from the original Raman spectra of the corn seeds (Schafer, 2011). Then, the smooth Raman spectra were corrected using the airPLS algorithm to remove fluorescent background interference (Zhang et al., 2010). The corrected Raman spectral data were used for subsequent spectral peak decomposition and spectral information extraction. The preprocessing of all raw Raman spectra was performed in Visual Studio Code (Microsoft Corporation, Redmond, WA, United States).

2.5 Spectral peak decomposition

Decomposition of overlapping spectral peaks can be used for separation and extraction of effective spectral information. Previous studies have shown that curve fitting is an effective spectral peak decomposition method. It is based on statistical principles, which aims to find a reliable function to fit a set of data points and minimize the error between the function and the data point. And the least square method is a common functional form. In this study, curve fitting based on nonlinear least square method was selected for spectral peak decomposition, and the Gaussian linear function was selected as the fitting model. The expression of the Gaussian function is shown in Equation 1:

$$y = ae^{-\frac{(x-\mu)^2}{2\sigma^2}} \quad (1)$$

where a is the peak intensity, μ is the peak position, and σ is the full width at half maximum. With three overlapping spectral peaks, the original spectral peaks were regarded as a ternary Gaussian linear distribution, and a function expression was constructed as shown in Equation 2:

$$y = a_1 e^{-\frac{(x-\mu_1)^2}{2\sigma_1^2}} + a_2 e^{-\frac{(x-\mu_2)^2}{2\sigma_2^2}} + a_3 e^{-\frac{(x-\mu_3)^2}{2\sigma_3^2}} \quad (2)$$

According to Equation 2, the original overlapping spectral peaks were iteratively analyzed by curve fitting to obtain the values of the Gaussian parameters a_1 , μ_1 , σ_1 , a_2 , μ_2 , σ_2 , a_3 , μ_3 , and σ_3 . Then, three Gaussian spectral peaks $a_1 e^{-\frac{(x-\mu_1)^2}{2\sigma_1^2}}$, $a_2 e^{-\frac{(x-\mu_2)^2}{2\sigma_2^2}}$, $a_3 e^{-\frac{(x-\mu_3)^2}{2\sigma_3^2}}$ were obtained by decomposition of the overlapping peaks and used for information extraction. All

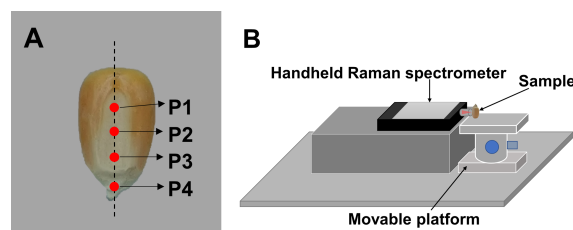


FIGURE 1

Schematic diagram of the Raman spectrum acquisition. (A) Locations of the four regions of interest in the embryo for detection, and (B) the acquisition system for the Raman spectra of the corn seeds.

overlapping peaks of Raman spectra were decomposed in Visual Studio Code.

3 Results and discussion

3.1 Analysis of Raman spectral characteristics of oil in corn seeds

Corn oil is mainly stored in the embryo of the seed. To analyze the Raman spectral characteristics of oil in the corn seeds, the standard spectra of corn oil, corn starch, cellulose, and hulls collected by the DXR Smart Raman system were regarded as the reference spectra and compared with the Raman spectra of the embryo collected by the hand-held Raman (Figure 2). Prominent characteristic peaks in the standard corn oil sample were located at 1656, 1439, 1301, and 1267 cm^{-1} , which are attributed to C=C stretching, CH_2 or CH_3 deformation vibrations, CH_2 twisting, and =C-H bending, respectively (Gelder et al., 2007; Anna et al., 2017). The 1656 cm^{-1} spectral peak in the seed embryo spectrum overlapped with spectral peaks at 1600 and 1632 cm^{-1} , which were attributed to C-H stretching of the aromatic ring and C=C stretching in coniferyl aldehyde, respectively, derived from lignin in the hull (Lupoi and Smith, 2012; Zeng et al., 2016). In the spectrum of the seed embryo, there was serious overlapping between the 1439 cm^{-1} peak of corn oil and the band located at approximately 1460 cm^{-1} for CH_2 bending of starch (Liu et al., 2004). Furthermore, the spectral peaks of corn oil located at 1301 and 1267 cm^{-1} overlapped with a peak at 1263 cm^{-1} related to starch (Kizil et al., 2002) and peaks at 1336 and 1379 cm^{-1} related to cellulose (Wiley and Atalla, 1987; Kryeziu et al., 2022). Compared with the standard spectrum of corn oil, the spectrum of the seed embryo had a very different ratio between the peaks at 1301 and 1267 cm^{-1} . These results indicate that the 1656 cm^{-1} peak is the

most suitable among the characteristic peaks for the spectral analysis of oil in corn seeds.

3.2 Raman peak decomposition analysis of oil in corn seeds

A Raman spectrum of the P1 ROI was selected from each group (D1, D2, and D3) of corn seeds, and the 1560–1680 cm^{-1} region was selected for spectral peak decomposition analysis to extraction information about the oil content. There were multiple overlapping peaks in the 1560–1680 cm^{-1} region (Figure 2). The original spectral peaks were regarded as a distribution of three Gaussian spectral peaks. A function expression was constructed as shown in Equation 2, and decomposition of the spectral peaks was carried out. The fitting parameters a_1 , μ_1 , σ_1 , a_2 , μ_2 , σ_2 , a_3 , μ_3 , and σ_3 for the three Gaussian spectral peaks (A, B, and C) were calculated (Table 1). The decomposition results for the overlapping peaks are shown in Figures 3A–C. There were slight differences in the positions of the peaks among the three groups of the seeds. Peaks A and B were consistent with lignin, and peak C could be used to determine the oil content. Our results showed that the overlapping spectral peaks were successfully decomposed into three Gaussian spectral peaks for each group of corn seeds. The relative errors between the fitted and original spectra were 8.68%, 7.71%, and 12.72% for D1, D2, and D3, respectively. The relative error was obtained by subtracting the fitting value from the original value, dividing by the original value, then taking the absolute value of the result, adding all the absolute values, and dividing by the total number of data points. The Raman peak for the oil content was successfully separated from any overlapping spectral peaks using the peak decomposition algorithm (Figure 3D). The spectra of the mature seeds (groups D1 and D3) were similar, whereas that of the waxy seeds (group D2) was very different.

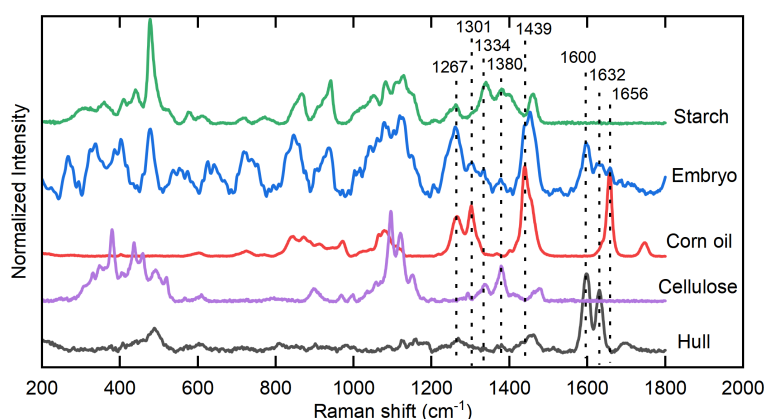


FIGURE 2

Analysis of the Raman spectral characteristics of oil in corn seeds. Characteristic peaks of corn embryo located at 1267, 1301, 1439, 1656 cm^{-1} are related to standard corn oil sample, 1334, 1380 cm^{-1} are related to standard cellulose sample, and 1600, 1632 cm^{-1} are related to hull. At the same time, 1267, 1301, 1334, 1380, 1439 cm^{-1} are affected by the peaks of starch.

TABLE 1 Fitting parameters for spectral peak decomposition in the 1560–1680 cm^{-1} region for corn seed spectra.

Seed	Fitting parameters of spectral peak									Decomposition spectral peaks			Relative error
	a_1	μ_1	σ_1	a_2	μ_2	σ_2	a_3	μ_3	σ_3	Peak A	Peak B	Peak C	
D1	1028	1599	15	661	1632	8	702	1657	10	$1028 \times e^{-\frac{(x-1599)^2}{450}}$	$661 \times e^{-\frac{(x-1632)^2}{128}}$	$702 \times e^{-\frac{(x-1657)^2}{200}}$	8.68%
D2	642	1598	15	292	1630	6	408	1654	13	$642 \times e^{-\frac{(x-1598)^2}{450}}$	$292 \times e^{-\frac{(x-1630)^2}{72}}$	$408 \times e^{-\frac{(x-1654)^2}{338}}$	7.71%
D3	618	1599	15	449	1631	8	705	1657	10	$618 \times e^{-\frac{(x-1599)^2}{450}}$	$449 \times e^{-\frac{(x-1631)^2}{128}}$	$705 \times e^{-\frac{(x-1657)^2}{200}}$	12.72%

3.3 Analysis of the oil content in the embryos of different corn seeds

To analyze the Raman characteristics of the oil content in the embryos of different corn seeds, the Raman spectra of the different groups (D1, D2, and D3; 25 seeds for each group) were decomposed using the Gaussian curve fitting algorithm in the 1560–1680 cm^{-1} region. The maximum intensity of the decomposed peak C for oil was extracted for analysis. To analyze the different ROIs (P1, P2, P3, and P4) in the embryos, scatter plots of the maximum intensities of peak C were constructed (Figures 4A–C). The maximum intensities of peak C in the P1, P2, and P3 ROIs were scattered throughout the same region of the plots and these ROIs could not be clearly distinguished. By contrast, all data points for the P4 ROI were located at the bottom of the scatter plots and clearly separated from the data points for the P1, P2, and P3 ROIs.

To analyze the differences in the Raman intensities in the four ROIs, the mean intensities of peak C for the four ROIs for the 25 seeds in each group were calculated. The distribution of mean intensities and the corresponding standard deviations for the three groups of seeds are shown in Figure 4D. There were slight differences in the mean spectral intensities of peak C for the P1, P2, and P3 ROIs in the embryos of the three groups of corn seeds. However, the mean intensity of peak C for the P4 ROI was significantly lower than in the P1, P2, and P3 ROIs. This difference is consistent with the fact that corn oil is mainly distributed in the germ (Moreau and Hicks, 2005) and shows that the Raman peak at 1657 cm^{-1} can be used to characterize the oil content. To better characterize the oil content in the seeds and improve the stability and reliability of detection, the mean maximum intensity of the 1657 cm^{-1} peak in the P1, P2 and P3 ROIs was selected.

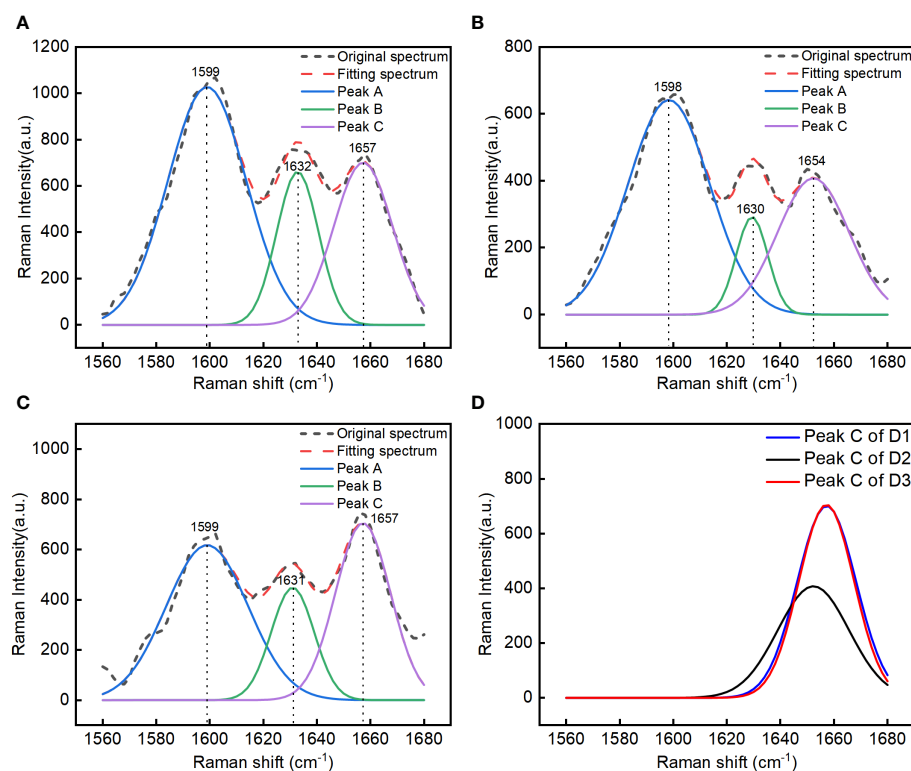


FIGURE 3

Spectral peak decomposition analysis of different kinds of corn seeds in the 1560–1680 cm^{-1} region: group D1 (mature Zhengdan 958) seeds (A), group D2 (waxy Zhengdan 958) seeds (B), and group D3 (Jingke 968) seeds (C). Comparative analysis of the separated spectral peak for oil in the three groups of seeds (D).

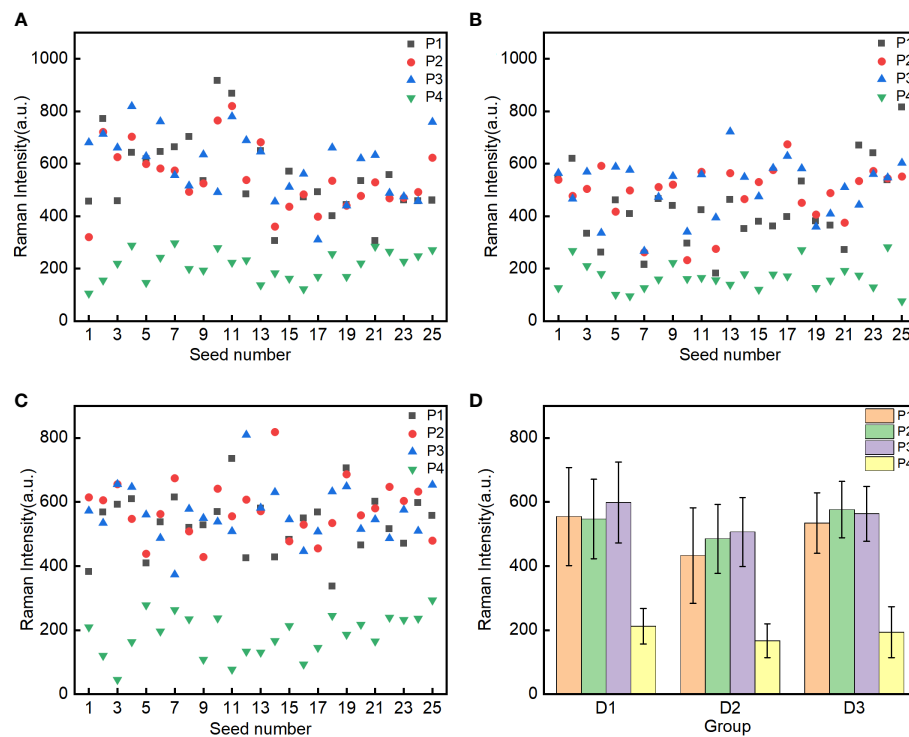


FIGURE 4

Spectral intensity analysis of peak C in the four regions of interest (P1-Point 1, P2-Point 2, P3-Point 3 and P4-Point 4 of embryo) in the three groups of seeds: mature Zhengdan 958 D1 (A), waxy Zhengdan 958 D2 (B) and Jingke 968 D3 (C). The mean spectral intensities in the P1, P2, P3, and P4 regions of interest in the embryo of three groups seeds (D).

To analyze the difference in the oil content between the groups of corn seeds, the oil characterization value was calculated for every individual seed in each group. The characterization values of the 25 seeds in each group were arranged in ascending order (Figure 5A). The characteristic values of the seeds in groups D1 and D2 fluctuate greatly with the number of seeds, while those of the D3 seeds are relatively stable. The characteristic values of the seeds in groups D1

and D2 were spread over a wider range than those for the D3 seeds. These results showed that the oil content of individual seed in the D1 and D2 groups is significantly different, and the oil content in the D3 group has little difference among individual seeds. To analyze the differences in the oil contents among the three groups of corn seeds, the mean oil characterization values of all 25 seeds in each group were calculated to characterize the overall oil content of

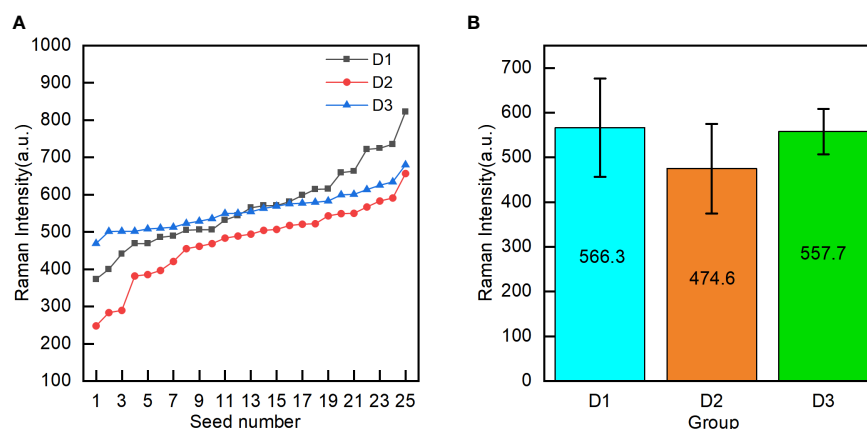


FIGURE 5

Oil content characterization values (the mean intensity of peak C in the embryo) of individual seeds in the three groups (D1-mature Zhengdan 958, D2-waxy Zhengdan 958, and D3-Jingke 968) (A), and the mean oil content characterization value for each group (B).

each group (Figure 5B). The seeds in group D2 had the lowest mean value (474.6). The seeds in group D1 had a mean value of 566.3, which was significantly higher than that of the seeds in group D2 and not significantly different from that of the seeds in group D3 (557.7). The seeds in group D1 and group D2 were the same variety (Zhengdan 958). For seeds of the same variety, the relative oil content was correlated with the seed maturity, with the oil content of mature seeds being higher than that of waxy seeds. Among different varieties, the oil content in the Jingke 968 (D3 group) was similar to that in the Zhengdan 958 variety; the results for the Jingke 968 variety showed less variation among the individual seeds in the group than was observed for the Zhengdan 958 variety.

4 Conclusions

The feasibility of detecting the oil content of corn seeds using a hand-held Raman spectrometer with a spectral peak decomposition algorithm was explored. The Raman peak at 1657 cm^{-1} for the oil content was successfully separated from overlapping spectral peaks using a Gaussian curve fitting peak decomposition algorithm. The intensity distribution characteristics of the 1657 cm^{-1} spectral peak in different ROIs of the embryo showed that the oil content of the corn seed was mainly distributed in the germ. The oil content for individual seeds was characterized using the maximum intensity of the 1657 cm^{-1} peak. For the same variety of corn seeds, the oil content was positively correlated with seed maturity, with the oil content of mature seeds being higher than that of waxy seeds. For different varieties of corn seeds, the oil content of Jingke 968 variety was similar to that of Zhengdan 958 variety, but the oil contents of individual seeds of the Jingke 968 variety showed less variation within the group than was observed for the Zhengdan 958 variety. Our results show that a hand-held Raman spectrometer combined with spectral peak decomposition can provide rapid and non-destructive determination of the oil content of corn seeds. This study provides a basis for the quantitative detection of oil in corn or other varieties of grain. This method could be used to rapidly identify and select corn seeds with high oil contents for selective breeding.

References

- Abbassian, A. (2006). *Maize International Market Profile* (Rome: Food and Agriculture Organization of the United Nations), 1–37.
- Aksoz, E., Korkut, O., Aksit, D., and Gokbulut, C. (2020). Vitamin e (α -, β + γ - and δ -tocopherol) levels in plant oils. *Flavour Frag. J.* 35 (5), 504–510. doi: 10.1002/ffj.3585
- Anna, I., Bartosz, P., Lech, P., and Halina, A. (2017). Novel strategies of raman imaging for brain tumor research. *Oncotarget* 8 (49), 85290. doi: 10.18632/oncotarget.19668
- Barrera-Arellano, D., Badan-Ribeiro, A. P., and Serna-Saldivar, S. O. (2019). “Corn oil: composition, processing, and utilization,” in *Corn*, ed. S. O. Serna-Saldivar (Amsterdam: AACC International Press), 593–613. doi: 10.1016/B978-0-12-811971-6.00021-8
- Beć, K. B., Grabska, J., and Huck, C. W. (2020). NIR spectroscopy of natural medicines supported by novel instrumentation and methods for data analysis and interpretation. *J. Pharm. Biomed. Anal.* 193, 113686. doi: 10.1016/j.jpba.2020.113686
- Chen, J. (2009). *Maize starch industry Manual (Fine)*. (Beijing: China Light Industry Press).
- Farber, C., and Kurouski, D. (2018). Detection and identification of plant pathogens on maize kernels with a hand-held raman spectrometer. *Anal. Chem.* 90 (5), 3009–3012. doi: 10.1021/acs.analchem.8b00222
- Fassio, A. S., Restaino, E. A., and Cozzolino, D. (2015). Determination of oil content in whole corn (zea mays L.) seeds by means of near infrared reflectance spectroscopy. *Comput. Electron. Agr.* 110, 171–175. doi: 10.1016/j.compag.2014.11.015

Data availability statement

The original contributions presented in the study are included in the article/supplementary material. Further inquiries can be directed to the corresponding author.

Author contributions

YJ, HT, ZG, GY and DD contributed to the conception and design of the study. YJ and HT carried out the experiment and analyzed the experimental data. YJ and ZG wrote the first draft of the manuscript. GY and DD presented the revision of the manuscript. All authors contributed to the article and approved the submitted version.

Funding

This research was financially supported by the National Key R&D Program of China (2022YFD2000800), Special financial Project of Beijing Academy of Agriculture and Forestry Sciences (CZZJ202204) and Beijing Innovation Consortium of Agriculture Research System (BAIC08-2023-FQ04).

Conflict of interest

The authors declare that the research was conducted in the absence of any commercial or financial relationships that could be construed as a potential conflict of interest.

Publisher's note

All claims expressed in this article are solely those of the authors and do not necessarily represent those of their affiliated organizations, or those of the publisher, the editors and the reviewers. Any product that may be evaluated in this article, or claim that may be made by its manufacturer, is not guaranteed or endorsed by the publisher.

- Gelder, J. D., Gussem, K. D., Vandenabeele, P., and Moens, L. (2007). Reference database of raman spectra of biological molecules. *J. Raman Spectrosc.* 38 (9), 1133–1147. doi: 10.1002/jrs.1734
- Huang, M., Wang, Q. G., Zhu, Q. B., Qin, J. W., and Huang, G. (2015). Review of seed quality and safety tests using optical sensing technologies. *Seed Sci. Technol.* 43 (3), 337–366. doi: 10.15258/sst.2015.43.3.16
- Jones, R. R., Hooper, D. C., Zhang, L., Wolverson, D., and Valev, V. K. (2019). Raman techniques: Fundamentals and frontiers. *Nanoscale Res. Lett.* 14 (1), 1–34. doi: 10.1186/s11671-019-3039-2
- Kizil, R., Irudayaraj, J., and Seetharaman, K. (2002). Characterization of irradiated starches by using FT-Raman and FTIR spectroscopy. *J. Agric. Food Chem.* 50 (14), 3912–3918. doi: 10.1021/jf011652p
- Kryeziu, A., Slovak, V., Parmentier, J., Zelenka, T., and Rigolet, S. (2022). Porous carbon monoliths from ice-NaOH templated dissolved cellulose. *Ind. Crop Prod.* 183, 114961. doi: 10.1016/j.indcrop.2022.114961
- Liu, Y., Himmelsbach, D. S., and Barton, F. E. (2004). Two-dimensional Fourier transform Raman correlation spectroscopy determination of the glycosidic linkages in amylose and amylopectin. *Appl. Spectrosc.* 58 (6), 745–749. doi: 10.1366/000370204873006
- Liu, C., Huang, W., Yang, G., Wang, Q., and Li, J. (2020). Determination of starch content in single kernel using near-infrared hyperspectral images from two sides of corn seeds. *Infrared Phys. Techn.* 110, 103462. doi: 10.1016/j.infrared.2020.103462
- Lupoi, J. S., and Smith, E. A. (2012). Characterization of woody and herbaceous biomasses lignin composition with 1064 nm dispersive multichannel Raman spectroscopy. *Appl. Spectrosc.* 66 (8), 903–910. doi: 10.1366/12-06621
- Moreau, R. A., and Hicks, K. B. (2005). The composition of corn oil obtained by the alcohol extraction of ground corn. *J. Am. Oil Chem. Soc.* 82 (11), 809–815. doi: 10.1007/s11746-005-1148-4
- Postnikov, E. B., Lebedeva, E. A., Zyubin, A. Y., and Lavrova, A. I. (2021). The cascade Hilbert-zero decomposition: A novel method for peaks resolution and its application to Raman spectra. *Mathematics* 9 (21), 2802. doi: 10.3390/math9212802
- Sadat, A., and Joye, I. J. (2020). Peak fitting applied to Fourier transform infrared and Raman spectroscopic analysis of proteins. *Appl. Sci.* 10 (17), 5918. doi: 10.3390/app10175918
- Schafer, R. W. (2011). What is a Savitzky-Golay filter? [Lecture notes]. *IEEE Signal Proc. Mag.* 28 (4), 111–117. doi: 10.1109/MSP.2011.941097
- Matthäus, B., and Brühl, L. (2001). Comparison of different methods for the determination of the oil content in oilseeds. *J. Am. Oil Chem. Soc.* 78 (1), 95–102. doi: 10.1007/s11746-001-0226-y
- Weng, Y., Shi, A., Ravelombola, W. S., Yang, W., Qin, J., Motes, D., et al. (2017). A rapid method for measuring seed protein content in cowpea (*Vigna unguiculata* (L.) Walp.). *Am. J. Plant Sci.* 8 (10), 2387. doi: 10.4236/ajps.2017.810161
- Wiley, J. H., and Atalla, R. H. (1987). Band assignments in the Raman spectra of celluloses. *Carbohydr. Res.* 160, 113–129. doi: 10.1016/0008-6215(87)80306-3
- Wu, X., Gao, S., Niu, Y., Zhao, Z., Ma, R., Xu, B., et al. (2022). Quantitative analysis of blended corn-olive oil based on Raman spectroscopy and one-dimensional convolutional neural network. *Food Chem.* 385, 132655. doi: 10.1016/j.foodchem.2022.132655
- Wu, T., Lu, C., Sun, T., and Li, Y. (2022). Study on Raman multi-peak fitting and structure quantitative analysis of PAN-based carbon fibers. *J. Mater. Sci.* 57 (32), 15385–15412. doi: 10.1007/s10853-022-07589-8
- Yang, G., Wang, Q., Liu, C., Wang, X., Fan, S., and Huang, W. (2018). Rapid and visual detection of the main chemical compositions in maize seeds based on Raman hyperspectral imaging. *Spectrochim. Acta A* 200, 186–194. doi: 10.1016/j.saa.2018.04.026
- Zeng, Y., Yarbrough, J. M., Mittal, A., Tucker, M. P., Vinzant, T. B., Decker, S., et al. (2016). *In situ* label-free imaging of hemicellulose in plant cell walls using stimulated Raman scattering microscopy. *Biotechnol. Biofuels* 9 (1), 1–16. doi: 10.1186/s13068-016-0669-9
- Zhang, Z. M., Chen, S., and Liang, Y. Z. (2010). Baseline correction using adaptive iteratively reweighted penalized least squares. *Analyst* 135 (5), 1138–1146. doi: 10.1039/b922045c
- Zhao, M., Lan, Y., Cui, L., Monono, E., Rao, J., and Chen, B. (2020). Formation, characterization, and potential food application of rice bran wax oleogels: Expeller-pressed corn germ oil versus refined corn oil. *Food Chem.* 309, 125704. doi: 10.1016/j.foodchem.2019.125704



OPEN ACCESS

EDITED BY

Leizi Jiao,
Beijing Academy of Agriculture and
Forestry Sciences, China

REVIEWED BY

Rui Shi,
North Carolina State University,
United States
Steven D. Karlen,
University of Wisconsin-Madison,
United States

*CORRESPONDENCE

Arthur J. Ragauskas
✉ aragausk@utk.edu

SPECIALTY SECTION

This article was submitted to
Technical Advances in Plant Science,
a section of the journal
Frontiers in Plant Science

RECEIVED 28 January 2023

ACCEPTED 03 April 2023

PUBLISHED 05 May 2023

CITATION

Bryant N, Zhang J, Feng K, Shu M, Ployet R,
Chen J-G, Muchero W, Yoo CG,
Tschaplinski TJ, Pu Y and Ragauskas AJ
(2023) Novel candidate genes for lignin
structure identified through genome-wide
association study of naturally varying
Populus trichocarpa.
Front. Plant Sci. 14:1153113.
doi: 10.3389/fpls.2023.1153113

COPYRIGHT

© 2023 Bryant, Zhang, Feng, Shu, Ployet,
Chen, Muchero, Yoo, Tschaplinski, Pu and
Ragauskas. This is an open-access article
distributed under the terms of the [Creative
Commons Attribution License \(CC BY\)](#). The
use, distribution or reproduction in other
forums is permitted, provided the original
author(s) and the copyright owner(s) are
credited and that the original publication in
this journal is cited, in accordance with
accepted academic practice. No use,
distribution or reproduction is permitted
which does not comply with these terms.

Novel candidate genes for lignin structure identified through genome-wide association study of naturally varying *Populus trichocarpa*

Nathan Bryant¹, Jin Zhang², Kai Feng², Mengjun Shu²,
Raphael Ployet², Jin-Gui Chen², Wellington Muchero²,
Chang Geun Yoo³, Timothy J. Tschaplinski², Yunqiao Pu²
and Arthur J. Ragauskas^{1,2,4*}

¹Department of Chemical and Biomolecular Engineering, University of Tennessee, Knoxville, TN, United States, ²Center for Bioenergy Innovation, Biosciences Division, Oak Ridge National Laboratory, Oak Ridge, TN, United States, ³Department of Chemical Engineering, State University of New York College of Environmental Science and Forestry, Syracuse, NY, United States, ⁴Center for Renewable Carbon, Department of Forestry, Wildlife, and Fisheries, University of Tennessee Institute of Agriculture, Knoxville, TN, United States

Populus is a promising lignocellulosic feedstock for biofuels and bioproducts. However, the cell wall biopolymer lignin is a major barrier in conversion of biomass to biofuels. To investigate the variability and underlying genetic basis of the complex structure of lignin, a population of 409 three-year-old, naturally varying *Populus trichocarpa* genotypes were characterized by heteronuclear single quantum coherence (HSQC) nuclear magnetic resonance (NMR). A subsequent genome-wide association study (GWAS) was conducted using approximately 8.3 million single nucleotide polymorphisms (SNPs), which identified 756 genes that were significantly associated ($-\log_{10}(p\text{-value}) > 6$) with at least one lignin phenotype. Several promising candidate genes were identified, many of which have not previously been reported to be associated with lignin or cell wall biosynthesis. These results provide a resource for gaining insights into the molecular mechanisms of lignin biosynthesis and new targets for future genetic improvement in poplar.

KEYWORDS

genome-wide association studies (GWAS), *Populus*, nuclear magnetic resonance (NMR) analysis, lignin, p-hydroxybenzoate

1 Introduction

Poplar (*Populus* sp.) is a promising lignocellulosic biomass feedstock due to its fast growth, ability to grow on marginal land, high cellulose content, and relatively low lignin content (Sannigrahi et al., 2010; Bryant et al., 2020). However, lignocellulosic biomass exhibits tremendous variability in cell wall traits, such as composition and structure. Cell

wall structure and composition depend on factors such as environmental conditions (i.e., drought, cold stresses), biomass type (i.e., woody vs. herbaceous), tissue (i.e., stem vs. leaf), and genetic variations. One cell wall component that demonstrates a high degree of variability is lignin. Lignin is a complex and heterogeneous biopolymer that accounts for 18–32% (dry weight) of *Populus* (Sannigrahi et al., 2010; Li et al., 2016). It serves several important biological functions, including water transport, providing mechanical strength, and response to environmental stresses (Liu et al., 2018). However, since it acts as a natural barrier against pathogens, it is one of the main factors contributing to biomass recalcitrance to biological conversion to biofuels. Lignin is typically comprised of three primary monomers synthesized through the general phenylpropanoid and monolignol specific pathways: sinapyl alcohol, coniferyl alcohol, and *p*-coumaryl alcohol. When exported to the apoplast, these monolignols are oxidized by laccases and/or peroxidases, and then undergo radical cross-coupling reactions. Once coupled into the lignin polymer, these alcohols are identified as syringyl (S), guaiacyl (G), and *p*-hydroxyphenyl (H) units, respectively (Bose et al., 2009). It has also been shown that lignin demonstrates plasticity by incorporating non-canonical monolignols into the polymer, such as *p*-hydroxybenzoates (PB) (del Río et al., 2020). These units are incorporated into the lignin polymer *via* a variety of interunit bonds, such as aryl ether (β -O-4), resinol (β - β), and phenylcoumaran (β -5), among others. The structure of lignin has potential bioenergy implications, as evidenced by the lignin S/G ratio association with biomass digestibility and conversion to biofuels (Li et al., 2016). Lignin structure can also influence lignin valorization. For instance, acetaminophen, the active ingredient in Tylenol, can be synthesized from the PB moiety (Ralph et al., 2019).

The formation of the secondary cell wall requires coordination of many metabolic pathways (Zhang et al., 2018a), presenting challenges in linking phenotypes to genetic mutations. Additionally, complex traits such as lignin are often controlled by several multigenic families. Genome-wide association studies (GWAS) are powerful tools for identifying polymorphic loci that contribute to phenotypic variation and sometimes trace-back to the genes or biological mechanisms involved. Due to the large sample size required for GWAS, high throughput techniques are typically utilized to analyze lignin traits. However, high throughput methods such as pyrolysis molecular beam mass spectroscopy (Py-MBMS) or near-infrared (NIR) spectroscopy provide limited information on lignin composition. These methods are generally used to estimate only the relative lignin to sugars ratio within the cell walls, or the S/G ratio for lignin itself. Genomic association mapping has been successfully employed on *Populus* for bioenergy traits including lignin content and S/G ratio (Porth et al., 2013; Fahrenkrog et al., 2017), biomass yield (Allwright et al., 2016), and cell wall sugars (Guerra et al., 2013). Consequently, the genetic basis of most lignin traits remains understudied by GWAS, and new methods for characterization of lignin phenotypes are urgently required. In comparison to Py-MBMS or NIR, the analytical technique heteronuclear single quantum coherence (HSQC) NMR, is more time and labor

intensive, but has the potential to provide substantially more information on lignin structure.

In this study, we performed a deep phenotyping of the lignin polymer of 409 *P. trichocarpa* genotypes by HSQC NMR. By performing a detailed phenotyping of twelve lignin traits in a large population of poplar trees, we found that the lignin composition is highly variable across individuals, with evidence of incorporation of non-canonical monolignols into the polymer of lignin. Subsequently, a GWAS analysis enabled the identification of novel candidate genes that could explain the diversity in lignin composition. Most of the candidate genes identified were not previously reported to be associated with lignin or cell wall biosynthesis. This provides a resource for gaining insights into the molecular mechanisms of lignin biosynthesis and new targets for future genetic improvement in poplar.

2 Materials and methods

2.1 Biomass preparation

Wood samples for this study were collected from three-year-old *Populus trichocarpa* grown in a common garden in Corvallis, OR (44°34'14.81"N 123°16'33.59"W). Site establishment and management practices were previously described by Muchero et al. (Muchero et al., 2015). One-centimeter-diameter increment cores were collected at breast height for the 409 genotypes in January 2013. Cores were stored in zip-lock bags at -20°C before processing. Wood cores were air dried at room temperature before they were ground using Wiley Mini-Mills (Swedesboro, NJ) with a 20-mesh screen. Ground samples were stored in glass vials at room temperature.

2.2 Lignin sample preparation

Each sample was Soxhlet extracted using toluene/ethanol (2:1, *v/v*) for at least eight hours and subsequently air-dried for at 24 hours. Approximately 500 mg of each extractives-free sample was ball-milled for two hours at 600 RPM (at five-minute intervals) on a Retsch planetary ball mill. The ball-milled biomass was then subjected to enzymatic hydrolysis with cellulase (Sigma-Aldrich) in a sodium acetate buffer at 37°C and 200 RPM for 48 hours. The solid lignin enriched residues were then separated *via* centrifugation and lyophilized for 48 hours for NMR analysis.

2.3 NMR analysis

Lignin structure was analyzed by 2D HSQC NMR with a Bruker Avance II 500-MHz spectrometer. Approximately 40 mg of lignin enriched residue was dissolved in 0.5 mL of DMSO-*d*₆ in a 5 mm NMR tube and sonicated for one hour. The Bruker pulse sequence hsqcetgpsip2.2 was utilized on a N₂ cryoprobe with the following parameters: spectra width of 12 ppm in the ¹H dimension with 1024

data points; spectra width of 220 ppm in the ^{13}C dimension with 256 increments and 32 scans. The HSQC spectra were analyzed with Bruker TopSpin 3.5pl6 software. The DMSO- d_6 solvent peak ($\delta_{\text{C}}/\delta_{\text{H}}$ at 39.5/2.49) was used to calibrate the chemical shifts. At least annually, the repeatability and experimental error of the HSQC measurement are quantified by analyzing a standard *Populus* sample. Lignin was isolated from the standard *Populus* sample per the method described above, and three separate samples were analyzed by the same pulse sequence. For this most recent analysis, the standard deviation of the three samples ranged from 0.1 (for H unit) to 1.4 (β -O-4 linkage). The coefficient of variation (CV) may be considered a better measurement of variability, since it is defined as the ratio of the standard deviation to the mean expressed as a percentage. The CVs of the standard *Populus* samples ranged from 1.4% (S unit) to 18.9% (β -5 linkage). A study utilizing ^1H NMR for biomarker analysis identified that larger peaks exhibited a CV of 5–10%, whereas smaller peaks had CV in the 15–30% range (Wang et al., 2013), which is consistent with our observed measurements.

2.4 Genome-wide association study

Whole genome resequencing, single nucleotide polymorphism (SNPs)/nucleotide insertions and deletions (indels) calling and SnpEff analysis for the 917 individuals of this *Populus* GWAS population was previously described by Zhang et al. (2018b). The *P. trichocarpa* Nisqually-1 reference genome v3.1 was used for read alignment and variant calling. The resulting SNP and indel dataset is available at <http://bioenergycenter.org/besc/gwas/>. This study utilized genotypic data for a subset of 409 genotypes from this dataset. To assess genetic control, we used the GEMMA software to calculate kinship for the *Populus* GWAS population as the correction factor for genetic background effects (Zhang et al., 2018b). Genotype-to-phenotype associations were performed using 8,301,860 SNP and indel variants with minor allele frequencies > 0.05. The HSQC spectra from 2D HSQC NMR were used as phenotypes. Statistical significance of associations was evaluated using the Storey's Q-value threshold. Deviation of p-values from normality was assessed using quantile-quantile (Q-Q) plots. Candidate gene identification and RNAseq mapping for co-expression analysis were performed using the *P. trichocarpa* v3.1 reference genome. RNAseq of xylem tissue of 378 *Populus trichocarpa* transgenics plants knockdown or overexpressing monolignol genes and transcription factors involved in the regulation of cell wall biosynthesis were downloaded from the Sequence Read Archive (SRA; accession: PRJNA314500) (Matthews et al., 2021). Library quality was assessed using FastQC (v0.11.9; <https://www.bioinformatics.babraham.ac.uk/projects/fastqc/>), residual adapters and low-quality reads were trimmed using Trimmomatic v0.39 (Bolger et al., 2014) reads were mapped to the reference genome using STAR v 2.7.6a (default parameters and `-outFilterMultimapNmax 100` (Dobin et al., 2013) and transcript per million (TPM) values were extracted for all annotated genes using Stringtie (Pertea et al.,

2015) 18 samples with low mapping rates (<80% of mapped reads) were excluded for the subsequent analysis. Co-expression of candidate genes with 86 phenylpropanoids and lignin-related genes (Table SI 3) was estimated by calculating pairwise Pearson correlation coefficient (PCC) across 360 samples using the function `rcorr()` from the Hmisc R package (Shi et al., 2010; Sundell et al., 2017). For each potential candidate gene, multiple individual scores were calculated: (a) significance threshold of $-\log_{10}(p\text{-value})=6, 7$, and 8 were assigned an individual score of 1, 2, and 3, respectively; (b) connectivity with SNPs was scored according to $\log_{10}(\text{number of connected SNPs})$; (c) connectivity of the SNPs with phenotypes; number and average value of significant co-expression associations ($|PCC| \geq 0.5$, $FDR < 0.001$) with lignin-related genes. All individual scores were scaled to obtain values ranging from 0 to 1. These individual scores were summed to obtain a final overall score, which was utilized to prioritize candidate genes for consideration (higher scoring genes were considered best candidates).

3 Results

3.1 Lignin chemistry

409 unique poplar genotypes were analyzed by HSQC NMR to elucidate structural information for twelve lignin phenotypes, including S units, G units, H unit, PB units, S/G ratio, cinnamyl alcohol end groups (I_{α} , I_{β}), cinnamyl aldehyde end groups (J_{β}), β -O-4 aryl ether linkages, β -5 phenylcoumaran linkages, β - β resinol linkages, and β -1/ α -O- α spirodienone linkages. with results summarized in Figure 1. As expected, the lignin of the *P. trichocarpa* population is comprised primarily of S and G units, with an average of approximately 72.0 and 27.2 units per 100 S+G+H units, respectively. As expected, H units were the least abundant monolignol, averaging 0.8 units per 100 S+G+H units. The quantity of S units was measured to be as low as 58.4% and as high as 82.8%. Similarly, G units ranged from 15.5% to 41.2%. This resulted in a population average S/G of 2.70, though values ranged from 1.42 to 4.96. The next most abundant phenotype was PB. While PB content averaged 4.87%, levels across the population varied significantly ranging from near background (0.39%) to a non-trivial 18.4% – approximately the lower limit of G unit content. However, within ± 0.1 of the average S/G ratio (i.e., 2.60–2.80), PB content ranges from near background levels (1.33%) to 14.6%. To further explore this relationship, the samples were subdivided into a low S/G ratio fraction (<2.70) and a high S/G fraction (>2.70), as shown in Figure 2 (right). In the low S/G ratio sample fraction, the correlation between PB and S/G ratio remains statistically significant, with an average PB content of 5.5%. However, in the high S/G ratio sample fraction, this correlation does not hold, and the average PB content is slightly lower at 4.0%. Additionally, 21 of 24 high PB outliers (i.e., PB >11.3%) appeared in the lower range of S/G ratios, with no high PB outlier coming from a sample with an S/G ratio above 2.77. It was confirmed that the H unit constituted only a minor fraction of the lignin polymer, averaging just 0.91%. However, like PB, H unit

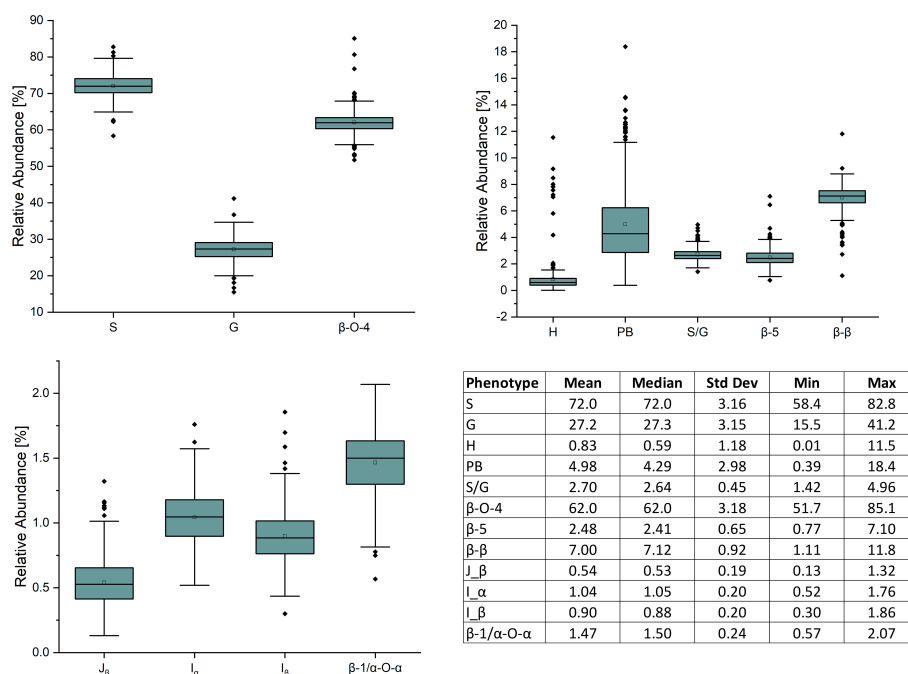


FIGURE 1

Box plot diagrams for the distributions of lignin phenotypes as measured by HSQC NMR – [Top left] syringyl (S), guaiacyl (G), and aryl ether linkages (β-O-4); [Top right] p-hydroxyphenyl (H), p-hydroxybenzoate (PB), syringyl:guaiacyl ratio (S/G), resinol linkages (β-β), and phenylcoumaran linkages (β-5); [Bottom left] cinnamyl aldehyde end groups (J_β), cinnamyl alcohol end groups (I_α/I_β), and spirodienone linkages (β-1/α-O-α). Bottom right: descriptive population statistics of each lignin phenotype.

levels were highly variable, ranging from nondetectable to as high as 11.5%. The β-O-4 aryl ether linkage was by far the most abundant interunit linkage, averaging approximately 62 per 100 aromatic units. It was also the most variable linkage, measuring as high as 85.1% and as low as 51.7%. The β-β resinol linkages were shown to make up a minority of interunit linkages, averaging 7 per 100 aromatic units, with an upper limit of 11.8% and a lower limit of 1.11%. On the other hand, β-5 phenylcoumaran, which averaged 2.48%, ranged from as low as 0.77% to as high as 7.10%. The spirodienone (β-1/α-O-α) linkage was present in small but detectable quantities, averaging 1.47%, but not exceeding 2.07%. The population statistics for these phenotypes are summarized in Table 1. The data is also displayed in box plot form in Figure 1 for a visual comparison. Altogether, the large variations observed in both the subunit content and the type linkages, suggest that a

number of polymorphisms segregating within the population can drastically affect the structure of the polymer of lignin.

3.2 Genome-wide association study (GWAS) of phenotypic variation

To identify the genomic loci controlling lignin phenotypes described above, we performed a GWAS using 409 unrelated *P. trichocarpa* accessions that had genotypic information represented in a panel of > 8.3 million single nucleotide polymorphisms (SNPs) and nucleotide insertions and deletions (indels) as described in the materials and methods. Associations with the phenotypes β-O-4, β-β, β-5, β-1/α-O-α, S, G, H, I, PB, and S/G ratio were tested in this analysis. The GWAS was conducted at increasing significance

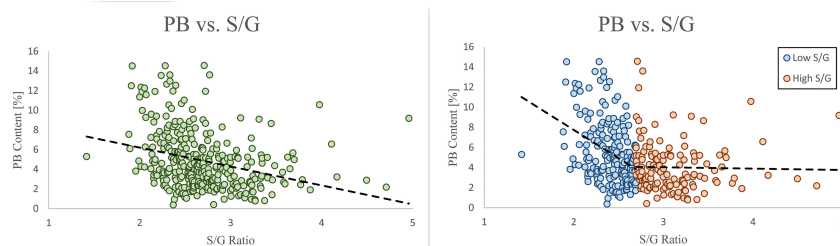


FIGURE 2

The PB and S/G ratio phenotypes have an overall negative correlation (left). This negative correlation is significantly stronger when the S/G ratio < 2.7, and significantly weaker when the S/G ratio is >2.7 (right).

TABLE 1 Summary of a select subset of candidate genes from GWAS results.

Phenotype	Gene ID	p-value	Connectivity with SNPs	Average co-expression with phenylpropanoid genes	Annotation (Arabidopsis alias)
H	Potri.006G169600	8.89E-11	17	0.63	4-coumarate:CoA ligase 2 (4CL2)
H	Potri.001G045100	3.63E-08	2	0.62	cinnamoyl CoA reductase 1 (CCR1)
β -5	Potri.003G059200	8.74E-07	28	0.67	lysophospholipase 2 (CSE)
S	Potri.008G155500	1.16E-07	16	0.58	20S proteasome beta subunit D1 (PBD1)
G		3.69E-09			
S/G		5.46E-08			
S	Potri.006G176600	1.06E-09	27	–	XB3 ortholog 2 in <i>Arabidopsis thaliana</i> (XBAT32)
G		7.88E-09			
S/G		4.52E-07			
PB	Potri.T017000	7.88E-08	1	0.58	glutamine dumper 1 (GDU1)
PB	Potri.T017100	7.88E-08	1	–	glutamine dumper 2 (GDU2)
β - β	Potri.004G077700	7.75E-08	4	0.64	P-loop containing nucleoside triphosphate hydrolases superfamily protein
β -O-4		1.11E-24			
H	Potri.015G082700	3.32E-08	1	0.66	PtrMYB074 (AtMYB50)
β - β	Potri.019G040900	3.72E-08	4	0.57	MYB domain protein 105
PB	Potri.004G073900	7.97E-07	1	–	Pectin lyase-like superfamily protein
PB	Potri.008G099300	8.78E-07	1	0.66	S-adenosylmethionine synthetase family protein (MAT4)
H	Potri.010G064000	1.51E-07	4	0.59	MYB domain protein 79
β -O-4	Potri.004G174200	5.18E-08	2	0.61	proteasome alpha subunit D2 (PAD2)
β -O-4	Potri.008G011100	1.99E-07	1	–	Plant invertase/pectin methylesterase inhibitor superfamily
PB	Potri.014G142000	3.75E-07	1	0.51	galacturonosyltransferase 15 (GAUT15)
I β	Potri.005G163900	1.91E-07	9	–	S-adenosyl-L-methionine-dependent methyltransferases superfamily protein (OSU1)

The full list of genes identified by GWAS can be found in the Supplementary Information.

Genes are selected based on criteria such as putative cell wall or lignin biosynthesis function, strength of association, connectivity with SNPs, and co-expression with phenylpropanoid genes.

thresholds (i.e., $-\log_{10}(p\text{-value})=6, 7, \& 8$) to differentiate the strength of the associations. At the threshold of $-\log_{10}(p\text{-value})>6$, the GWAS identified 756 genes that were significantly associated with at least one phenotype. The Manhattan plots and associated QQ plots for each lignin phenotype are displayed in [Figure 3](#).

At the lowest threshold ($-\log_{10}(p\text{-value})=6$), a total of 907 unique genes were detected in the vicinity or overlapping with the significant SNPs associated with at least one phenotype. A gene ontology (GO) analysis was performed to detect any enrichment in specific biological function among these candidate genes. A significant enrichment in cell wall related GO terms was detected for the highest significance thresholds ($-\log_{10}(p\text{-value})=7$ and $-\log_{10}(p\text{-value})=8$) ([Supplementary Figure SI 4](#)). The enrichment in cell wall related genes (relative to total number of genes) identified at each of these levels were 1.52, 1.87, and 2.48, respectively, when considering Poplar gene annotations. When considering Arabidopsis gene annotations, a similar trend was observed with the enrichment increasing from 2.70 to 5.79 between the $-\log_{10}(p\text{-value}) = 6$ and $-\log_{10}(p\text{-value}) = 8$ thresholds. The increase in enrichment for specific GO terms for higher GWAS significance thresholds provides evidence that the approach is successful at capturing the most likely causal genes for phenotyping variations in lignin composition, as opposed to a simple random sampling of genes from the genome. At the $-\log_{10}(p\text{-value})=6$ threshold, 32 of the 756 genes identified by GWAS have previously been associated with cell wall biosynthesis in *Populus* or *Arabidopsis*. The GWAS identified several genes (Potri.006G169600, Potri.001G045100 and Potri.003G059200), which are predicted to encode key enzymes of the phenylpropanoids pathway: 4-coumarate: CoA ligase 2 (4CL2), cinnamoyl CoA reductase 1 (CCR1), and caffeoyl shikimate esterase (CSE), respectively. In addition, possible homologs of AtTRA2 (Potri.003G161900) and AtMAT4 (Potri.008G099300) were found associated with H-lignin and PB content ([Table SI 4](#)). In previous studies, perturbations in these two genes induced drastic changes in lignin content and structure in Arabidopsis ([Shen et al., 2002](#); [de Vries et al., 2018](#)). In addition to effector genes directly involved in metabolic pathways, the GWAS highlighted higher level regulators as potential candidates, including major transcriptional regulators. PtrMYB074 (Potri.015G082700), strongly associated with H-lignin content in our GWAS, is a master regulator of secondary cell wall formation in poplar, and was shown to directly regulate the biosynthesis of lignin in wood forming tissues of mutant *P. trichocarpa* ([Chen et al., 2019](#)). Potri.001G346600 encoding a possible homolog of AtMYB21 was also found strongly associated with H-lignin content. In Arabidopsis AtMYB21 promotes flavonol biosynthesis through the regulation of FLS1, and was related to stress response and hormonal signaling ([Zhang et al., 2021](#)).

Interestingly, numerous candidate genes highlighted by this approach are predicted to be involved in the biosynthesis of cell wall polysaccharides, such as Potri.002G135500, a possible homolog of ATRAB6A involved in cellulose biosynthesis ([He et al., 2018](#)). Additionally, Potri.013G082200 and Potri.003G074600 are predicted to be a cellulose synthase (AtCSLD3) and a pectin lyase (AtQRT3), respectively. This GWAS approach also identified a significant association with Potri.001G248700, the closest putative ortholog of the *Arabidopsis* LACCASE 4, shown to be directly involved in lignin polymerization ([Berthet et al., 2011](#)).

The GWAS pointed to several other genes ([Figure SI 4](#); [Table SI4](#)) which have not been previously associated with lignin or cell wall biosynthesis. To highlight top candidates, all genes were scored based on criteria such as strength of association (p -value of nearby SNPs), connectivity with SNPs, and co-expression with phenylpropanoid genes computed from external datasets ([Figure 4](#); [Supplemental Table 1](#)). One of the highest scored candidate genes was Potri.008G155500, which is annotated as 20S proteasome beta subunit D1 (PBD1). This candidate gene was highly associated with 16 SNPs across the S, G, and S/G phenotypes ([Figure SI 4](#)). Another highly scored candidate gene was Potri.006G176600, which is annotated as XBAT32. The XBAT32 associations are peculiar in that this gene exhibits strong associations with the S and G phenotypes, but is not strongly associated with the S/G ratio, as presented in the Manhattan plots in [Supplementary Figure SI 4](#). Together with major regulators such as PtrMYB074, and possible homologs of key biosynthetic enzymes such as AtMAT4 and AtTRA2, as mentioned previously, other candidate genes were found strongly co-expressed with lignin biosynthesis genes across transcriptomes of lignin perturbed poplar transgenic plants ([Figure 4](#)) ([Wang et al., 2018](#)). Notably, this approach highlighted candidates for the formation of PB. Glutamine dumper 1 (GDU1; Potri.T017000), associated with the PB phenotype, was found to be co-expressed with CALD5H3, a key gene in the lignin biosynthesis pathway that is known to influence S/G ratio ([Figure 4](#)). Among the other candidates associated with the PB phenotype, Potri.005G145500 was found negatively co-expressed with PtrCOMT2 and two CSE-encoding genes, involved in lignin biosynthesis in poplar. Potri.005G145500 is a potential ortholog of a group of LBD transcription factors AtLBD37/38/39 that were shown to regulate anthocyanin biosynthesis in Arabidopsis ([Rubin et al., 2009](#)). The candidate genes reported here, as well as other potential candidate genes of interest, are summarized in [Table 1](#). All together, these results demonstrate that the GWAS performed highlighted multiple classes of candidate genes for the biosynthesis of the different moieties and linkages that constitute the lignin polymer.

4 Discussion

An advantage of analyzing 409 *P. trichocarpa* samples by HSQC is that the variation of lignin phenotypes, even those difficult to elucidate by other analytical methods or present at low levels, across the entire population can be better understood. The population statistics of the PB phenotype from this GWAS population was unique as it was the only phenotype which did not conform to a normal (or approximately normal) distribution. *Populus* is one of the few species which contain PB – a free phenolic pendant unit which has been shown to be conjugated to the γ -position of syringyl units ([Stewart et al., 2009](#); [Ralph et al., 2012](#)). The abundance of PB could be of special interest to biorefinery considerations, either by utilizing PB derivatives as value-added products ([Ralph et al., 2019](#)) or as a method of improving biomass deconstruction by increasing the number of ester-linked phenolics ([Sibout et al., 2016](#)). While the biological function and biosynthesis remain largely unknown,

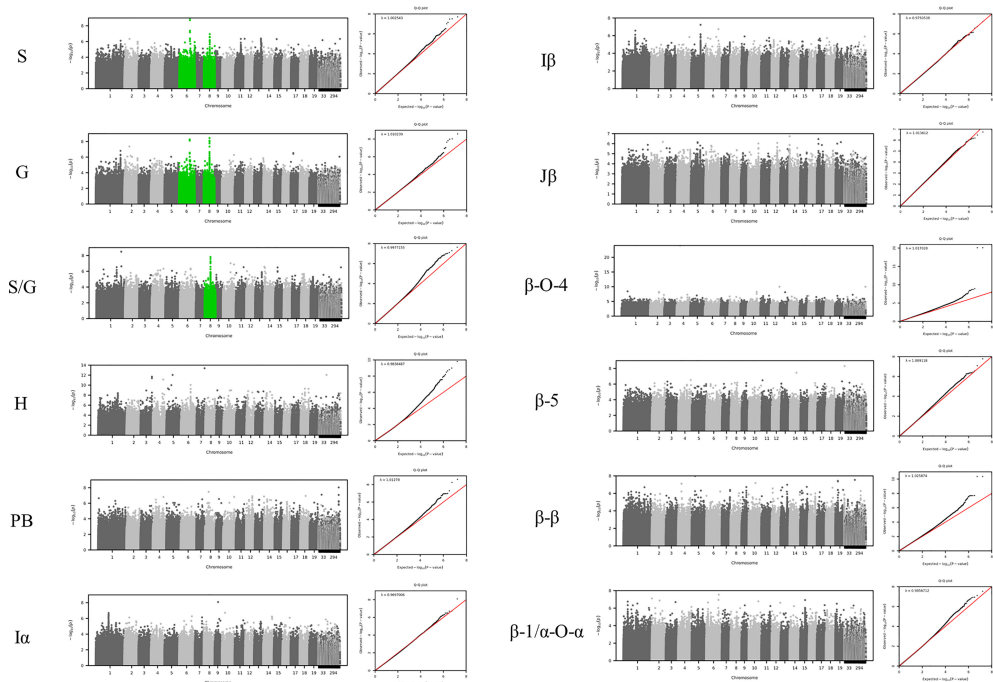


FIGURE 3
GWAS Manhattan plots below display correlations between SNPs and the specified lignin phenotype. Chromosome 8 is highlighted green for the S, G, and S/G phenotypes to indicate a significant association of 20S proteasome beta subunit D1 (PBD1) was observed for each of these phenotypes. Chromosome 6 is highlighted green for the S and G phenotypes to indicate that XB3 ortholog 2 (XBAT32) was significantly associated with these phenotypes. However, Chromosome 6 is not highlighted green for the S/G phenotype to indicate a lack of significant association of XBAT32 with this phenotype.

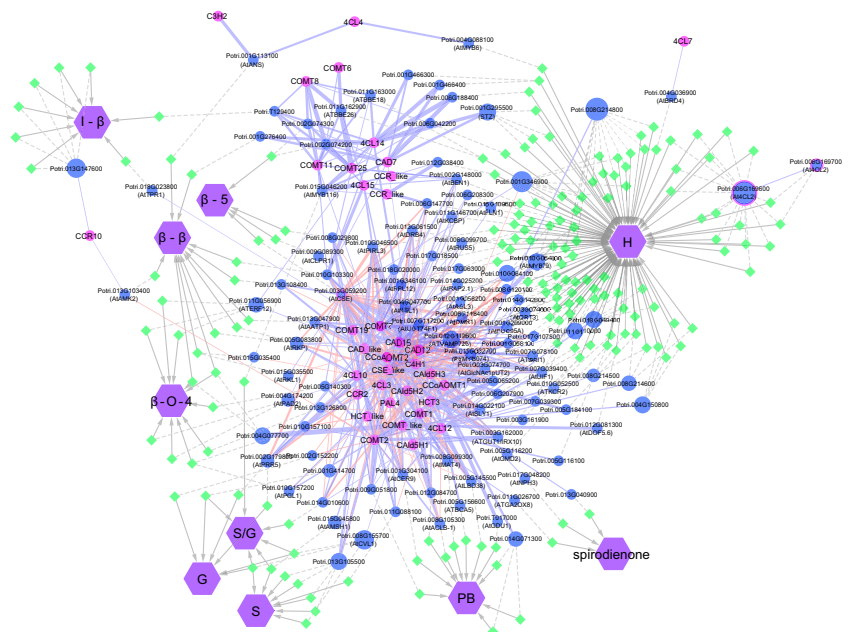


FIGURE 4
Visual representation of the network analysis connecting phenotypes, SNPs, flanking genes, and phenylpropanoid/lignin biosynthesis genes. Genes involved in lignin biosynthesis in *Populus* are named according to Shi et al. (2010). For candidate genes co-expressed with lignin biosynthesis genes, the *Populus* accession number is provided, with the gene alias of the closest *Arabidopsis* match in brackets.

recent work has identified an acyltransferase (Potri.001G44800) which was shown to control *p*-hydroxybenzoylation (de Vries et al., 2021; Zhao et al., 2021). This acyltransferase is co-expressed with lignin biosynthesis genes ferulate 5-hydroxylase/coniferaldehyde 5-hydroxylase (F5H/CAL5H), which have been shown to influence lignin S/G ratio (Baucher et al., 1999; Al-Haddad et al., 2009), which would support an observed relationship between PB and S/G ratio. However, these studies observed changes in PB content without an associated impact on S/G ratio (and other lignin phenotypes), demonstrating that the two can be delineated. Further understanding of PB biosynthesis and its relationship with S/G ratio could provide valuable insight towards engineering lignin for biorefinery applications. For the 409 genotypes considered in this study, PB is negatively correlated with S/G ratio (Figure 2, left), which is consistent with previous observations (Stewart et al., 2009; Yoo et al., 2018). More recently, a similar negative correlation was observed in a collection of 316 *P. trichocarpa* analyzed by saponification and HPLC (Mottiar & Mansfield, 2022). It has previously been hypothesized that PB (and other acylated units) are produced as a method of promoting syringyl-rich lignin. However, a negative correlation between PB and S units suggests this is not the case. Indeed, PB is a non-canonical monolignol that remains poorly understood. Therefore, GWAS associations related to PB may be considered especially interesting and shed new light underlying the genetic mechanisms underlying PB biosynthesis. As previously mentioned, one of the highest scored candidate genes associated with PB is GDU1. This is due, in part, to its co-expression to CAL5H3, which is known to catalyze a key reaction step in the lignin biosynthesis pathway and therefore heavily influence the S/G ratio. Because there is a clear correlation between PB and S/G, one may attribute this to being an artifact of CAL5H3 expression, rather than GDU1. However, manipulation of CAL5H3 in rice did not impact *p*-coumarate (the analogous PB ester in grasses) (Takeda et al., 2017). It has previously been shown that GDU1 is localized at the plasma membrane and is involved with nonselective amino acid export from plant cells into the apoplast (Réjane Pratelli et al., 2012). Export of amino acids (including phenylalanine) increased when GDU genes were overexpressed in *Arabidopsis* (Pratelli et al., 2009). However, the transport mechanism(s) by which lignin monomers are transferred from the cytosol to the apoplast remain unresolved (Perkins et al., 2019). Additionally, the association of glutamine synthesis with ammonia removal following phenylalanine and tyrosine conversion to *trans*-cinnamic acid and *p*-coumaric acid, respectively, early in the lignin pathway, has recently been reported in *Brachypodium distachyon* (Barros et al., 2022). Given such, GDU1 may play a role in preventing excessive accumulation of glutamine associated with the synthesis of lignin precursors. As another point of emphasis, glutamine dumper 2 (Potri.T017100) was also associated with the PB phenotype. Based on these factors, GDU1 could be further evaluated for potential impacts of PB incorporation into the lignin polymer.

The S/G ratio is perhaps the most well-studied lignin trait. Yet, the GWAS analyses identified strong associations with several genes

which have not been previously linked to lignin biosynthesis. This is not entirely surprising, as the formation of the secondary cell wall requires coordination of many metabolic pathways (Zhang et al., 2018a), and as previously mentioned, one highly associated candidate gene is the 20S proteasome gene PBD1. This candidate gene, located on chromosome 8, is strongly associated with the S, G, and S/G ratio. The 20S proteasome has been shown to degrade client proteins to amino-acid residues (Tanaka, 2009). It is also the proteolytic core of the 26S proteasome, which mediates proteolysis and plays a key role in the regulation of critical cellular processes, such as transcriptional control, cell cycle progression, and stress response. Staszczak et al. (Staszczak, 2007), using *in vivo* blocking of proteasome function, indicated that the proteasomal pathway is involved in the regulation of activity of some ligninolytic enzymes (such as laccase) under nutrient deprivation in lignin-degrading Basidiomycete *Phlebia radiata*. The 26S proteasome pathway has been implicated in aspects of secondary cell wall biosynthesis, such as in cotton fiber development (Feng et al., 2018). Transgenic lines exhibited differences in expression of both cellulose and lignin biosynthesis genes, resulting in increased levels of lignin or lignin-like phenolics (Feng et al., 2018). Another strong association identified by the GWAS analysis was XBAT32. The association of XBAT32 is interesting, as it was observed to be associated with the S and G phenotypes independently, but was not observed to be associated with the S/G ratio. This is quite peculiar since the S/G ratio is quite literally the quotient of the S and G unit measurements. Of the three primary monolignols found in poplar, H units are typically present in low abundance (approximately 1%), and as a result, the ratio of S and G units tend to vary proportionally. XBAT32 was initially identified as a regulator of lateral root development in *Arabidopsis* plants with an XBAT32 mutation (Nodzon et al., 2004). It was later shown that XBAT 32 mutants produced increased levels of ethylene (Prasad et al., 2010) and therefore, by extension, plays a role in abiotic stresses response (Prasad & Stone, 2010). Another XBAT protein, XBAT35, has also been shown to be involved in ethylene signaling (Carvalho et al., 2012). A similar gene identified in cotton, GhXB32A, was also shown to function in response to stress (Ge et al., 2021). It is well-documented that stress can induce changes to lignin properties (Moura et al., 2010). It is therefore quite reasonable to implicate the stress related XBAT32 gene could be influencing lignin structure.

In conclusion, the lignin of 409 unique, natural variant *P. trichocarpa* genotypes were analyzed by HSQC NMR. A subsequent GWAS analysis identified 756 SNPs significantly associated among the twelve lignin phenotypes. The GWAS results include putative lignin and cell wall biosynthesis related genes. Subsequent gene ontology analyses show that cell wall related term enrichment increases with GWAS significance levels. These results provide evidence that the GWAS analyses identified causal genes, rather than randomly sampling the genome. Several candidate genes not previously associated with lignin or cell wall biosynthesis were identified by GWAS, including GDU1, PBD1, and XBAT32. These GWAS results can be used as targets for future work investigating lignin structure, and the functional characterization of these genes may reveal novel genetic mechanisms controlling lignin biosynthesis.

Data availability statement

The datasets presented in this study can be found in online repositories. The names of the repository/repository and accession number(s) can be found in the article/[Supplementary Material](#).

Author contributions

J-GC, WM, and AR conceived and designed the study. NB, CY, and YP characterized lignin structure. JZ, KF, MS, RP, and WM conducted the GWAS, GO enrichment, and network analyses. NB, JZ, KF, MS, RP, TT, and WM wrote the manuscript. All authors contributed to the article and approved the submitted version.

Funding

Funding provided by The Center for Bioenergy Innovation, a U.S. Department of Energy Research Center supported by the Office of Biological and Environmental Research in the DOE Office of Science. This manuscript has been authored by UT-Battelle, LLC under Contract No. DE-AC05-00OR22725 with the U.S. Department of Energy. The United States Government retains and the publisher, by accepting the article for publication, acknowledges that the United States Government retains a non-exclusive, paid-up, irrevocable, world-wide license to publish or reproduce the published form of this manuscript, or allow others to do so, for United States Government purposes. The Department of Energy will provide public access to these results of federally sponsored research in accordance with the DOE Public Access Plan (<http://energy.gov/downloads/doe-public-access-plan>). The

views and opinions of the authors expressed herein do not necessarily state or reflect those of the United States Government or any agency thereof. Neither the United States Government nor any agency thereof, nor any of their employees, makes any warranty, expressed or implied, or assumes any legal liability or responsibility for the accuracy, completeness, or usefulness of any information, apparatus, product, or process disclosed, or represents that its use would not infringe privately owned rights.

Conflict of interest

The authors declare that the research was conducted in the absence of any commercial or financial relationships that could be construed as a potential conflict of interest.

Publisher's note

All claims expressed in this article are solely those of the authors and do not necessarily represent those of their affiliated organizations, or those of the publisher, the editors and the reviewers. Any product that may be evaluated in this article, or claim that may be made by its manufacturer, is not guaranteed or endorsed by the publisher.

Supplementary material

The Supplementary Material for this article can be found online at: <https://www.frontiersin.org/articles/10.3389/fpls.2023.1153113/full#supplementary-material>

References

- Al-Haddad Kang, K.-Y., Mansfield, S. D., and Telewski, F. W. (2013). Chemical responses to modified lignin composition in tension wood of hybrid poplar (*Populus tremula* x *Populus alba*). *Tree Physiology* 33 (4), 365–373. doi: 10.1093/treephys/tpt017
- Allwright, M. R., Payne, A., Emiliani, G., Milner, S., Viger, M., Rouse, F., et al. (2016). Biomass traits and candidate genes for bioenergy revealed through association genetics in coppiced European populus nigra (L.). *Biotechnol. Biofuels* 9 (1), 195. doi: 10.1186/s13068-016-0603-1
- Baucher, M., Bernard-Vailhé, M. A., Chabbert, B., Besle, J.-M., Opsomer, C., Van Montagu, M., et al. (1999). Down-regulation of cinnamyl alcohol dehydrogenase in transgenic alfalfa (*Medicago sativa* L.) and the effect on lignin composition and digestibility. 39 (3), 437–447. doi: 10.1023/A:1006182925584
- Barros Shrestha, H. K., Serrani-Yarce, J. C., Engle, N., Abraham, P. E., Tschaplinski, T. J., Hettich, R. L., et al. (2022). Proteomic and metabolic disturbances in lignin-modified *Brachypodium distachyon*. *The Plant Cell* 34 (49), 3339–3363. doi: 10.1093/plccl/koac171
- Berthet, S., Demont-Caulet, N., Pollet, B., Bidzinski, P., Cézard, L., Le Bris, P., et al. (2011). Disruption of LACCASE4 and 17 results in tissue-specific alterations to lignification of *Arabidopsis thaliana* stems. *The Plant Cell* 23 (3), 1124–1137. doi: 10.1105/tpc.110.082792
- Bolger, A. M., Lohse, M., and Usadel, B. J. B. (2014). Trimmomatic: a flexible trimmer for illumina sequence data. *Bioinformatics* (Oxford, England), 30 (15), 2114–2120. doi: 10.1093/bioinformatics/btu170
- Bose, S. K., Francis, R. C., Govender, M., Bush, T., and Spark, A. (2009). Lignin content versus syringyl to guaiacyl ratio amongst poplars. *Bioresour. Technol.* 100 (4), 1628–1633. doi: 10.1016/j.biortech.2008.08.046
- Bryant, N. D., Pu, Y., Tschaplinski, T. J., Tuskan, G. A., Muchero, W., Kalluri, U. C., et al. (2020). Transgenic poplar designed for biofuels. *Trends Plant Sci* 25 (9), 881–896. doi: 10.1016/j.tplants.2020.03.008
- Carvalho, S. D., Saraiva, R., Maia, T. M., Abreu, I. A., and Duque, P. (2012). XBAT35, a novel *Arabidopsis* RING E3 ligase exhibiting dual targeting of its splice isoforms, is involved in ethylene-mediated regulation of apical hook curvature. *Mol. Plant* 5 (6), 1295–1309. doi: 10.1093/mp/sss048
- Chen, H., Wang, J. P., Liu, H., Li, H., Lin, Y.-C. J., Shi, R., et al. (2019). Hierarchical transcription factor and chromatin binding network for wood formation in populus trichocarpa. *Plant Cell* 31 (3), 602–626. doi: 10.1105/tpc.18.00620
- del Río, J. C., Rencoret, J., Gutiérrez, A., Elder, T., Kim, H., Ralph, J., et al. (2020). Lignin monomers from beyond the canonical monolignol biosynthetic pathway: another brick in the wall. *ACS Sustainable Chemistry & Engineering* 8 (13), 4997–5012. doi: 10.1021/acssuschemeng.0c01109
- de Vries, L., MacKay, H. A., Smith, R. A., Mottiar, Y., Karlen, S. D., Unda, F., et al. (2021). pHBMT1, a BAHD-family monolignol acyltransferase, mediates lignin acylation in poplar. *Plant Physiol* 188 (2), 1014–1027. doi: 10.1093/plphys/kiab546
- de Vries, L., Vanholme, R., Van Acker, R., De Meester, B., Sundin, L., and Boerjan, W. (2018). Stacking of a low-lignin trait with an increased guaiacyl and 5-hydroxyguaiacyl unit trait leads to additive and synergistic effects on saccharification efficiency in *Arabidopsis thaliana*. *Biotechnol. Biofuels* 11 (1), 1–14. doi: 10.1186/s13068-018-1257-y
- Dobin, A., Davis, C. A., Schlesinger, F., Drenkow, J., Zaleski, C., Jha, S., et al. (2013). STAR: ultrafast universal RNA-seq aligner. *Bioinformatics* 29 (1), 15–21. doi: 10.1093/bioinformatics/bts635

- Fahrenkrog, A. M., Neves, L. G., Resende, M. F. Jr., Vazquez, A. I., de Los Campos, G., Derwinis, C., et al. (2017). Genome-wide association study reveals putative regulators of bioenergy traits in populus deltoides. *J. New Phytol.* 213 (2), 799–811. doi: 10.1111/nph.14154
- Feng, H., Li, X., Chen, H., Deng, J., Zhang, C., Liu, J., et al. (2018). GhHUB2, a ubiquitin ligase, is involved in cotton fiber development via the ubiquitin–26S proteasome pathway. *J. Exp. Bot.* 69 (21), 5059–5075. doi: 10.1093/jxb/ery269
- Ge, D., Jiang, J., An, X., Wang, L., Pan, T., Liu, K., et al. (2021). Genomics, expression, and function analyses of XB3 family genes in cotton. *Genomics* 113 (1), 245–256. doi: 10.1016/j.ygeno.2020.12.022
- Guerra, F. P., Wegrzyn, J. L., Sykes, R., Davis, M. F., Stanton, B. J., and Neale, D. B. (2013). Association genetics of chemical wood properties in black poplar (*Populus nigra*). *J. New Phytol.* 197 (1), 162–176. doi: 10.1111/nph.12003
- He, M., Lan, M., Zhang, B., Zhou, Y., Wang, Y., Zhu, L., et al. (2018). Rab-H1b is essential for trafficking of cellulose synthase and for hypocotyl growth in arabidopsis thaliana. *J. Integr. Plant Biol.* 60 (11), 1051–1069. doi: 10.1111/jipb.12694
- Li, M., Pu, Y., and Ragauskas, A. J. (2016). Current understanding of the correlation of lignin structure with biomass recalcitrance. *Front. Chem.* 4, 45. doi: 10.3389/fchem.2016.00045
- Liu, Q., Luo, L., and Zheng, L. (2018). Lignins: biosynthesis and biological functions in plants. *Int. J. Mol. Sci.* 19 (2), 335. doi: 10.3390/ijms19020335
- Matthews, M. L., Wang, J. P., Sederoff, R., Chiang, V. L., and Williams, C. M. (2021). A multiscale model of lignin biosynthesis for predicting bioenergy traits in populus trichocarpa. *Comput. Struct. Biotechnol. J.* 19, 168–182. doi: 10.1016/j.csbj.2020.11.046
- Mottiar, Y., and Mansfield, S. D. (2022). Lignin p-hydroxybenzoylation is negatively correlated with syringyl units in poplar. *Frontiers in Plant Science* 13, 938083–938083. doi: 10.3389/fpls.2022.938083
- Moura, J. C. M. S., Bonine, C. A. V., de Oliveira Fernandes Viana, J., Dornelas, M. C., and Mazzafera, P. J. (2010). Abiotic and biotic stresses and changes in the lignin content and composition in plants. *Journal of Integrative Plant Biology* 52 (4), 360–376. doi: 10.1111/j.1744-7909.2010.00892.x
- Muchero, W., Guo, J., DiFazio, S. P., Chen, J.-G., Ranjan, P., Slavov, G. T., et al. (2015). High-resolution genetic mapping of allelic variants associated with cell wall chemistry in populus. *BMC Genomics* 16 (1), 1–14. doi: 10.1186/s12864-015-1215-z
- Nodzon, L. A., Xu, W. H., Wang, Y., Pi, L. Y., Chakrabarty, P. K., and Song, W. Y. (2004). The ubiquitin ligase XBAT32 regulates lateral root development in arabidopsis. *Plant J.* 40 (6), 996–1006. doi: 10.1111/j.1365-3113.2004.02266.x
- Perkins, M., Smith, R. A., and Samuels, L. (2019). The transport of monomers during lignification in plants: anything goes but how? *J. Curr. Opin. Biotechnol.* 56, 69–74. doi: 10.1016/j.copbio.2018.09.011
- Pertea, M., Pertea, G. M., Antonescu, C. M., Chang, T.-C., Mendell, J. T., and Salzberg, S. L. (2015). StringTie enables improved reconstruction of a transcriptome from RNA-seq reads. *Nature Biotechnology* 33 (3), 290–295. doi: 10.1038/nbt.3122
- Porth, I., Klápště, J., Skjya, O., Lai, B. S., Geraldes, A., Muchero, W., et al. (2013). P opulus trichocarpa cell wall chemistry and ultrastructure trait variation, genetic control and genetic correlations. *New Phytol.* 197 (3), 777–790. doi: 10.1111/nph.12014
- Prasad, M. E., Schofield, A., Lyzenga, W., Liu, H., and Stone, S. L. (2010). Arabidopsis RING E3 ligase XBAT32 regulates lateral root production through its role in ethylene biosynthesis. *Plant Physiol.* 153 (4), 1587–1596. doi: 10.1104/pp.110.156976
- Prasad, M. E., and Stone, S. L. (2010). Further analysis of XBAT32, an arabidopsis RING E3 ligase, involved in ethylene biosynthesis. *Plant Signaling Behav.* 5 (11), 1425–1429. doi: 10.4161/psb.5.11.13294
- Pratelli, R., Guerra, D. D., Yu, S., Wogulis, M., Kraft, E., Frommer, W. B., et al. (2012). The ubiquitin E3 ligase LOSS OF GDU2 is required for GLUTAMINE DUMPER1-induced amino acid secretion in arabidopsis. *Plant Physiol.* 158 (4), 1628–1642. doi: 10.1104/pp.111.191965
- Pratelli, R., Voll, L. M., Horst, R. J., Frommer, W. B., and Pilot, G. (2009). Stimulation of nonselective amino acid export by glutamine dumper proteins. *Plant Physiol.* 152 (2), 762–773. doi: 10.1104/pp.109.151746
- Ralph, J., Akiyama, T., Coleman, H. D., and Mansfield, S. D. (2012). Effects on lignin structure of coumarate 3-hydroxylase downregulation in poplar. *Bioenergy Res.* 5 (4), 1009–1019. doi: 10.1007/s12155-012-9218-y
- Ralph, J., Karlen, S., and Mobley, J. (2019). “Synthesis of paracetamol (acetaminophen) from biomass-derived p-hydroxybenzamide,” in *Google Patents* (Washington, DC: U.S. Patent and Trademark Office).
- Rubin, G., Tohge, T., Matsuda, F., Saito, K., and Scheible, W.-R. D. (2009). Members of the LBD family of transcription factors repress anthocyanin synthesis and affect additional nitrogen responses in arabidopsis. *Plant Cell* 21 (11), 3567–3584. doi: 10.1105/tpc.109.067041
- Sannigrahi, P., Ragauskas, A. J., and Tuskan, G. A. (2010). Poplar as a feedstock for biofuels: a review of compositional characteristics. *Biofuels Bioproducts Biorefining* 4 (2), 209–226. doi: 10.1002/bbb.206
- Shen, B., Li, C., and Tarczynski, M. C. (2002). High free-methionine and decreased lignin content result from a mutation in the arabidopsis s-adenosyl-L-methionine synthetase 3 gene. *Plant J.* 29 (3), 371–380. doi: 10.1046/j.1365-3113.2002.01221.x
- Shi, R., Sun, Y.-H., Li, Q., Heber, S., Sederoff, R., Chiang, V. L., et al. (2010). Towards a systems approach for lignin biosynthesis in populus trichocarpa: transcript abundance and specificity of the monolignol biosynthetic genes. *Plant and Cell Physiology* 51 (1), 144–163. doi: 10.1093/pcp/pcp175
- Sibout, R., Le Bris, P., Legée, F., Cézard, L., Renault, H., and Lapierre, C. (2016). Structural redesigning arabidopsis lignins into alkali-soluble lignins through the expression of p-coumaroyl-CoA: monolignol transferase PMT. *Plant Physiol.* 170 (3), 1358–1366. doi: 10.1104/pp.15.01877
- Staszczak, M. (2007). The 26S proteasome of the lignin-degrading basidiomycete phlebia radiata. *Enzyme microbial Technol.* 40 (2), 347–353. doi: 10.1016/j.enzmictec.2006.05.005
- Stewart, J. J., Akiyama, T., Chapple, C., Ralph, J., and Mansfield, S. D. (2009). The effects on lignin structure of overexpression of ferulate 5-hydroxylase in hybrid poplar 1. *Plant Physiol.* 150 (2), 621–635. doi: 10.1104/pp.109.137059
- Sundell, D., Street, N. R., Kumar, M., Mellerowicz, E. J., Kucukoglu, M., Johnsson, C., et al. (2017). AspWood: high-spatial-resolution transcriptome profiles reveal uncharacterized modularity of wood formation in populus tremula. *The Plant Cell* 29 (7), 1585–1604. doi: 10.1105/tpc.17.00153
- Takeda, Y., Koshiba, T., Tobimatsu, Y., Suzuki, S., Murakami, S., Yamamura, M., et al. (2017). Regulation of CONIFERALDEHYDE 5-HYDROXYLASE expression to modulate cell wall lignin structure in rice. *J. Planta* 246 (2), 337–349. doi: 10.1007/s00425-017-2692-x
- Tanaka, K. (2009). The proteasome: overview of structure and functions. *Proc. Japan Academy Ser. B* 85 (1), 12–36. doi: 10.2183/pjab.85.12
- Wang, B., Goodpaster, A. M., and Kennedy, M. A. (2013). Coefficient of variation, signal-to-noise ratio, and effects of normalization in validation of biomarkers from NMR-based metabolomics studies. *Chemometrics Intelligent Lab. Syst.* 128, 9–16. doi: 10.1016/j.chemolab.2013.07.007
- Wang, J. P., Matthews, M. L., Williams, C. M., Shi, R., Yang, C., Tunlaya-Anukit, S., et al. (2018). Improving wood properties for wood utilization through multi-omics integration in lignin biosynthesis. *Nat. Commun.* 9 (1), 1–16. doi: 10.1038/s41467-018-03863-z
- Yoo, C. G., Dumitrache, A., Muchero, W., Natzke, J., Akinoshio, H., Li, M., et al. (2018). Significance of lignin S/G ratio in biomass recalcitrance of populus trichocarpa variants for bioethanol production. *ACS Sustain. Chem. Eng.* 6 (2), 2162–2168. doi: 10.1021/acssuschemeng.7b03586
- Zhang, X., He, Y., Li, L., Liu, H., and Hong, G. (2021). Involvement of the R2R3-MYB transcription factor MYB21 and its homologs in regulating flavonol accumulation in arabidopsis stamen. *J. Exp. Bot.* 72 (12), 4319–4332. doi: 10.1093/jxb/erab156
- Zhang, J., Xie, M., Tuskan, G. A., Muchero, W., and Chen, J.-G. (2018a). Recent advances in the transcriptional regulation of secondary cell wall biosynthesis in the woody plants. *J. Front. Plant Sci.* 9, 1535. doi: 10.3389/fpls.2018.01535
- Zhang, J., Yang, Y., Zheng, K., Xie, M., Feng, K., Jawdy, S. S., et al. (2018b). Genome-wide association studies and expression-based quantitative trait loci analyses reveal roles of HCT 2 in caffeoylquinic acid biosynthesis and its regulation by defense-responsive transcription factors in populus. *New Phytol.* 220 (2), 502–516. doi: 10.1111/nph.15297
- Zhao, Y., Yu, X., Lam, P.-Y., Zhang, K., Tobimatsu, Y., and Liu, C.-J. (2021). Monolignol acyltransferase for lignin p-hydroxybenzoylation in populus. *Nat. Plants* 7 (9), 1288–1300. doi: 10.1038/s41477-021-00975-1



OPEN ACCESS

EDITED BY

Jinchang Ren,
Robert Gordon University,
United Kingdom

REVIEWED BY

Guanghui Niu,
ETH Zürich, Switzerland
Vincenzo Palleschi,
National Research Council (CNR), Italy

*CORRESPONDENCE

Hongwu Tian,
✉ tianhw@nercita.org.cn,
✉ miketian007@163.com

RECEIVED 04 March 2023

ACCEPTED 31 May 2023

PUBLISHED 09 June 2023

CITATION

Zhu Y, Ma S, Yang G, Tian H and Dong D
(2023), Rapid automatic detection of
water Ca, Mg elements using laser-
induced breakdown spectroscopy.
Front. Phys. 11:1179574.
doi: 10.3389/fphy.2023.1179574

COPYRIGHT

© 2023 Zhu, Ma, Yang, Tian and Dong.
This is an open-access article distributed
under the terms of the [Creative
Commons Attribution License \(CC BY\)](#).
The use, distribution or reproduction in
other forums is permitted, provided the
original author(s) and the copyright
owner(s) are credited and that the original
publication in this journal is cited, in
accordance with accepted academic
practice. No use, distribution or
reproduction is permitted which does not
comply with these terms.

Rapid automatic detection of water Ca, Mg elements using laser-induced breakdown spectroscopy

Yijun Zhu^{1,2}, Shixiang Ma^{2,3}, Guiyan Yang^{2,3}, Hongwu Tian^{2,3*} and Daming Dong^{1,2,3}

¹School of Mechanical Engineering, Guangxi University, Nanning, China, ²Research Center of Intelligent Equipment, Beijing Academy of Agriculture and Forestry Sciences, Beijing, China, ³Key Laboratory of Agricultural Sensors, Ministry of Agriculture and Rural Affairs, Beijing, China

Ca, Mg, as the main components in water, are not only essential nutrients for life but are also an important index of water hardness. Rapid detection of the element content is of great significance for water quality evaluation and nutrient balance in planting and breeding water. Traditional laboratory analysis methods are time consuming and involve complex procedures. Ion cross sensitivity and response drift also limit the application of online sensors. These disadvantages are not in line with the precise control and rapid response required for practical applications. Here, we propose a rapid automatic Ca, Mg ion concentration detection method using Laser-induced breakdown spectroscopy. Based on a cation exchange membrane, an automatic control system integrating water sampling, hybrid reacting, attachment drying and spectra measuring was constructed. The testing time for one sample could be compressed to 5 min. Consequently, it met the requirements of accuracy and timeliness of water element regulation. The proposed system can provide new technical means for large-scale aquaculture, soilless cultivation of facilities and other scenarios aiming at accurate measurement and control of elements in water body.

KEYWORDS

laser-induced breakdown spectroscopy (LIBS), automatic detecting system, water hardness, cation exchange membrane (CEM), precise control

1 Introduction

Water is the source of all living beings, Ca and Mg are important elements of the water body [1]. The concentration and proportion of these elements have different impacts on water quality, and these influences affect every aspect of human activity through environmental water circulation [2, 3]. For drinking water, the concentration of Ca and Mg ions is an important evaluation index for water hardness. They not only affect the water taste and aroma, but also the heavy metal toxicity in water. Moreover, subacute health effects such as cardiovascular disease (CVD) and muscle spasms have been proved to be associated with water hardness [1, 4]. Particularly, in aquaculture, Ca and Mg are vital components of shrimp and crab bones, scales and carapaces, and the supplement of Ca and Mg during a critical period plays an important role for assurance of survival rate and yield [5]. As the single source of soilless culture, a slight change of nutrient solution element type and concentration has an obvious effect on crop growth, and crops will quickly show symptoms of deficiency and poisoning [6, 7]. Therefore, in terms of both long-term and short-term

effects, timely detection of Ca and Mg content in water bodies has important practical value for production and daily life.

Atomic Emission Spectroscopy [8] is regarded as an effective tool for trace metal detection in aqueous solutions. Laboratory analysis methods including Atomic Absorption Spectroscopy (AAS) [9], Inductively Coupled Plasma-Atomic Emission Spectroscopy (ICP-AES) [10], and Inductively Coupled Plasma-Mass Spectrum (ICP-MS) [11] have also been widely used. The methods above have the advantages of high detection accuracy and comprehensive indicators. However, requirements for professional operation and a complex process lead to time-consuming detection cycles which cannot satisfy the necessary fast response for practical applications. An electronic conductivity (EC) sensor combined with a pH sensor can be used for online detection of ions in aqueous solution [12, 13]. However, EC values can only reflect the total ion concentration of soluble salt and cannot distinguish the type of ions. As a result, precise composition control cannot be achieved based on EC and pH alone [14]. As an alternative, an ion-selective electrode (ISE) has good selectivity, and it can be used for specific ion detection in solution. Due to the limitations of measurement principle and electrode material, cross-sensitivity and response drift constitute the major obstacle for Ion-selective electrode widely range application [15]. Therefore, a method that can realize the identification of multiple components and meet the requirements of rapid detection is of great importance for the development of water quality monitoring and regulation technology.

Laser-induced breakdown spectroscopy (LIBS) [16, 17], as a spectral detection technology [18–21], uses a high energy laser to ablate the sample surface and the constituent elements are excited into a high-energy plasma. Element type and content are determined by measuring the emission line of the plasma deexcitation. LIBS has the advantage of non-sample pretreatment and multi-component *in situ* rapid detection [22, 23], and it has been widely used in geology [24, 25], industry [26, 27], food [28, 29], biomedicine [30, 31] and other fields, which provides the possibility for the realization of rapid detection of water elements [32]. To avoid water sputtering and absorption of laser energy, researchers made good progress toward overcoming these obstacles by converting water to a jet flow, droplet and spray [33, 34], but the measurement stability could not be guaranteed. Although liquid-solid conversion can significantly improve the stability of the measurements, electrospray deposition (ESD) [35], solid-phase extraction (SPE) [36], and solid-phase microextraction (SPME) [37] have also been demonstrated to improve the limit of detection (LOD), the experimental equipment is complicated and not suitable for practical applications. The combination of LIBS and advanced materials including nano-particles [38, 39], graphene [37], and metal-organic frame (MOF) [40, 41] have been demonstrated for the improvement of water trace element detection sensitivity. The selectivity of specific elements can be further realized by material surface modification. Although the above method can realize highly sensitive detection of water elements, it cannot realize online detection, so it cannot meet the application scenarios which are sensitive to changes of water element content (such as aquaculture, or soilless cultivation in facilities).

Herein, we propose a new water Ca^{2+} and Mg^{2+} online detection system using LIBS combined with cation exchange membranes

(CEM). The integration and automatic control of sampling, reacting, attachment moving, drying, and spectrum measuring procedure was realized and the quantity calibration curves for these two elements were also established. The system can provide technical support for automatic and precise control of water quality in practical production.

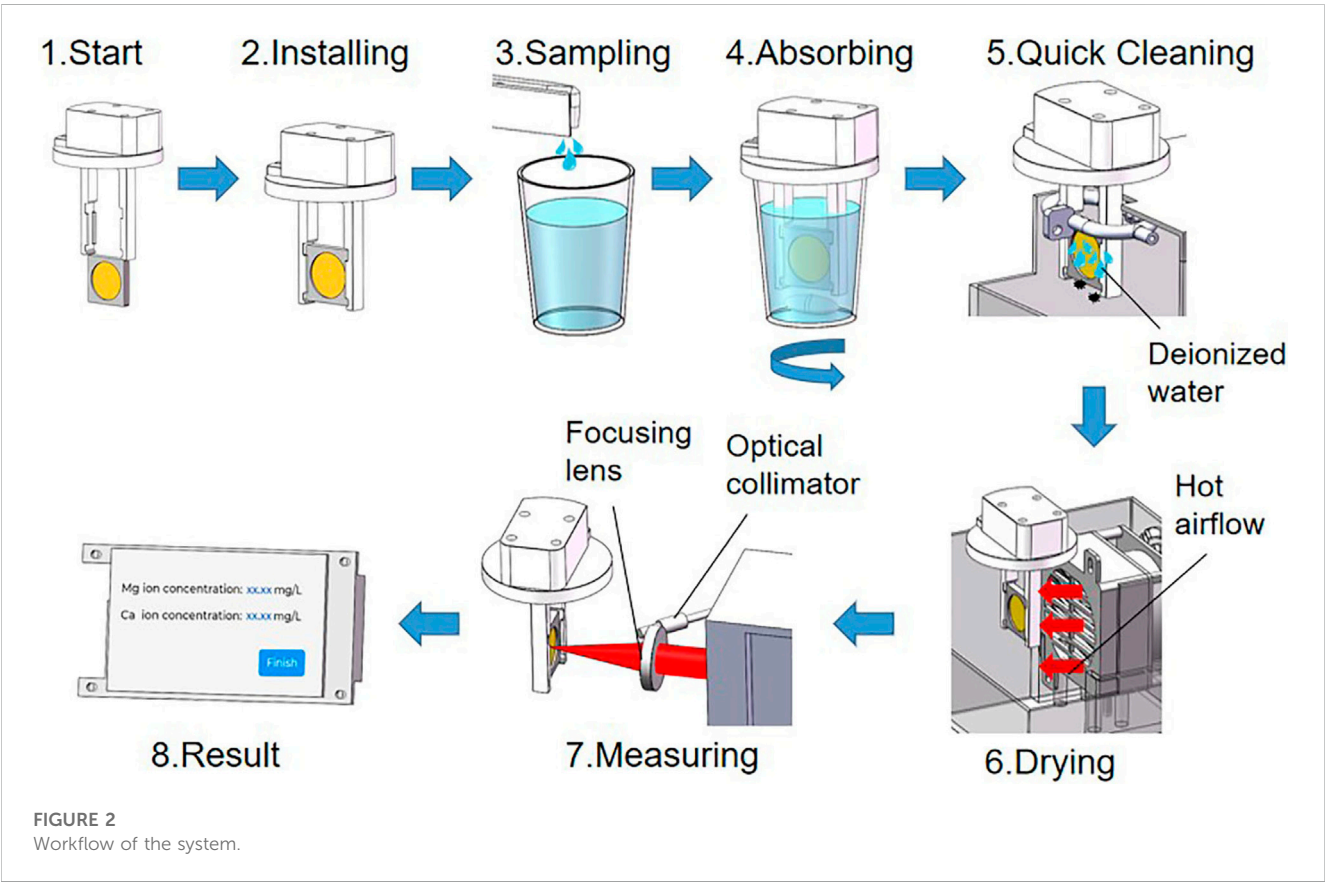
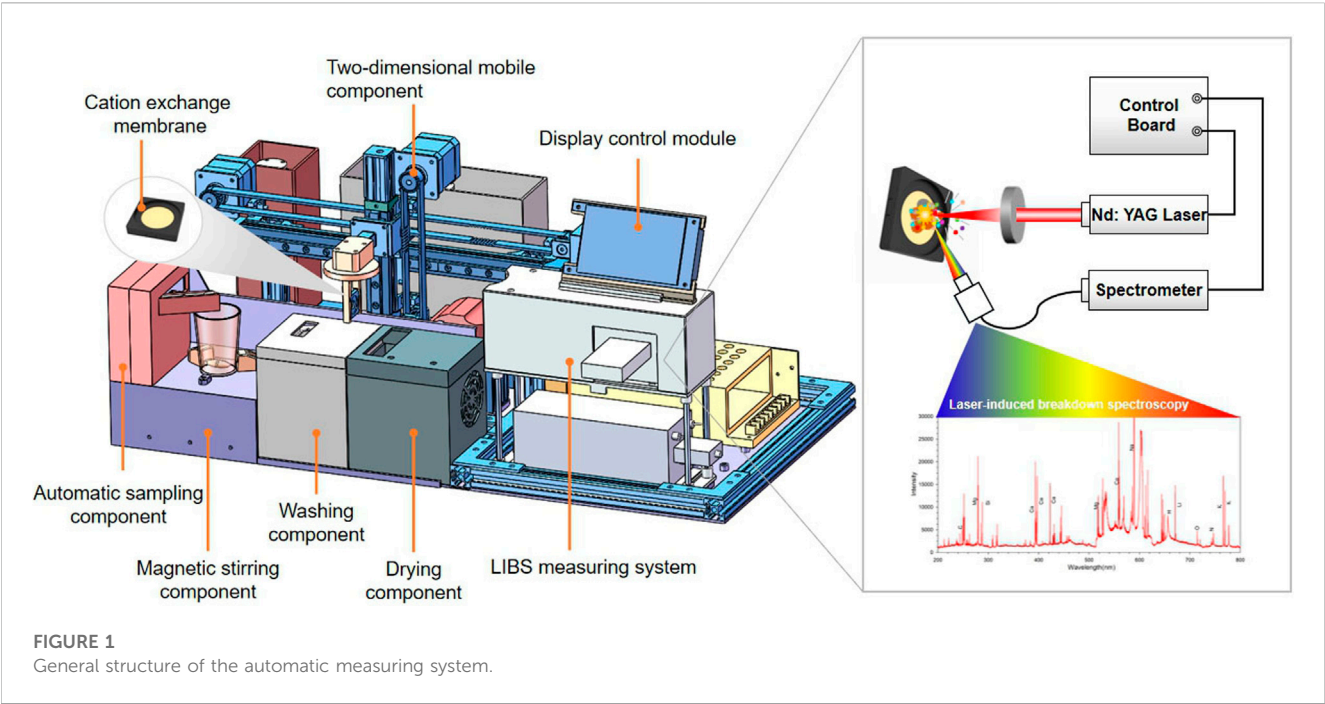
2 Materials and methods

2.1 Experimental samples

The sample solutions used in the experiment were CaCl_2 and MgCl_2 solutions, the concentration of Ca^{2+} was 160 mg/L and Mg^{2+} was 48 mg/L. CEM CMI-7000 S (Membrane International Inc., American) was used as an adsorbent with a thickness of 0.42mm, its exchange group was $\text{SO}_3\text{-Na}$, exchange capacity was 1.6 meq/g, and it was applicable in solution with pH 1–14. Ion exchange is the process of substituting ions between an insoluble solid with exchangeable ions and ions of the same charge in a solution. In this way, CEM can extract other cations from the solution and convert the target ions from liquid to solid state. Therefore, CEM was used as both an adsorbent and spectral-detecting matrix. To ensure the effectiveness of the CEM, it was saturated in 1 mol/L HCl for 24 h and rinsed with deionized water until pH = 7 before it was used. Considering the upper limit of the exchange capacity of CEM, we used 3 cm^2 CEM each time to prevent it from reaching the limit during the exchange of Ca^{2+} and Mg^{2+} .

2.2 Design of automatic measuring system

An automatic device was designed for sample handling and detecting. As shown in Figure 1, the device consisted of an automatic sampling component, an element ion extraction component, a sample cleaning and drying component, and a LIBS spectroscopy measuring system. The workflow of the device is shown in Figure 2. First, the automatic sampling module injected the sample solution directly into the container after the CEM was installed with fixture and started the device. A magnetic stirring device at the bottom of the container ensured that Ca^{2+} and Mg^{2+} were uniformly and fully exchanged on the surface of the CEM. Next, the two-dimensional mobile component held the CEM with a fixture in the sample container. After stirring the sample solution for the set time of the program, the two-dimensional mobile component automatically moved the CEM to the cleaning and drying component successively so that the residuals on the CEM surface can be removed and the moisture interference can be minimized. Deionized water was used for CEM cleaning. The target object Ca^{2+} , Mg^{2+} were absorbed on the CEM surface through covalent bonding which was strong enough that it could not be broken under the water cleaning condition. Therefore, there was no analyte loss during the water cleaning process. At last, the CEM was taken to the detecting position which was precisely the focal plane of the laser. At this point, the LIBS system measured the Ca^{2+} and Mg^{2+} on the CEM and the results were displayed on the screen of the control module. The



CEM exposed area is round, and the position of the CEM surface coincides precisely with the laser focal plane. The spectral intensity of each sample was obtained by averaging five spectra

collected at different positions on the CEM surface. The position switching was realized by the stepper motor to control the vertical movement of CEM in the laser focal plane position.

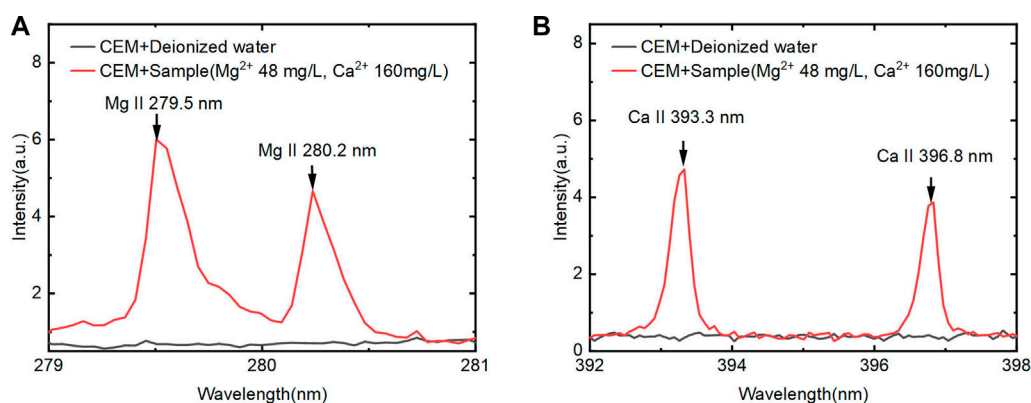


FIGURE 3
Characteristic spectral lines for element (A) Mg. (B) Ca.

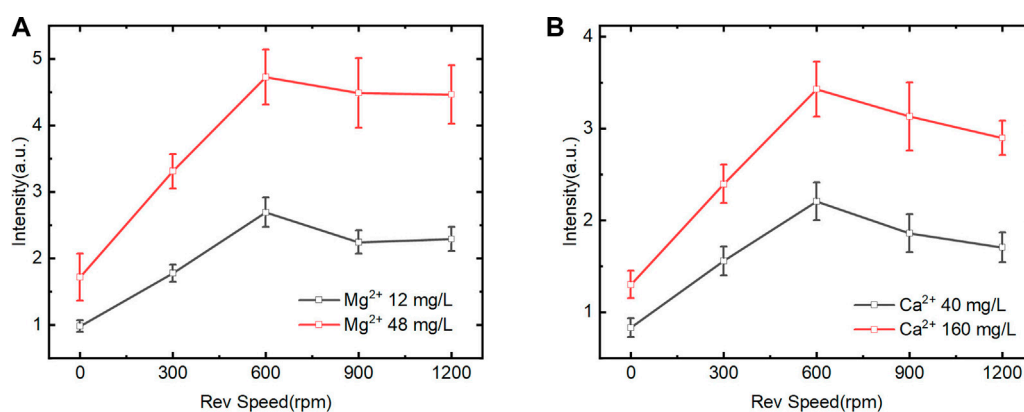


FIGURE 4
Effect of magnetic stirring speed on LIBS spectral intensity of Mg^{2+} and Ca^{2+} (CEM exchange at 3 min) (A). Mg^{2+} on spectral intensity of Mg II 279.5 nm. (B). Ca^{2+} on spectral intensity of Ca II 393.3 nm.

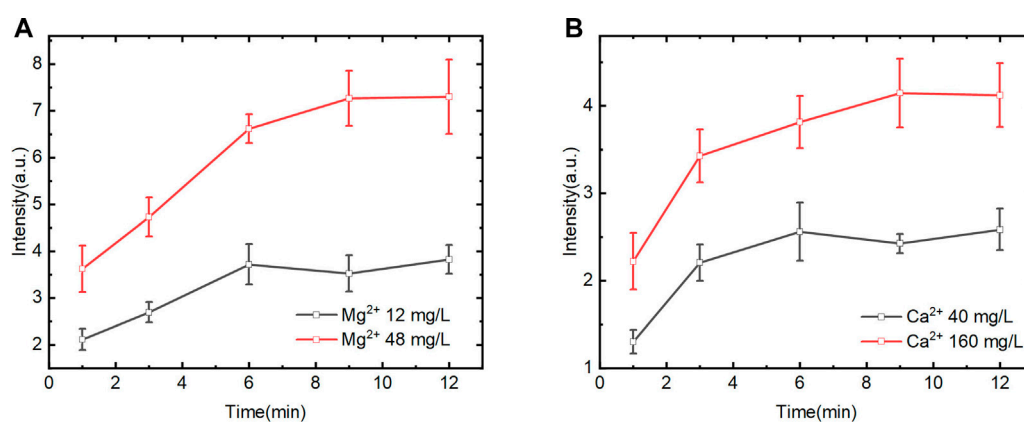


FIGURE 5
Effect of different exchange time on LIBS spectral intensity of Mg^{2+} and Ca^{2+} (magnetic stirring speed of 600rpm) (A). Mg^{2+} on spectral intensity of Mg II 279.5 nm. (B). Ca^{2+} on spectral intensity of Ca II 393.3 nm.

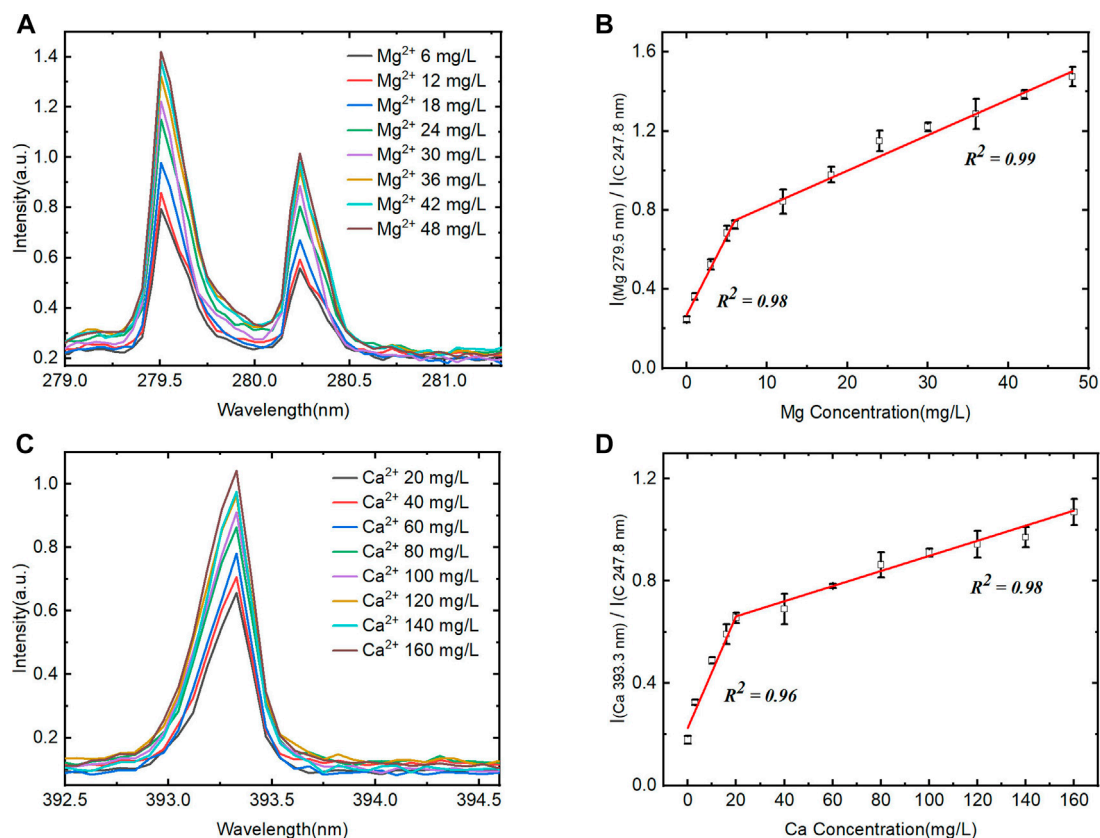


FIGURE 6

Quantification of the system for Mg^{2+} and Ca^{2+} detection. (A) and (B) Averaged LIBS spectra for different concentration of Mg^{2+} and the corresponding calibration curve (0–48 mg/L). (C) and (D) Averaged LIBS spectra for different concentration of Ca^{2+} and the corresponding calibration curve (0–160 mg/L).

TABLE 1 Parameters of the quantitative model.

Element	Detection range (mg/L)	R^2	RMSEC
Mg	6–48	0.99	1.84
Ca	20–160	0.98	7.61

The LIBS measuring system, as shown in Figure 1, mainly included a laser, spectrometer and control board. The laser source was a diode pumped solid state laser (LD201B, Lemeng Company, China) with wavelength 1,064 nm, maximum output energy 50 mJ, pulse width 8 ns, and repetition rate 1 Hz. The spectrometer was a USB2000 + fiber optic spectrometer (Ocean Optics, America), which had a spectral response range of 200–1,100 nm, spectral resolution of 0.2 nm, and signal to noise ratio 250:1. In order to obtain the best spectral, the laser energy was set to 50 mJ, the spectrometer CCD integration gate width was set to 1 ms and the detector sampling delay was set to 1 μ s. The LIBS system worked in paraxial mode, the laser focused on the CEM surface through a focusing lens, and the optic lens collected laser plasma emission spectra from the 45° direction. The focal length of the laser focusing lens is 30 mm. For the

collection of laser plasma, we installed an optical collimator at one end of the optical fiber, and the other end of the optical fiber was connected to the spectrometer. The spectral intensity of each sample was obtained by averaging five spectra collected at different positions on the CEM surface. The position switching was realized by a stepper motor to control the CEM vertical movement in the laser focal plane position.

3 Results and discussion

3.1 LIBS characteristic spectra for Ca and Mg

First, we used the device to detect Ca^{2+} and Mg^{2+} in solution and the spectrums are shown in Figure 3. According to the NIST spectrum library, Ca II 393.3 nm and Mg II 279.5 nm were selected for the characteristic peak of Ca and Mg for further analysis. Figure 3 showed that no spectral signal of Ca^{2+} and Mg^{2+} elements could be observed on blank CEM. However, when CEM was used for Ca^{2+} and Mg^{2+} elements detection, there was no spectral interference near the characteristic peak of Ca and Mg elements. Consequently, it was feasible to use CEM combined with LIBS for Ca and Mg ions determination in solution.

TABLE 2 Determination of Ca²⁺ and Mg²⁺ in spiked samples with and without interfering ions.

Sample number	Ion type and concentration (mg/L)	Mg ²⁺ predictive value (mg/L)	Mg ²⁺ recovery (%)	Ca ²⁺ predictive value (mg/L)	Ca ²⁺ recovery (%)
#1	Mg ²⁺ 16 Ca ²⁺ 70 (Mn ²⁺ 60 Cu ²⁺ 60)	17.5 ± 0.8	109.38	64.5 ± 5.7	92.17
#2	Mg ²⁺ 16 Ca ²⁺ 70	15.4 ± 0.7	96.25	63.4 ± 6.1	90.57
#3	Mg ²⁺ 21 Ca ²⁺ 90 (K ⁺ 180 Fe ³⁺ 60 Cu ²⁺ 60)	22.6 ± 1.1	107.62	88.6 ± 9.1	98.44
#4	Mg ²⁺ 21 Ca ²⁺ 90	20.3 ± 0.9	96.67	88.9 ± 8.6	98.77

3.2 Experimental parameter optimization

The ion extraction of CEM in solution was affected by many factors, including the CEM dosage (size), solution volume, ion concentration, stirring speed and time. In this study, the sample volume was set to 20 mL and CEM size was 3 cm². In order to achieve optimal working condition, we mainly investigated the effects of magnetic stirring speed and adsorption time on spectral signals. As shown in Figure 4, the spectral intensity of Mg²⁺ and Ca²⁺ increased first and then slowly decreased with the stirring speed increased. It indicated that within a certain range of magnetic stirring speed, high speed led to high exchange efficiency between ions on CEM surface and in solution. However, when the magnetic stirring speed exceeded the range, the exchange efficiency reduced. The reason was that excessive speed led to unstable ion exchange reaction and there was not enough time for Ca²⁺ and Mg²⁺ forming stable chemical bonding with CEM matrix. The inadequate reaction also led to weak spectral intensity. Based on above, we chose the magnetic stirring speed of 600 rpm to get good spectrum.

We further investigated the effect of time on spectral intensity. Figure 5 shows that the spectral intensity of Mg²⁺ and Ca²⁺ increased at first and then stabilized gradually with time. It illustrates that the reaction between the exchange group of CEM and the Mg²⁺ and Ca²⁺ in the solution progressed gradually from a rapid reaction to a dynamic equilibrium state. Moreover, the exchange efficiency of Mg²⁺ in different concentrations kept stable from 1–3 min and 3–6 min. In contrast, the CEM exchange efficiency of Ca²⁺ with different concentrations was high from 1 to 3 min and gradually decreased after 3 min. Within 3–6 min, the Ca²⁺ exchange reaction rate decreased and was in the transition stage from rapid exchange to exchange equilibrium. After 6 min, the ion exchange reaction reached equilibrium and the spectral intensity kept in a certain range. To achieve quantitative analysis, 3 min was selected as the adsorption time for rapid determination. This time point was in the linear range of ion exchange reaction and the CEM could be prevented from reaching adsorption saturation state at the same time.

3.3 Calibration curve construction for element Mg and Ca

Aiming to verify the detection ability of the automatic device for Ca and Mg in solution, the quantification model was established using characteristic spectral lines of Mg II at 279.5 nm and Ca II at 393.6 nm with C I 247.8 nm as the internal standard. The spectrums and calibration curves are shown in Figure 6. The spectral intensity increased with the increase of the Mg²⁺ and Ca²⁺ concentrations, but the trend is nonlinear. Inflection points turn out at Mg 5 mg/L and Ca

20 mg/L, and the whole range can be divided into two parts, in which the signal intensity shows linear variety with the concentration gradient change separately. Moreover, the slope in the low concentration part (Mg²⁺ 0–5 mg/L and Ca²⁺ 0–20 mg/L) is obviously high than that in high concentration. The reason might be that the ion exchange speed was high in high concentration difference between target ions and exchange groups in the CEM matrix under certain setup parameters including stirring speed and time. Meanwhile, the other part of the curve also shows linear after the inflection point and does not appear nonlinear caused by the self-adsorption effect.

In the calibration curve, the signal intensity is not zero when the Ca²⁺ and Mg²⁺ analyte concentrations are zero, which is probably due to the interference of other element lines emitted close to the wavelength. Meanwhile, in the real water sample, the emitted lines intensity of Ca and Mg are much higher than that of interferential element on the CEM matrix, so it does not represent to be a problem for real sample quantitative analysis. Moreover, the purpose of the device and method is to meet the detection needs of Ca²⁺ and Mg²⁺ concentrations in the real water sample, and their concentrations are mainly in the linear range of the second part of the calibration curve. Therefore, we choose the second part of the calibration curve for quantitative analysis, and the correlation coefficient R^2 for Mg is 0.99 and Ca is 0.98.

We also investigated a new definition for the LOD of a given element in a univariate calibration. We used the linear part of the calibration curve at low concentrations to calculate the LOD by Eqs 1, 2, [42]. The LOD of Mg is 1.63 mg/L and that of Ca is 3.62 mg/L. Then, in the second part of the calibration curve, root-mean-square error (RMSE) was calculated using Eq. 3, and more detailed parameters of the quantitative model are shown in Table 1. Furthermore, we verified the prediction ability of the established mode by calculating the standard recovery rate of samples with and without interfering cations. The results are shown in Table 2. The results demonstrate that the device is applicable for the automatic rapid detection of Mg²⁺ and Ca²⁺ in solution.

$$LOD = \frac{3.3\sigma_{y/x} \sqrt{1 + \frac{\bar{C}^2}{(C_i - \bar{C})^2}}}{b} \quad (1)$$

$$\sigma_{y/x} = \frac{\sqrt{(I_i - \hat{I}_i)^2}}{N} \quad (2)$$

In Eqs 1, 2, N represents the number of points in the calibration curve, b is the slope of calibration curve. I_i are spectral signal, \hat{I}_i are the value predicted by the calibration curve. C_i are the concentrations of the standards, \bar{C} is the average of these concentrations.

$$RMSEC = \sqrt{\frac{(Y_i - Y_i^{pre})^2}{n}} \quad (3)$$

In Equation 3, n is the number of points in the calibration curve. Y_i are the concentrations of the standards, Y_i^{pre} are the predicted value of the concentrations.

4 Conclusion

In this study, an automatic and rapid system for measuring calcium and magnesium in water was developed based on LIBS. The system realized the automation of the detection process through integration of sampling, elements adsorption, attachment moving, and spectrum detection. The system also achieved automatic enrichment and spectral measurement of calcium and magnesium in water within 5 min. Moreover, we analyzed the quantitative ability of this system for Ca and Mg elements. The results showed that there was a good linear relationship between spectrum intensity and concentration of the two elements. In general, a rapid measuring system for calcium and magnesium in water based on LIBS technology is proposed. Errors introduced by manual operation were significantly reduced through establishing standard sample operating process. Furthermore, the combination of LIBS rapid detecting technique and an automatic control system is expected to provide equipment and technology support for Ca and Mg detection in water bodies under large-scale production modes, such as aquaculture and factory farming.

Data availability statement

The raw data supporting the conclusion of this article will be made available by the authors, without undue reservation.

Author contributions

YZ was responsible for the design of the device, the implementation of the experiment, and the visualization of the experimental data. SM

wrote the draft and analyzes the experimental data. GY contributed to the analysis of experimental data, experimental implementation and supervision. HT conceived the experimental ideas, proposed the experimental methods, wrote the draft, and modified the final manuscript. DD provided financial support and process supervision. All authors contributed to the article and approved the submitted version.

Funding

This research was financially supported by National Natural Science Foundation of China (32171627), Distinguished Scientist Development Program of Beijing Academy of Agriculture and Forestry Sciences (JKZX202209) and National Agricultural Major Science and Technology Project of China (NK2022180102).

Acknowledgments

We thank Alison McGonagle, from Liwen Bianji (Edanz) (www.liwenbianji.cn), for editing the English text of a draft of this manuscript.

Conflict of interest

The authors declare that the research was conducted in the absence of any commercial or financial relationships that could be construed as a potential conflict of interest.

Publisher's note

All claims expressed in this article are solely those of the authors and do not necessarily represent those of their affiliated organizations, or those of the publisher, the editors and the reviewers. Any product that may be evaluated in this article, or claim that may be made by its manufacturer, is not guaranteed or endorsed by the publisher.

References

- Kozisek F. Regulations for calcium, magnesium or hardness in drinking water in the European Union member states. *Regul Toxicol Pharmacol* (2020) 112:104589. doi:10.1016/j.yrtph.2020.104589
- Liang W, Wang X, Zhang X, Niu L, Wang J, Wang X, et al. Water quality criteria and ecological risk assessment of lead (Pb) in China considering the total hardness of surface water: A national-scale study. *Sci Total Environ* (2023) 858:159554. doi:10.1016/j.scitotenv.2022.159554
- Lopes RH, Silva C, Salvador P, Silva ID, Heller L, Uchoa SAD. Surveillance of drinking water quality worldwide: Scoping review protocol. *Int J Environ Res Public Health* (2022) 19(15):8989. doi:10.3390/ijerph19158989
- Monarca S, Donato F, Zerbini I, Calderon RL, Craun GF. Review of epidemiological studies on drinking water hardness and cardiovascular diseases. *Eur J Cardiovasc Prev Rehabil* (2006) 13(4):495–506. doi:10.1097/01.hjr.0000214608.99113.5c
- Sathyanarayan SR, Warke VG, Mahajan GB, Annappure US. Soil free nutrient availability to plants. *J Plant Nutr* (2022) 46(5):801–14. doi:10.1080/01904167.2022.2071736
- Savvas D, Gruda N. Application of soilless culture technologies in the modern greenhouse industry – a review. *Eur J Horticult Sci* (2018) 83(5):280–93. doi:10.17660/eJHS.2018/83.5.2
- Langenfeld NJ, Pinto DF, Faust JE, Heins R, Bugbee B. Principles of nutrient and water management for indoor agriculture. *Sustainability* (2022) 14(16):10204. doi:10.3390/su141610204
- Banerjee P, Prasad B. Determination of concentration of total sodium and potassium in surface and ground water using a flame photometer. *APPLIED WATER SCIENCE* (2020) 10(5):113. doi:10.1007/s13201-020-01188-1
- Ferreira SLC, Bezerra MA, Santos AS, dos Santos WNL, Novaes CG, de Oliveira OMC, et al. Atomic absorption spectrometry - a multi element Technique. *Trac Trends Anal Chem* (2018) 100:1–6. doi:10.1016/j.trac.2017.12.012
- Manousi N, Deliyanni E, Zachariadis G. Multi-element determination of toxic and nutrient elements by ICP-aes after dispersive solid-phase extraction with modified graphene oxide. *Appl Sci* (2020) 10(23):8722. doi:10.3390/app10238722
- Wilschefske SC, Baxter MR. Inductively coupled plasma mass spectrometry: Introduction to analytical aspects. *Clin Biochem Rev* (2019) 40(3):115–33. doi:10.33176/AACB-19-00024
- Sequeira MD, Castilho A, Tavares AO, Dinis P. The rural fires of 2017 and their influences on water quality: An assessment of causes and effects. *Int J Environ Res Public Health* (2023) 20(1):32. doi:10.3390/ijerph20010032

13. Edeki PE, Isah EC, Mokogwu N. Assessment of physicochemical and bacteriological quality of drinking water in Sapele local government area of Delta State, South-South, Nigeria. *J Water Health* (2023) 21:286–98. doi:10.2166/wh.2023.246
14. Lin J-Y, Tsai H-L, Lyu W-H. An integrated wireless multi-sensor system for monitoring the water quality of aquaculture. *Sensors* (2021) 21(24):8179. doi:10.3390/s21248179
15. Krishnakartik M, Satyaveni S, Machiraju PVS. Serological response to SARS-CoV-2 vaccination in multiple sclerosis patients treated with fingolimod or ocrelizumab: An initial real-life experience. *Int J Environ Anal Chem* (2022) 102(1):39–43. doi:10.1007/s00415-021-10663-x
16. Radziemski L, Cremers D. A brief history of laser-induced breakdown spectroscopy: From the concept of atoms to LIBS 2012. *Spectrochimica Acta B: At Spectrosc* (2013) 87:3–10. doi:10.1016/j.sab.2013.05.013
17. Evans EH, Pisonero J, Smith CM, Taylor RN. Atomic spectrometry update: Review of advances in atomic spectrometry and related techniques. *J Anal At Spectrom* (2020) 35(5):830–51. doi:10.1039/d0ja90015j
18. Guo Z, Chen P, Yosri N, Chen Q, Elseedi HR, Zou X, et al. Detection of heavy metals in food and agricultural products by surface-enhanced raman spectroscopy. *Food Rev Int* (2023) 39 (3):1440–61. doi:10.1080/87559129.2021.1934005
19. Huang G, Ming YL, Shi W, Chen X, Chen X. Using one-class autoencoder for adulteration detection of milk powder by infrared spectrum. *Food Chem* (2022) 372:131219. doi:10.1016/j.foodchem.2021.131219
20. Chen R, Huang H, Yu Y, Ren J, Wang P, Zhao H, et al. Rapid detection of multi-QR codes based on multistage stepwise discrimination and a compressed mobilenet. *IEEE Internet Things J* (2023):1–1. doi:10.1109/JIOT.2023.3268636
21. Yan Y, Ren J, Zhao H, Windmill JFC, Ijomah W, De Wit J, et al. Non-destructive testing of composite fiber materials with hyperspectral imaging—evaluative studies in the EU H2020 fibreEUSe project. *IEEE Trans Instrum Meas* (2022) 71:1–13. doi:10.48550/arXiv.2111.03443
22. Senesi GS, Harmon RS, Hark RR. Field-portable and handheld laser-induced breakdown spectroscopy: historical review, current status and future prospects. *Spectrochimica Acta Part B: At Spectrosc* (2021) 175:106013. doi:10.1016/j.sab.2020.106013
23. Zhang Y, Zhang T, Li H. Application of laser-induced breakdown spectroscopy (LIBS) in environmental monitoring. *Spectrochim Acta B* (2021) 1:106218. doi:10.1016/j.sab.2021.106218
24. Botto A, Campanella B, Legnaioli S, Lezzarini M, Lorenzetti G, Pagnotta S, et al. Applications of laser-induced breakdown spectroscopy in cultural heritage and archaeology: A critical review. *J Anal At Spectrom* (2019) 34(1):81–103. doi:10.1039/c8ja00319j
25. Li Q, Zhang W, Tang Z, Zhou R, Yan J, Zhu C, et al. Determination of uranium in ores using laser-induced breakdown spectroscopy combined with laser-induced fluorescence. *J Anal Spectrom* (2020) 35(3):626–31. doi:10.1039/C9JA00433E
26. Legnaioli S, Campanella B, Poggialini F, Pagnotta S, Harith MA, Abdel-Salam ZA, et al. Industrial applications of laser-induced breakdown spectroscopy: A review. *Anal Methods* (2020) 12(8):1014–29. doi:10.1039/c9ay02728a
27. Sheta S, Afgan MS, Hou ZY, Yao SC, Zhang L, Li Z, et al. Coal analysis by laser-induced breakdown spectroscopy: A tutorial review. *J Anal At Spectrom* (2019) 34(6):1047–82. doi:10.1039/c9ja00016j
28. Markiewicz-Keszycka M, Cama-Moncunill X, Casado-Gavaldà MP, Dixit Y, Cama-Moncunill R, Cullen PJ, et al. Laser-induced breakdown spectroscopy (LIBS) for food analysis: A review. *Trends Food Sci Tech* (2017) 65:80–93. doi:10.1016/j.tifs.2017.05.005
29. gSingh J, Kumar R, Awasthi S, Singh V, Rai AK. Laser induced breakdown spectroscopy: A rapid tool for the identification and quantification of minerals in cucurbit seeds. *Food Chem* (2017) 221:1778–83. doi:10.1016/j.foodchem.2016.10.104
30. Moon Y, Han JH, hee CJ, Shin S, Kim YC, Jeong S. Mapping of cutaneous melanoma by femtosecond laser-induced breakdown spectroscopy. *JBO* (2018) 24(3):031011. doi:10.1117/1.JBO.24.3.031011
31. Gaudioso R, Melikechi N, Abdel-Salam ZA, Harith MA, Palleschi V, Motto-Ros V, et al. Laser-induced breakdown spectroscopy for human and animal health: A review. *Spectrochim Acta B* (2019) 152:123–48. doi:10.1016/j.sab.2018.11.006
32. Harmon RS, Senesi GS. Laser-Induced Breakdown Spectroscopy - a geochemical tool for the 21st century. *Appl Geochem* (2021) 128:104929. doi:10.1016/j.apgeochem.2021.104929
33. Meneses-Nava MA, Rosas-Roman I, Barbosa-García O, Rodríguez M, Maldonado JL. Stability evaluation of water droplets levitated by a TinyLev acoustic levitator for laser induced breakdown spectroscopy. *Spectrochim Acta B* (2020) 168(1):105855. doi:10.1016/j.sab.2020.105855
34. Maji S, Kumar S, Sundararajan K. Enhanced laser induced breakdown spectroscopy signal intensity in colloids: An application for estimation of Cu and Cr in aqueous solution. *Spectrochim Acta B* (2021) 175:106010. doi:10.1016/j.sab.2020.106010
35. Ripoll L, Hidalgo M. Electrospray deposition followed by laser-induced breakdown spectroscopy (ESD-LIBS): A new method for trace elemental analysis of aqueous samples. *J Anal At Spectrom* (2019) 34(10):2016–26. doi:10.1039/c9ja00145j
36. Papai R, Sato RH, Nunes LC, Krug FJ, Gaubeur I. Melted paraffin wax as an innovative liquid and solid extractant for elemental analysis by laser-induced breakdown spectroscopy. *Anal Chem* (2017) 89(5):2807–15. doi:10.1021/acs.analchem.6b03766
37. Ruiz FJ, Ripoll L, Hidalgo M, Canals A. Dispersive micro solid-phase extraction (D μ SPE) with graphene oxide as adsorbent for sensitive elemental analysis of aqueous samples by laser induced breakdown spectroscopy (LIBS). *Talanta* (2019) 191:162–70. doi:10.1016/j.talanta.2018.08.044
38. Fazio E, Gokce B, De Giacomo A, Meneghetti M, Compagnini G, Tommasini M, et al. Nanoparticles engineering by pulsed laser ablation in liquids: Concepts and applications. *Nanomaterials* (2020) 10(11):2317. doi:10.3390/nano10112317
39. Dell'Aglio M, Alrifai R, Giacomo A. Nanoparticle enhanced laser induced breakdown spectroscopy (NELIBS), a first review. *Spectrochim Acta B* (2018) 148:105–12. doi:10.1016/j.sab.2018.06.008
40. Papai R, da Silva Mariano C, Pereira CV, Ferreira da Costa PV, de Oliveira Leme F, Nomura CS, et al. Matte photographic paper as a low-cost material for metal ion retention and elemental measurements with laser-induced breakdown spectroscopy. *Talanta* (2019) 205:120167. doi:10.1016/j.talanta.2019.120167
41. Liu X, Liu J, Lin Q, Liao W, Yang T, Qian C, et al. Nanoparticle-assisted metal-organic framework (MOF) enhanced laser-induced breakdown spectroscopy for the detection of heavy metal ions in liquid samples. *J Anal At Spectrom* (2021) 36(10):2173–84. doi:10.1039/d1ja00182e
42. Poggialini F, Legnaioli S, Campanella B, Cocciaro B, Lorenzetti G, Raneri S, et al. Calculating the limits of detection in laser-induced breakdown spectroscopy: Not as easy as it might seem. *Appl Sci* (2023) 13(6):3642. doi:10.3390/app13063642

Frontiers in Physics

Investigates complex questions in physics to understand the nature of the physical world

Addresses the biggest questions in physics, from macro to micro, and from theoretical to experimental and applied physics.

Discover the latest Research Topics

[See more →](#)

Frontiers

Avenue du Tribunal-Fédéral 34
1005 Lausanne, Switzerland
frontiersin.org

Contact us

+41 (0)21 510 17 00
frontiersin.org/about/contact

